E-735

A STUDY OF THE RELATIONSHIP BETWEEN AVERAGE TRANSVERSE MOMENTUM AND CHARGED PSEUDORAPIDITY DENSITY FOR PIONS AND ANTIPROTONS AT TEVATRON ENERGIES

A Thesis

Submitted to the Faculty

of

Purdue University

by

Philip Lawrence Cole

In Partial Fulfillment of the

Requirements for the Degree

of

Doctor of Philosophy

December 1991

For Joyann

ACKNOWLEDGEMENTS

Although E–735 was small on the scale of the behemouth collider experiments, the man and woman hours invested in the design, construction, testing and installation of the separate detectors and the acquisition and analysis of the data is daunting. I thank the senior physicists for providing the political acumen necessary for funding the experiment and bringing E–735 to fruition.

I am particularly indebted to my two advisors, Andy Hirsch and Rolf Scharenberg. Both Andy and Rolf complemented each other; Andy for his skills in analysis and Rolf with his insight into detector design. I learned much from them both. I thank Charles Allen, Young Choi, Norman Morgan and Blair Stringfellow for their dedication and hard-work in designing, constructing and the thorough analysis of the Central Tracking Chamber. I am grateful to Adam Bujak for his friendship and unparalleled wizardry in the arcane art of CTC data acquisition.

I appreciate the many physics tutorials that Frank Turkot always found time for, his ideas and patience. Thanks also to Albert Erwin, Laszlo Gutay, Carlos Hojvat and Seog Oh for their instruction and knowledge. I appreciate the labor and talent Chiho Wang invested in making the E–735 trigger a success.

I won't forget the pleasant company of my two office mates, Jadwiga Warchol and Clark Lindsey, and the countless discussions and arguments triggered by articles in the New York Times. I am indebted to Jadwiga Warchol for her work in the calibration and analysis of the Time of Flight detectors. Her efforts were fundamental to this thesis. Thanks to Clark Lindsey for his work on the barrel hodoscope and leadership in the multiplicity analysis.

Mark Gilkes deserves especial mention for his outstanding efforts in the development of the detector simulation code (More so since his thesis is not related to E–735).

The Amdahl is an unforgiving system and one can easily asphyxiate from the muck of the IBM VM operating system. Chuck Debaun, of the FNAL computing division, taught me much on how to thrive and flourish in such a hostile environment.

To my friends Brajesh Choudhary and Silhacène Aïd, for our many pleasant discussions. And to Theodouros Alexopolous, for his mediterranean wit and making those gritty owl shifts fun.

I owe the completion of this thesis to the love and encouragement given me from both my mother, Deborah, and my brother, Tony. They helped me keep an even keel and weather these tempestuous times of graduate research.

Most importantly, I express my heartfelt gratitude for the loving support of my wife, Joyann Binsley. She was always there and married me despite my pathologically canned response of 'I'll graduate by next year.' I dedicate this work to her.

TABLE OF CONTENTS

LIST OF TABLES

LIST OF FIGURES

ABSTRACT

Cole, Philip Lawrence. Ph.D., Purdue University, December 1991. A Study of the Relationship between Average Transverse Momentum and Charged Pseudorapidity Density for Pions and Antiprotons at Tevatron Energies. Major Professors: Andrew S. Hirsch and Rolf P. Scharenberg.

The transverse momentum of $\pi^{\pm}$ and $\bar{p}$ produced within the pseudorapidity range of $\eta = -0.36$ to $+1.0$ and azimuthal range of $\phi = +2°$ to $\phi = +18°$ has been measured in $\bar{p}p$ collisions at $\sqrt{s} = 546$, 1000 and 1800 GeV. The charged multiplicity of each event was measured by either the 240 element cylindrical hodoscope covering the range $-3.25 < \eta < +3.25$ or the central drift chamber, which spans a pseudorapidity range of 3.2 units. The average transverse momentum as a function of the pseudorapidity density for mass-identified particles is presented. Pseudorapidity densities as high as 30 particles per unit pseudorapidity have been observed.

1. INTRODUCTION

1.1 Backgrounder on the Standard Model

The standard model describes how matter and force interrelate. Matter is composed of either quarks or leptons and these particle interact by exchanging force particles. In this model, there exist six types of quarks (up, down, strange, charm, bottom and top) and six leptons (e, ν_e, μ, ν_μ, τ and ν_τ, where ν denotes the neutrino). Up to now, only the top quark has not been directly identified experimentally. There are four forces in nature, i.e. gravitional, electromagnetic, weak and strong, and gauge particles mediate the forces between matter particles. Quarks and leptons differ primarily in two respects. Whereas quarks are fractionally charged ($2/3e^-$ or $-1/3e^-$), the leptons possess either negative unit or zero charge. Secondly, quarks can interact via all four forces. The leptons, the other hand, do not interact strongly and the neutrino members of the leptons interact only through the weak force.

Gluons are the force particles which bind the quarks together. An assembly of quarks is termed a hadron and hadrons come in two classes: mesons and baryons. A meson is formed of a quark-antiquark pair, $q\bar{q}$, and baryons consist of three quarks (qqq) or three antiquarks ($\bar{q}\bar{q}\bar{q}$). For example, a proton is formed of two up quarks and one down quark (uud) and a π^- meson consists of a $\bar{u}d$ pair.

In 1975, Collins and Perry [1] suggested that for energy densities exceeding the energy density of normal nuclear matter, the color charge of any given quark will be screened by all the other nearby quarks and consequently the colored partons are free to roam throughout the superdense medium, as in a plasma. This dense phase can be achieved by either collapsing hadrons into one another or by exciting the vacuum.

By raising the temperature, new hadrons emerge from the vacuum and thereby serve to increase the energy density [2].

1.2 Brief Review of the Theory

1.2.1 Quark Gluon Plasma

Let us select the laboratory frame and assume that the impact parameter of the two closing nucleons is zero. We envision, then, two Lorentz contracted nucleons with three constituent valence quarks and antiquarks, moving randomly in the transverse direction. In this picture, the total longitudinal and transverse momentum is zero. Furthermore, the longitudinal contraction of the nucleons is limited to the dimension of the matter wavelength of either the up or down quark, which is around 1 fm. Assuming $v \simeq c$, at the moment of impact, the proton and antiproton will occupy the same volume for 3×10^{-24} seconds. As the nucleons interpenetrate, a central 'fireball' of matter is formed in the central region between the two separating baryons [3]. Quantum Chromodynamics (QCD), a theory on the the nature of strong interactions, has agreed remarkably well with experiment. Although the precise mechanism leading to the deconfinement transition from a hadron gas to the a quark gluon plasma (QGP) is not yet known, nonperturbative QCD lattice gauge [4] calculations predict this transition to be of first order. These calculations anticipate a large latent heat or a sharp discontinuity between the two phases for the temperature as a function of entropy density.

For temperatures of 200 MeV, or densities of quarks between $n = 2$ to $n = 4$ particles per cubic fermi, the collision mean free path ($\lambda = 1/n\sigma$), varies between 0.5 and 0.25 fm for $\sigma = 1$ fm^2. Like quarks, gluons are sources of the color field and will interact with other gluons and quarks. In the QGP phase, the number of color degrees of freedom is expected to reach 40 [3], [5] which exceeds the number of degrees of freedom accessible to the hadron gas by one order of magnitude. For mean free paths much smaller than the dimensions of the fireball, the quarks and gluons

can suffer several collisions while in the deconfined state. It is conceivable, then, after a few collisions, these partons could thermalize. As the plasma expands, the energy density decreases and the mean free path increases. When the mean free path extends to the order of the size of the fireball, the partons freeze out. The majority of these partons will combine into pions. However, should three quarks be localized in phase space, they can coalesce into a baryon.

1.2.2 Van Hove Picture

Nonjet, isotropic, high multiplicity events combined with a dependence of the transverse momentum spectrum on the central multiplicity have been observed at the $\bar{p}p$ collider at CERN by UA1 [6] and by E–735 [7], [8] at FNAL. This correlation between the average transverse momentum, $\langle p_\perp \rangle$, and the pseudorapidity has been measured at energies ranging from 540 to 1800 GeV.

Rapidity, y, is the angle of rotation in Minkowski space and is defined as a boost to the frame such that all the momentum is entirely transverse. Mathematically:

$$y = \tanh(\beta \cos\theta)$$

Where θ is the polar angle in the lab frame. The rapidity[1] variable is a useful quantity. Rapidity is additive, i.e. $y = y_1 + y_2$, and the invariant cross section is factorizable in y [9]. Furthermore, particle production in the central region is uniform in rapidity. Pseudorapidity, η is defined as:

$$\eta = \tanh(\cos\theta)$$

As $\beta \to 1$, $\eta \to y$

In 1982, L. Van Hove observed that charged particles produced in the central region displayed two very distinct properties [10]:

1. The multiplicity increases with $\sqrt{s}$.

[1]Alternatively, rapidity can be defined: $y = \frac{1}{2}\ln(\frac{E+p_L}{E-p_L})$ for a particle with 4-momentum $(E, \vec{p})$ and p_L is the longitudinal component of the momentum.

2. There is a multiplicity dependence on the $p_\perp$ spectrum:

$$N = \int_{-y_o}^{y_o} (dN/dy)dy$$

where $|y_o| < 3$.

Property (1) could simply be a kinematic effect. Property (2), however, was not so easily dismissed. In Ref. [6], UA1 plotted the mean transverse momentum of charged hadrons as a function of charged track multiplicity. They found that the $\langle p_\perp \rangle$ increases linearly with charge rapidity density for $dN/dy < 8$. Beyond a dN/dy of 8 charged particles, $\langle p_\perp \rangle$ becomes constant. If one identifies $\langle p_\perp \rangle$ with the combined effects of temperature and transverse expansion and equates the entropy density, σ, with dN/dy, then this relationship between the mean transverse momentum and the rapidity density may signal a phase transition in hadronic matter. Van Hove then argued that experimental data extends only out to the mixed phase or latent heat region of the phase transition.

At higher $\sqrt{s}$, it is conjectured that a second rise will occur. As the number of degrees of freedom in the fireball are exhausted, the excess energy goes into imparting higher transverse momentum to the deconfined partons.

1.2.3 Bjorken Model

In 1953, L. Landau applied a thermodynamic model to describe particle production [11]. The three main assumptions were:

- In a collision, a large fraction of the available energy is dumped into a small region of space in a short period of time.
- The hadronic matter produced in the fireball is treated as relativistic fluid, where the expansion of the fireball is governed by the hydrodynamics of perfect fluids. Most importantly, the entropy is conserved throughout the expansion.
- Once the system achieves thermodynamic equilibrium, hydrodynamic flow begins and lasts only as long as the partons interact.

For an excellent review of the hydrodynamics of QGP, refer to [12].

In 1983, J. D. Bjorken reinvigorated Landau's hydrodynamic model and instilled two more assumptions predicated on recent experimental evidence:

- Particle production is flat in rapidity in the central region.
- There exists a 'leading baryon' effect, where the net baryon number of the collision is found in several units of rapidity away from the central region.

Using this hydrodynamic model of expanding QGP, Bjorken developed a formula which relates the energy density to the charge pseudorapidity density [3]:

$$\epsilon = \frac{3}{2}\frac{dN_c}{d\eta}\frac{(\langle p_\perp\rangle^2 + m_\pi^2)^{1/2}}{\tau_0 \pi r_0^2} \tag{1.1}$$

Where the τ_0 reflects the interaction time for the deconfined partons in the fireball and r_0 is the initial (transverse) radius of the fireball.

Further papers on QGP theory are listed in ref. [13].

1.3 Goal

In the search for a new phase of matter, one wishes to extract clear signals of the quark gluon plasma created in the wake of a colliding proton and an antiproton at Tevatron energies. The experiment E–735, was designed specifically to search for this phase of bulk matter by probing the yield products of $\bar{p}p$ collisions at $\sqrt{s} = 1.8$ TeV. E–735 is a high statistics-minimum bias experiment located at the FNAL Tevatron collider. The experiment collected data from two runs; a five month commissioning run in 1987 and and eleven month run in 1988/89. In this thesis, we discuss the analysis of and the results from the second run. The primary thrust of this thesis will be to extract the relationship between the average transverse momentum, $\langle p_\perp \rangle$ and the pseudorapidity density, $dN_c/d\eta$ for both positively and negatively charged pions and antiprotons at Tevatron energies. The preliminary results of this thesis are published in [14]. E–735 has also pursued other analyses, such as Bose-Einstein correlations

[15], multiplicity and pseudorapidity distributions [16], [17], hyperon production [18], and strangeness production as a function of $p_\perp$ and $dN/d\eta$ [19]. These topics will not be covered in this thesis.

2. ACCELERATOR

We carried out our experiment at the interaction region CØ of the Fermilab Tevatron. Experiment E–735 was one of three experiments which took data in the 1988/89 collider run. The other two experiments were the Central Detector Facility (CDF) located at BØ and E–710 positioned at EØ. CDF is an all-purpose detector designed to measure almost everything and E–710 measures the elastic scattering cross-section and total cross-section of $\bar{p}p$ collisions.

At the time of this writing, the Fermilab Tevatron is the world's most powerful $\bar{p}p$ accelerator. Because the Tevatron Collider makes our experiment possible, I will briefly discuss the design and operation of this machine.

2.1 Multistaging and $\bar{p}p$ production

The Fermi National Accelerator Laboratory, FNAL, consists of a series of accelerators, which inject the beam of charged nucleons to the next accelerator at higher momentum. This multistage arrangement of accelerators provides the most economical and efficient means of accelerating protons and and antiprotons to 900 GeV [20]. Such a design reduces the absolute range over which the magnetic fields must operate on any given machine. Moreover, since the cost of magnets rapidly swells with increasing transverse dimension, one wants to make use of all the available aperture.

Louiville's Theorem offers a way out. Because of the invariance of phase space, the square of the transverse dimension of the beam scales as the reciprocal of the beam momentum. This physical fact is termed adiabatic shrinkage. The multistaging solution makes fine use of adiabatic shrinkage by reducing the aperture of each successive accelerator.

I will first focus on the protons. Before finally attaining an energy of 0.9 TeV, the beam of protons will have traveled through five separate accelerators. The journey begins with injecting Hydrogen nuclei from a gas bottle into the ion source of the Cockroft-Walton electrostatic accelerator. The H^- ions gain an energy of 750 keV. Next the 200 MeV H^- ions are injected from the LINAC into the 8 Gev Booster synchrotron. Thes ions are then directed onto a thin foil and are stripped of their two electrons. These newly formed protons are deflected into a central orbit of the Booster synchrotron and circle back and join the incoming H^- ions in the injection orbit. This process allows for multi-turn injection and increases the intensity of the accelerated beam [22]. There the protons are bunched into 84 'buckets' grouped by a periodic array of Radio Frequency, rf, cavities. These bunches are then accelerated to 8 GeV and injected into the Main Ring accelerator. The Main Ring sychrotron uses conventional bending and focusing magnets and can accelerate protons to 150 GeV. Up until 1982, the Main Ring was the final stage of acceleration (450 MeV) and the name remains as a historical artifact. The Main Ring is one kilometer in radius and resides within the same tunnel as the Tevatron.

Positioned below the Main Ring are the cryogenically cooled superconducting dipole, quadrupole and multipole niobium-nickel-titanium Tevatron magnets. These magnets are cooled to 4° K allowing 4000 amps of current to flow through the dipole and quadrupole coils without resistive impedance. The superconducting magnets can more tightly deflect and focus the protons than by employing conventional magnet technology. This allows for higher energy protons to circulate within the existing ring. The Tevatron accelerates the beam of protons by a factor of 6 over the Main Ring to 900 GeV.

Before $\bar{p}p$ collisions can occur, antiprotons must be produced. In antiproton production mode, protons are accelerated to 120 GeV in the Main Ring. The beam is then extracted and directed onto a copper or tungsten target. Only a minute fraction of these interactions produce an antiproton of the acceptable momentum of 8.9 GeV/c. The antiprotons are then focused by a lithium lens into the debuncher

ring. The accumulated $\bar{p}$'s are then stochasically cooled, so that $\Delta p_\perp$ is minimized. Further details can be found in [21].

2.2 Beam Characteristics

The transverse size of the beam traveling in a synchrotron is characterized by the quantities: the transverse emittance, ϵ, relativistic factor, γ, and the betatron oscillation, described by the lattice β function, one of the Twiss parameters [23]. Betatron oscillation was first observed in the Betatron at the Brookhaven National Laboratory. A quadrupole magnet focuses in one plane transverse to the direction of the beam and simultaneously defocus in the other transverse plane. Pairs of quadrupoles rotated 90° with respect to one another are combined to provide alternating focusing and defocusing in both transverse planes. These focusing/defocusing aspects of quadrupoles gives rise to periodic motion in the direction transverse to the central orbit. The parameter β describes the amplitude of this oscillatory motion. The transverse emittance is a measure of the distribution of position and relative angle of the circulating particles in the beam. 95% of the particles will be contained within a circle of diameter normal to the central orbit:

$$s = \sqrt{\frac{\epsilon\beta}{\pi\gamma}}$$

The luminosity, $\mathcal{L}$, is a measure of the intensity of the beam and is defined:

$$\mathcal{L} = f\frac{BN_pN_{\bar{p}}}{\pi s^2}$$

where

f = the frequency of revolution of the bunches around the ring

B = the number of bunches

N_p = number of protons in a bunch

$N_{\bar{p}}$ = number of antiprotons in a bunch

s = the transverse diameter of the beam

The CDF luminosity at BØ was 10^{30} $cm^{-2}sec^{-1}$. Low β quadrupole magnets located at either end of CDF further squeezed the beam. CØ, however, lacked these low β magnets and consequently the beta amplitude function was bigger at CØ. The ratio of the β factor at BØ to that of CØ for the 88-89 collider run was $\sim$100. Because the diameter of the transverse size of the beam goes as $\sqrt{\beta}$, implies that the luminosity at CØ was 1% that of BØ or $\mathcal{L} = 10^{28}$ $cm^{-2}sec^{-1}$.

Of primary interest to the experimentalist is the rate of collisions. Knowing the number of collisions per second gives the experimentalist a handle on how to best implement the trigger in order to reduce detector dead time and a feeling for what type of statistics to expect as a function of multiplicity. The rate is defined as:

$$R = \mathcal{L}\sigma$$

where σ is the cross-section of the colliding particles. For $\bar{p}p$ collisions at $\sqrt{s} = 1.8$ TeV, $\sigma = 60$ mb. At CØ, then, the rate is 600 Hz (see Appendix A).

3. APPARATUS

The experiment E–735 at the CØ interaction zone of the Tevatron collider was designed to measure centrally-produced charged particle pseudorapidity densities and particle identify low transverse momentum $\pi^{\pm}$'s, $K^{\pm}$'s and $p/\bar{p}$'s. Fig.'s 3.1 and 3.2 give the plan and elevation view, respectively, of the experimental setup.[1] Surrounding the intersection region are hodoscopes, a cylindrical jet multiwire proportional chamber (CTC) and two endcap drift chambers which measure the multiplicity in the central region. Perpendicular to the beam axis is a one arm spectrometer which covers a total solid angle 0.5 sr. The spectrometer consists of a 3.8 kilogauss magnet, tracking chambers and two TOF systems, which together sample momenta spectra up to 3 GeV/c and particle identify low mass hadrons.

3.1 Constraints

3.1.1 Geometrical

Prior to the installation of the Tevatron magnets, CØ was the internal target region of FNAL. In order to ready CØ for the collider run, Fermilab excavated a 400 cm × 203 cm × 45.7 cm pit. This pit provided us room to install azimuthally symmetric detectors surrounding the Tevatron beampipe. Space at CØ was at a premium. The severest geometrical constraint was the proximity of the Main Ring to the Tevatron beampipe. The beampipes and abort lines for both the Main Ring and the Tevatron were contained within cylindrical shells. The distance between the

[1]The CØ coordinate system: $\hat{x}$ points towards the spectrometer arm, $\hat{z}$ points along the collision axis in the direction of flow of the proton beam and $\hat{y} = \hat{z} \times \hat{x}$, forming a right-handed coordinate system.

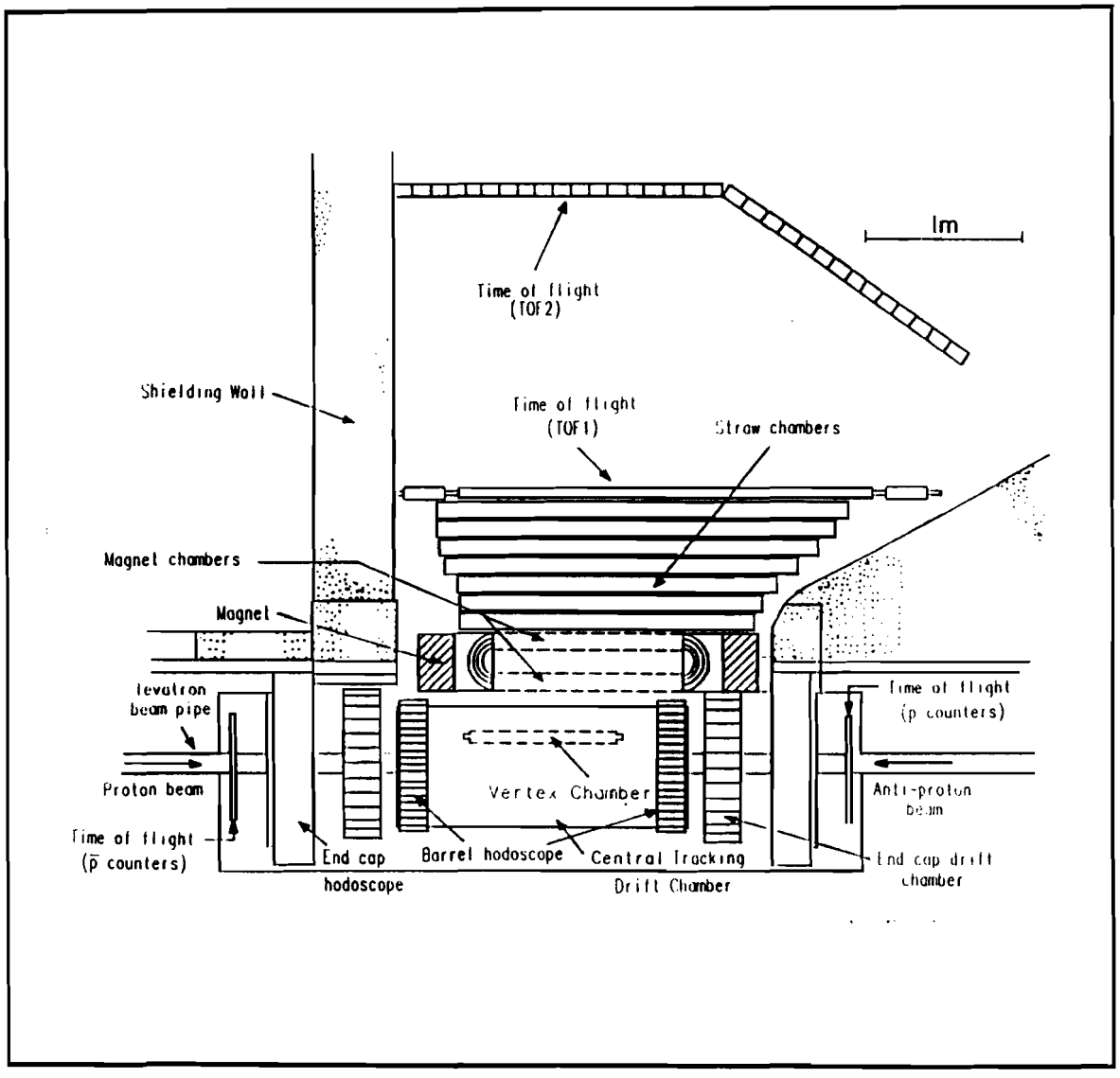

Figure 3.1 Plan view of E–735 apparatus.

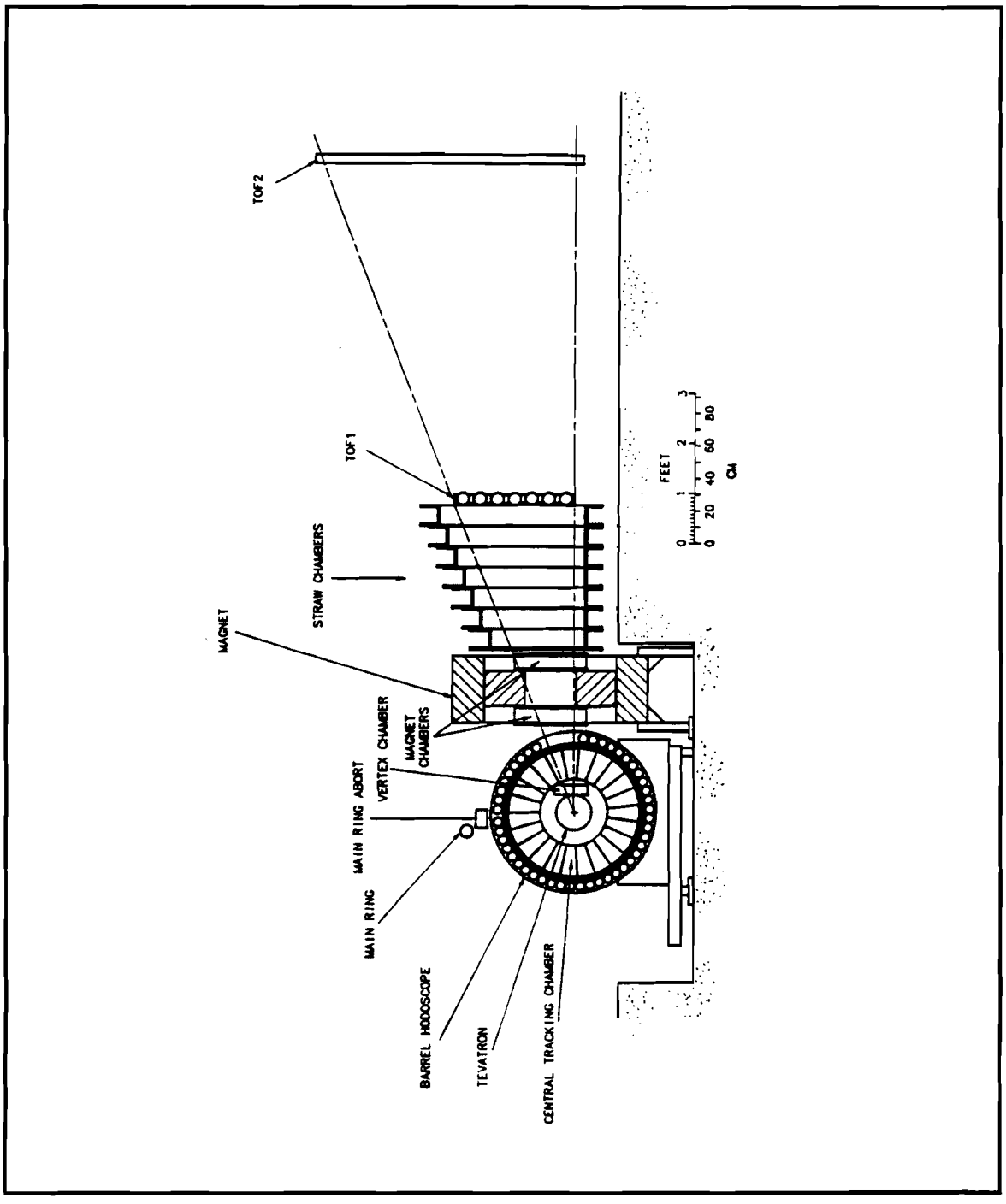

Figure 3.2 Elevation view of E–735 apparatus.

outer radii of these cylinders is 54.6 cm. This means the biggest radial dimension for the CØ detectors surrounding the central region could not exceed half a meter. The asymmetrical geometrical acceptance of the one arm spectrometer was defined and limited by the dimensions of the room adjoining the tunnel. The Lambertson abort magnets used for deflecting the beam out of the Tevatron during a quench[2] defined the length of the experiment and hence the rapidity byte which E–735 could measure.

3.1.2 Radiation

Besides the space limitations, the nearness of the Main Ring beampipe and the abort lines made for a harsh radiation environment. We designed the detectors to withstand this radiation and positioned the preamps and other electronics as far away from the Main Ring as possible. The Main Ring is ramped every 1.2 seconds for antiproton production. The protons in this beam frequently scraped the walls of Main Ring beampipe and produced secondaries which then scattered into our detectors. This source of periodic intense background compelled us to implement additional electronic logic to reduce the harmful effects of radiation. During the Main Ring ramp we lowered the voltages to the detectors to prevent overwhelming the detector electronics. We had, however, no safeguards protecting us against aborts; their very nature is unpredictable. We have measured several Rads of radiation deposited into our detectors during the short time span of an abort. We monitored the radiation online with a proportional counter, which was positioned near the Main Ring, and when the radiation exceeded 1 Rad/hr, we promptly informed the Accelerator Control Room of the radiation loss.

Thermal Luminescent Dosimeters (TLDs) are Lithium Flouride crystals, which are used for measuring radiation dosage [24]. We used nine $3 \times 3 \times 0.9$ mm TLD scintillators contained in separate plastic cylinders of 3 cm length and 0.5 cm outer diameter to measure the radiation loss at CØ. These TLDs were placed in various

[2]A quench occurs when the cryogenically cooled Tevatron magnets go to normal temperatures.

Table 3.1 TLD positions.

TLD identifier	*Location of TLD*
TOF1	Behind TOF1 counters
PIT	Upper edge of pit nearest to tunnel
MR	Main Ring abort beampipe
DVC	Downstream Veto Counter
NAI	Sodium Iodide Detector
PROTON	Downstream trigger hodoscope
PBAR	Upstream trigger hodoscope
UVC	Upstream Veto Counter
SCRCRW	Scarecrow (CØLOSS1) ionization chamber

locations around the experiment [25], [26] (see Table 3.1). We replaced the batches anywhere from once every two to eight weeks depending upon when we could gain access to the tunnel. The retrieved TLDs were then read out and scaled to an equivalent dosage of Roentgens.

The integrated dosage from 31 August 1988 to 31 May 1989, as measured by the nine TLDs, is plotted in Fig. 3.3. The line connecting t_0 to t_1 has been suppressed because of the misleading slope it would give due to the logarithmic scale of the vertical axis — the line would span several decades from zero to the first dosage. The other missing lines indicate corrupted data and consequently this data have not been added to the previous integrated dosage. In Fig. 3.4, the integrated dosage measured by the 'scarecrow'[3] ionization chamber is plotted. Fig. 3.5 is the ratio of the of the radiation recorded by the scarecrow ionization chamber monitor (aka. CØLOSS1) to the dosage measured the i^{th} TLD over the time that a given batch was exposed.

[3]The name is historical, presumably. I have no idea why it is called such.

Ideally, these ratios ought to be flat. Of special interest is the so call SCRCRW TLD, which was mounted directly to the scarecrow ionization chamber. This TLD, in particular, should scale identically with the ionization chamber and it does, more or less. Also note that the PROTON and PBAR TLDs track one another. These two TLDs were mounted on the Tevatron beampipe at opposite points equidistant from the nominal $\bar{p}p$ collision point. In our ten months of running, the scarecrow ionization chamber recorded 11.3 kRads of radiation. All the detectors performed satisfactorily.

E–735 can roughly be divided into two subsets of detectors: Those detectors for measuring the central multiplicity and the detectors used for tracking through the magnet and identifying the particle type. I will call these two components the *Central Region* and the *Spectrometer Arm*.

3.2 Central Region

3.2.1 Central Tracking Chamber

3.2.1.1 Description

The Central Tracking Chamber, CTC, is the heart of the multiplicity tracking in the central region. The CTC is a self-enclosed, slightly overpressured drift chamber that can measure pseudorapidity densities of up to $|dN/d\eta| \simeq 30$. The chamber is fully cylindrically symmetric and samples the pseudorapidity interval: $-1.6 \leq \eta \leq +1.6$. For reasons given in the next section, we chose a design similar to the successful *jet* super-cell drift chamber of the JADE experiment at DESY in Hamburg, Germany. We constructed the endplates and walls of the chamber out of a rigid polymethacrylimide foaming plastic laminated with the composite material Carbon-Fiber Epoxy. This lower mass material presents fewer interaction and radiation lengths than that of standard building materials (see Table 3.2). The chamber is divided into 24 15° sectors, each containing 24 individual detecting elements. These detecting elements record the the x, y and z information of the point where the charged particle interacted with the drift gas. From these spatial points, we can reconstruct the trajectory of the

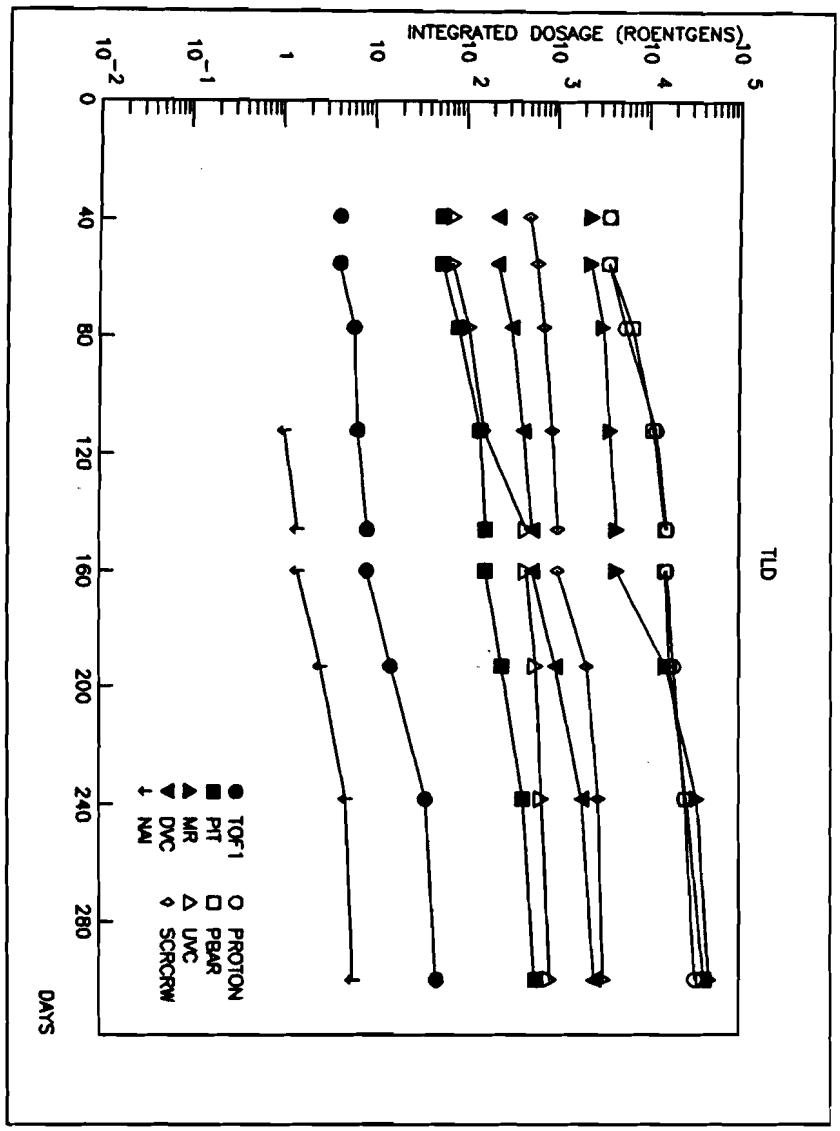

Figure 3.3 Integrated radiation dosage as a function of time as measured by nine separate TLDs which were located at various points around CØ.

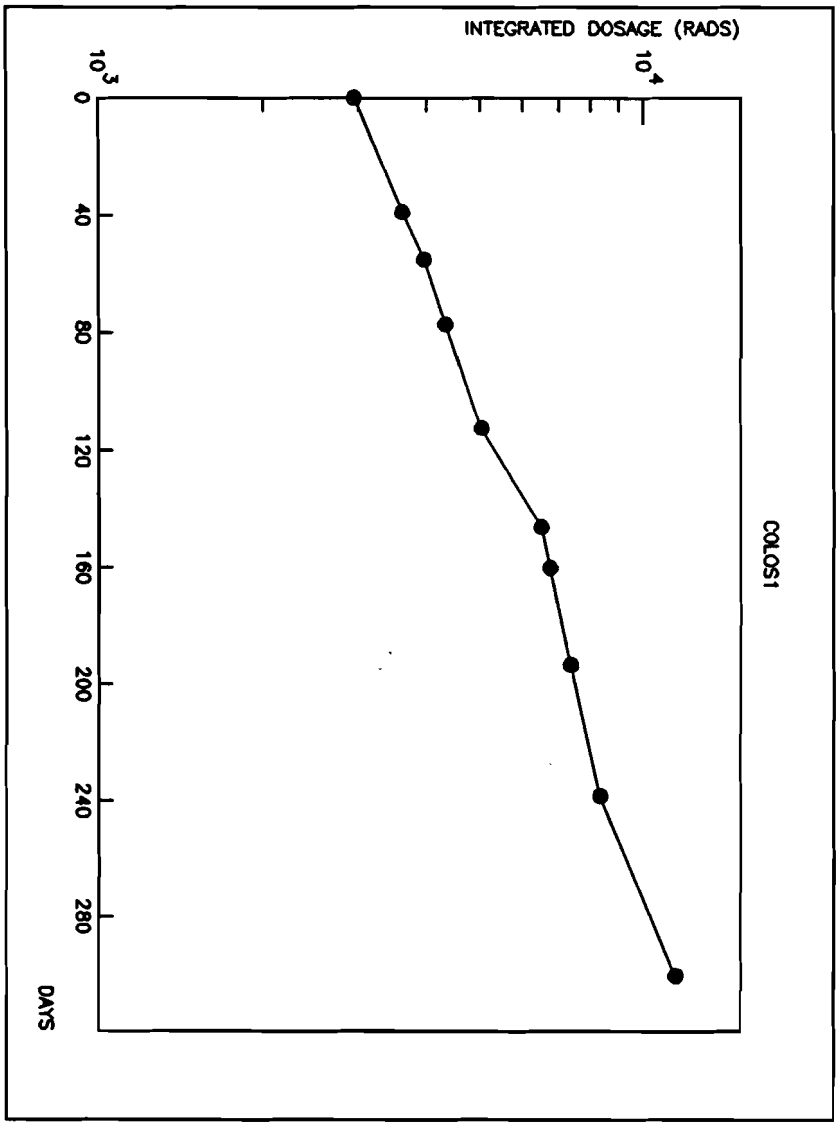

Figure 3.4 Integrated radiation dosage as a function of time as measured by the 'scarecrow' (CØLOSS1) ionization chamber.

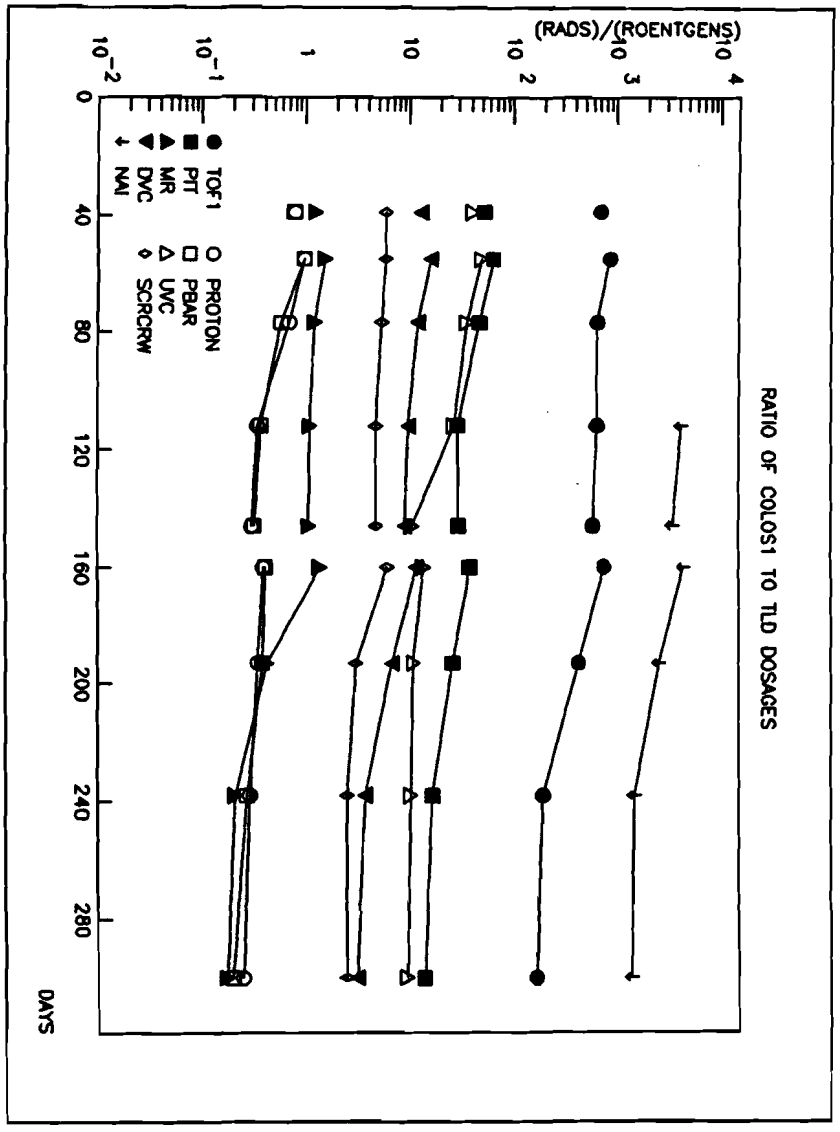

Figure 3.5 Ratio of CØLOSS1 to TLD radiation dosages.

Table 3.2 CTC material presented to charged particle.

Direction	*Density* [g/cm^2]	X_{rad}	X_{int}
Spectrometer	0.18	0.011	0.0016
Barrel Hodoscope	1.20	0.035	0.0140
Endcaps	2.80	0.130	0.0290

charge particle in three dimensions. In the following sections, I will discuss the design considerations and construction techniques of, our operational experience with and the results from the Purdue Central Tracking Chamber.

3.2.1.2 Design Considerations

Accurately reconstructing the trajectories in x, y and z of the 80 or more particles expected to form during the hadronization phase of the expanding quark-gluon plasma, coupled with the high radiation background and geometrical constraints of CØ, placed particularly stringent demands on the design of the drift chamber. To extend the sensitivity of the detector to higher multiplicities and reduce spraying the other detectors with secondaries, we chose to minimize the mass of the chamber structure. Minimizing the mass, of course, introduced more problems. The anode wire is situated in the center of four cathode wires and is in a state of unstable equilibrium. The wire tension determines the amount of droop. We tensioned the wires so that the distance between wires along the length of the chamber did not vary more than a few percent of the nominal interwire distance. We also considered the breaking point or elastic limit of the high tension end. While the accumulated tensions for all the wires give a bulkhead load of nearly 3400 lbs, the compression of the chamber could not exceed 10 mils. This last condition inhibits local variation of interwire

distance by keeping the tensions fixed. The design therefore calls for two nearly dichonomous properties: a low mass yet highly incompressible building material. We found the composite material Carbon-Fiber Epoxy, CFE, suitable for the structural requirements at the unfortunate cost of difficulty to work with. Unlike Aluminum, CFE cannot simply be machined to the desired dimensions. I discuss the construction techniques below. Constructing the chamber out of CFE provided an additional benefit: CØ is not a conditioned environment; the temperature in the tunnel varies with the season. Because CFE has a low coefficient of thermal expansion, the length of the chamber did not perceptively vary with the weather and the tensions stayed fixed. As was discussed in section 3.1, space was at a premium at CØ. Since the barrel hodoscope fits coaxially around the CTC, the maximum allowable outer radii of the CTC and barrel hodoscope were bounded by the Main Ring beampipe and abort line. The harsh background of CØ governed our choice of materials. We selected materials able to withstand a year's exposure of the intense radiation and used a low gain drift gas to minimize space-charge degradation effects.

3.2.1.3 Mechanical Construction

The Central Tracking Chamber is a 2 m long cylindrical annular vessel with an inner diameter of 44 cm and an outer diameter of 84 cm. It was built in two lengthwise halves so that the CTC could be installed without disrupting the Tevatron vacuum. The two halves thus joined straddled the Tevatron beampipe (see Fig. 3.6). The walls and the endplates of the drift chamber are formed of a rigid polymethacrylide foaming plastic ($C_9H_{13}NO_2$) substrate wrapped with layers of Carbon-Fiber Epoxy laminate. The inner (outer) wall was 8 mm (12 mm) thick with 0.9 mm (0.5 mm) of CFE on each face. The endplates were 2.5 cm thick encased with a 1 mm CFE shell. The foaming plastic is known by the product name Rohacell. We chose Rohacell on the basis of its light weight and dimensional stability under heat. It was important that the substrate expand isotropically during the baking process as will soon become clear. Carbon-Fiber Epoxy is the generic name for unidirectional graphite strands

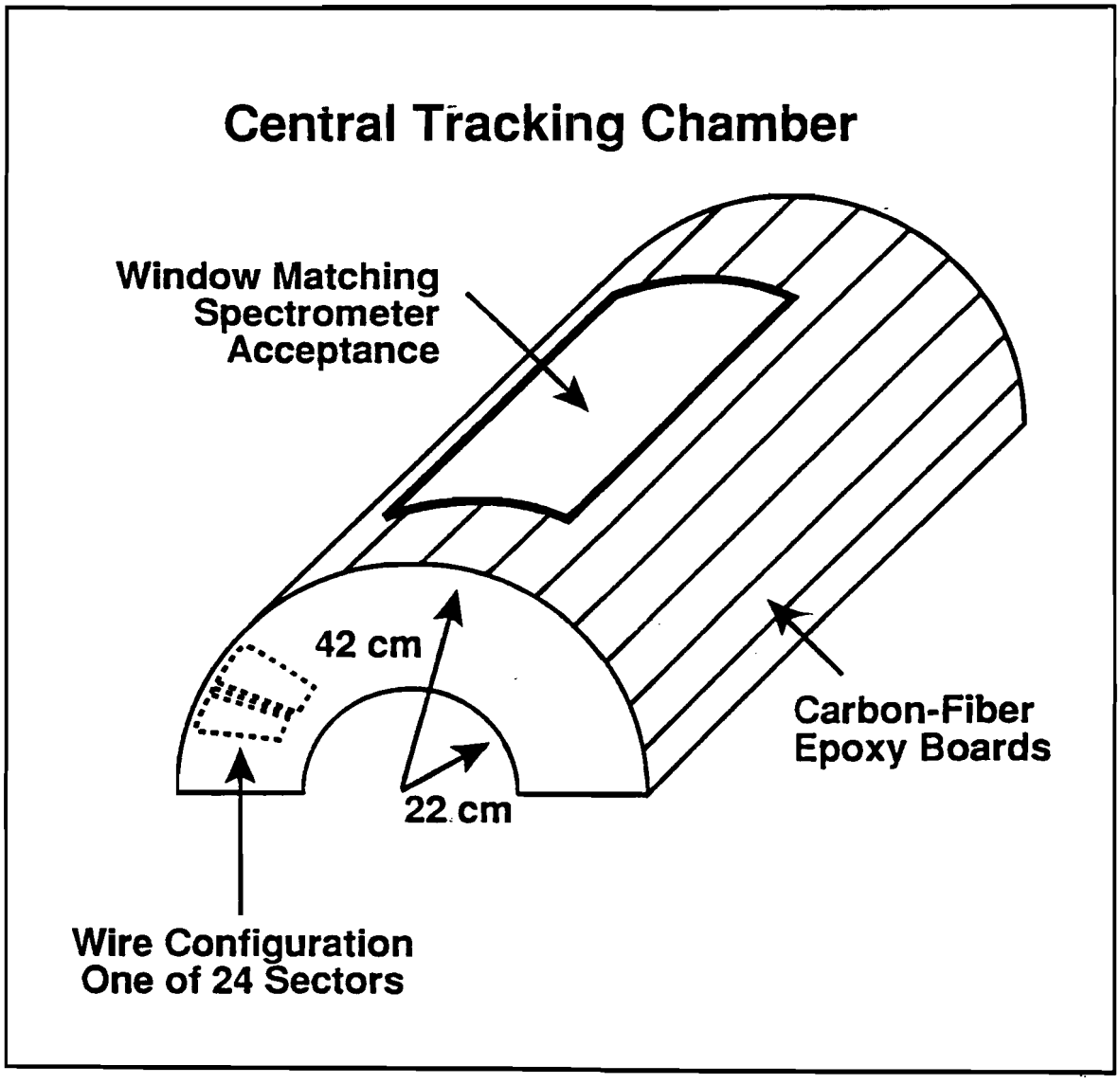

Figure 3.6 Carbon fiber epoxy structure showing one half of the CTC.

embedded in an epoxy matrix. Both the inner and outer walls of each chamber half were made of twelve box beam staves. These staves formed the load bearing members of the CTC structure. The manufacture of the boards was a straightforward albeit painstaking process. Other than sizing the Rohacell to the desired dimensions and blowing off the aggregated crumbs, we did not prepare the surface in any special way. The Rohacell piece was then wrapped with several layers of CFE. We took care to crosshatch the directions of the carbon fibers of each successive layer. This technique increased lateral strength and prevented possible cracking between fiber bundles. After centering the laminated piece on the bottom plate of the precision mold, we set the top plate loosely in place. It required around 15 iterations using an hydraulic jack and involved compression pressures of up to 500 psi to butt the top plate firmly flush against the bottom plate. Compressing in the lateral and longitudinal directions demanded less effort. Next we placed the assembly into a $2.5 \times 1 \times 1$ m oven. The precision mold had been machined to expand to the correct dimensions at 280°F. The mold, coupled with the expansion properties of the Rohacell under heat, defined the configuration of the board. As the rohacell expanded isotropically, it pushed the CFE lamination against the interior surfaces of the mold. Because of the combined thermal inertias of the mold and laminated board, it took approximately 3 hours to bring the interior of the mold to the curing temperature of 280°F when driven at 500°F. Once the board temperature reached 280°F, we turned the oven down to this temperature and let it cure for an additional 2 hours and 10 minutes.

After pulling the mold out of the oven, we let it cool overnight. We soon discovered, to our chagrin, that taking the board out of the mold prematurely, the rohacell would continue to expand—being no longer confined by the mold—and cause the board to puff out and thus become unuseable. Finally we had to file and sand each board. All in all, it took around 30 hours to produce one board. Unfortunately, we suffered an attrition rate of around 50%. This loss was primarily due to temperature gradients in the oven leading to differential heating of the mold. The mold therefore expanded unevenly, causing the board to become warped. Parenthetically, it occurred

to us only after we nearly had produced all the boards that we could have easily circumvented this problem of board warpage. Had we filled the oven with flakes and chips from fire-bricks, the heat in the oven would have been more evenly distributed. Notwithstanding any problems of manufacture, the result gave us a strong low-mass box beam having an average density of 0.3 gm/cm^3.

Besides the standard load-bearing members of the chamber, the design called for the fabrication of specialized boards. For a particle traveling in the direction of the spectrometer aperture, we wished to further reduce the effects of multiple scattering, energy loss and the production of secondaries. We took out the section of the Rohacell-CFE wall subtended by the solid angle of the spectrometer acceptance and replaced it with a Cu-Mylar-Cu (shield-insulator-ground plane) window. We created slotted boards in order to accomodate this window.

We needed to find a way to suffuse and cycle the drift gas without disrupting the electrostatics of the chamber. Simply running a tube into the chamber was unacceptable. We created special boards to house the gas intake of the chamber. We milled a channel lengthwise into the Rohacell piece and in this groove we snugly fit an aluminum tube (outer diameter 5/16″ and inner diameter 1/4″). The lamination, molding, and baking of the gas perfusion board followed standard procedure. In the finished product we drilled five holes with a diameter of 0.025″ into the tube. The holes were spaced at equal intervals and clustered halfway along the length of the board. We produced two such boards for each chamber half. Our calculations showed that these twenty 0.025″ holes were sufficient to exchange one gas volume per day.

Finally, we produced edge boards. That the chamber was constructed in two lengthwise halves necessitated the production of these boards. An edge board for either the inner and outer wall was half the width of the associated standard stave. The surface that joined the opposing edge board was built of 3/16″ CFE. This extra CFE furnished the material into which the holes for the clasps joining the halves could be drilled.

Table 3.3 CTC boards.

Type	*Inner*	*Outer*
Regular	20	16
Window	2	3
Edge	4	4
Gas	0	4

Each endplate half was composed of 24 1″ thick Rohacell-CFE wedges. The fabrication process of the endplate wedges was identical to that of the boards, but were baked in a separate oven. We could produce two to three of these pieces in a day. To form the endplate, these 24 wedges were then wrapped together with three crosshatched layers of CFE, compressed in a master mold and baked a second time.

We assembled the inner and outer walls using a precision polygonal jig. The inner and outer jigs were machined to 30 mil tolerance. In the process of making the barrel structure, we first applied 3-M Scotch-Weld 2216 epoxy to the trapezoidal sides of the boards. We chose this epoxy on the basis of its strength and outgassing properties. We then set the regular and special boards into place upon the jig. Once all the boards were so glued and positioned, we strapped them down securely with several bandclamps along the length of the jig and let them sit for a couple days to allow the epoxy to set.

CFE is not a particularly good conductor. We clad the interior surface of the chamber walls with 36 μm thick copper tape. Besides isolating the CFE surface and the associated CFE dust particles from the gas volume, the copper tape provided an image charge plane which reduced fringe field effects. The tape also served as an electrostatic shield and its electrically conducting surface prevented static charge build up on the chamber walls from drift gas ions. Conducting epoxy and solder

were applied periodically between adjacent strips to ensure good electrical contact. Cladding the staves was quite easy; we simply rolled copper tape down the length of the boards. Affixing an adaquate ground plane foil to the endplates, however, proved to be an entirely different matter. First, we had to consider how well the foil would adhere to the endplate under drilling the feedthrough holes. Secondly, the foil had to lay flat, for there could no be no creases or wrinkles. We glued the 36 μm layer of copper foil to the inner surface of the endplate with Ablefilm 561; this side would later be exposed to the gas volume. Ablefilm is a solid at room temperature. We cut the desired semi-annular pattern out of both the sheet of ablefilm and the copper foil and carefully smoothed the foil over the epoxy, which lay flat on the endplate. We next placed the clad endplate into a rigid plastic bag, sealed it and evacuated the air, which provided around one atmosphere pressure. We then put the entire assembly into the oven for 1 hour at 180°F, high enough to allow the epoxy to flow and yet not cause the Rohacell to foam. However, we lost one endplate employing this technique due to a faulty thermocouple. The oven temperature was set too high and the endplate swelled up.

Once the copper foil had been affixed to the endplate, the next step was to drill the feedthrough holes. A computer controlled milling machine was used to drill the holes into the endplate, with a center to center precision of 1 mil. CFE is not easy to machine. If the endplate is improperly supported, the feed or spin rate of the drill is not just quite right or the drill enters the CFE layer from the wrong direction, the CFE will splinter, rendering the entire endplate useless. Unfortunately, our first endplate became our test piece. We reduced the number of holes drilled to 60 per hour. Even though we cooled the dual-fluted carbide drill bits with jets of cold water, it was necessary to replace the dulled drill after every 60 holes. And finally by drilling the holes only halfway through on one side and then flipping the endplate over and completing the hole from the other side, we mastered the splintering problem.

After the endplates were drilled, we lined the 6336 feedthrough and gas exhaust holes with stainless steel sleeves of wall thickness 100 μm. The sleeves served the

primary purpose of electrically connecting the two faces of each endplate with a smooth ground surface. Beads of conducting epoxy (Tra-Duct BB-2902) were used to attach the tubes to the copper foil. These sleeves provided the additional benefit of sheathing the Delrin feedthroughs from CFE dust particles or Rohacell crumbs. A feedthrough inserted into an unlined hole will collect carbon dust on its delrin surface. These dust particles can then transfer to the cathode wires and thereby become a source of high voltage breakdown.

The opposing endplates were then aligned and pinned to the inner and outer walls on an optical table. The entire structure was glued together elsewhere with a strong high-viscosity epoxy (Epo-tek 370). After the epoxy cured, the chamber half was pre-stressed in preparation for stringing the wires. The structure of the half chamber was so rigid that it compressed less than 4 mils under a 1700 lbs load.

From our experiences with the prototype, we learned it was not practical to string the 3168 wires horizontally. We built a 16′ high clean room to accomodate the vertically supported 2 m chamber half. This arrangement allowed us to exploit gravity. The stringer positioned on top threaded the wire through a feedthrough and attached a plumb bob to the end of the wire. The wire, then, was allowed to descend and the bottom stringer guided it through the opposing feedthrough hole. The wires were tensioned with the appropriate weight and secured by crimping [27]. Immediately after crimping, the wire tension was checked, and poorly strung wires were removed. To measure the tension, the wires were bathed in a 100 gauss magnetic field. We resonated the wire with a variable alternating current and from the frequency at which the waveform of the driven wire traced out a Lisajous figure on the oscilloscope, we could determine the tension. The wires were checked periodically to insure that none lost tension. Indeed, none of 3168 wires did lose tension during the course of the 10 month collider run.

3.2.1.4 Gas, Wires and Feedthroughs

In selecting the anode and cathode wires, we had to optimize the desired electrostatic qualities with mechanical properties. The density of the electric lines of force terminating on an anode wire is inversely proportional to the radius of the wire and is proportional to the voltage squared. Therefore, for fixed V, the the gain in the Townshend avalanche region can be increased by selecting a finer wire. The wires, however, had to be highly tensioned to inhibit sagging. This places critical demands on the mechanical properties of the wires.

We chose a mixture of 95% Argon 4% Methane and 1% CO_2 for the drift gas on the basis of the following five criteria:

- Maximize the Signal to Noise ratio.
- Minimize the space charge build up.
- Reduce chamber aging.
- Low drift field saturation.
- Low drift velocity.

Care must be taken to avoid operating the chamber near the point of high voltage breakdown of the gas. This condition is known as the Raether limit [28] and governs the maximum gain attainable. The effects of space charge accumulation alters the electric field resulting in the loss of wire efficiency. In the high counting rates at CØ and the intense radiation background from the Main Ring, an excessive gain can lead to polymerization of the quenching components causing whisker growth on the wires and leading to the rapid aging of the multiwire CTC. Selecting a lower gain drift gas (Gain $= 5 \times 10^4$) which saturates at $|\vec{E}| = 500$ V/cm both prolongs the life of the drift chamber and reduces the attractive force between the anode and cathode wires. An uncentered anode wire surrounded by four nearest neighbor cathode wires will be pulled in the direction of the closest cathode wire. I have calculated, however,

that even a 0.25 mm displacement from the center (7.5% of the nominal interwire distance), the restoring force, Tsin(θ) exceeds the electrostatic force by two orders of magnitude. Finally, our relatively low drift velocity of 31.5 μm/nsec improved the two track resolution. Fig. 3.7 shows the relationship between the drift velocity and the electric field strength.

Each half chamber is divided into twelve cells, each of which span an azimuthal angle of 15°. Each cell contains 24 sense wires which ideally function as 24 independent measuring elements. The nefarious effects of crosstalk, however, capacitively couple the wires and severely distort the longitudinal component (see Appendix B). A cell is comprised of two radial field wire planes, two gain wire planes in rows symmetric about the sense wire plane and top and bottom rows of field-shaping wires. The wires are parallel to the beam axis. The field wire planes define the the drift region for the cell which ranges from 3.3 cm at r = 25.7 cm to 4.9 cm at the outer radius of r = 37.2 cm. This wire pattern allowed the 24 sense wires to be spaced only 5 mm apart. The cell geometry is shown in Fig. 3.8 and Table 3.4 lists various CTC parameters. The entire cell is tilted 5° with respect to the radial direction to permit resolving the left-right ambiguity of tracks. The electrons liberated in the wake of a charged particle traversing the chamber assume a mostly uniform drift velocity, $\vec{v}_d$, in the direction transverse to the sense wire plane. The perpendicular distance of the hit to the fired sense wire, $|\vec{d}|$, is calculated by means of solving:

$$\vec{d} = \int_{t_0}^{t_d} \vec{v}_d(t)dt \tag{3.1}$$

Here, t_0 is the time at which the charged particle traversed the gas and t_d is the time it takes the electrons to drift over to the sense wire (Fig. 3.9). The magnitude of the drift velocity, $|\vec{v}_d(t)|$, is constant until the drift electrons enter the region of the rapidly increasing high electric field very near the sense wire ($\vec{E} \propto \hat{r}/r$). The sign of $\vec{d}$ is yet unknown; the electrons could be coming from the left or the right, since only a time of drift is measured. Several sense wires sample the hits resulting from the passage of the charged particle. The 5° tilt is fundamental in distinguishing the real

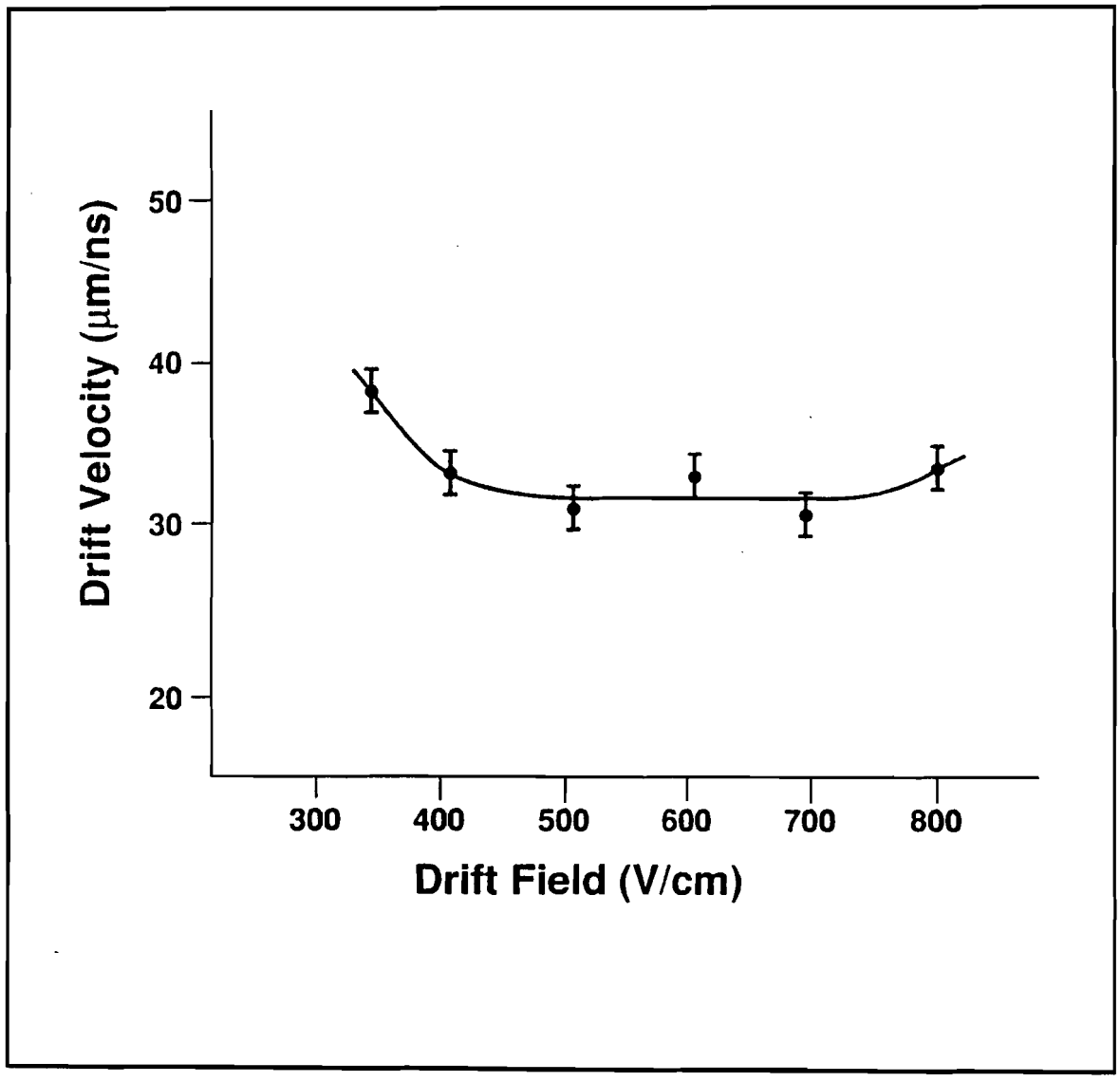

Figure 3.7 Drift velocity versus drift field for 95% argon 4% methane and 1% carbon dioxide.

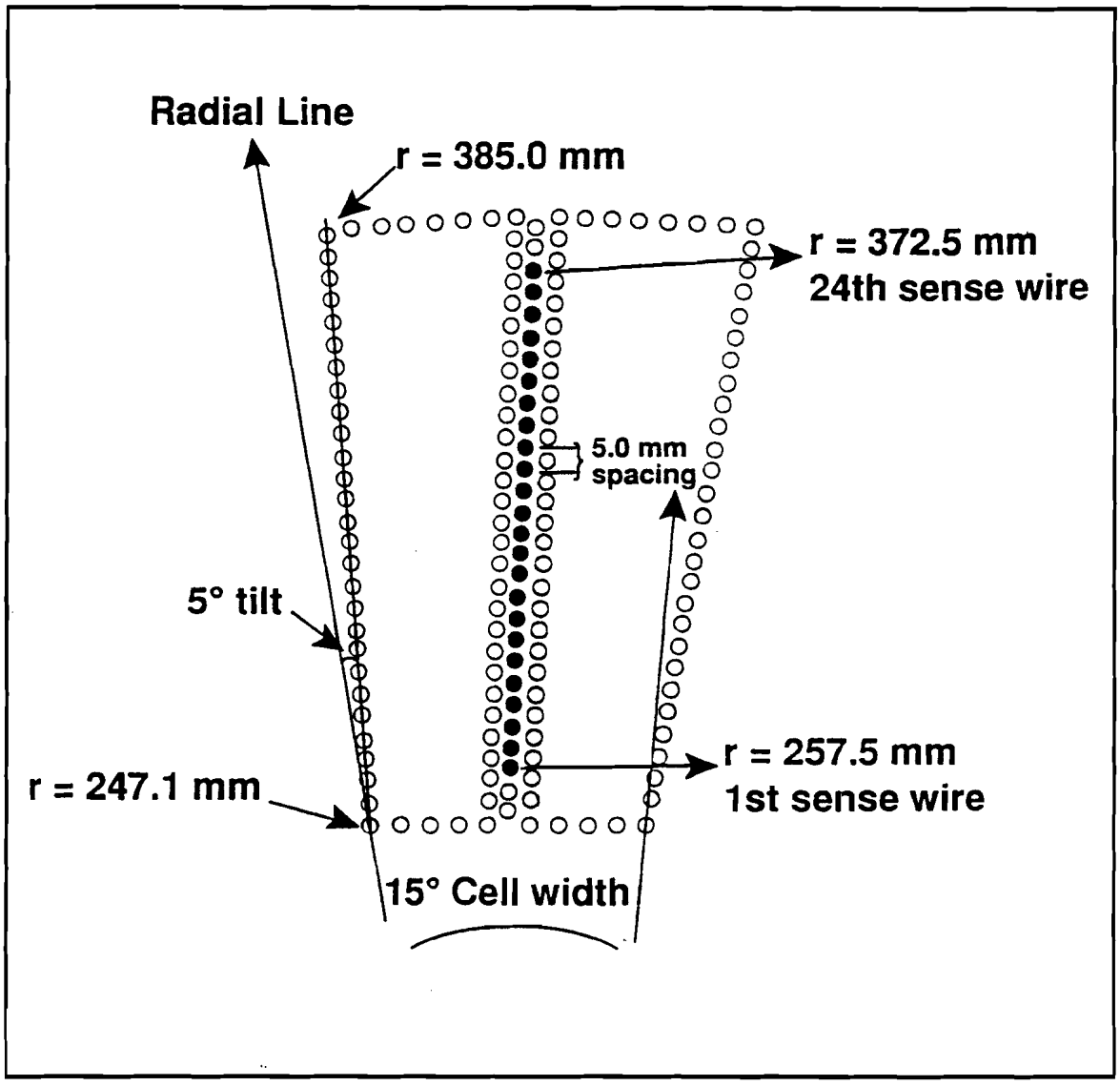

Figure 3.8 Wire configuration for the drift plane. One of the 24 15° sectors.

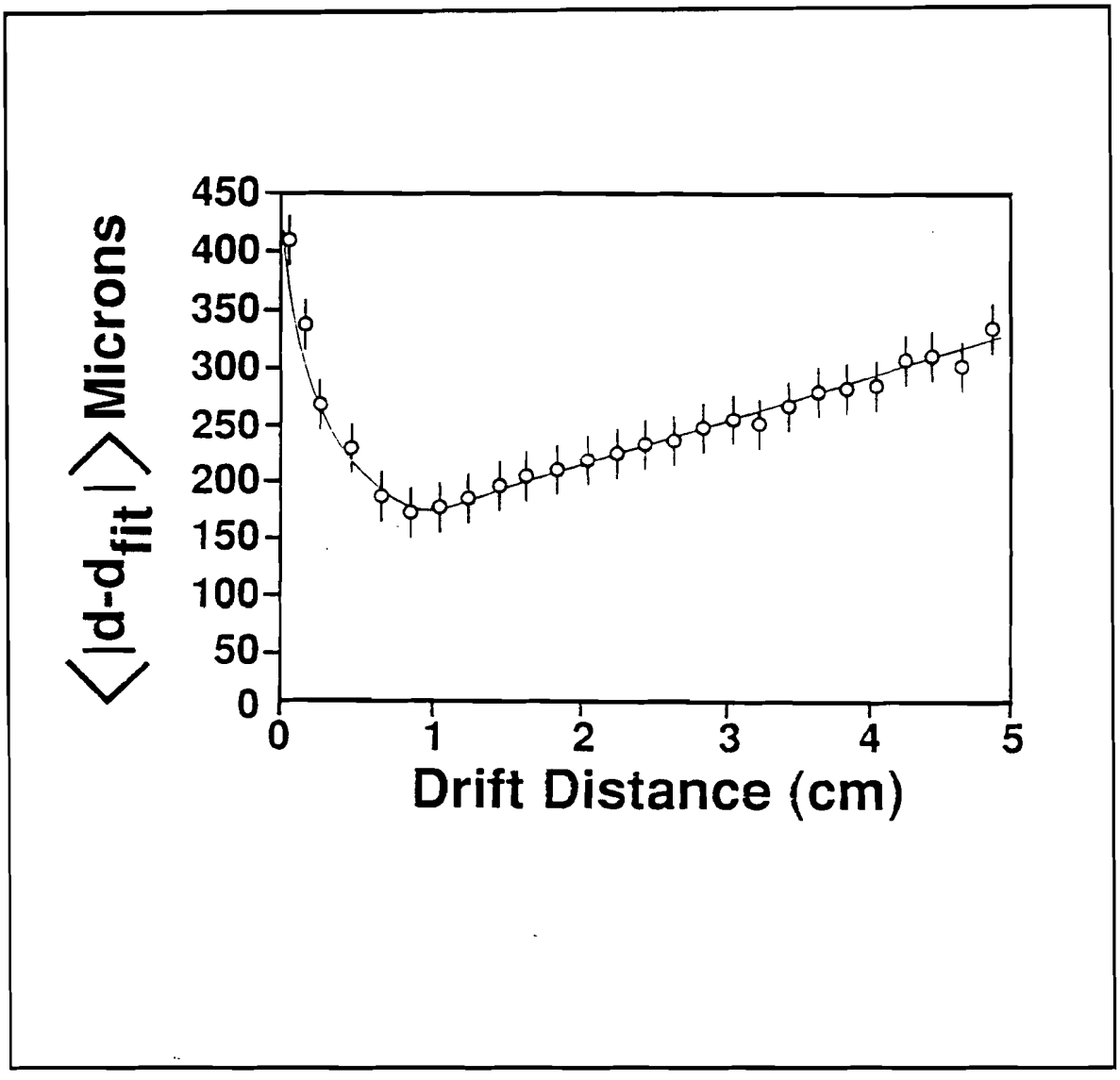

Figure 3.9 Average error in the drift plane coordinate versus drift distance.

from the false track. The true trajectory of the reconstructed track points towards the beamline at the chamber's center, for a track originating from the collision axis. The 'ghost' track points elsewhere. This tilting of the cell also provided improved two track resolution, for it reduces the likelihood of tracks completely overlapping one another. The gain wires focus the drift electrons onto the anode wires as is shown in Fig. 3.10. This focusing reduces pulse width and improves two hit separation. In the region close to the anode (typically at a distance no more than a few wire radii), a teardrop shaped avalanche of electron-ion pairs is formed. The faster moving electrons occupy the head. Less than 1% of the signal comes directly from the actual collection of elecrons; the rest is induced by much slower moving positive ions traveling towards the cathodes [28].

The wire feedthroughs insulated and accurately positioned the wires. They were lathed out of Delrin plastic by a Japanese firm. Fig. 3.11 shows the feedthrough assembly and the endplate structure. At the tip of these feedthroughs were sapphire beads with 160 μm holes for the field and gain wires and 60 μm holes for the sense wires. There is no particular physical reason for picking sapphire over other hardened insulators for the alignment feedthrough beads. There just happened to be a glut of jeweler quality sapphire on the Japanese market at the time. The 2592 gold-plated copper-beryllium field and gain wires ranged in diameter from 100 to 150 μm and were tensioned with 5.4 to 10.8 N. The larger diameters were used to reduce surface field effects. The 576 sense wires were gold-plated Tungsten-Rhenium with a diameter of 25 μm and were tensioned with a 80 gm mass, which is about half their breaking strength. We determined z, the coordinate parallel to the beam axis, by means of charge division. Wires with higher resistivity, ρ, are less subject to crosstalk effects than those of lower ρ. Crosstalk arises chiefly from capacitive coupling which distorts the signal and consequently degrades the z coordinate accuracy (This subject will be covered in Appendix B). Ideally we would have used sense wires with a much higher resistance than the 190 Ω/m W-Rh ones in order to improve our z resolution. We tested several high ρ alloys of iron derivative (stablohm) wires. Although they were

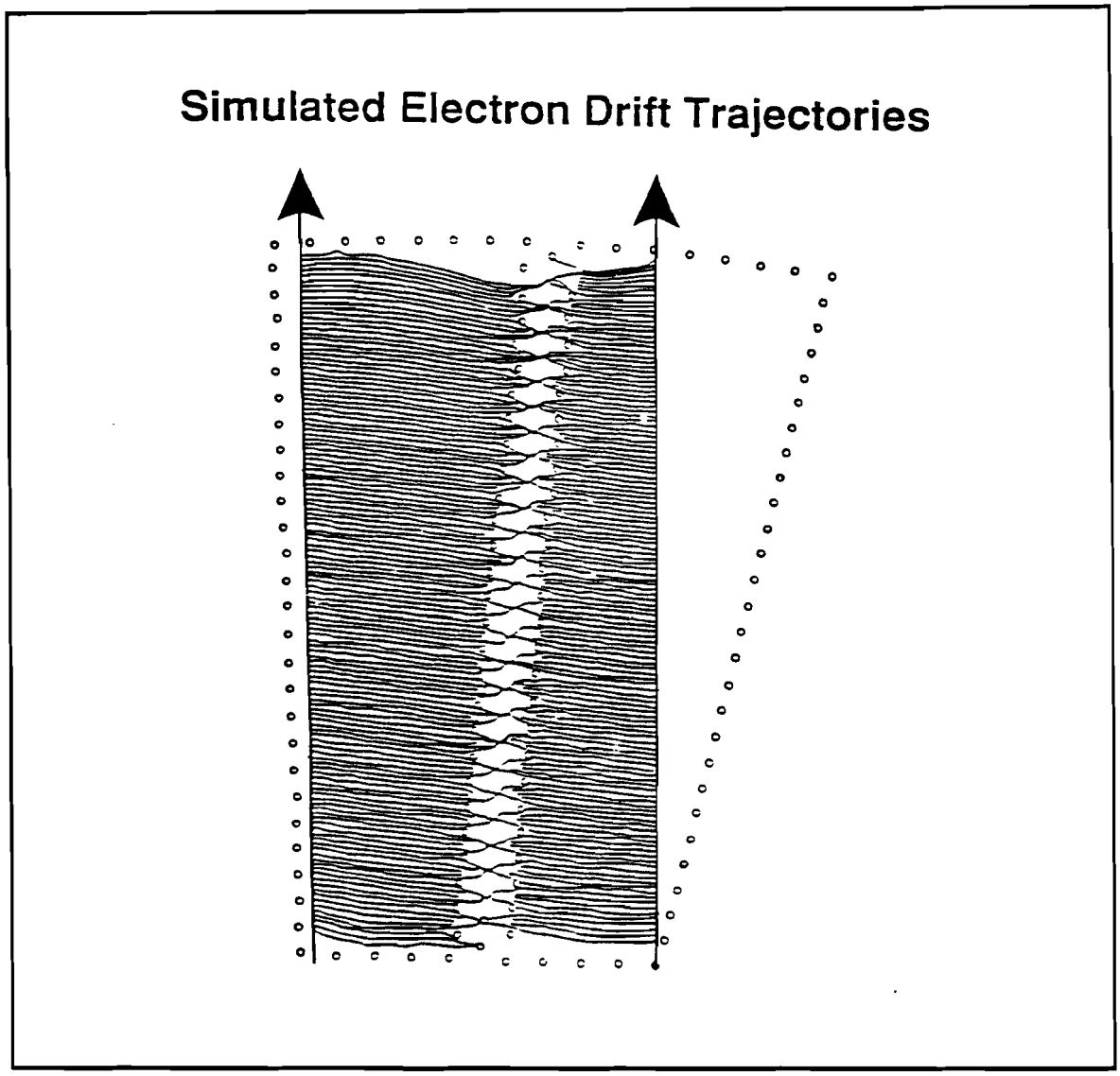

Figure 3.10 Simulation of electron drift trajectories showing the focusing effect of the double row of gain wires.

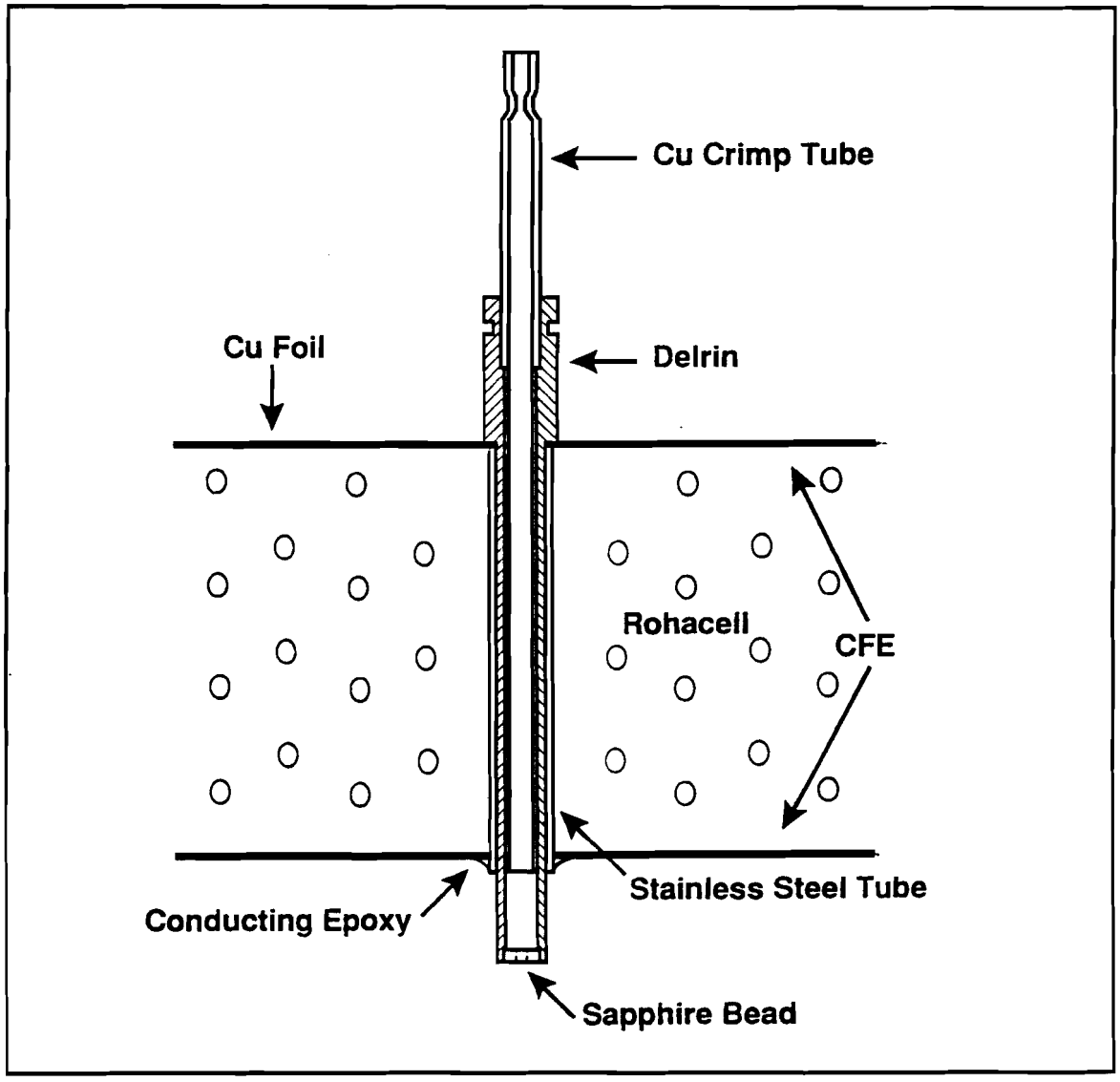

Figure 3.11 Wire feedthrough assembly and cross section of CFE/Rohacell composite endplate.

nearly completely free of crosstalk effects and had a z rms error of less than 1% of the wire length, they proved too fragile for our application; the requisite tension was near its elastic limit. The Tungsten-Rhenium alloy possessed far superior mechanical attributes and was more thermally durable than the stablohm wires.

3.2.1.5 Gas Distribution System

The gas distribution system governed the flow of the drift gas (95% Ar, 4% CH_4 and 1% CO_2) through the chamber and was designed to exchange one CTC gas volume per day. Care was taken to avoid contaminating the gas mixture. The inner surface of the copper tubing forming part of the gas intake system was thoroughly cleaned: first it was rinsed in acetone, then etched with a mixture 10% Nitric and 10% Hydroflouric acid, followed by a distilled water rinse and finally the tubing was cleansed in methanol to remove water residue.

The gas was injected from a Matheson bottle into copper and polypropylene tubing and the flow branched off into the intake pipes embedding in the four gas perfusion boards of the chamber. On the return, it flowed out through the endplate exhaust holes into the electronics region, where the capacitors and network resistors were housed. There the gas formed a diffusion barrier which prevented the contaminates outgassing from the electronic components from entering the chamber. The gas then flowed into the exhaust line, passed through a proportional tube and finally dumped into a bubbler. We monitored the characteristics and purity of the gas mixture with the proportional tube using an ^{55}Fe radioactive source.

Thunderstorms are common in the plains of the midwestern United States and the accompanying plummeting air pressure could well spell disaster for the CTC. An emergency gas dump monitor constantly measured the difference in pressure between the interior and the exterior of the chamber. If the difference exceeded a conservatively set value, the monitor shut off the electricity which held the emergency valve closed. The gas was then dumped into the tunnel equalizing the inner and outer pressures.

Table 3.4 Parameters of the CTC.

Inner Radius	220 mm
Outer Radius	420 mm
Length	2000 mm
Innermost sense wire radius	257.48 mm
Outermost sense wire radius	372.49 mm
Number of sense wires per cell	24
Number of cells	24
Cell Dimensions	
Height	120 mm
Length	2000 mm
Width	67.6 to 97.9 mm
Number of Wires	3168
25 μm Au-W/Rh (Sense)	576
101.6 μm Au-Cu/Be	1729
127.0 μm Au-Cu/Be	32
152.0 μm Au-Cu/Be	831
Bulkhead Load	1541 kg
Nearest wire spacing	5 mm
Gas	95% Ar 4% CH_4 1% CO_2
Drift velocity	31.5 μm/nsec
Average drift field	500 V/m
Maximum field voltage	-4.2 kV
Gain (potential) voltage	-1.975 kV
Average field at field wires	22 kV/cm
Average field at gain wires	15 kV/cm

3.2.1.6 High Voltage and Grounding

The high voltage power supplies were crated next to the signal processing FADC modules in the CØ trailer complex, located above the Tevatron accelerator tunnel. 40 m length Reynolds type 167 - 2669 cables connected the high voltage supplies to the cathode wires of the CTC. The field shaping wires of each individual sector were connected via a resistor chain. This chain stepped the voltages down providing the appropriate charge to each radial layer. Each of the 24 resistor networks were separately powered by Bertan model 377N power supplies, which delivered 4.2 kV. The gain or potential wires were partitioned into three radial segments. The gain wires of the each segment were bussed together and terminated with a low pass RC (50 MΩ resistor and 1 nF capacitor) circuit to ground (Fig. 3.12).

This buss arrangement provided both a utilitarian high frequency filter and a redundancy should a gain wire develop corona discharge and force the sector down. A charge traveling down the sense wire will induce currents on the nearby gain wires. If the boundary impedence is mismatched, the pulse will reflect. This reflected pulse will superimpose an induced current on the sense wire signal and obliterate the precision of finding the z coordinate by means of charge division. Bussing the gain wires together, moreover, obviated the need to terminate the ends of each gain wire individually. This reduced incorporating additional components and thereby complemented the low-mass design criterion of the chamber. Usually a Kiebler model 5900 power supply delivered 1.975 kV to all three gain wire segments simultaneously. If, however, a gain wire developed problems and could not hold voltage, we could power the offending segment separately and not be compelled to switch off the entire cell.

The grounding scheme strongly influenced the qualitity of the charge division. As was mentioned earlier, the interior of the chamber was clad with a 36 μm copper coating which provided the chamber ground. A 5 kΩ resistor decoupled the chamber and HV cable grounds. To filter out high frequency pickup, an RC circuit formed of a 1 MΩ resistor and a 1 nF capacitor was connected from the center conductor

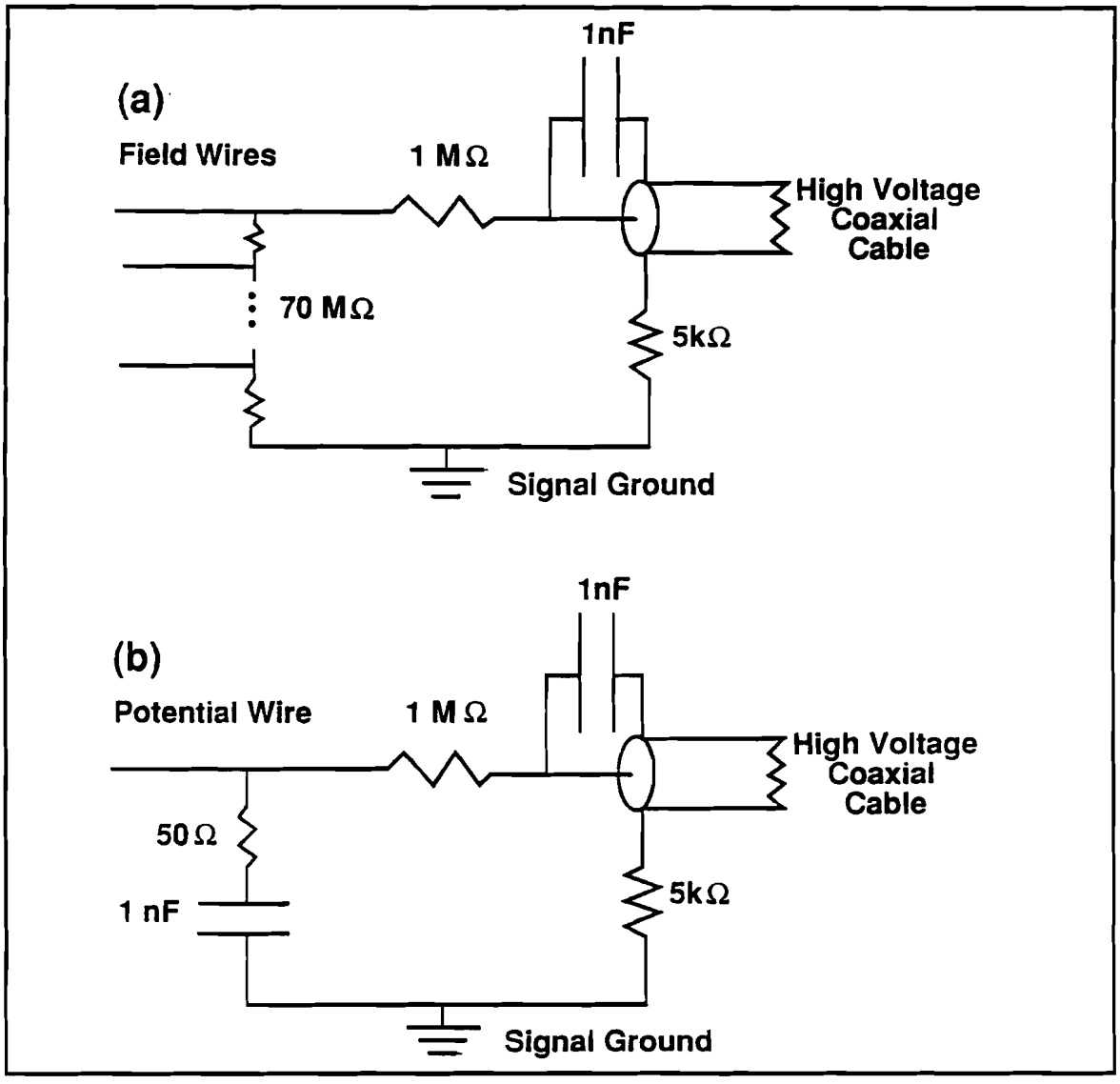

Figure 3.12 (a) Field wires high voltage connection to signal ground and (b) gain wire high voltage to signal ground.

of the HV coax cables to HV ground. The chamber was then shielded with 100 μm aluminum foil. This shield was connected to the preamplifier ground and was located approximately 1 m away.

3.2.1.7 Signal Processing

The signal processing electronics sampled the timing and the amplitude profile of the minute pulses registered at the ends of the fired sense wire. The FWHM of the average pulse on the sense wire is 100 nsec and has an integrated charge of around $10^4 e^-$. We had to boost this faint signal sufficiently to drive it down the 38 m trek to the CØ trailer complex, where it could be processed and recorded to 9 track magnetic tape. Snapped onto each end of the sense wires were miniature 50 Ω coaxial cables. These cables varied in length from 5 to 17 cm and carried the signal to the outer radius of the chamber. From there, the signal was transferred to 50 Ω coaxial ribbon cable (Amp type 1-22698-7) and traveled 2.74 m to the preamplifier mother boards. Because of the aforementioned space contraints and the intense radiation from the Main Ring, the preamplifiers were stationed about 1 m away from the chamber. Although carrying the signal through these series of cables introduced impedance mismatching and potential rf noise pickup, which further degraded the accuracy of the charge division, this prudent positioning of the preamplifier boards reduced the radiation dosage by a factor of 10. None of the preamplifiers failed during the 10 month run.

We periodically applied test pulses to check sense wire continuity, the preamplifier gain and Flash ADC module operation. These test pulses were distributed by (1% tolerance) 4.99 kΩ resistors, which were connected to each end of the 576 sense wires.

The preamplifier circuitry, as shown in Fig. 3.13, provided a gain of 100. Centralab Inc. manufactured this hybrid chip based upon a CLEO design [30]. To cancel out the opposite polarity pulses induced from crosstalk, a resistor network at the output of the preamplifiers fed 7.8% of the signal to the nearest and 3.5% to the next nearest neighbor preamplifiers. The differential output of the preamplifiers then drove the

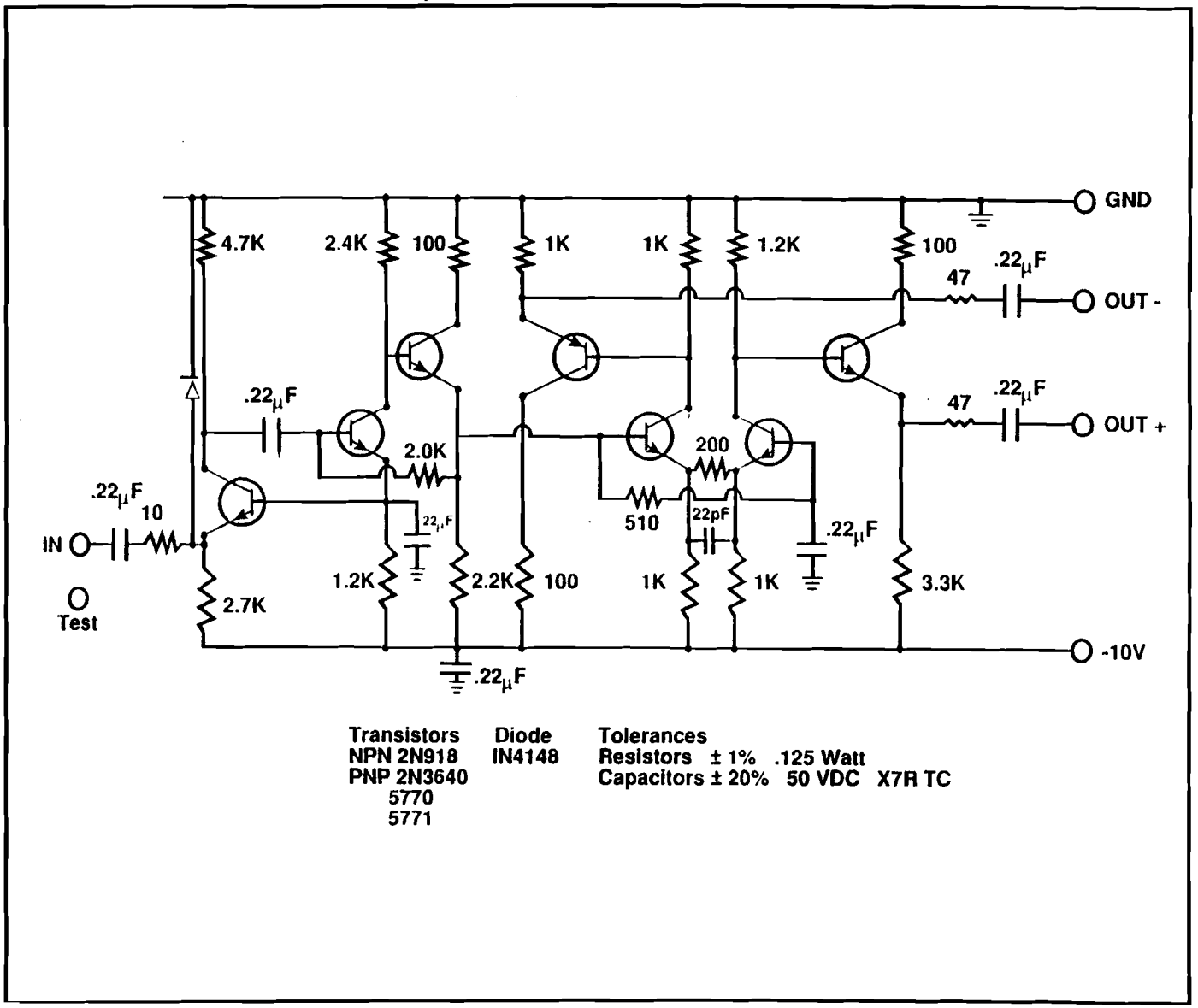

Figure 3.13 Preamplifier circuit diagram.

boosted signal through the 38 m of individually shielded twisted pair ribbon cables (Precicable cable no. 20 RE297). The signal was then digitized by a 100 MHz Flash ADC (FADC) DL300 series modules made by Struck of Germany [33]. These FADC's are based upon the Siemens SDA5010 chip [31] and are 6 bit nonlinear analog to digital converters which give an effective dynamic range of 8 bits. The two ends of the 576 sense wires were read out by 1152 FADC's, which were controlled by 12 microprocessers and operated in parallel in a VME bus architecture. Each microprocessor controlled a programmable DL302 scanner module, which provided fast hit detection and zero suppression for the 24 FADC's in each Eurocrate. Additional microprocessors assembled the data from the 12 front end processors for online monitoring and recording to magtape.

3.2.1.8 Offline Hit Detection

The multiple hits that a single wire could record necessitated offline analysis of the FADC data. A hit was defined as a maximum in the digitized σ having at least two consecutive FADC measurements above threshold. The threshold was set at four counts above the pedestal or background level which typically had a one count standard deviation. The time coordinate was found by first computing the difference between adjacent measurements of the digitized pulse and locating the channel for which a maximum in this difference distribution occurred. Then, by using the two linearized amplitudes on either side of this maximum, the hit time was calculated using a center of gravity technique [32]. In this fashion, the hit times of both ends of the wire were calculated and averaged. Fig. 3.14 shows a typical pulse and the difference of consecutive samples calculated from it.

3.2.1.9 Performance

The chamber could resolve a hit to within a gaussian σ of 250 μm in the ρ–ϕ plane. From the technique of charge division, the z component of the hit could be determined to about 5 cm. The offline algorithms could separate two hits with an

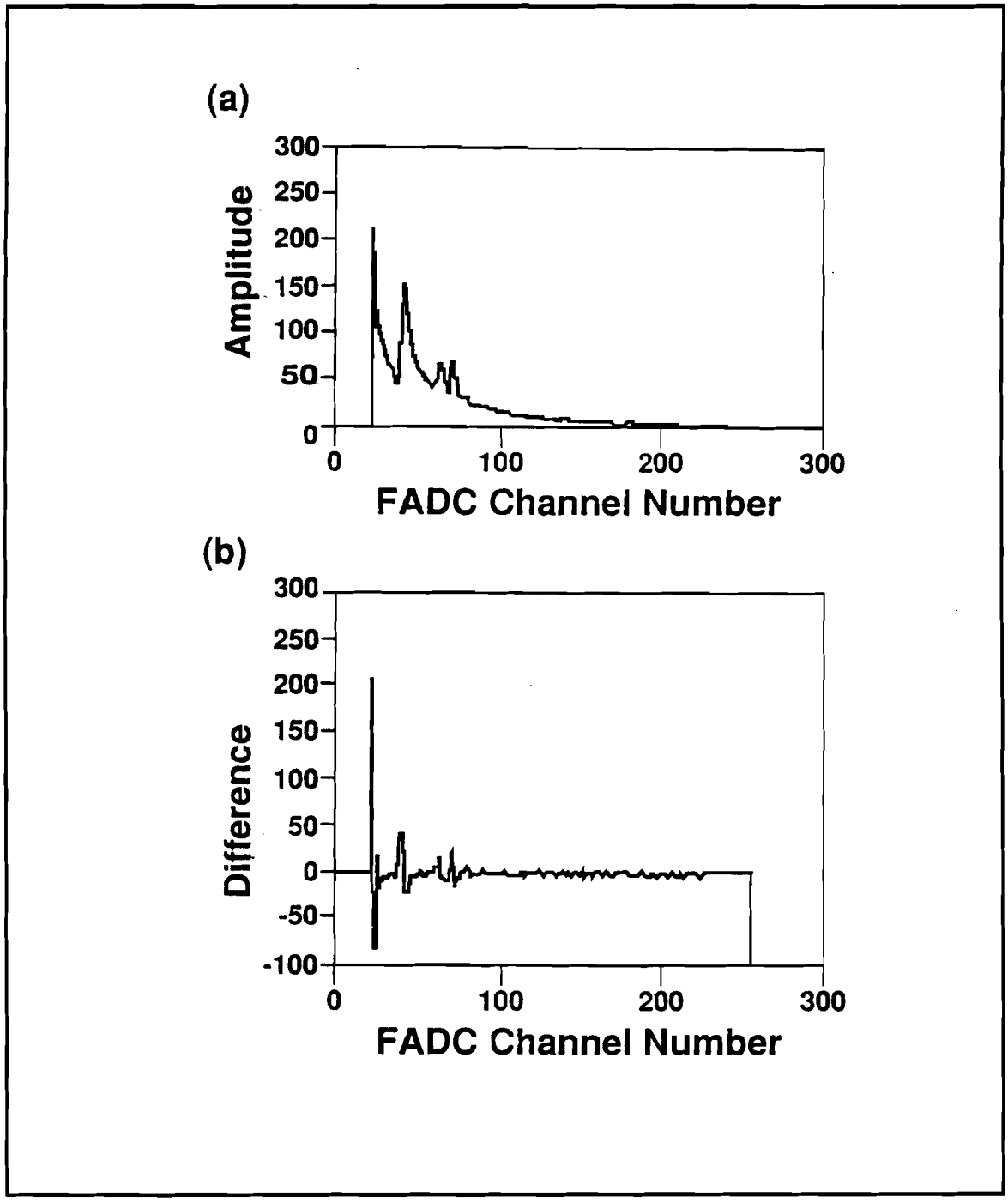

Figure 3.14 (a) Pulse shape and (b) difference of consecutive samples as measured by the FADC system.

efficiency of 60% for two hits distanced at 3 mm apart. In summary, the chamber performed reliably in a very harsh environment for nearly a year. The success of the CTC can be summed up in one picture, Fig. 3.15, which surely is worth a thousand words.

3.2.2 Barrel and Endcap Hodoscopes

The barrel and endcap hodoscopes served the dual roles of providing an online event trigger and an independent measurement of particle multiplicity in offline analysis.

The shape of barrel hodoscope is cylindrical, surrounds the central region and entirely encases the CTC. It was longitudinally split into fore and aft halves to sample, respectively, the positive and negative pseudorapidity regions for a collision at $z_0 = 0.0$ cm. Each half is partitioned into 48 sectors, where each sector spans 7.5°. Except for the region subtended by solid angle of the aperture of the spectrometer acceptance, the hodoscope elements extend the entire half length of the barrel. Both halves give nearly full 2π coverage for the pseudorapidity range $|\eta| \leq 1.56$, where pseudorapidity is defined by: $\eta = -\ln\tan(\theta/2)$, θ being the polar angle. Corresponding to each CTC sector, there are two upstream and two downstream barrel hodoscope scintillator elements.

The endcap hodoscopes extend the pseudorapidity range to $1.63 \leq |\eta| \leq 3.25$. Like the barrel hodoscope, the endcap hodoscopes were also divided into upstream and downstream portions. Each endcap hodoscope was further divided into three annuli. Starting from the innermost ring and ascending radially outward, the rings were labelled A, B and C. Each ring contained 24 sectors each spanning 15° in ϕ, the azimuthal angle.

Table 3.5 lists the geometry of the barrel and endcap hodoscopes. Because of its resilience to radiation, we chose to make the 240 scintillator elements out of the material Bicron BC-408 PVT. Attached to the far end of each of the hodoscope elements were Hamamutsu 1398 Photo Multiplier Tubes, PMT. The gain of these

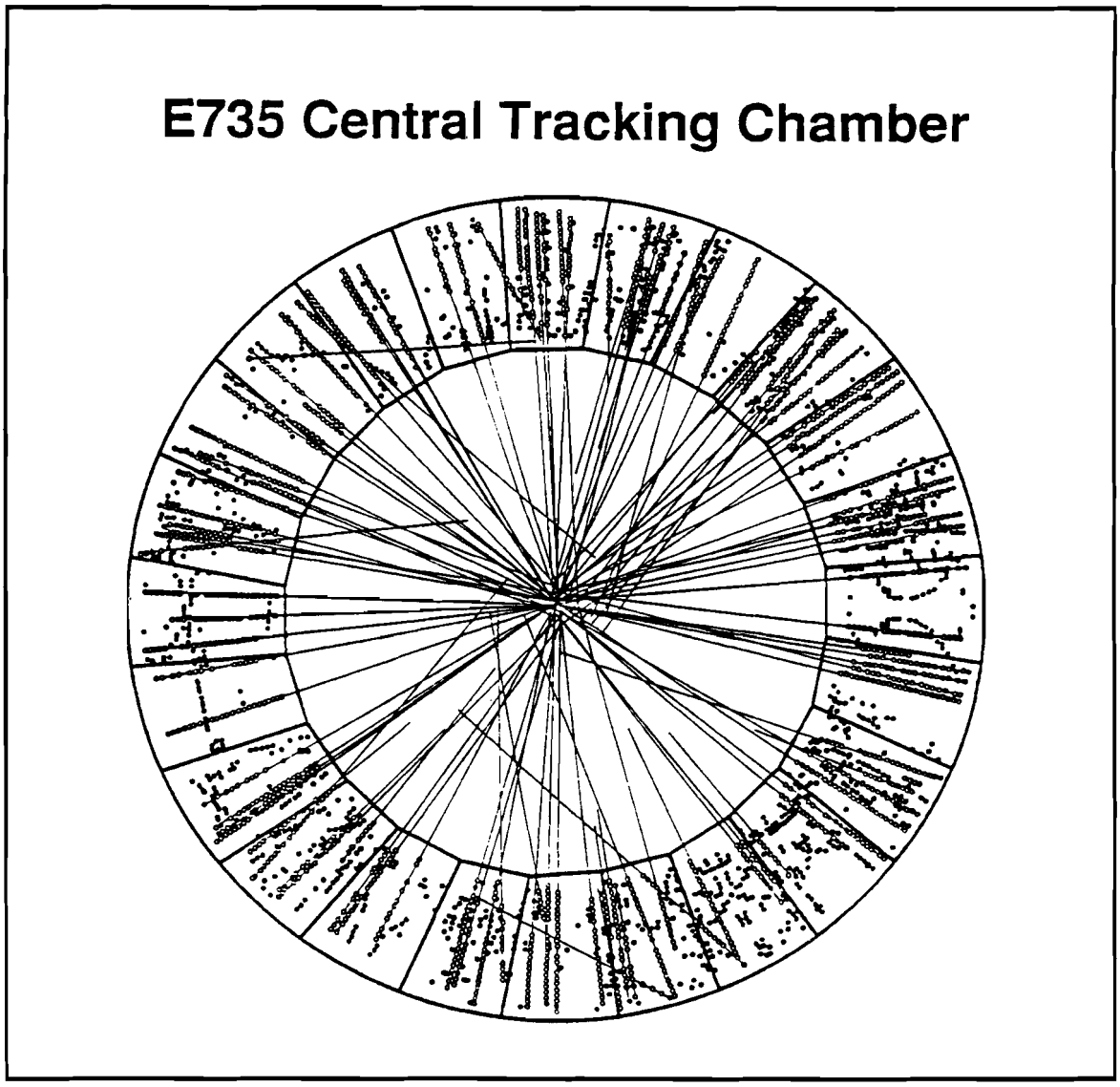

Figure 3.15 ρ–ϕ view of a high multiplicity event showing 104 reconstructed tracks. The open circles denote hits assigned to tracks. Unused hits are depicted by the solid circles.

PMT's was 6×10^6. Moreover, each hodoscope element was instrumented with model 2285 24-channel ADC's and model 2228A TDC's. Combining the TDC and ADC information provided whether the timing of the hit was consistent with the $\overline{p}p$ crossing and the amplitude profile of the hit was good

We employed the endcap hodoscopes in our trigger. The upstream-downstream arrangement of the hodoscope provided us a crude means of filtering out beam-gas and single diffractive events. If the event was highly asymmetric, i.e many upstream and few downstream counters hit, we did not accept the event. We also used the hodoscopes to preferentially accept high multiplicity events in certain triggers. See chapter 4 for details on the various E–735 triggers.

3.2.3 Trigger Time of Flight

Located 2 m upstream (downstream) of the nominal interaction point were the TOF_p ($TOF_{\bar{p}}$) arrays. Both the TOF_p and $TOF_{\bar{p}}$ arrays consist of 15 scintillating counters spanning the pseudorapidity range of $2.7 \leq |\eta| \leq 4.6$. The segmentation was selected on the basis of Monte Carlo studies. Because the counters cannot distiguish multiple hits from a single hit, this arrangement of counters minimized the likelihood of more than one particle hitting a given counter for the fixed physical dimensions of the counters. Like the elements in the two Time of Flight systems in the spectrometer arm, the scintillators were formed of polished Bicron BC-408 PVT doped with an agent which extended attenuation length by shifting the scintillation light towards the blue wavelengths. Attached to each end of a trigger hodoscope counter was an nonscintillating PVT light guide and an Amperex XP-2020 PMT assembly. The photons created in the wake of the passage of the charged particle through the counter were converted to an amplified electronic pulse. The signal was then fed into a LeCroy 220L discriminator which in turn sent a stop pulse to LeCroy 2228A TDC's. These Time to Digital Converters sampled the pulse in 50 psec bins with a dynamic range of 12 bits or 100 nsec.

Table 3.5 Barrel and endcap hodoscope elements.

Hodoscope Unit	*Number of Elements*	*Range in* η	$\Delta\eta\Delta\phi$
Upstream Endcap			
Ring A	24	-1.63 to -2.16	0.139
Ring B	24	-2.16 to -2.71	0.144
Ring C	24	-2.71 to -3.25	0.141
Upstream Barrel	48	0.0 to -1.56	0.204
Downstream Barrel	48	0.0 to $+1.56$	0.204
Downstream Endcap			
Ring A	24	$+1.63$ to $+2.16$	0.139
Ring B	24	$+2.16$ to $+2.71$	0.144
Ring C	24	$+2.71$ to $+3.25$	0.141

We accepted an event if and only if at least one counter in both the upstream and downstream trigger hodoscopes registered a hit consistent with the interaction time of the $\overline{p}p$ crossing. This logic formed our minimum bias trigger. The trigger hodoscopes also provided the time of the interaction, TØ, which is necessary for reconstructing the masses and afforded an independent means of finding the point at which the proton and antiproton collided along the beam axis.

3.3 Spectrometer Arm

3.3.1 Z Chamber

Situated in the limited confines between the CTC and the Tevatron beampipe was the Z Chamber. The design criterea of this vertexing chamber were threefold:

- Miminize mass to reduce secondary particle production.
- Resolve the z component of trajectory to better than 700 μm.
- Set dimensions to fit in limited space and subtend full solid angle of the spectrometer aperture.

The Z chamber was comprised of three layers of wires. For further details refer to [15] and [34].

3.3.2 Magnet

The bend plane of the dipole magnet is located at $x = 75$ cm, in the direction perpendicular to the collision axis. The pole pieces and the magnet coils define the spectrometer acceptance in y and z respectively. The center of the magnet is displaced 25 cm upstream of the nominal interaction point due to the geometry of the spectrometer room adjoining the tunnel. The pseudorapidity acceptance of the magnet is then $-0.36 \leq \eta \leq 1.0$. In the absence of an electric field the Lorentz force becomes, $\vec{F} = q\vec{v} \times \vec{B}$. Because the $\vec{B}$ field is fairly uniform in z and points

towards positive y, the particle will be deflected either in the positive or negative z direction depending on the charge of the particle. The peak magnetic field is 3.8 kilogauss and the integrated field strength $\int \vec{B} \cdot d\vec{\ell}$ imparts a transverse kick of around a 50 MeV/c. Field maps are presented in [15] and [36]. The components of $\vec{B}$ as a function of x, y and z were measured by the ZIPTRACK device from the Accelerator Division of Fermilab. The name ZIPTRACK aptly describes the device. Three mutually orthogonal search coils zip along a track a preset distance. Should $\vec{B}$ change in time, a voltage will be induced on the coils (cf. $\nabla \times \vec{E} = -\partial \vec{B}/\partial t$). The coil voltages are read out through a Data Translation 1712 ADC [37]. The accuracy of the horizontal and vertical positions is 50 μm. A total of 179,952 field measurements were made with this device [36]. For regions outside the magnet aperture and not readily accessible to ZIPTRACK, the $\vec{B}$ field components were measured with a Hall probe. Because the magnitude of the magnetic field is much less here and varies slowly, only 2106 measurements were necessary. Armed with this precise knowledge of the $\vec{B}$ field, our tracking routines can reconstruct the sagitta of particles with momenta up to 3 GeV/c with a $\Delta p/p < 5\%$.

3.3.3 Magnet Wire Chambers

Two chambers consisting of four wire planes each resided directly within the spectrometer magnet aperture. The chambers were fundamental in determining the curvature of charge particle as it traveled in the magnetic field. See [15] for further details.

3.3.4 Straw Drift Chambers

The Straw Drift Chambers reconstruct the path of the charged particle exiting the magnet aperture. Behind the magnet were seven layers of straw drift chambers. Each layer contained two rows of tubes which were staggered 3.048 cm in z to minimize gaps in coverage. The center-to-center distance of the tubes in a row was 6.096 cm There were 14 rows in all, 6 xv (layers 2,4 & 6) and 8 xy. The xv rows were tilted 4°

with respect to the vertical to provide for stereoscopic reconstruction of the particle trajectory. The tubes were 5.1 cm in diameter having a wall thickness of 168 μm and were composed of an aluminum, cardboard and mylar sandwich which together presents 0.04% radiation lengths. The inner row was made up of 32 tubes and the outer row held 48 tubes. The 100 μm gilded copper-beryllium wires were tensioned to 0.25 kg and were aligned with a Delrin endplug and feedthrough assembly. The two rows of tubes in each layer were fitted into holes (milled to a 100 μm tolerance) in a sturdy aluminum frame. The drift gas was a 90% Argon and 10% Methane mixture. The 14 rows of straw drift tube extend in x from 107.6 to 186.4 cm. For a more detailed exposition refer to [38] and [39]

3.3.5 TOF1 and TOF2

The two Time of Flight systems (TOF1 & TOF2) form the basis of identifying particle type. A particle passing through a TOF scintillator deposits energy in the counter. The amplitude and timing of the signal from the PMT's, instrumented on both ends of the scintillator, is then sampled by ADC's and TDC's. After applying the appropriate calibration compensations[4] and offsets to the registered pulses and averaging the time components of the two PMT signals, we can determine the time of arrival of the particle, $t_{\rm hit}$. Subtracting TØ, the time of the $\bar{\rm p}$p crossing, from $t_{\rm hit}$ gives the flight time, $t_{\rm TOF}$, for the particle to travel from the event vertex through the dipole magnetic field to the hit TOF counter. As was mentioned above, the Straw Drift Chambers combined with the Z and Pre- & Postmagnetic Chambers track the particle and reconstruct its sagitta (hence knowledge of its path length, ℓ, and momentum, p). We can then calculate the mass of the particle from the relativistic relationship:

$$m^2 = |\vec{p}|^2 \frac{1-\beta^2}{\beta^2} \tag{3.2}$$

[4]In particular the *time-walk* effect slews larger pulses to earlier times due the faster rise-time of the signal registered by the discriminator threshold. See [35] or [42]

where

$$\beta = \frac{1}{c}\frac{\ell}{t_{\mathrm{TOF}}} \tag{3.3}$$

The material and electronic instrumentation of the TOF arrays were identical to that of the TOF trigger hodoscopes. The TOF1 system was segmented horizontally into seven 300 cm length scintillators and was positioned at x = 200 cm. Space constraints in the spectrometer room necessitated laying the scintillator elements along the $\hat{z}$ direction instead of vertically. The TOF2 system, on the other hand, was vertically segmented and was formed of 32 elements. 20 of the elements were parallel to $\hat{z}$ and set at $x = 400$ cm from the collision axis. The remaining scintillating counters sloped towards the beamline, following the contours of the spectrometer room.

The proximity of the TOF counters to the beamline, along with their time resolution (σ_t = 150 psec), limited the mass reconstruction of high momentum particles. TOF1 and TOF2 complemented one another. TOF1 could separate π's from K's up to 1.0 GeV/c and for TOF2 these two mesons could be distinguished up to 1.5 GeV/c. The nearness of TOF1 enhanced the acceptance of low momentum charged kaons, which would decay before reaching TOF2.

4. DATA ACQUISITION

The E-735 data acquisition (DAQ) system read and recorded the raw data in two separate streams. The hit information registered, processed and recorded by the Central Tracking Chamber will be called the *CTC stream*. Data from the remaining detectors, i.e. the eight planes of the magnetic wire chambers, the three planes of the z vertex chamber, the 14 layers of straw drift tubes, the two banks of TOF counters, the $p\bar{p}$ trigger hodoscope, barrel and endcap hodoscope elements, will be referred to as the *Spectrometer stream*. This arrangement of separating the data into two streams offered a less than ideal solution in terms of our later analysis (see p. 56), but afforded us the most expedient and cost-effective approach in readying our DAQ system in time for the second run. The data-taking rate of the CTC stream ranged between 10 and 20% of that of the Spectrometer stream, but contained approximately 3.5 times the amount of information for each event. So the number of raw data tapes produced for each of these streams were roughly in the ratio of 1.5:1. That is to say a CTC data tape contained 2200 events as compared to the 11000 events written to the 9 track 6250 bpi tape by the spectrometer stream for permanent storage.

4.1 Trigger Logic

Every 3.5 μs a beam of 10^9 protons swept through an equal number of oppositely rotating antiprotons at the CØ interaction region of the FNAL Tevatron. These nucleons were spatially contained in what we called a bunch, where 99% of the particles are confined within a longitudinal length of 20 cm and a lateral dimension of 2 mm. Once every 0.002 seconds, on the average, (see Appendix A) a proton and antiproton interacts and a portion of the collision energy converts into matter which gives rise to

particle production. The principle aim for the E-735 triggers was to sample minimum bias events but still remain active for the rarer but *more interesting* high multiplicity events. We accomplished this feat by employing a trigger processor [43], which scaled down the low multiplicity events.

We define a minimum bias event as an event that satisfies the Primary Trigger (PT) logic. The PT trigger requires the following conditions to be met for an event to be accepted:

1. At least one hit in the upsteam trigger hodoscope.
2. At least one hit in the downstream trigger hodoscope.
3. Both hits coincident in time.
4. The hits are in tight coincidence with the accelerator beam signal TØ, the Tevatron rf signal, which signals the time of the beam crossing.

The proton (antiproton) trigger hodoscope array of counters are located 2 m upstream (downstream) from the nominal collision point, i.e. $z_o = 0$, and span the pseudorapidity range of $2.7 \leq |\eta| \leq 4.6$ units. Each array contains 15 scintillator elements. The timing of both the upstream and downstream hits and the TØ signal must coincide in order for the event to come from a beam-beam interaction. Situated 19 ns behind each beam bunch was a satellite bunch containing $\sim$ 1 % as many nucleons. The halo of these satellite bunches could interact with the beampipe and the resulting particles could spray into the trigger hodoscope counters. We took care to accept only those events with a timing consistent with a proton-antiproton collision.

The PT trigger formed the basis of all further triggers. A preponderance of our data was collected under the S1 triggers, where S1 stands for 1 Spectrometer Track. The principle idea behind the S1 triggers was to enhance the number of events containing tracks in the spectrometer and yet be active for accepting the rarer high multiplicity events. The following conditions formed the logic of the S1 triggers:

1. Minimum Bias trigger conditions.

2. Forward - Backward event symmetry.

3. At least one track in the spectrometer.

4. High multiplicities enhanced by trigger processor.

The axially symmetric condition of item 2 reduces triggering on beam-gas events, since the yield products arising from non beam-beam interactions will tend to spray in one direction. We compare the number of hits registered in the upstream hodoscope to those in the downstream and if the ratio is far from unity, we do not accept the event. Condition 3 requires that at least three out of the four planes for each of the pre-magnet and post-magnet wire chambers recorded hits. This condition enriched our data sample by enhancing the acceptance of events containing at least one spectrometer track. Condition 4 of the trigger augmented our sensitivity to the rarer higher multiplicity events. Had we not scaled the lower multiplicities to a fraction of the incoming rate of these frequent events, we would have almost never have been receptive to the higher multiplicity events. The hodoscope hit multiplicity was divided into six regions. Each of these regions were scaled so that the final multiplicity distribution was fairly flat over the interval $0 < N_{\text{hodo}} < 120$, where N_{hodo} is the total number of hodoscope hits.

Because the CØ luminosity, $\mathcal{L}$, could vary by a factor of 20 ($10^{28} < \mathcal{L} < 2{\cdot}10^{29}$), the multiplicity scale factors appropriate for one luminosity were completely inappropriate for another. We developed five separate S1 type triggers, i.e. S1D, S1C, S1BC, S1B and S1A, which varied only by the multiplicity scaling factors. For luminosities in excess of 10^{29}, we set the trigger to S1D and for $\mathcal{L} \simeq 10^{28}$, we collected data under the S1A trigger. S1C, S1BC and S1B were used for the intermediate luminosities.

However, since I was not involved in developing the trigger, I urge the reader to refer to [16] for an expert discussion on the VME and CAMAC readout system, PDP RSX DA, VAXONLINE, the design and implementation of the trigger processor and

the complete schematics of the trigger logic used in all the CTC and spectrometer triggers.

5. DATA PROCESSING AND DATA SAMPLE

In this chapter, I will first briefly describe how we merged the raw data from the two independent data streams of the CTC and Spectrometer. Next, I will detail how we produced the Data Summary Tapes (DSTs) by clandestinely exploiting the CPU resources of the Amdahl and will then discuss how we compressed this DST data into Ntuple format for our MiniDST set. Finally, I broach the subject of which cuts were employed for refining this entire data set into a manageable number of μDSTs and will show some vertex, rapidity and multiplicity distributions contained on the μDSTs.

5.1 Merging the CTC and Spectrometer Data Streams

In the chapter on the data acquisition, we discussed that the raw data were written to 9 track tape for permanent storage in two separate streams. Separating the CTC data from the other E-735 detectors may have afforded the most straightforward approach in terms of implementing the DAQ, but in terms of later merging the two data streams, it was a bookkeeping nightmare. The time spent merging the data postponed the analysis and delayed the publication of our results.

Before we could commence the DST production, we had to combine the CTC and spectrometer information for each and every event. Each event is tagged by a unique hexidecimal number, known as the event time clock (ETC). We used this ETC identifier to unambiguously match the CTC and spectrometer events. Recall from chapter 4 that the correspondence between the number of CTC raw data tapes and spectrometer raw data tapes were not one-to-one, but rather varied between one and three spectrometer tapes for each CTC tape. In merging the data, all the

spectrometer data were saved, more or less. Compression algorithms, however, were used on some of the wire chambers and channels less than pedestal for the hodoscope data were not included [44]. No tracking was performed at this merging stage. We compressed and combined the 1254 spectrometer and 1720 CTC raw data tapes into a set of 969 merged data tapes. We spent nine months merging the tapes.

5.2 Data Summary Tape Production

The next link in the chain of data processing was to combine and condense the electronic amplitude and timing information from our detectors into a reduced set of tracking and hit parameters. The DST package consists of several algorithms which process the raw data from the input merged tapes and outputs a summary of the data. Among the algorithms contained in the DST package are:

- Track Reconstruction
  - Spectrometer Tracking: A track was fit through the hits in the z chamber, premagnet, postmagnet and the 14 layers of straw drift tube wire chambers using the method of a fourth order Runga-Kutta formula in the presence of a nonuniform magnetic field [45], [46]. Refer to [47] for a detailed derivation and explanation.
  - CTC Tracking: Because the **B** field in the CTC is negligible, compared to the chamber's longitudinal (z) resolution, tracks will travel in straight line trajectories. A "line fit" algorithm exploiting this stiffness was implemented in the CTC track reconstruction. This technique was sensitive to reconstructing secondaries, i.e. particles not originating from $\bar{p}p$ collisions [17].
- Vertex Finding Algorithms
  - Z Chamber: Employed the residual minimization technique of Yatsuneko [48]. This method does not require tracking. (See [15])

- $\bar{p}p$ Trigger Hodoscopes: The time difference measured by the two trigger hodoscope arrays provide z vertex information. ($z_o = c(t_{\bar{p}} - t_p)/2$).

- Event Interaction Time: Determined from the $\bar{p}p$ Trigger Hodoscopes.

- Amplitude and Timing of Hodoscope Hits: [16]

Data Summary Tape production is CPU intensive and we turned to the powerful FNAL Amdahl mainframe to crunch the data. I wrote a 1200 line command procedure to automate the production of the E-735 DSTs. This command procedure allowed for batch jobs to be submitted from batch and possessed extensive recovery procedures, so that if a given job bombed or was killed by the operator, the command procedure would submit the next tape on the list. At the time of the DST production, the VM operating system did not provide for submitting batch jobs from batch. I used the utility VMSCHEDULER to circumvent this deficit and emulate the submission of batch jobs from batch. In order to increase the number of cycles per unit time dedicated to our DST jobs, we partitioned the data contained on one merged tape into several subjobs and submitted each subjob at the *medium* classification. Had we simply submitted the jobs at the *large* classification, our throughput would have decreased since the *medium* classification of the batch queue runs at higher priority. At any given time, two sets of eight subjobs were queued in batch, so that our jobs would always be next in line for processing. The jobs ran 24 hours per day at high priority.

Unfortunately after processing all the data into DST format, we uncovered egregious errors in the coding of some of our algorithms and were compelled to redo the DSTs. We diplomatically termed this set of data the first generation of DSTs. After thoroughly diagnosing all the algorithms contained in DST package, we implemented the following improvements:

- Correct relationship between H_x, H_y & H_z and x, y & z. The **B** lookup table for the First Generation DSTs was incorrectly shifted 2.545 cm upstream.

- TOF vertex resolution narrowed to a FWHM of 8 cm. (i.e. the FWHM was 11 cm on the First Generation.)
- z vertex determined from the Z Chamber independent of the $\bar{p}p$ trigger hodoscope z vertex. (The earlier algorithm biased the Z Chamber z vertex to within 20 cm of the z vertex found from the trigger hodoscopes.)
- Endcap wire chamber tracking algorithm thoroughly modified and improved.
- Improved the z coordinate resolution of CTC track finding algorithm.

It took around 3 Amdahl CPU hours to process one merged tape. To give the reader a measure of this endeavor, it would have taken over 7 years to process both generations of our DSTs on a μVAX — running 24 hours a day unabated and dedicated solely to DST production. Good thing we had access to the Amdahl.

5.3 Data Reduction

5.3.1 MiniDSTs

The DST data sample spanned over 240 9 track reel tapes. Clearly, this calls for further data reduction — one cannot cycle through 240 tapes each time an improvement to the analysis code is implemented. So we next compressed the DSTs into miniDSTs. These miniDSTs are formatted in terms of PAW Ntuples [49], so that the data is now accessible to nonexperts. We kept each and every DST event (see [17]). These miniDSTs were compressed onto around 50 reel tapes.

5.3.2 μDSTs

For my personal sample of data, I reduced the MiniDSTs to μDSTs. The data on these μDSTs were divided into 5 separate ntuples. (Refer to Appendix C). They are:

1. Event: Global parameters per each event, e.g. x, y and z components of the $\bar{p}p$ interaction vertex, hodoscope hit maps, etc.

2. CTC η: The z corrected primaries binned in terms of the pseudorapidity, η, where the η resolution is 0.12 units (see Appendix B)

3. Window CTC η: z corrected CTC primaries, binned in η and residing within the solid angle of the spectrometer aperture (sectors 6 & 7).

4. Spectrometer: Parameters related to the spectrometer tracks

5. TOF: x, y, z and t information of the hits measured by TOF1 and TOF2

At the μDST stage, I invoked the following cuts:

1. Beam-Gas Cut: Events with multiplicity distributions asymmetric in polar angle are not indicative of a $\bar{p}p$ collision. Such events arise from either a beam proton striking a gas molecule in the Tevatron or by an outlying particle scraping the beampipe. In either case such events are not of interest. In a detailed study of proton only stores [16], it is found that less than 1% of the non beam-beam interactions survive this beam-gas cut. We demanded that the following conditions be met for an event to be considered:

   - At least two counters in both the upstream and downstream trigger hodoscopes register hits in tight coincidence with the $\bar{p}p$ interaction timing signal (see Fig. 5.1).
   - Event $|z|$ vertex be within 60 cm.
   - Endcap asymmetry cut, i.e.

$$\left|\frac{N_{ec}^{d} - N_{ec}^{u}}{N_{ec}^{d} + N_{ec}^{u}}\right| \leq A_{Cut}(N_{hodo})$$

     where N_{ec}^{d} and N_{ec}^{u} are the number of counters registering hits in the downstream and upstream endcap hodoscopes, respectively, and A_{Cut} is a function of the hodoscope multiplicity (see Fig. 5.2).

   - Averaged timing on upstream and downstream endcap hodoscope hits be consistent with interaction timing signal.

2. The event have z vertex information from both the Z chamber, $|z_{\text{Zchmbr}}|$, and the trigger time of flight, $|z_{\bar{\text{p}}\text{p}}|$ and:

   - Both $|z_{\bar{\text{p}}\text{p}}|$ and $|z_{\text{Zchmbr}}|$ be less than 50 cm.
   - $|z_{\bar{\text{p}}\text{p}} - z_{\text{Zchbmr}}| \leq 10$ cm.

3. At least one track in the spectrometer. This track must satisfy the following conditions:

   - $\chi^2 \leq 3.0$
   - $\Delta p/p \leq 0.2$
   - $0.1 \leq |p| \leq 4.0$ GeV/c.
   - The z intercept of the track at $x = 0$ be within 15 cm of the weighted average of the z_o determined by the Z Chamber and the trigger hodoscope arrays.

In Fig 5.3, one can see the effect of these cuts on the data sample.

All in all, the μDSTs span 15 reel tapes and contain approximately 4.3 million events in total

5.3.3 The Final Cuts

Although we possessed a redundant means for measuring the z component of the event vertex, only the weighted average was kept, i.e.

$$z_o = \frac{1}{\sigma_{\bar{\text{p}}\text{p}}^{-2} + \sigma_{\text{Zchmbr}}^{-2}} \left(\frac{z_{\bar{\text{p}}\text{p}}}{\sigma_{\bar{\text{p}}\text{p}}^2} + \frac{z_{\text{Zchmbr}}}{\sigma_{\text{Zchmbr}}^2}\right)$$

The weighted z distribution, z_o, is plotted in Fig. 5.4. The weighted z resolution adds in parallel to the resolutions for the $\bar{\text{p}}\text{p}$ trigger array and the Z chamber. Since the resolution of the Z chamber, σ_{Zchmbr}, is 2.5 cm and the $\bar{\text{p}}\text{p}$ trigger array can resolve the z vertex to a $\sigma_{\bar{\text{p}}\text{p}}$ of 3.1 cm, we expect the resolution of the weighted vertex, σ_z, to be $\sim$2 cm. In the upper plot of Fig 5.5, we plot the difference of the z intercepts

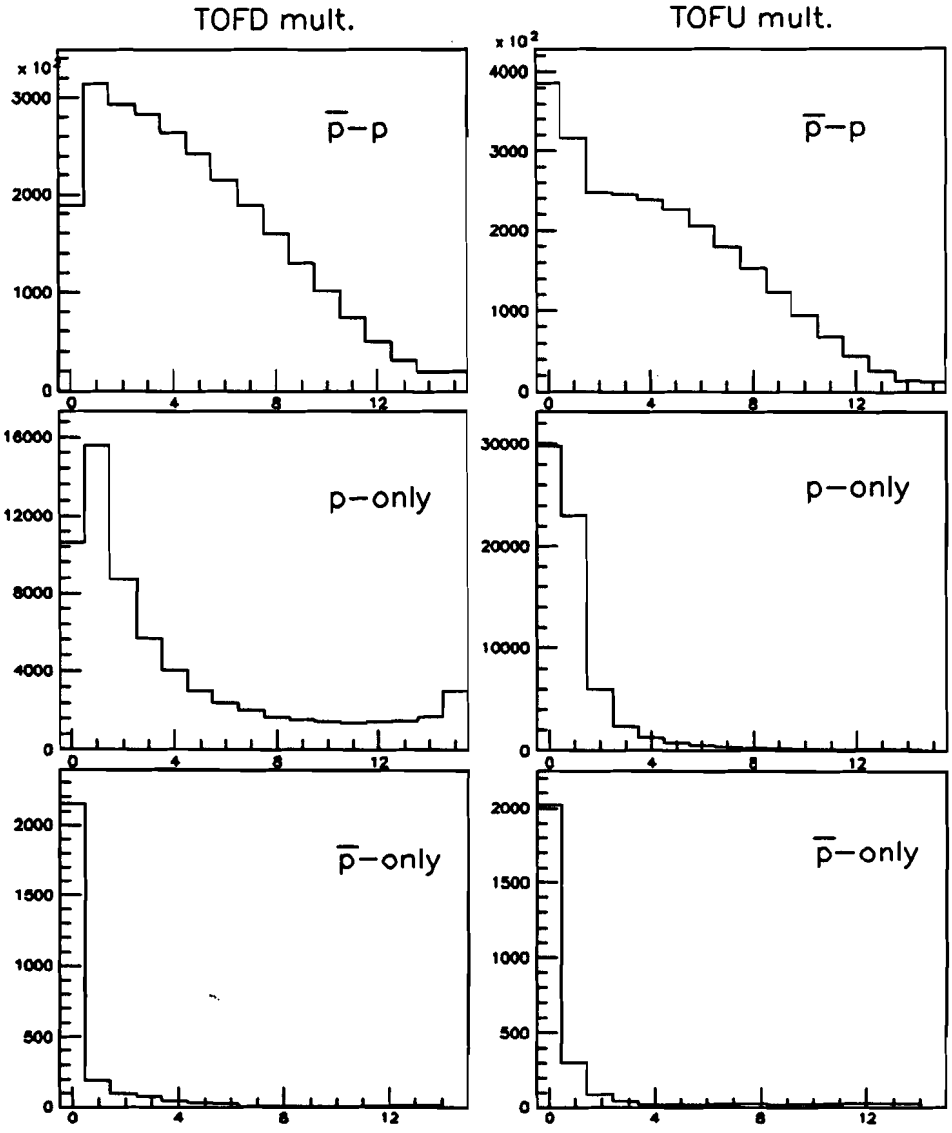

Figure 5.1 Frequency distribution of number of upstream and downstream trigger hodoscope counters hit for: (Top) $\bar{p}p$ collisions, (Middle) proton only stores and (Bottom) antiproton only stores.

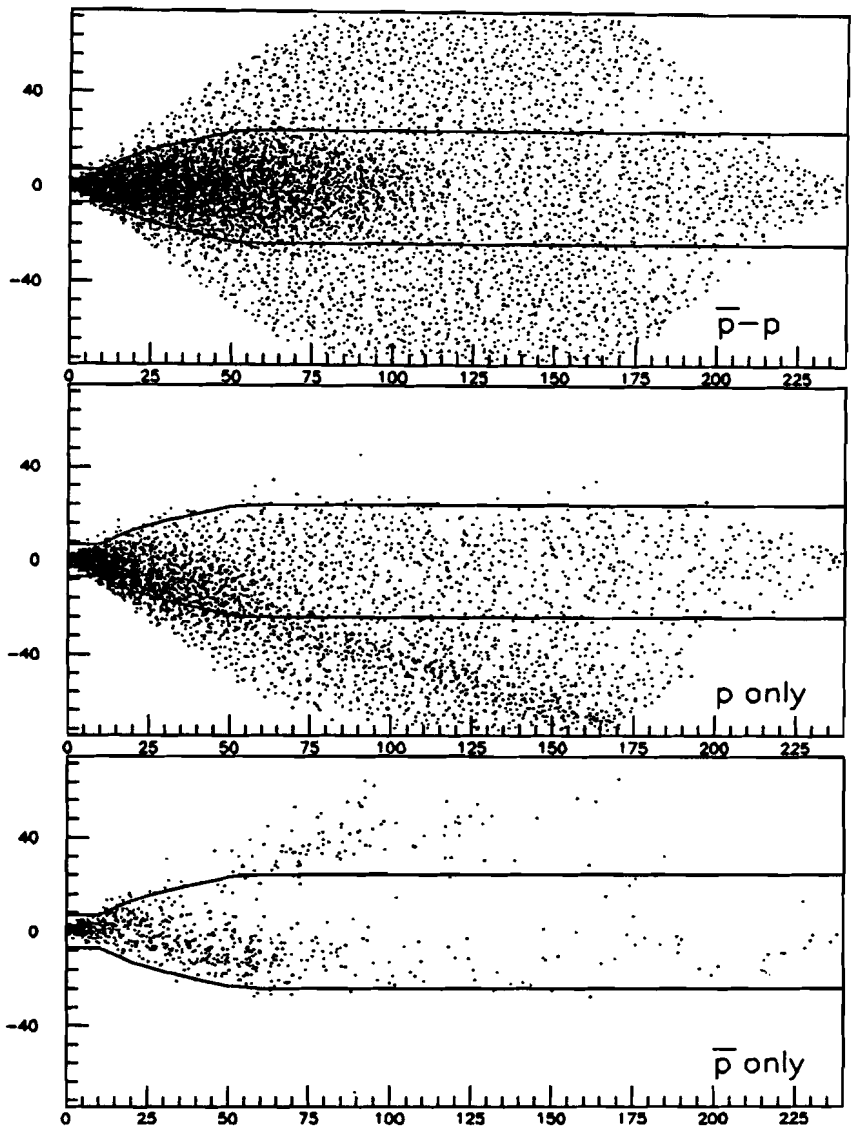

Figure 5.2 Asymmetry of event as a function of $N_{\mathbf{hodo}}$. Only events within lines pass the beam-gas selection criterion.

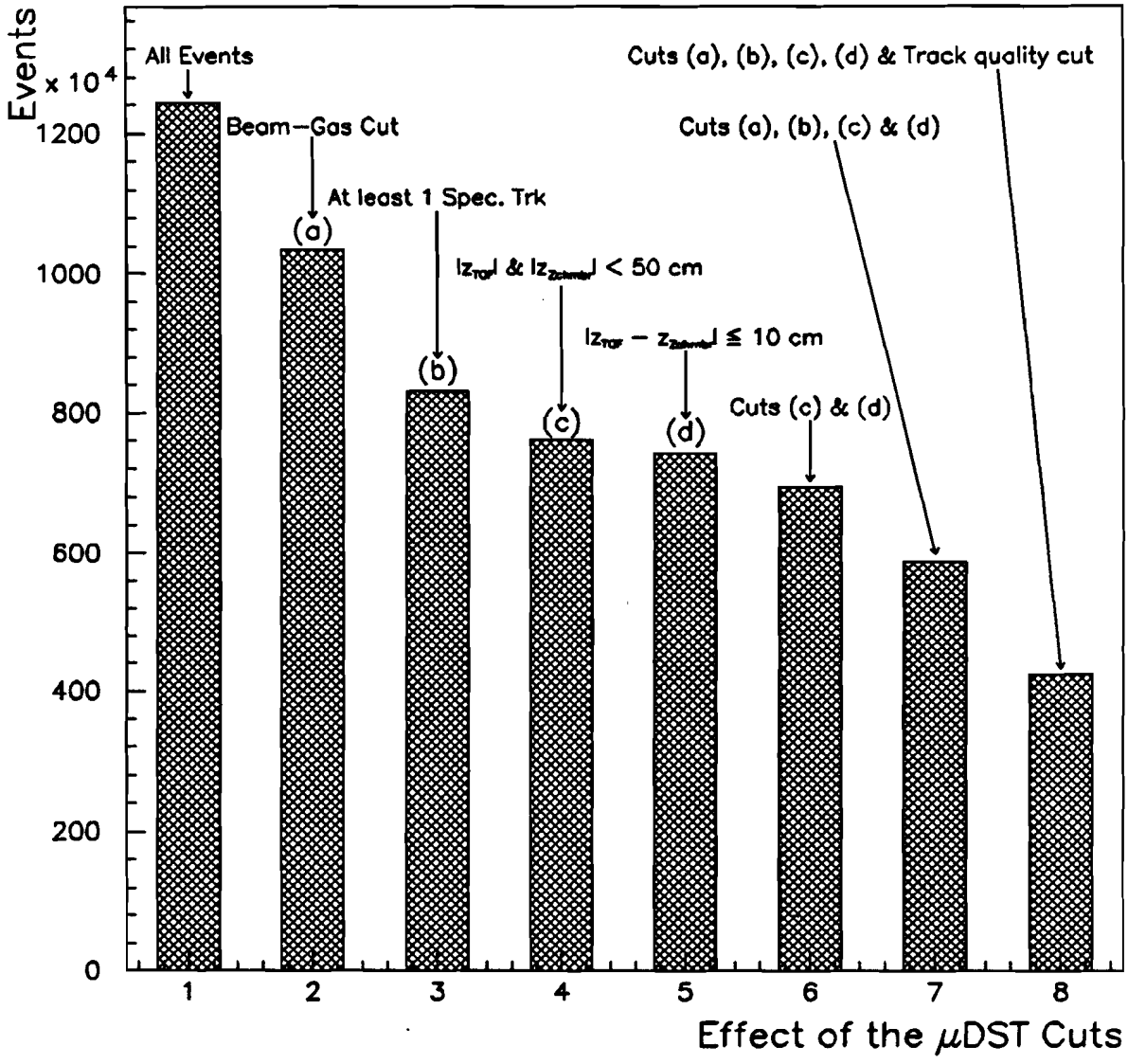

Figure 5.3 μDST cuts.

of two or more intersecting spectrometer tracks at the beamline and the weighted z event vertex. Intersecting spectrometer tracks are defined as two or more tracks with z intercepts within 2 cm of each other. If we fit a gaussian over the interval $|\Delta z| \leq 3.0$ cm, we extract a σ of 1.71 cm for the intersecting spectrometer case and for the all track sample, σ increases by only 7.5%. This result exceeds the expected resolution of the weighted z vertex. These tracks were also subjected to the *final cuts*, which are:

- $|z_o| \leq 17.5$ cm, where z_o is the weighted z event vertex.
- $p_\perp \geq 0.15$ GeV/c.
- $+2° \leq \phi \leq +18°$.
- $|z_{\rm trk}(x = 0) - z_o| \leq 10$ cm.
- $|y(x = 0)| \leq 8$ cm.

In Fig. 5.6, the difference histograms for $y_{\rm trk} - y_{\rm TOF}$ and $z_{\rm trk} - z_{\rm TOF}$ are plotted.

Because the vertical component of the hit cannot be resolved within the counter, TOF1 y information is quantized in units of counters. The granularity is 12 cm, which corresponds to the height of one TOF1 counter. The crosshatched regions for the Δz and Δy represent the candidates for matching the spectrometer tracks and the registered TOF1 hits. The criterea are:

- $|z_{\rm trk}(x = 197.2) - z^{\rm hit}_{\rm TOF1}| \leq 6$ cm.
- $|y_{\rm trk}(x = 197.2) - y^{\rm hit}_{\rm TOF1}| \leq 1$ counter.

Finally, we show the multiplicity distributions of the CTC and hodoscope counters (Fig. 5.7). These distributions are clearly not from nor corrected for minimum bias. Our trigger processor scaled down low multiplicity events so that we were sensitive to the rarer and more *interesting* high multiplicity events. What we have then is the trigger multiplicity. Only those events containing spectrometer tracks with a

matching TOF1 hit and which satisfied our mass cuts for either pions or antiprotons (see Table 6.18) were entered into these multiplicity distributions. Note that 16.6% of the events possess CTC information. In Fig. 5.8, the x and y distributions at the beamline for the CTC tracks are plotted along with the azimuthal and y intercept distributions for the spectrometer tracks. We conclude this section by showing the rapidity distributions for the mass identified spectrometer tracks with the condition that there be at least two intersecting tracks in the event (see Fig. 5.9).

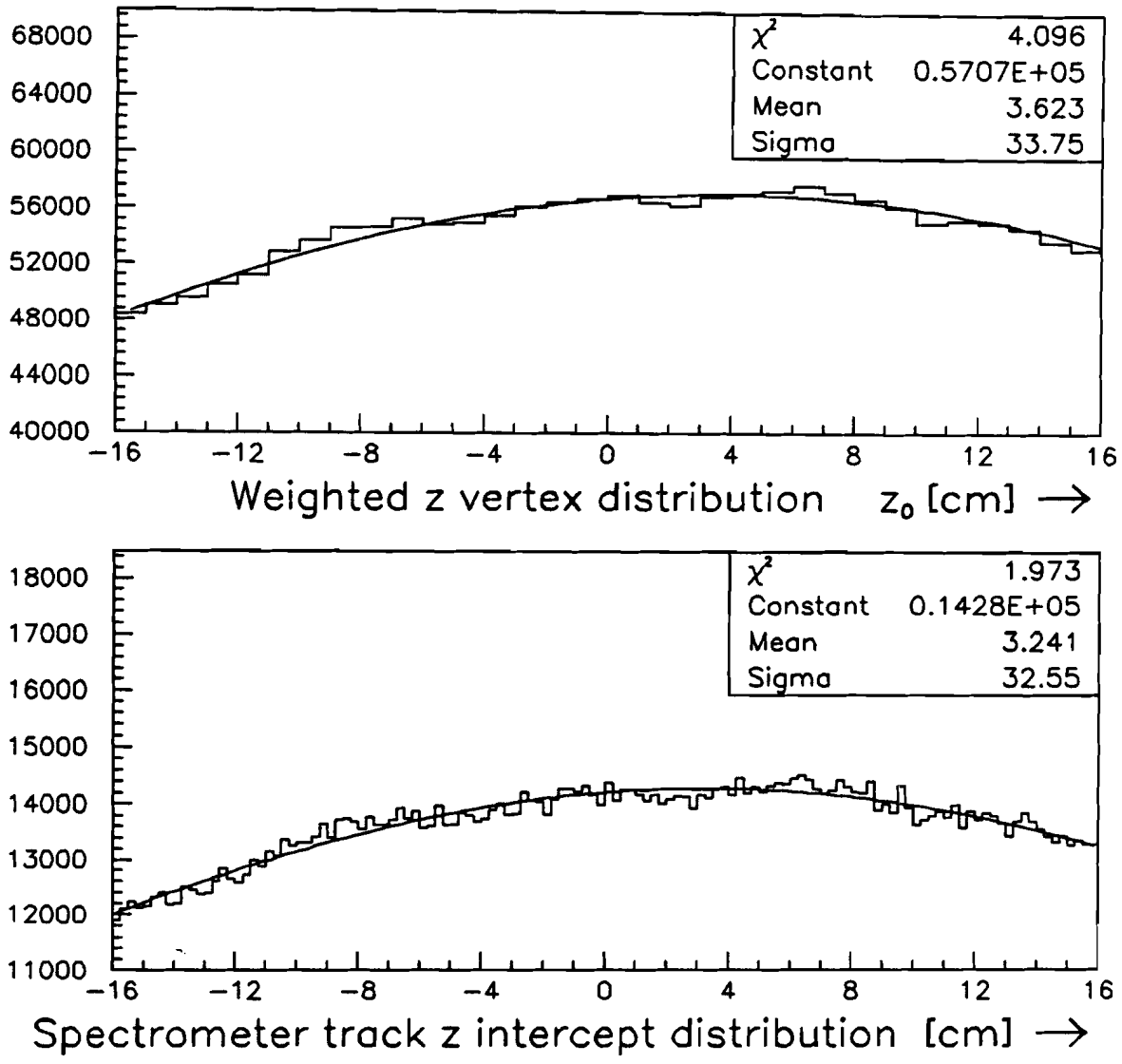

Figure 5.4 Distribution of the $\bar{p}p$ points of collision along the beamline. (Upper) Weighted z event vertex and (Lower) z intercept of spectrometer track at the beamline.

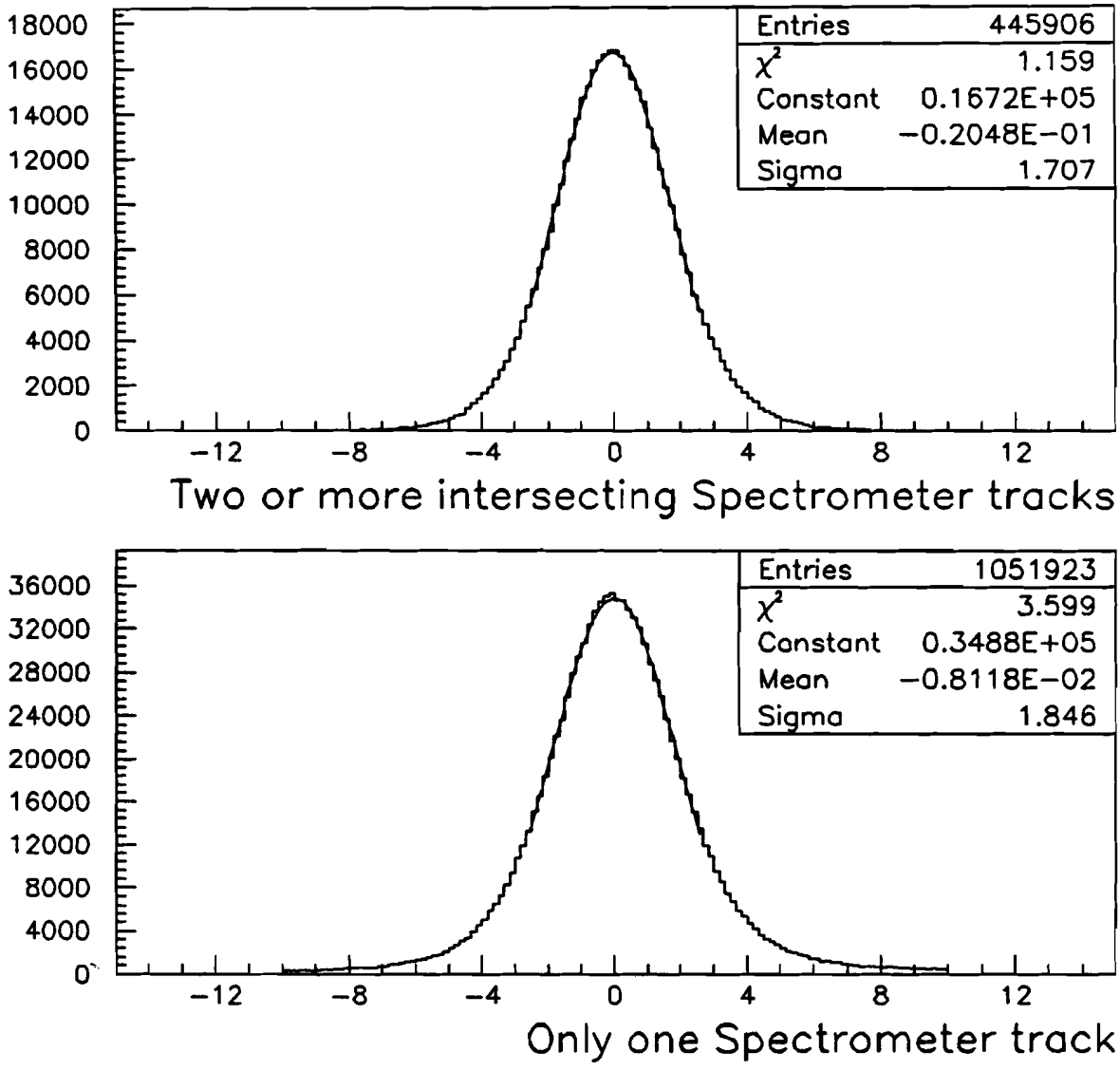

Figure 5.5 Difference histograms of spectrometer track z intercept at beamline and the weighted event z vertex. (Upper) An event with two or more spectrometer tracks all having z intercepts with 2 cm of each other. (Lower) Event with only one spectrometer track.

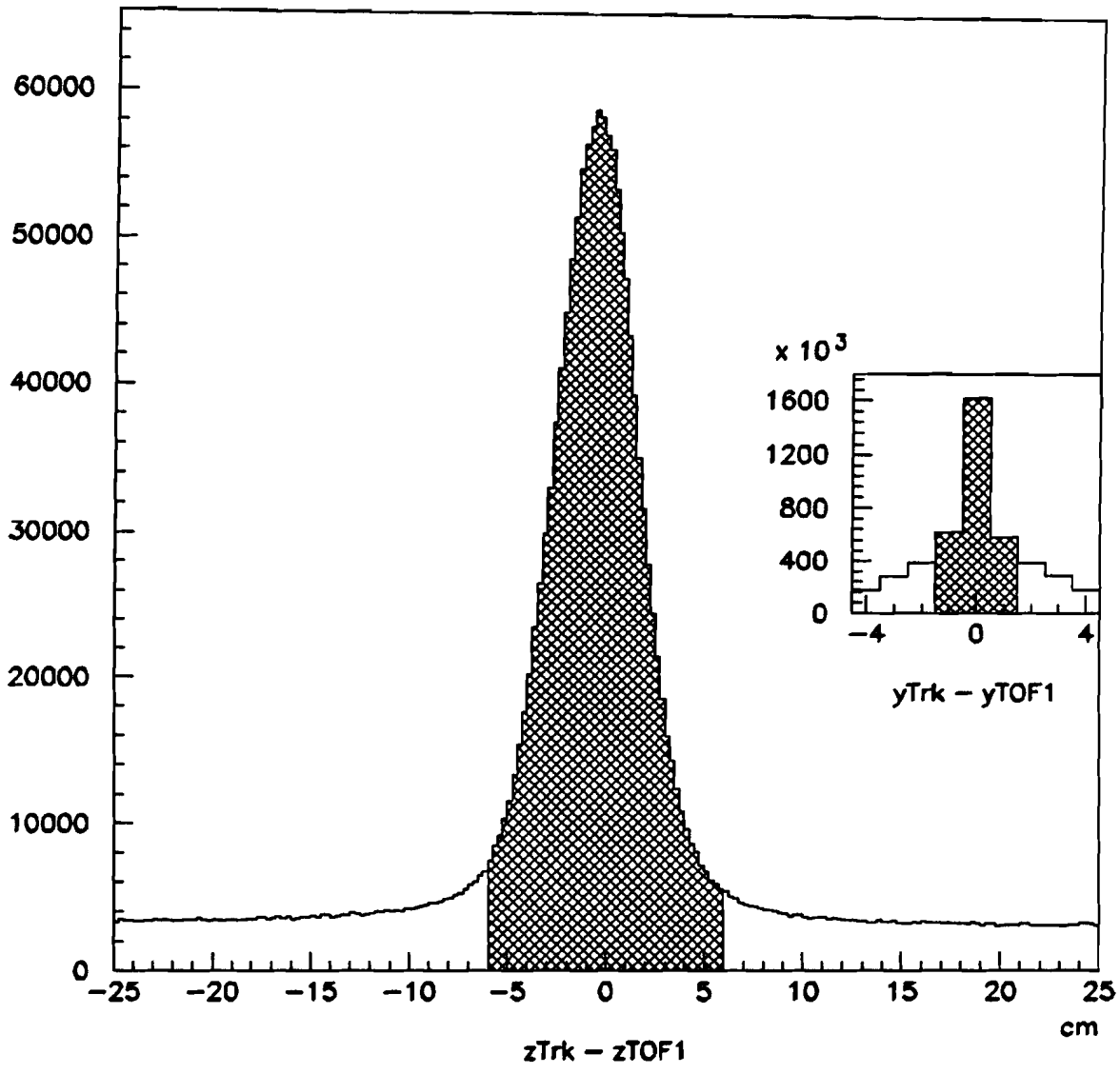

Figure 5.6 Difference histogram of spectrometer track z intercept at TOF1. The inlaid plot is the difference histogram of y intercept of track and which counter registered a hit. The crosshatched regions identify the conditions for matching a TOF1 hit with a spectrometer track.

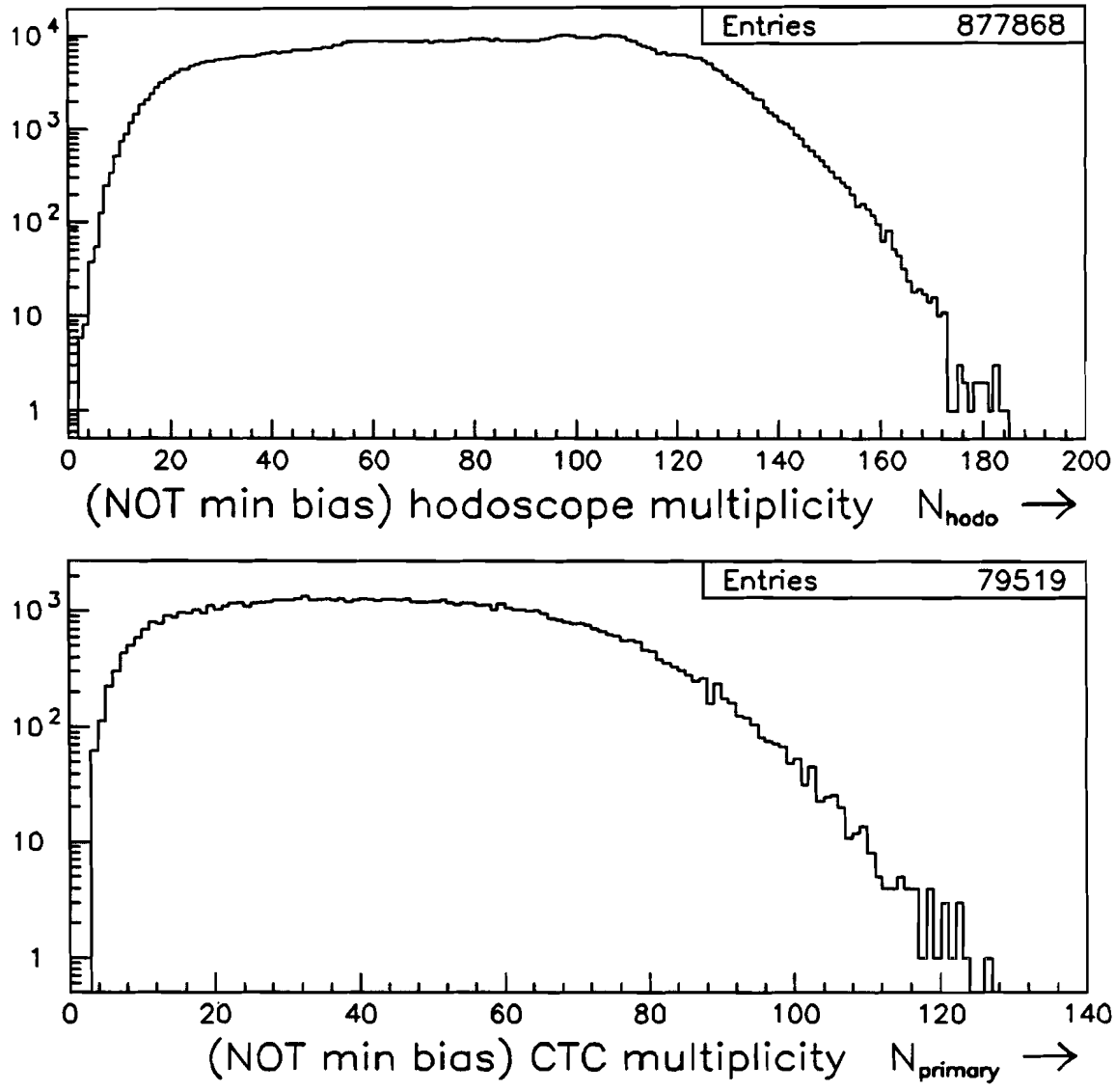

Figure 5.7 Trigger processor enhanced multiplicity distributions for events with at least one $\pi^{\pm}$ or antiproton in the spectrometer arm.

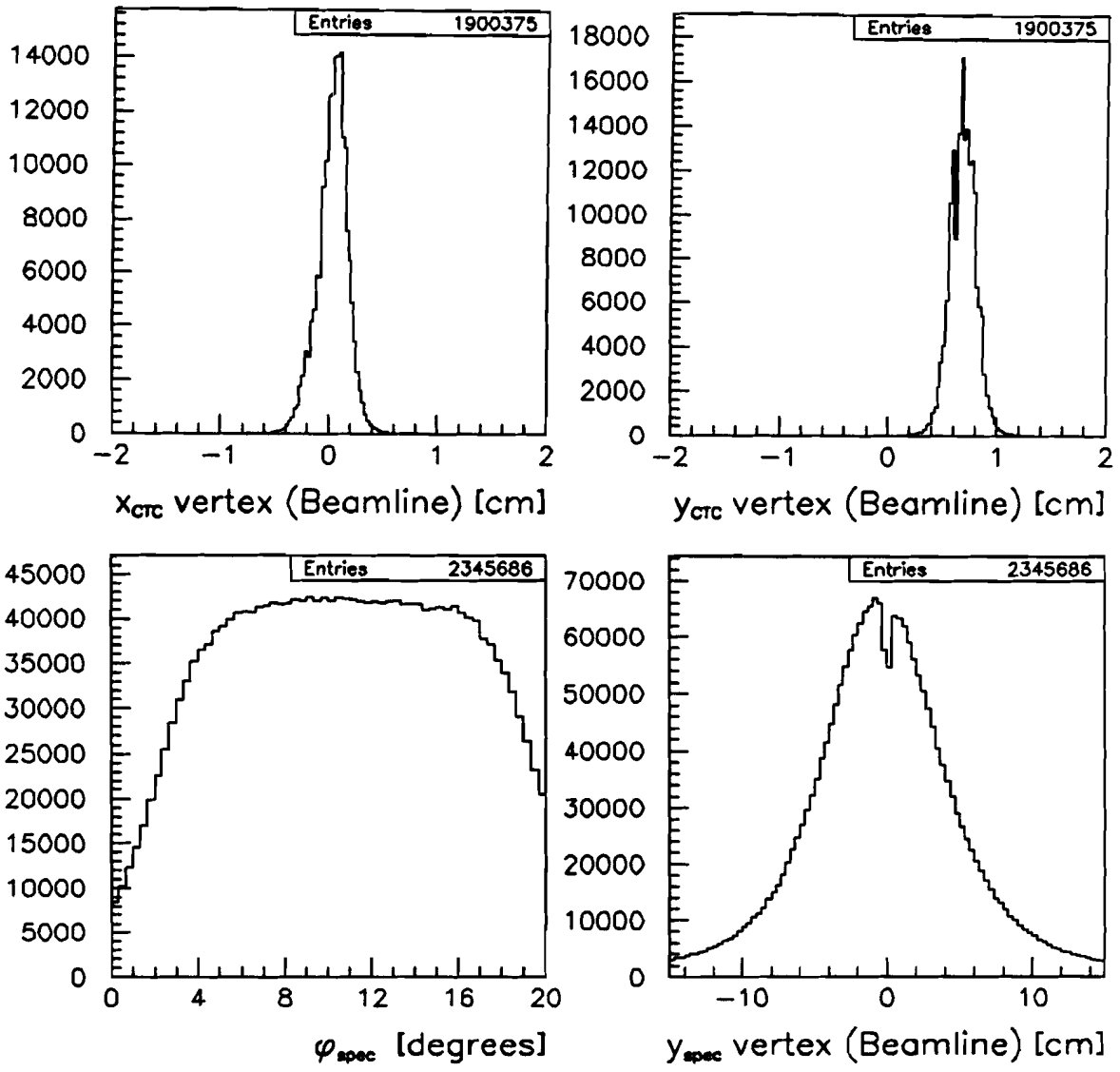

Figure 5.8 (Upper Left) x of Beamline determined from the CTC, (Upper Right) y of Beamline determined from the CTC, (Lower Left) Azimuthal distribution of spectrometer tracks and (Lower Right) y intercept distribution of spectrometer tracks.

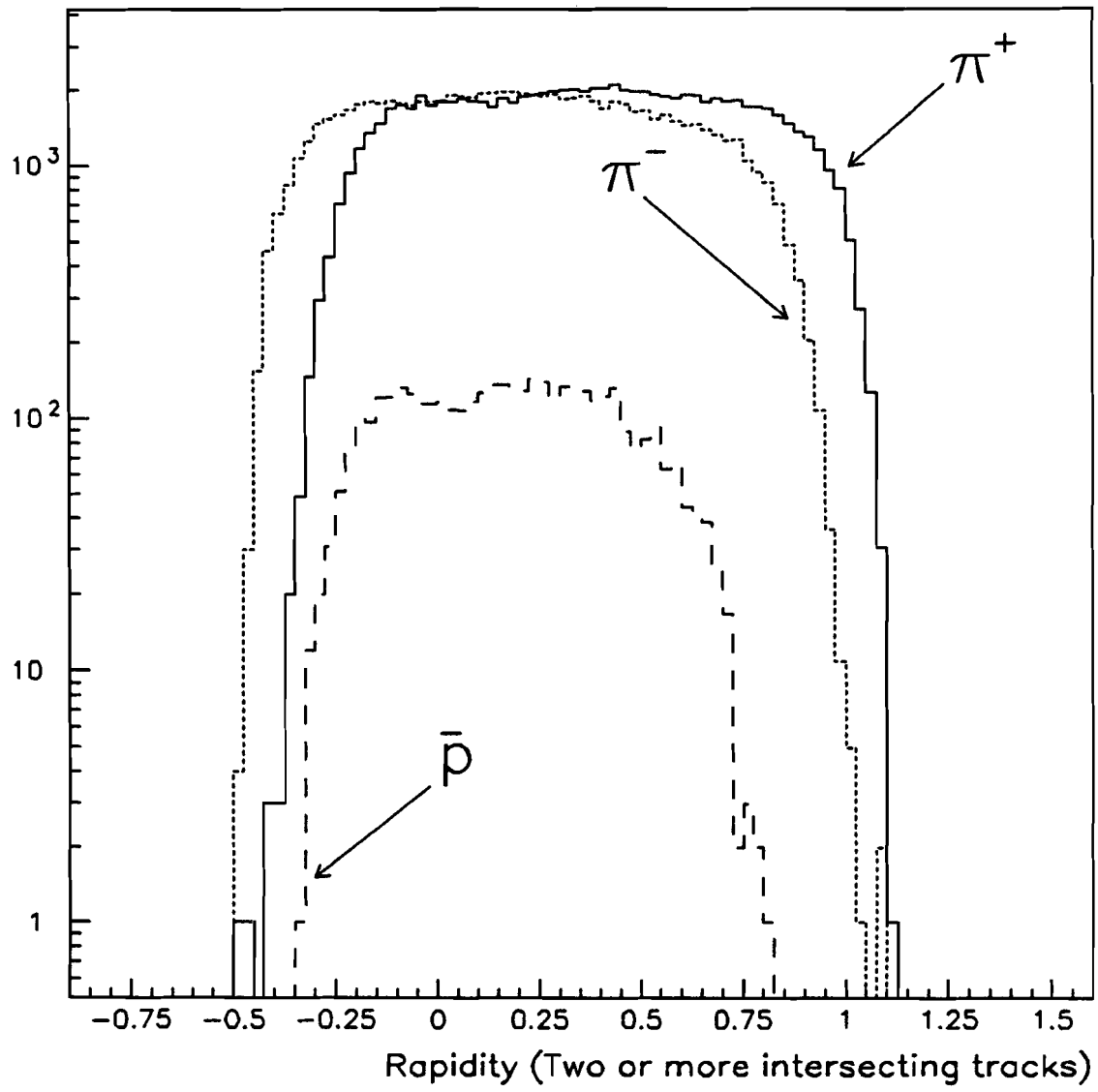

Figure 5.9 Rapidity distributions for $\pi^{\pm}$ and $\bar{p}$. There must be at least two spectrometer tracks in the event with z intercepts within 2 cm of each other.

6. SPECTROMETER ACCEPTANCE STUDIES

The primary objective of the E–735 experiment is to decipher the relationship between the average tranverse momentum and the event multiplicity for both all charged and mass-identified particles. However, before we start drawing conclusions on whether or by how much the the $p_\perp$ spectrum flattens as the pseudorapidity density increases, we must first ascertain whether the values that we measure truly reflect the physical properties of the passing particle. In other words, are we really seeing what's really there? This turns out to be a tough question. Not only do we need to understand the limits imposed by geometrical acceptance, the errors introduced by both detector mismeasurement and magnetic field uncertainities and potential trajectory misreconstruction due to particle decay, dE/dX losses, showers and ambiguities arising from overlapping tracks in the spectrometer, we must further contend with correctly modelling the horribly complicated process of parton-parton interactions in $\bar{p}p$ collisions, which give rise to these particles. Such a multi-faceted problem is not analytically tractable and we must turn to computer simulation to quantify the relationship between measurement and reality. In the following I will discuss the PYTHIA event generator, describe the GEANT simulation of tracking particles through the E–735 experiment setup and finally elucidate the methodology of our acceptance calculations.

6.1 Event Generator

The framework of hadronic collisions is complicated stuff. No one to date, for example, has successfully derived, from first principles, the minimum bias multiplicity

probability distribution for $\bar{p}p$ collisions at *any energy*. The QCD Langragian is simply not amenable to the perturbative method of solution in the low $p_\perp$ realm.

We are then faced with the problem of how to correctly model such things as the number, particle type and momentum of the products which result from nucleonic collisions. First of all, we must keep in mind that hadrons are expansive and extensive objects. Nucleons are composite particles consisting of the bound state of three valence quarks swimming in a gluonic sea. In a collision any of the partons associated with the proton can interact with any of those of the antiproton. Furthermore, unlike leptons, nucleons are not pointlike objects; they possess spatial dimension. Secondly, the initial conditions of the collisions will vary from one event to the next. The impact parameter, or the degree of hadronic matter overlap, certainly is not a constant. And naturally, by varying the impact parameter, the coupling between the interacting partons will change. The PYTHIA program version 5.4 reflects the current state of knowledge of the physical processes involved in hadronic interactions. Unlike the UA5 generator,[1] PYTHIA makes no *a priori* assumptions on the multiplicity probability distribution. I assumed that the GENCL simulation program [51] gives the correct minimum bias charged multiplicity distribution for $\sqrt{s}$ = 1.8 TeV. I adjusted the input parameters of PYTHIA to endow the same average multiplicity and standard deviation for the multiplicity distribution as was predicted by GENCL. (Below I list and discuss the input parameters which were used for the E-735 acceptance studies). It should be emphasized that these input parameters were chosen neither on the basis of the expected relationship between $\langle p_\perp \rangle$ and N_c nor from the ratios of K/π or the $\bar{p}/\pi$ as a function of multiplicity. That PYTHIA gives reasonable results for the $\langle p_\perp \rangle$ vs. N_c at Tevatron energies, I believe, tends to vindicate the efficacy of the model. The

[1]The UA5 $\bar{p}p$ simulation program, GENCL, generates the event multiplicity in accordance with the Negative Binomial Distribution. It employs a cluster of sources distributed in rapidity which then radiate the expected percentage of π's, K's and $p/\bar{p}$'s, etc. This program was tuned at $\sqrt{s}$ = 546 GeV. Although the UA5 event generator excellently predicts the multiplicity distributions, we found that it systematically overestimates the average transverse momentum by at least a factor of 10% for pseudorapidity densities of less than 10 at $\sqrt{s}$ = 1800 GeV [16], [17].

PYTHIA event generator adheres to Julius Caesar's time-honored principle of divide and conquer. It incorporates a potpourri of QCD processes, treats the expansive and extensive nature of hadrons and extends the perturbative parton-parton scattering into the low $p_\perp$ region by introducing a regularization of the divergence in the cross section as $p_\perp \to 0$. PYTHIA firmly resides within the framework of the LUND string model, where the partonic systems hadronizes by string fragmentation. The string represents a color flux tube connecting the interacting partons. The amplitude of any color flow is then obtained through the $2 \to 2$ Feynman diagrams. PYTHIA 5.4 is run in tandem with JETSET 7.3. These two packages together incorporate the following QCD components in processing an event:

- Hard-scattering Matrix Elements
- Structure Functions
- Initial State Radiation
- Beam Jets
- Final State Radiation
- Fragmentation of Hadrons

We used the default Eichten-Hinchliffe-Lane-Quigg set 1 (EHLQ1) parameterization for the structure functions. I tuned the following parameters:

1. MSEL = 0. Select appropriate subprocesses for minimum bias physics.
   (a) MSUB(93) = 1. Include double diffractive events.
   (b) MSUB(95) = 1. Allow for low $p_\perp$ scattering. (e.g. soft gg interactions)
2. ECM = 1800. Center of Mass energy at the Tevatron. (units are in GeV)
3. MSTP(2) = 1. Calculate α_s to first order, where α_s is the running coupling constant for strong interactions.

4. MSTP(33) = 3. The Q^2 value in $\alpha_s = \alpha_s(Q^2/\Lambda^2_{QCD})$ is multiplied by a factor of 0.075 to account for higher order corrections to the hard-scattering cross section for any given QCD subprocess.

5. MTP(82) = 4. The nucleon is described as consisting of two concentric regions: a core and shell. The distribution of matter is modeled by a double gaussian, where half the matter is concentrated in the core and the radius of the core is one fifth that of the shell. The impact parameter is allowed to vary.

6. PARP(82) = 2.10. The boundary between Perturbative and Non-Perturbative QCD. For an interaction below a $p_\perp$ of 2.1 GeV/c, only very soft $gg \rightarrow gg$ interactions take place so that the color flow is redirected. This is the regularization scale for multiple interactions.

The value for PARP(82) comes from the formula [50]:

$$p_{t_o} = 2.0 \text{ GeV} + (0.08 \text{ GeV}) \ln[\frac{\sqrt{s}}{540 \text{ GeV}}]$$

I had initially set the parameter MSTP(2) to 2, which allows for α_s to calculated to second order. It soon became apparent, however, that with this value of MSTP(2), charged pseudorapidity densities of greater than 15 particles per unit pseudorapidity could not be produced. There just was no tail.

To see if this change in the calculation of α_s affects the $p_\perp$ spectrum for fixed N_c, I compared the $\langle p_\perp \rangle$ for all negatively charged particles in the η byte of the spectrometer for the two α_s's. $\langle p_\perp \rangle$ was calculated in the region of $0 \leq p_\perp \leq 3$ GeV/c. The most striking difference is in the region of $0 \leq N_c < 10$. However, since we will not be including events of full phase space multiplicities of less the 10 in our final analysis, this discrepancy is unimportant. Plotted in Fig. 6.1 is the full phase space charged multiplicity distribution from the PYTHIA event generator (α_s of order 1).

We were finally prepared to start producing the computer generated $\bar{p}p$ collisions. We chose to bin the events in terms of the full phase space charged multiplicity where

Table 6.1 Comparison of $\langle p_\perp \rangle$ for two different α_s.

Multiplicity	$\langle p_\perp \rangle$ with α_s of Order 1 [Gev/c]	$\langle p_\perp \rangle$ with α_s of Order 2 [GeV/c]
$0 \leq n_c < 10$	$0.46 \pm .025$	$0.35 \pm .020$
$10 \leq n_c < 20$	$0.34 \pm .009$	$0.36 \pm .010$
$20 \leq n_c < 30$	$0.41 \pm .008$	$0.41 \pm .009$
$30 \leq n_c < 40$	$0.43 \pm .006$	$0.43 \pm .006$
$40 \leq n_c < 50$	$0.44 \pm .006$	$0.44 \pm .006$
$50 \leq n_c < 60$	$0.46 \pm .005$	$0.46 \pm .005$
$60 \leq n_c < 70$	$0.48 \pm .005$	$0.48 \pm .005$
$70 \leq n_c < 80$	$0.47 \pm .004$	$0.49 \pm .005$
$80 \leq n_c < 90$	$0.50 \pm .004$	$0.49 \pm .004$
$90 \leq n_c < 100$	$0.50 \pm .004$	$0.50 \pm .004$

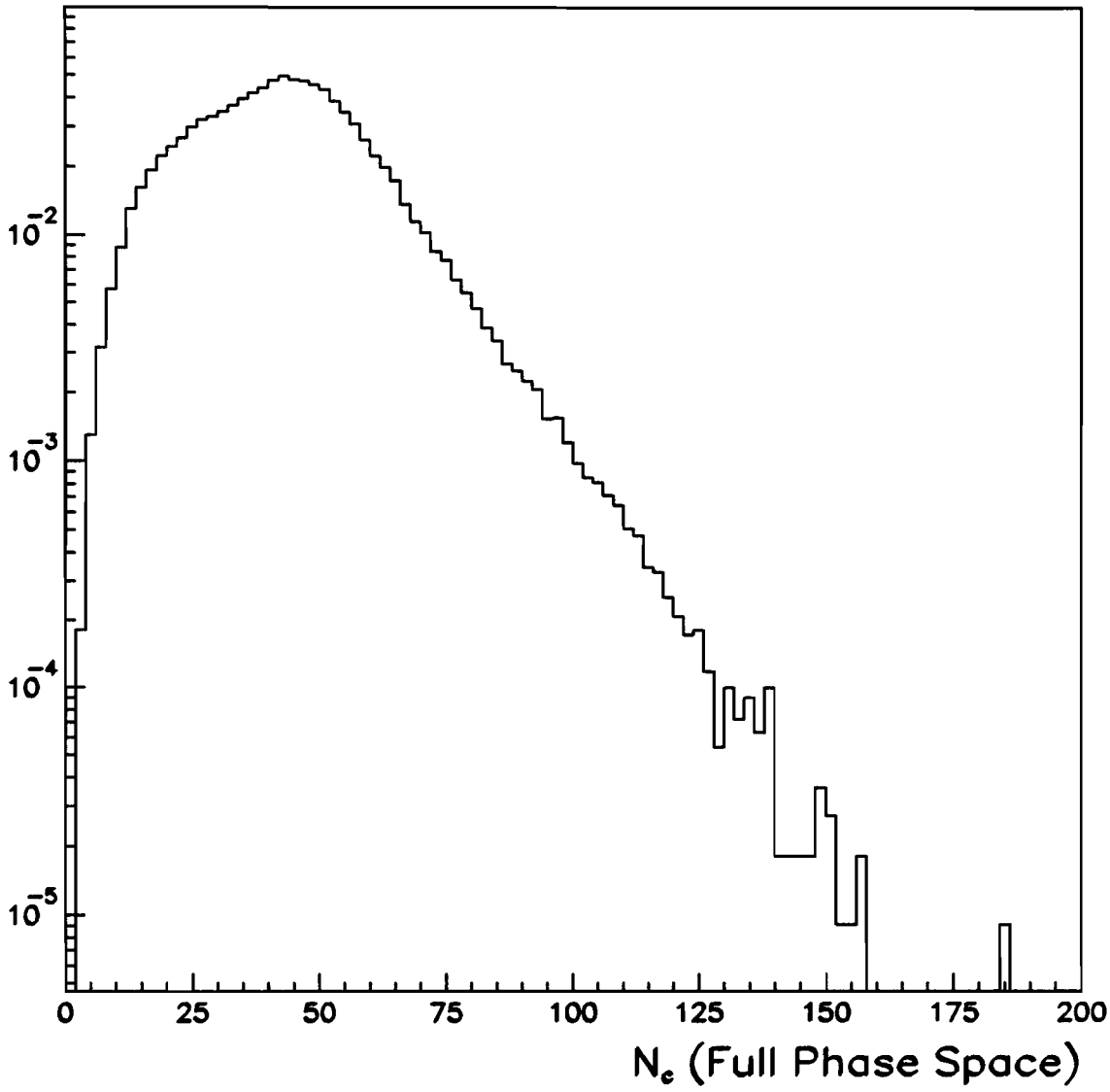

Figure 6.1 Full phase space charged multiplicity distribution from the PYTHIA event generator. The selected switches are discussed in the text.

the binwidth for each of these files was $\Delta N_c = 10$. In the effort to minimize CPU resource wastage, The PYTHIA production program produced 10 of these event files simultaneously.[2] We first processed events in the multiplicity range of $0 \leq N_c < 100$. For example, if the multiplicity of the event fell between $N_c = 40$ and $N_c = 50$, say, the PYTHIA output would then be directed to the fifth file. In this case, events with multiplicities exceeding 100 were discarded. All in all, 30 multiplicity binned PYTHIA event files were produced. I might add, the production program checked each and every event to insure that energy, momentum and charge were conserved to within one part in a thousand. As the reader can see in Fig. 6.1, events with a charged multiplicity greater than 200 are exceedingly rare. Even with the powerful CPU resources of the Amdahl mainframe, it took 120 CPU hours (i.e. 5 VAX 11/780 CPU months) to produce 1100 PYTHIA events with multiplicities in the interval: $220 \leq N_c < 230$. The relationship between the full phase space event multiplicity and the average transverse momentum is plotted in Fig. 6.2 for negatively charged particles residing within the pseudorapidity of the aperture of the spectrometer.

Note that PYTHIA predicts a rise in $\langle p_\perp \rangle$ for N_c less than 100 (i.e. $dN_c/d\eta = 10$). Thereafter, the average tranverse momentum is flat with increasing event multiplicity. The rise and leveling off characteristic in $\langle p_\perp \rangle$ vs dN_c/dy holds true for the π's, K's and $\bar{p}$'s separately, see Fig's 6.3, 6.4 and 6.5.

6.2 Geant

The next link in the chain of our Acceptance Studies was to render a realistic representation of the geometry and mass composition of the E-735 experiment. We made use of the GEANT 3.13 Monte Carlo [52] package to describe the experimental layout and simulate the decays, showers, $\int \vec{B} \cdot d\vec{\ell}$ effects, and the energy losses of the particles. Clearly, this link demands especial scrutiny if the acceptance analysis is to

[2]FORTRAN i/o limitations places an upper limit of the total number of files that can be opened at a given time. For our PYTHIA production, we had room for only 10 output files.

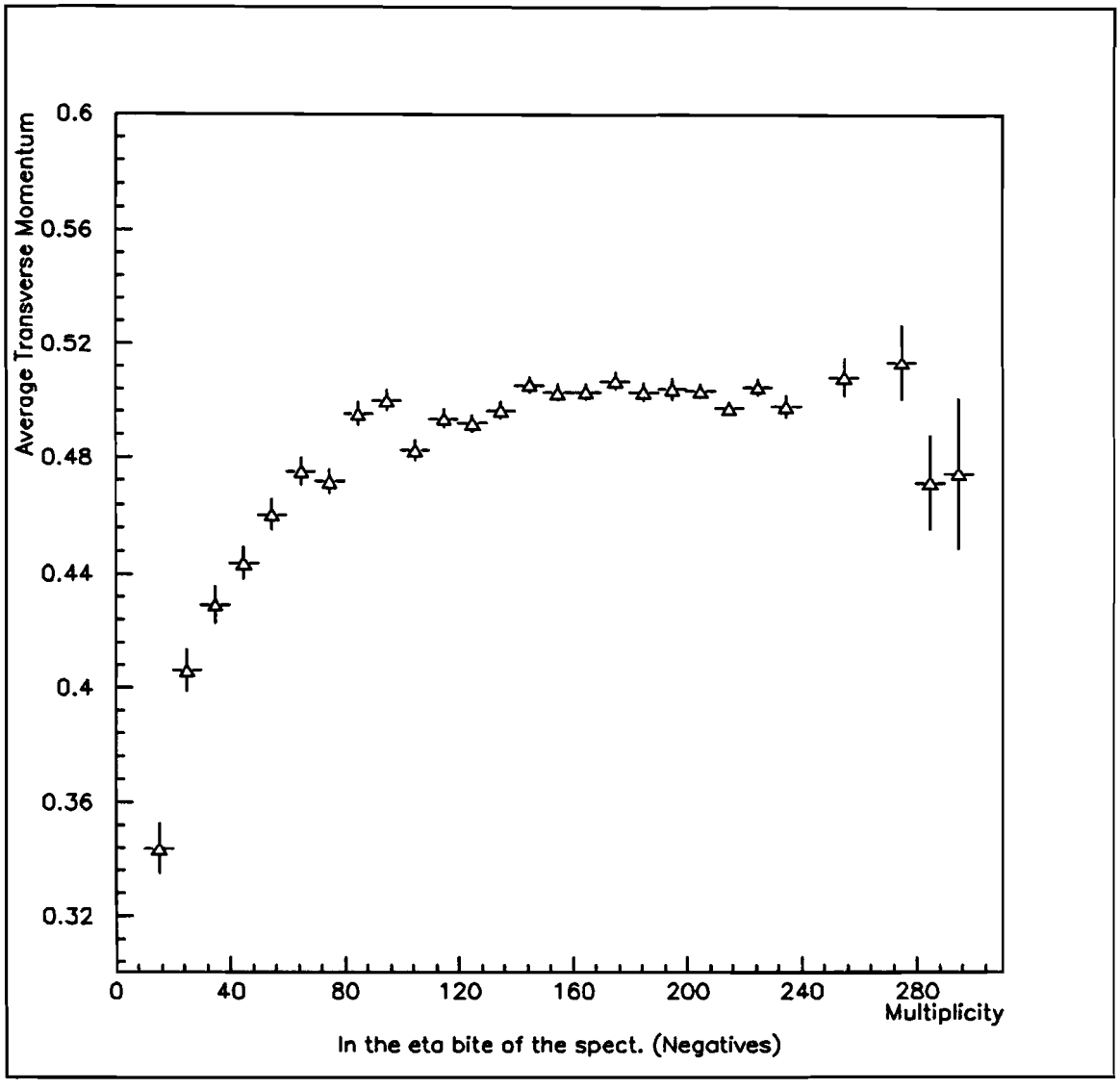

Figure 6.2 PYTHIA: $\langle p_\perp \rangle$ vs n_c for negatively charged particles in the pseudorapidity of the spectrometer.

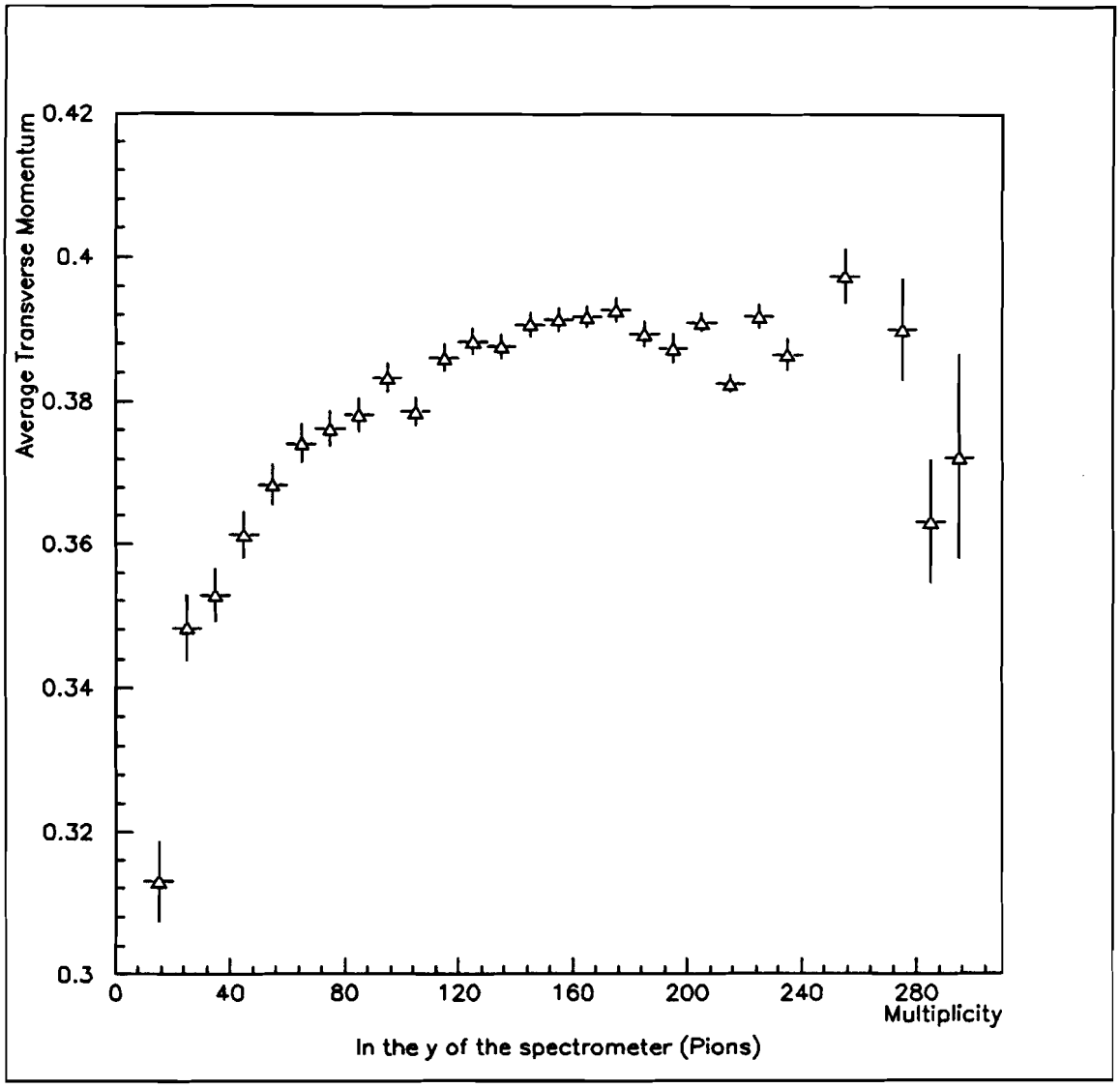

Figure 6.3 PYTHIA: $\langle p_\perp \rangle$ vs n_c for $\pi^\pm$'s in the rapidity of the spectrometer.

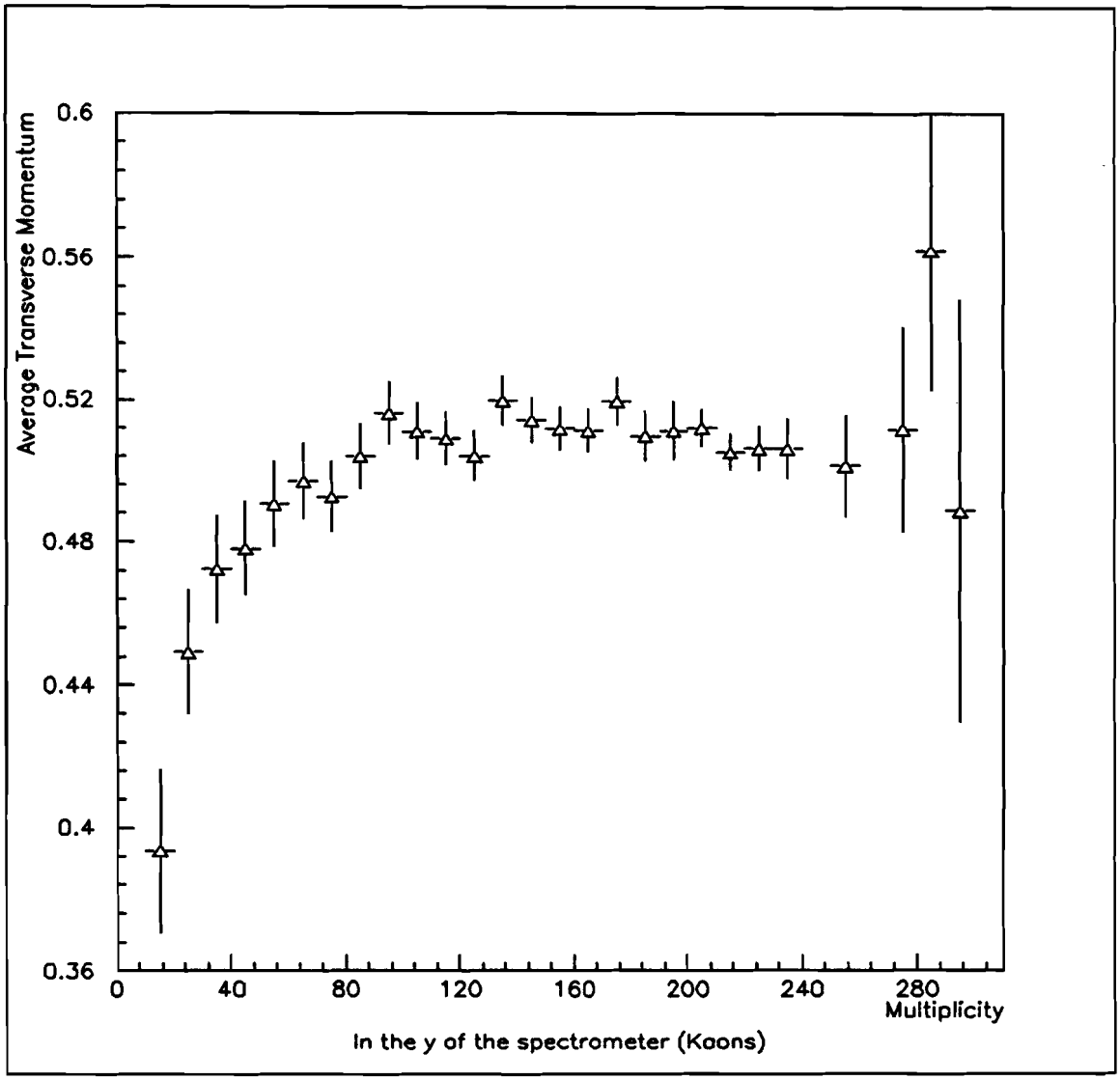

Figure 6.4 PYTHIA: $\langle p_\perp \rangle$ vs n_c for $K^\pm$'s in the rapidity of the spectrometer.

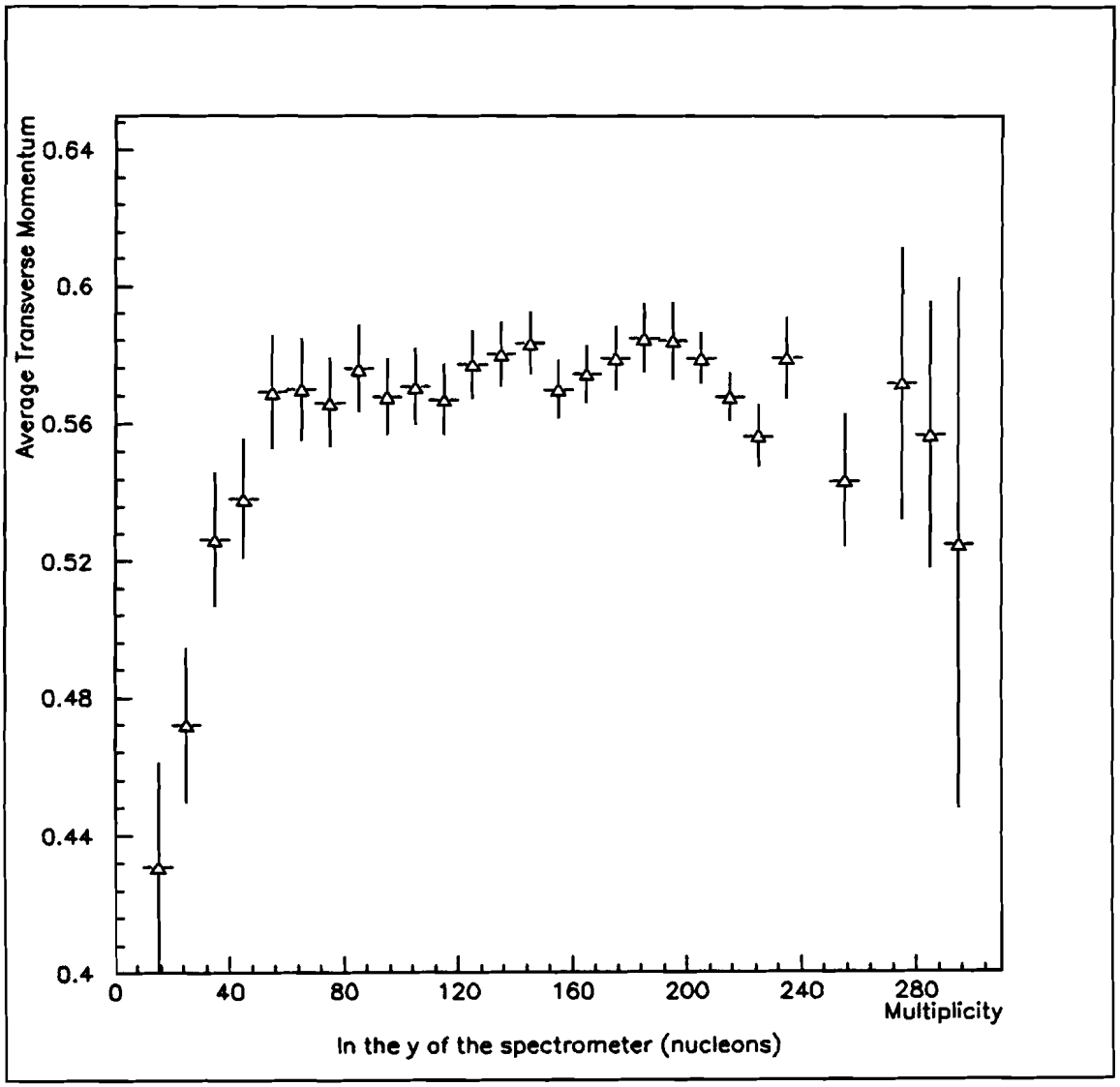

Figure 6.5 PYTHIA: $\langle p_\perp \rangle$ vs n_c for $p/\bar{p}$ in the rapidity of the spectrometer.

pass muster. GIGO or Garbage In – Garbage Out is the bane of all CPU intensive Monte Carlo productions and the fear of GIGO guided our work. We ran tests for nearly a year before we commenced the production of the GEANT Monte Carlo on the Amdahl mainframe. Among the checks we made were:

- Hodoscope hit distributions [16], [53].
- Distribution of secondary vertices [16].
- Reconstruction efficiency for π's, K's and $\bar{p}$'s with fixed transverse momentum.
    1. No dE/dX nor decays.
    2. dE/dX but no decays.
    3. dE/dX and decays.
    4. Fixed Polar and azimuthal angles.
    5. Flat in rapidity and azimuth.

We uncovered and corrected subtle and not-so-subtle errors in the coding of the geometry, detector mass composition and the description of the magnetic field. We optimized the code for production on the Amdahl and took care to avoid some of the special features peculiar to IBM FORTRAN and the CP/CMS operating system. For example, if one unwittingly underdimensions an array, IBM FORTRAN will blithely overwrite memory without bothering to issue an error message. Furthermore, one must be aware of the precision limitations on floating point operations imposed by IBM FORTRAN. This flavor of FORTRAN suffers from two major deficits: First of all, the representation of a floating point number varies from 21 to 24 bits as opposed to the uniform 24 bits for the VAX machines and secondly, numbers are not rounded in floating point operations — they are truncated. This particular precision problem reared its ugly head for low energy particles traveling within the magnetic field. As the particles curled up in the field, the loss of precision in the floating point operations would cause the GEANT code to fall into the trap of the infinite loop. We

inserted additional code to halt tracking if the number of tracking steps exceeded 4000. (i.e. the average number of steps required for tracking a particle was less than 200). Finally, one should be aware of the deficiencies of the system supplied random number generator on the Amdahl. Although the distribution of the random numbers is uniform over the interval $[0,1)$, I found that the cycle length was outstandingly small. I define the cycle length as the number of iterations before the sequence repeats the input values. After 8192 iterations the system supplied random number generator repeats the first two numbers. To make the existing random number generator more reasonable, I employed the Bays-Durham algorithm.[3] By selecting $N = 200$, the cycle length is upped to $117,751,964$ iterations, or a $1.4 \cdot 10^4$–fold improvement.

After all these diagnostics, we were finally prepared to start the production of the E-735 Spectrometer Acceptance Studies.

6.3 Acceptance Calculations

6.3.1 Introduction

The center of the spectrometer magnet is offset 32 cm downstream from the nominal $\bar{p}p$ collision point and as a consequence of this asymmetric geometry, slightly fewer π^-'s strike the TOF1 counters that π^+'s. Furthermore, as the momentum of the particle approaches zero, the rapidity interval that the spectrometer aperture spans will become smaller. This kinematic fact implies that for an antiproton and a pion of equal transverse momentum, the pion will more likely enter the spectrometer aperture. Besides the differences in acceptance introduced by the geometry, our tracking algorithms more efficiently reconstruct low momentum π^+'s over the negatively charged counterparts. This is because the magnetic field tends to sweep low $p_\perp$ π^-'s

[3] a) Initialize by generating and storing N random numbers in an array v of dimension N, using the system supplied generator. Generate a new random number u and save it. (b) On the next call, use this u as an address $j = 1+$(integer part of the product of N and u) to select v_j as the random number to be returned. Also save this v_j as u for the next call. Replace v_j in the array with a new random number using the available generator. On the next call, go to (b). See [54] and [55].

Table 6.2 Switches for GEANT 3.13.

Switch	Value	Description
MFLD	1	Magnetic Field on
PSEL	1	Halt tracking if $\|\vec{p}\| < 3$ MeV/c
PAIR	1	γ pair production
HADR	1	Hadronic interactions
DRAY	1	Delta rays
DCAY	1	Particle decays
ANNI	1	Particle annihilation
PHOT	1	Photo-electric effect
PFIS	0	No photofission
BREM	1	Bremsstrahlungen
MUNU	1	Muon nuclear interactions
LOSS	1	Energy loss
MULS	2	Molière scattering
COMP	1	Compton scattering

Kinetic Energy Cuts

Cutoff [GeV]	Description
0.001	γ
0.001	e^-
0.010	neutral hadrons
0.010	charged hadrons
0.010	μ
0.001	e^- bremsstrahlung
0.001	μ & hadron bremsstrahlung
0.001	δ's by e^-
0.001	δ's by μ

into the less efficient regions of the detectors. We therefore have a confluence of two primary factors, i.e. geometrical and track reconstruction efficiencies, which dictate our overall spectrometer acceptance, $\varepsilon_{\rm tot}$. Moreover, pions decay into muons. Should a pion decay directly in front of a TOF1 counter, the muon will be reconstructed as a pion. In order not to underestimate the overall acceptance of pions, we must therefore include this effect of muons masking as pions. In our acceptance studies, we factored $\varepsilon_{\rm tot}$, into three components, $\varepsilon_{\rm decay}$, $\varepsilon_{\rm geom}$ and $\varepsilon_{\rm tre}$. The first term takes into account the $\pi \rightarrow \mu\nu$ effect and the latter two terms arise from the geometry of the spectrometer and the track reconstruction efficiency, respectively. We have:

$$\varepsilon_{\rm tot}(p_\perp, {\rm ID}, N_c) = \varepsilon_{\rm decay}(p_\perp, {\rm ID}) \cdot \varepsilon_{\rm geom}(p_\perp, {\rm ID}) \cdot \varepsilon_{\rm tre}(p_\perp, {\rm ID}, N_c)$$

The overall efficiency, then, is a function of three variables, which are the transverse momentum, the particle type and the event multiplicity. In the following subsections, I will discuss our event binning procedures, Monte Carlo analysis chain and our efficiency studies.

6.3.2 Event Binning

How well we can reconstruct the trajectory of a $\pi^\pm$, $K^\pm$'s or a $\bar{p}$'s as a function of the event multiplicity, event z vertex and the transverse momentum of the particle is the fundamental question of our study of the spectrometer acceptance. We modeled the event multiplicity using the PYTHIA event generator. We chose this generator because it predicts reasonable values of the $\langle p_\perp \rangle$ as a function of charged event multiplicity, N_c.

We binned the acceptance in terms of:

1. Event z vertex: The $\bar{p}p$ points of collision along the beamline are binned in steps of 5 cm. This 5 cm step is the approximate resolution of the $p\bar{p}$ trigger hodoscope z vertex finding algorithm on the Amdahl DSTs. The z binning ranges from -15cm to $+15$cm (7 bins). The events are generated discretely at $z = [\pm 15, \pm 10, \pm 5, 0]$.

2. Transverse momentum: 16 bins (see Table 6.3). The events are generated uniformly within the bin.

3. Particle type: π^+, π^- and $\bar{p}$. (3 bins).

4. Event multiplicity: $N_c = 45, 95$ and 195 for full phase space, i.e. $dN_c/dy \simeq 4, 9$ and 19, respectively. (3 bins)

5. Rapidity: Flat between $y = -0.9$ and $y = 1.6$ (1 bin). Note that the rapidity, y, $y = y(\text{mass}, p_\perp, \theta, z_{\text{vert}})$, where θ is the polar angle. These limits exceed the spectrometer rapidity acceptance for all $p_\perp, \theta, z_{\text{vert}}$ for the lower mass hadrons.

6. Azimuth: Flat between $\phi = +2°$ and $\phi = +18°$. (1 bin).

To process one high multiplicity PYTHIA event through the GEANT Monte Carlo is CPU intensive. For example, it requires nearly two CPU minutes of Amdahl time (i.e. 1 VAX 11/780 CPU Hour!) to run a single high multiplicity event of $N_c = 195$ through our GEANT program. Clearly, if we were to collect sufficient statistics with reasonable binnings in the event multiplicity, $p_\perp$, particle type and event z vertex and stay within our allotted quota of 2000 CPU hours on the Amdahl demanded that we be somewhat clever in finding an efficient means to produce these acceptance files. Instead of plodding down the porcine path of wasteful CPU exploitation and merrily generate 7 z vertex bins × 16 $p_\perp$ bins × 3 particle type bins × 3 multiplicity bins × 5000 events/bin, which altogether comes to $5.05 \cdot 10^6$ events[4], we chose to recycle our events. We split the acceptance production into two parts: a PYTHIA component for mimicking the event background and a *known track* component which serves as the signal. This signal was binned in terms of $p_\perp$, and particle type (see 2 & 3 above and also Table 6.3). Before either the PYTHIA or the *known track* event were tracked through our GEANT package, the event was given a discrete z vertex, which simulates the point along the beamline where the proton collided into the

[4]This comes to 4.8 years if we assume it takes 30 seconds to process one event

Table 6.3 $p_\perp$ binning.

$p_\perp$ bin	$p_\perp$ interval [GeV/c]
1	0.15 — 0.17
2	0.17 — 0.20
3	0.20 — 0.25
4	0.25 — 0.30
5	0.30 — 0.35
6	0.35 — 0.40
7	0.40 — 0.50
8	0.50 — 0.60
9	0.60 — 0.70
10	0.70 — 0.95
11	0.95 — 1.15
12	1.15 — 1.35
13	1.35 — 1.55
14	1.55 — 1.75
15	1.75 — 2.00
16	2.00 — 2.50

antiproton. This z vertex was gaussian distributed with a σ of 0.01 cm, which, in essence, describes a δ function. Later we combined the PYTHIA and *known track* files which shared common z vertices for our [(noise + signal) - noise] studies. (More on this below).

6.3.3 Monte Carlo Analysis Chain

A PYTHIA or *known track* event was run through the gamut of several programs and packages for processing. First, the event was fed into our GEANT detector simulation package, Q735MOD, which models the E–735 experiment. After processing an event, Q735MOD output two data files, HIT.DAT and GEANT.DAT. The GEANT.DAT contained GEANT tracking information and HIT.DAT kept the hit information (see Table 6.4). We saved these two output data files on 9 track magnetic tape for each and every PYTHIA or *known track* file inputted into Q735MOD. The hits in the HIT.DAT file were then passed to the HITSMEAR program. The magnet wire chambers and the straw drift tubes all could resolve a hit to within 500 μm. HITSMEAR smeared the hits, with a gaussian σ consonant with the resolution of the spectrometer wire chambers. Moreover, the detector efficiencies were modeled in HITSMEAR. For example, if a detector were 90% efficient, then 10% of the time a given hit in this detector would be tossed out of the event hit pool. And to model the event z vertex resolution of the $p\bar{p}$ trigger hodoscope, the event vertices were evenly spread within the z bin. This smeared hit and z vertex information were then passed to the intermediate data file HITMAP.DAT, which in turn was read in by the Monte Carlo track reconstruction program, MCRCT. We applied the selfsame algorithms in reconstructing spectrometer tracks from the Monte Carlo hits as were used on the real data for producing the Amdahl Data Summary Tapes. The reconstructed tracking information was then output to the data file TRACK.DAT. The program GENTUPLE merged and condensed the two data files GEANT.DAT and TRACK.DAT and output the results into Ntuple FZ format. The FZ format is an option of the CERN ZEBRA memory management package which formats the file so that it can easily be tranferred to and read on any

machine. I then ported the Ntuple file over to the FNAL VAX cluster and there converted the FZ file back to binary, or RZ in ZEBRA parlance. These Ntuple files were then accessible to users operating within the friendly VAX VMS environment.

6.3.4 Geometrical Effects

The aperture of the spectrometer is shifted 32 cm downstream and spans the pseudorapidity range of $\eta = -0.36$ to $\eta = +1.0$ units (for a track originating at $z = 0$) and azimuthal range of $\phi = 0°$ to $\phi = 20°$. The spectrometer, then, subtends the solid angle of 0.5 sr. The geometrical acceptance *is not uniform* in z_o (the $\bar{p}p$ interaction point) nor in the transverse momentum of the particle. Indeed, as $p_\perp \rightarrow 0$, the rapidity the spectrometer spans becomes smaller. $p_\perp$ and y are related via the expression [9]:

$$\cosh^2 y = \frac{m^2 + p_\perp^2 / \sin^2 \theta}{E_\perp^2}$$

where m denotes the mass, θ reflects the polar angle and the transverse energy, $E_\perp$, is defined as $(m^2 + p_\perp^2)^{\frac{1}{2}}$. The most glaring shortcoming of our geometry is that $\bar{p}$'s are less likely to enter the spectrometer aperture than π's. As will soon be demonstrated, however, π^+'s and π^-'s are equally accepted *geometrically.*

We employed the ***known track*** component to simulate the effects of the spectrometer geometry. Recall that the events are generated discretely from -15 cm to $+15$ cm in 5 cm intervals or at 7 points along the beamline. (See above). The z vertex, z_0, is then smeared uniformly within the range of $z_0^i \pm 2.5$ cm to form z vertex used in reconstructing the spectrometer track. This i^{th} z bin is of width 5 cm. The tracks are binned in terms of transverse momentum, particle type and z vertex and were generated uniformly in rapidity and azimuth. A track was defined as geometrically accepted if it originated from the event vertex and deposited energy in one of the TOF1 counters. The ratio of the number of accepted tracks, N_{acc} to the number of generated tracks, N_{gen}, defines the geometrical acceptance. Namely:

$$\epsilon_{\text{geom}} = N_{\text{acc}}/N_{\text{gen}}$$

Table 6.4 Information contained in GEANT.DAT and HIT.DAT.

TRACK.DAT
Event:
Number of primaries
Number of charged primaries
Number of hodoscope elements hit
Which hodoscope elements hit
Number of spectrometer tracks
Number of secondaries in spectrometer
Number of charged secondaries in the spectrometer
$p\bar{p}$ collision point (x_0,y_0,z_0)
Track:
Track tag number
Particle type
TOF1: x,y,z,t and Energy deposited in counter
TOF2: x,y,z,t and Energy deposited in counter
p_x, p_y and p_z

HIT.DAT
Event tag
Number of hits for this track
Particle type of track
Event z vertex
z vertex of track
$\|\vec{p}\|$ of particle
Spatial components of hits in all active detectors

5000 events were generated for each bin of the $\pi^{\pm}$'s. Because there are 16 transverse momentum and 7 z vertex bins, the total number of events generated comes to 1.12 million. For the $\bar{p}$'s, however, $N_{\rm gen}$ ranged from 6000 to 10000. The number of events generated was set so that $N_{\rm acc}$ did not fall below at least 1100. All in all, we generated $\sim$ 640 000 tracks for the $\bar{p}$'s.

The results of the geometrical acceptance studies for each and every z and $p_\perp$ bin are listed in Tables 6.6, 6.7 and 6.8. The efficiencies are reckoned in percent, i.e. $\varepsilon_{\rm geom} = N_{\rm acc}/N_{\rm gen} \times 100$.

In order to attain a Monte Carlo event z vertex distribution that resembled that of the data, we modulated the z component of the event vertices in accordance with a gaussian σ of 31 cm in the range of $|z| \leq 17.5$ cm (see Fig. 6.6 for the z event vertex distribution for the real data). The weights used for the z vertex modulation are listed in Table 6.5. The weighted average over z for our geometrical acceptance, then, is defined as

$$\langle \varepsilon_{\rm geom}(p_\perp) \rangle = \sum_{i=1}^{7} w_{z_i} \varepsilon_{\rm geom}(z_i, p_\perp)$$

The results of this calculation are shown in Table 6.9. Except for the lowest two $p_\perp$ bins, the geometrical acceptance for the π^+'s and π^-'s are within 2% of one another.

In Fig. 6.7, the unnormalized geometrical efficiency is plotted as a function of transverse momentum for the π^+, π^- and $\bar{p}$. I then fitted these data points with a three parameter function of the form:

$$\varepsilon_{\rm geom}({\rm ID}, p_\perp) = \alpha - \beta e^{-\gamma p_\perp}$$

where α, β and γ vary upon particle type. The parameters of the fit for the geometrical acceptance are listed in Table 6.10. Note that the χ^2 per degree of freedom is less than 0.30 for the pions. The fit for the antiprotons, unfortunately, is not nearly as good, but does manage, nonetheless, to go through the data points fairly well.

Table 6.5 Modulation of Monte Carlo Event z bins.

Range [cm]	*Weight*
$-17.5 < z \leq -12.5$	0.134
$-12.5 < z \leq -7.5$	0.143
$-7.5 < z \leq -2.5$	0.148
$\|z\| \leq 2.5$	0.151
$2.5 < z \leq 7.5$	0.148
$7.5 < z \leq 12.5$	0.143
$12.5 < z \leq 17.5$	0.134

Table 6.6 Geometrical acceptance for π^-'s as a function of $p_\perp$ and z_o. The efficiencies are reckoned in percentages.

$p_\perp$[GeV/c] \ z[cm]	−15	−10	−5	0	5	10	15
0.15 to 0.17	22.4	22.8	24.7	24.8	27.3	28.5	28.7
0.17 to 0.20	25.8	26.7	28.5	29.7	31.5	31.2	31.6
0.20 to 0.25	29.9	31.7	32.7	34.6	34.2	35.2	34.2
0.25 to 0.30	33.6	35.4	36.7	37.4	37.7	38.4	39.5
0.30 to 0.35	36.5	38.2	39.3	41.1	41.0	41.7	40.6
0.35 to 0.40	39.3	40.1	41.0	41.0	42.2	43.7	44.0
0.40 to 0.50	42.0	41.2	43.6	42.8	45.0	44.2	44.9
0.50 to 0.60	43.4	44.2	44.9	46.1	46.9	46.4	47.2
0.60 to 0.70	44.2	45.6	46.7	46.0	46.2	46.9	47.1
0.70 to 0.95	45.7	47.0	46.3	48.2	48.2	47.7	47.9
0.95 to 1.15	46.8	47.2	47.9	48.2	48.9	49.3	48.7
1.15 to 1.35	46.7	48.1	48.2	48.4	48.5	48.8	48.8
1.35 to 1.55	47.1	47.8	47.9	48.5	49.5	48.9	48.6
1.55 to 1.75	47.4	47.6	48.8	49.2	?	49.7	50.0
1.75 to 2.00	48.3	48.5	49.0	49.3	49.8	50.2	49.2
2.00 to 2.50	48.7	49.2	49.7	50.5	50.5	50.7	49.6

Table 6.7 Geometrical acceptance for π^+'s as a function of $p_\perp$ and z_o. The efficiencies are reckoned in percentages.

$p_\perp$[GeV/c] \ z[cm]	−15	−10	−5	0	5	10	15
0.15 to 0.17	29.6	29.4	28.7	28.4	27.4	27.2	26.1
0.17 to 0.20	32.1	32.5	31.2	31.1	30.2	29.7	29.7
0.20 to 0.25	34.0	34.8	33.9	35.0	32.9	31.7	31.8
0.25 to 0.30	38.8	38.9	38.6	37.6	36.6	35.4	36.2
0.30 to 0.35	41.5	40.0	41.4	38.6	39.6	38.6	37.7
0.35 to 0.40	43.0	42.8	41.7	40.5	40.7	39.5	39.1
0.40 to 0.50	45.1	45.9	44.9	44.4	42.4	42.3	41.3
0.50 to 0.60	46.1	47.2	45.8	45.8	44.9	44.8	44.2
0.60 to 0.70	47.7	47.8	47.4	46.5	46.2	45.5	45.4
0.70 to 0.95	48.0	48.6	48.5	46.7	47.3	48.1	45.9
0.95 to 1.15	50.3	48.6	49.2	49.5	48.9	48.1	47.2
1.15 to 1.35	49.1	49.3	48.8	49.1	48.6	48.7	47.1
1.35 to 1.55	49.9	50.6	49.1	49.7	50.0	48.9	47.3
1.55 to 1.75	49.4	49.2	49.7	50.2	50.1	49.4	49.2
1.75 to 2.00	49.7	50.2	50.2	49.7	49.6	49.7	48.5
2.00 to 2.50	49.5	49.8	50.8	51.1	50.1	48.6	49.1

Table 6.8 Geometrical acceptance for antiprotons as a function of $p_\perp$ and z_0. The efficiencies are reckoned in percentages.

$p_\perp$[GeV/c] \ z[cm]	−15	−10	−5	0	5	10	15
0.30 to 0.35	10.8	11.3	11.4	11.4	11.2	12.0	12.1
0.35 to 0.40	15.8	16.4	16.3	16.9	16.9	17.2	17.4
0.40 to 0.50	19.4	19.9	20.4	20.4	20.6	20.3	20.6
0.50 to 0.60	24.1	23.8	24.5	24.5	24.4	24.5	24.9
0.60 to 0.70	27.6	27.8	27.9	27.5	28.6	28.5	28.8
0.70 to 0.95	32.7	32.0	33.4	32.4	34.1	34.5	33.5
0.95 to 1.15	36.6	36.8	36.4	37.2	36.7	38.2	38.1
1.15 to 1.35	38.6	39.9	39.4	40.0	40.6	40.7	40.0
1.35 to 1.55	41.6	41.4	41.4	41.5	41.5	42.5	42.6
1.55 to 1.75	42.6	42.9	43.2	43.6	43.9	42.8	42.9
1.75 to 2.00	44.4	43.4	44.4	45.7	44.9	45.4	44.3
2.00 to 2.50	45.2	45.7	46.4	46.1	47.4	46.5	45.4

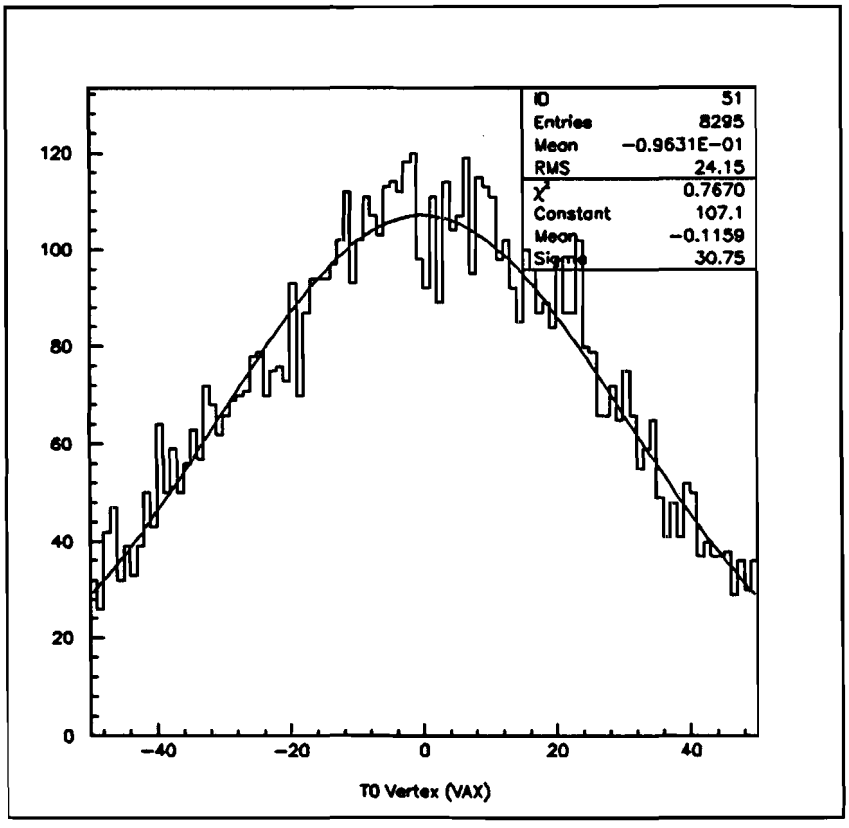

Figure 6.6 Distribution of the z component of the event vertex (*Real Data* after all μDST cuts).

Table 6.9 Weighted average of geom. acceptance in the range $|z| \leq 17.5$ cm for $\pi^{\pm}$ and $\bar{p}$.

$p_{\perp}$ bin	$\langle \varepsilon_{\pi^+} \rangle$	$\langle \varepsilon_{\pi^-} \rangle$	$\langle \varepsilon_{\pi^-} \rangle / \langle \varepsilon_{\pi^+} \rangle$	$\langle \varepsilon_{\bar{p}} \rangle$
0.15 to 0.17	28.1	25.6	0.911	–
0.17 to 0.20	30.9	29.3	0.948	–
0.20 to 0.25	33.4	33.3	0.997	–
0.25 to 0.30	37.4	37.0	0.989	–
0.30 to 0.35	39.6	39.8	1.005	11.5
0.35 to 0.40	41.0	41.6	1.015	16.7
0.40 to 0.50	43.8	43.4	0.991	20.2
0.50 to 0.60	45.5	45.6	1.002	24.4
0.60 to 0.70	46.6	46.1	0.989	28.1
0.70 to 0.95	47.6	47.3	0.994	33.3
0.95 to 1.15	48.8	48.2	0.988	37.1
1.15 to 1.35	48.7	48.2	0.990	39.9
1.35 to 1.55	49.3	48.3	0.980	41.8
1.55 to 1.75	49.6	48.9	0.986	43.2
1.75 to 2.00	49.7	49.2	0.990	44.7
2.00 to 2.50	49.9	49.9	1.000	46.1

Table 6.10 Geometrical acceptance fit parameters.

	α	β	γ	χ^2_{dof}
π^-	.4841	0.5296	5.296	0.277
π^+	.4915	0.4218	4.346	0.229
$\bar{p}$	.4464	0.6751	2.171	3.530

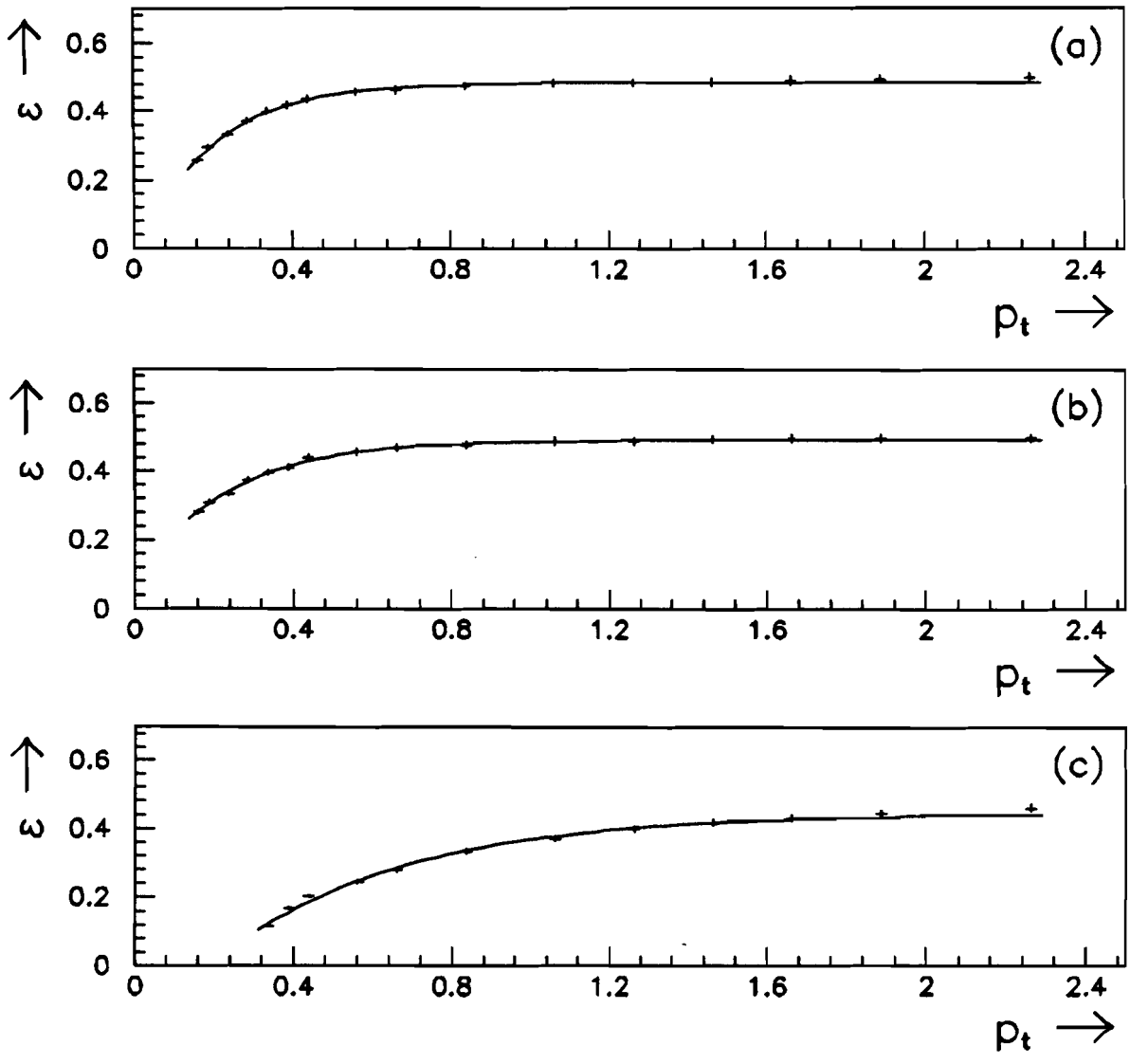

Figure 6.7 Unnormalized geometrical efficiencies for (a) π^-, (b) π^+ and (c) $\bar{p}$.

6.3.5 [(noise + signal) − noise] Studies

We chose the

$$[\overbrace{(N-1)}^{\mathcal{N}}+\overbrace{1}^{\mathcal{S}}]-\overbrace{(N-1)}^{\mathcal{N}}$$

approach to the E-735 spectrometer track reconstruction studies. Here $\mathcal{N}$ and $\mathcal{S}$ depict the noise and signal, respectively. Here 'noise' denotes the background multiplicity and not noise in the sense of random hits or tracks. We first fed the z vertex and multiplicity binned PYTHIA events through Q735MOD. The output files GEANT.DAT and HIT.DAT formed what we termed our N files. Our objective was to overlay a signal track, binned in $p_\perp$ and z vertex, upon the simulated multiplicity background of the event without introducing undue bias. So we took care not to overestimate the number of tracks entering the spectrometer. We selected events from the N files sample which contained primary tracks that had deposited energy in one of the TOF1 counters. These events were our $N-1$ file candidates. For each N file event, we culled the first spectrometer track that satisfied the above two conditions of striking TOF1 and emanating from the $\bar{p}p$ collision point. Picking the first track does not bias our sample — the tracks in PYTHIA input data file are sequenced in random order. More convincingly, perhaps, is that the ratio of the particle types of these candidate tracks fall within the expected values; we are not just grabbing π^-'s, say. To make the $N-1$ files, we must operate on the two N files: HIT.DAT and GEANT.DAT. We discarded the information associated with the candidate track from the two N files, i.e. we pulled the detector hits, TOF timing and all other parameters related to this track from these N files and decremented the number of charged primaries and spectrometer tracks in the event portion of GEANT.DAT. Before we were to overlay the signal track upon the $N-1$ PYTHIA event and form the $(N-1)+1$ event, we had to combine all the various events binned in z for each and every event which was binned in terms of $p_\perp$ and multiplicity. Each $p_\perp$ and multiplicity bin file contains 1992 events and the event z vertex modulation is described in Table 6.11. We used

Table 6.11 Modulation of Monte Carlo event z bins.

Range [cm]	*Contents*
$-17.5 < z \leq -12.5$	267
$-12.5 < z \leq -7.5$	284
$-7.5 < z \leq -2.5$	295
$\|z\| \leq 2.5$	300
$2.5 < z \leq 7.5$	295
$7.5 < z \leq 12.5$	284
$12.5 < z \leq 17.5$	267

the same subset of $N-1$ PYTHIA events for each and every signal, aka. *known track* or 1, file.

We were now prepared to address the issue of how the spectrometer acceptance varies as a function of event multiplicity and particle momentum. From the Monte Carlo, we extracted the following information from each and every $[(N-1)+1]-(N-1)$ file binned in $p_\perp$ and multiplicity:

- The overall track reconstruction efficiency, ε.
- The root mean square spread in the reconstructed transverse momentum of the signal, $\sigma_{p_\perp}$.

6.3.6 Track Reconstruction Efficiency

The ratio of the number of events that passed our standard track selection cuts and in which we retrieved the correct transverse momentum of the signal track to the number of events generated for each bin gave us the track reconstruction acceptance. We binned our Monte Carlo track reconstruction data sample in terms of full phase

space charged multiplicity, particle type and transverse momentum. This Monte Carlo DST sample contained a total of 251 000 events.

The $N-1$ 'noise' events for the three different multiplicity backgrounds are shown in Fig.'s 6.8a through 6.8c. Because processing the PYTHIA Events was terribly CPU intensive, we used the same background for each of the signal tracks. We shuffled the hits from the signal track into the hit pool of the noise event. These combined hits were then fed our track reconstruction package.

Examples of the *noise + signal*, or $[(N-1)+1]$, data are shown in Fig. 6.9a through Fig. 6.9d. The background, in this case, is from the PYTHIA $(N-1)$ file with multiplicities in the range of $190 < N_c \leq 200$. These $[(N-1)+1]$ files, incidentally, were processed independently of the $(N-1)$ files. We next had to make a background subtraction. We extracted the signal by subtracting the $(N-1)$ background from the $[(N-1)+1]$ file. Subtracting the $p_\perp$ distribution in Fig. 6.8c from the $p_\perp$ distribution of Fig.'s 6.10 result in the distributions depicted in Fig.'s 6.10. The crosshatched regions in Fig.'s 6.10 are the signal candidates. In the case of Fig. 6.10a, we find nnnn events in the crosshatched region. Because 1992 tracks were generated, we discover the track reconstruction efficiency to be nnnn/1992 (x%). We performed this operation on 3 multiplicity and 14 $p_\perp$ bins for each of the π^-, π^+ and $\bar{\text{p}}$. Note that the resolution of the reconstructed signal does not significantly deteriorate as the multiplicity increases (see Fig. 6.11). The results are tabulated in Tables 6.12, 6.13 and 6.14 and plotted in Fig's 6.12, 6.13 and 6.14.

As in the case of the geometrical acceptance, the track reconstruction efficiencies can be fit with a function of the form:

$$\varepsilon_{\text{tre}}(\text{ID}, p_\perp, N_c) = \alpha' - \beta' e^{-\gamma' p_\perp}$$

where $\alpha' = \alpha'(ID, N_c)$, $\beta' = \beta'(ID)$ and $\gamma' = \gamma'(ID, N_c)$. The values of these parameters are entered in Table 6.15. Note the phenomenal reduced χ^2 for the fit. By fixing β' to be a function of only the particle ID, forces α' and γ' to be linear in N_c, the total phase space charged multiplicity (See Figures 6.15 through 6.17 and

Table 6.16). We have:

$$\alpha' = a_{\alpha'} + b_{\alpha'} N_c$$

$$\beta' = a_{\beta'} + b_{\beta'} N_c$$

Three dimensional representations of the track reconstruction efficiency as a function of multiplicity and transverse momentum for the pions and antiprotons are plotted in Fig.'s 6.21, 6.22 and 6.23.

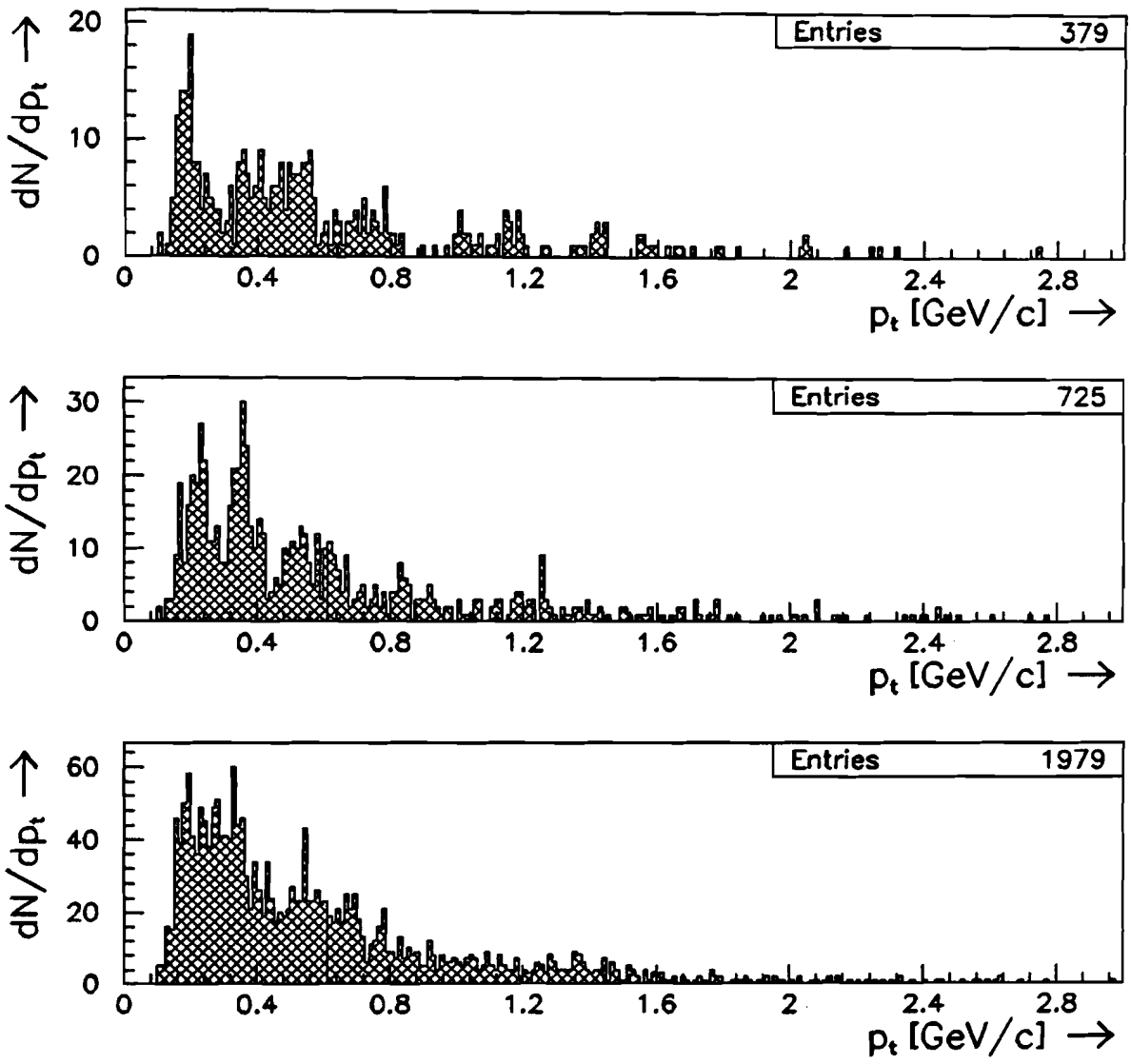

Figure 6.8 $N-1$ multiplicity background. (Top) $40 < N_c \leq 50$, (Middle) $90 < N_c \leq 100$ and (Bottom) $190 < N_c \leq 200$.

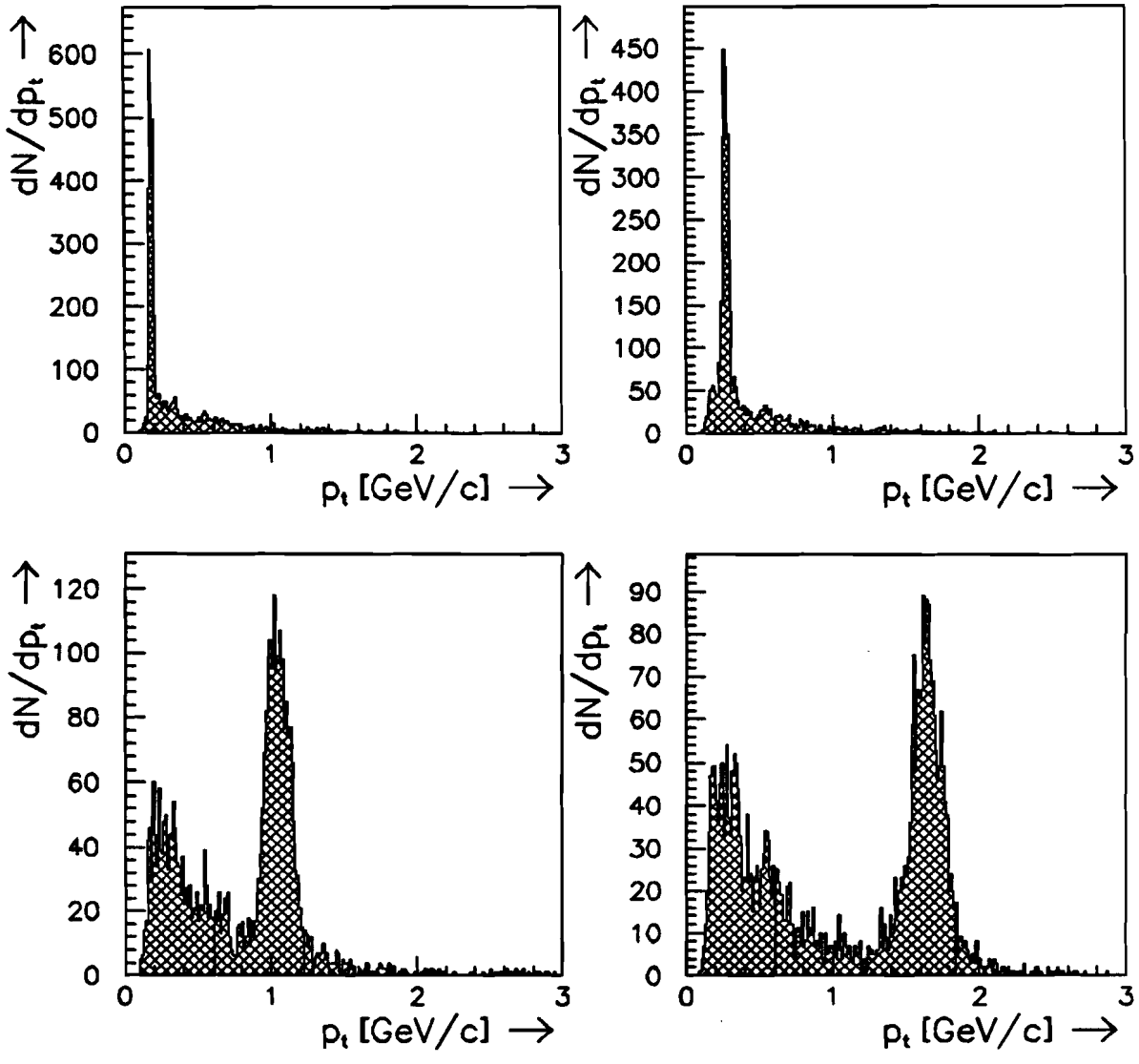

Figure 6.9 $[(N-1)+1]$ for a π^+ signal overlayed upon a $190 < N_c \leq 200$ full phase space charged multiplicity background. (a) $0.17 < p_\perp \leq 0.20$ (b) $0.25 < p_\perp \leq 0.30$ (c) $0.95 < p_\perp \leq 1.15$ (d) $1.55 < p_\perp \leq 1.75$.

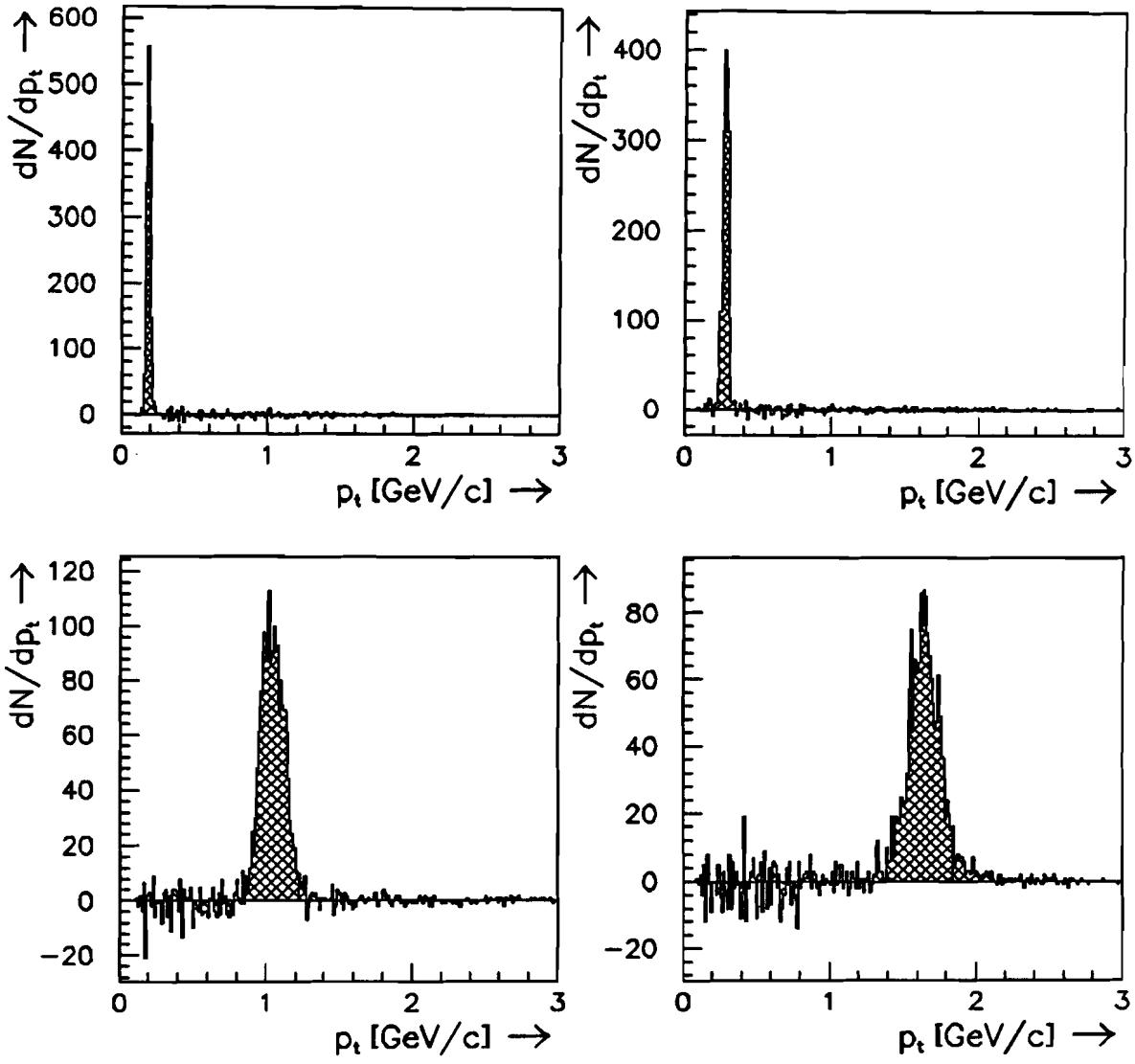

Figure 6.10 $[(N-1)+1]+(N-1)$ events for a π^+ signal. (a) $0.17 < p_\perp \leq 0.20$ (b) $0.25 < p_\perp \leq 0.30$ (c) $0.95 < p_\perp \leq 1.15$ (d) $1.55 < p_\perp \leq 1.75$. $p_\perp$ is measured in units of GeV/c The $190 < N_c \leq 200$ full phase space charged multiplicity background was subtracted. Refer to previous Figure.

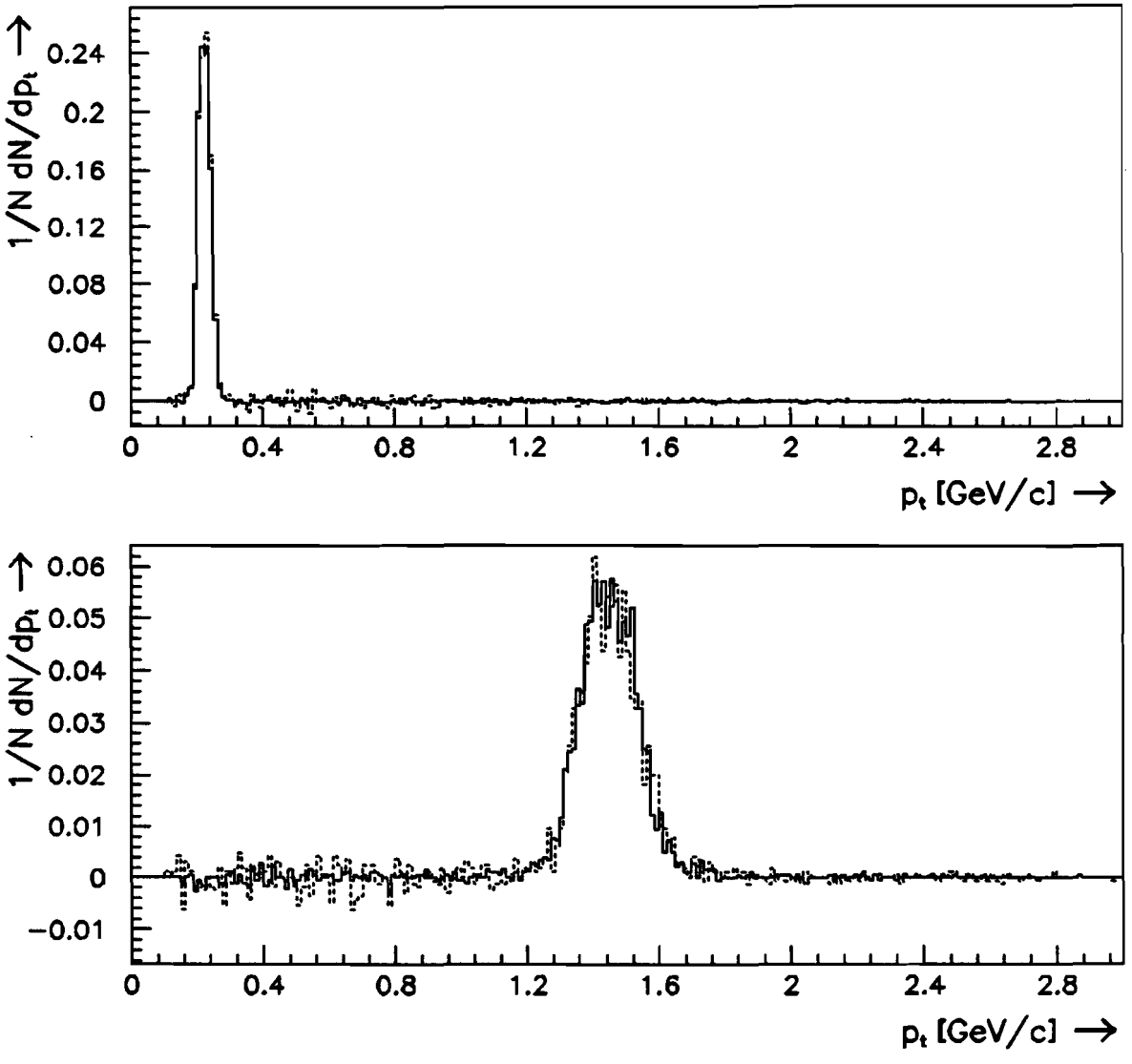

Figure 6.11 Retrieved π^- signals for $N_c = 45$ (solid) overlayed upon $N_c = 195$ (dashed). Note that the FWHM of the signal appears independent of the multiplicity background. (Upper) $0.25 < p_\perp \leq 0.30$ GeV/c (Lower) $1.35 < p_\perp \leq 1.55$ GeV/c.

Table 6.12 Track reconstruction efficiency for π^-. These efficiencies are tabulated as a function of multiplicity and $p_\perp$ bins and are reckoned in terms of absolute percentage accepted.

$p_\perp$ [GeV/c]	$40 < N_c \leq 50$	$90 < N_c \leq 100$	$190 < N_c \leq 200$
0.15 to 0.17	67.2	66.4	62.3
0.17 to 0.20	83.3	81.3	77.7
0.20 to 0.25	87.9	87.6	83.4
0.25 to 0.30	89.5	87.0	84.4
0.30 to 0.35	89.9	88.4	83.3
0.35 to 0.40	89.1	89.8	83.0
0.40 to 0.50	89.8	87.8	82.0
0.50 to 0.60	89.4	88.1	82.6
0.60 to 0.70	89.6	86.5	79.3
0.70 to 0.95	89.1	86.8	83.0
0.95 to 1.15	88.5	86.6	83.2
1.15 to 1.35	87.6	85.3	81.3
1.35 to 1.55	87.5	86.9	79.3
1.55 to 1.75	89.0	86.7	81.2

Table 6.13 Track reconstruction efficiency for π^+. These efficiencies are tabulated as a function of multiplicity and $p_\perp$ bins and are reckoned in terms of absolute percentage accepted.

$p_\perp$ [GeV/c]	$40 < N_c \leq 50$	$90 < N_c \leq 100$	$190 < N_c \leq 200$
0.15 to 0.17	81.3	81.0	75.6
0.17 to 0.20	86.7	85.6	80.1
0.20 to 0.25	89.9	87.5	84.1
0.25 to 0.30	89.3	87.6	84.3
0.30 to 0.35	90.5	88.0	82.9
0.35 to 0.40	89.9	87.2	82.4
0.40 to 0.50	91.1	89.8	79.6
0.50 to 0.60	89.2	88.5	81.9
0.60 to 0.70	90.1	88.6	82.7
0.70 to 0.95	90.2	88.2	81.8
0.95 to 1.15	90.7	88.4	82.7
1.15 to 1.35	89.9	87.9	80.1
1.35 to 1.55	89.4	87.7	81.8
1.55 to 1.75	89.8	87.6	81.5

Table 6.14 Track reconstruction efficiency for $\bar{p}$. These efficiencies are tabulated as a function of multiplicity and $p_\perp$ bins and are reckoned in terms of absolute percentage accepted.

$p_\perp$ [GeV/c]	$40 < N_c \leq 50$	$90 < N_c \leq 100$	$190 < N_c \leq 200$
0.30 to 0.35	79.8	80.1	74.2
0.35 to 0.40	85.2	82.1	76.6
0.40 to 0.50	87.6	85.4	80.6
0.50 to 0.60	89.2	88.0	81.1
0.60 to 0.70	88.5	86.1	81.8
0.70 to 0.95	89.8	87.4	80.4
0.95 to 1.15	88.7	87.1	81.2
1.15 to 1.35	89.7	87.6	80.3
1.35 to 1.55	88.1	87.8	80.6
1.55 to 1.75	89.1	87.1	81.8

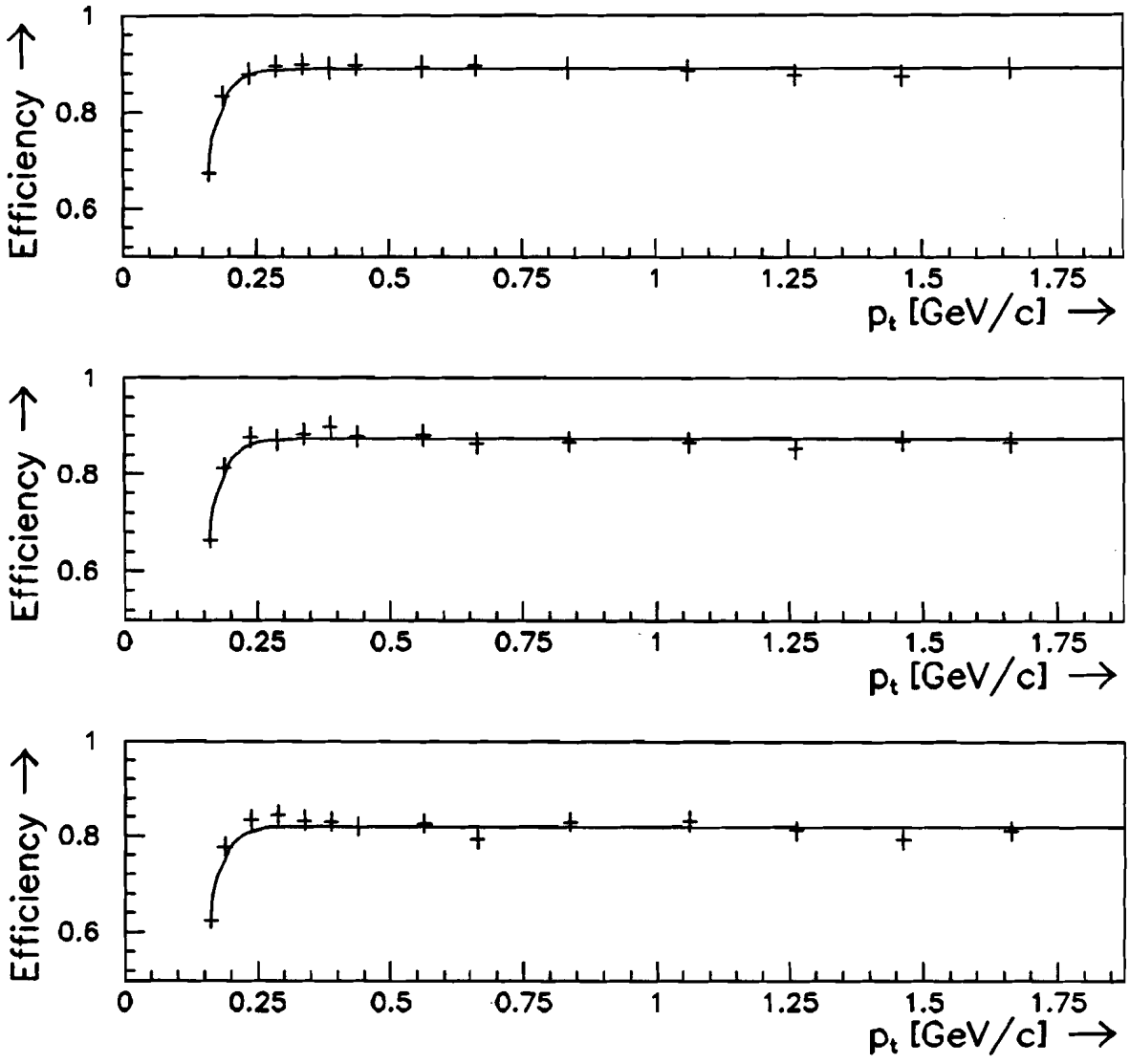

Figure 6.12 Track reconstruction efficiency for π^- (a) $40 < N_c \leq 50$, (b) $90 < N_c \leq 100$ and (c) $190 < N_c \leq 200$.

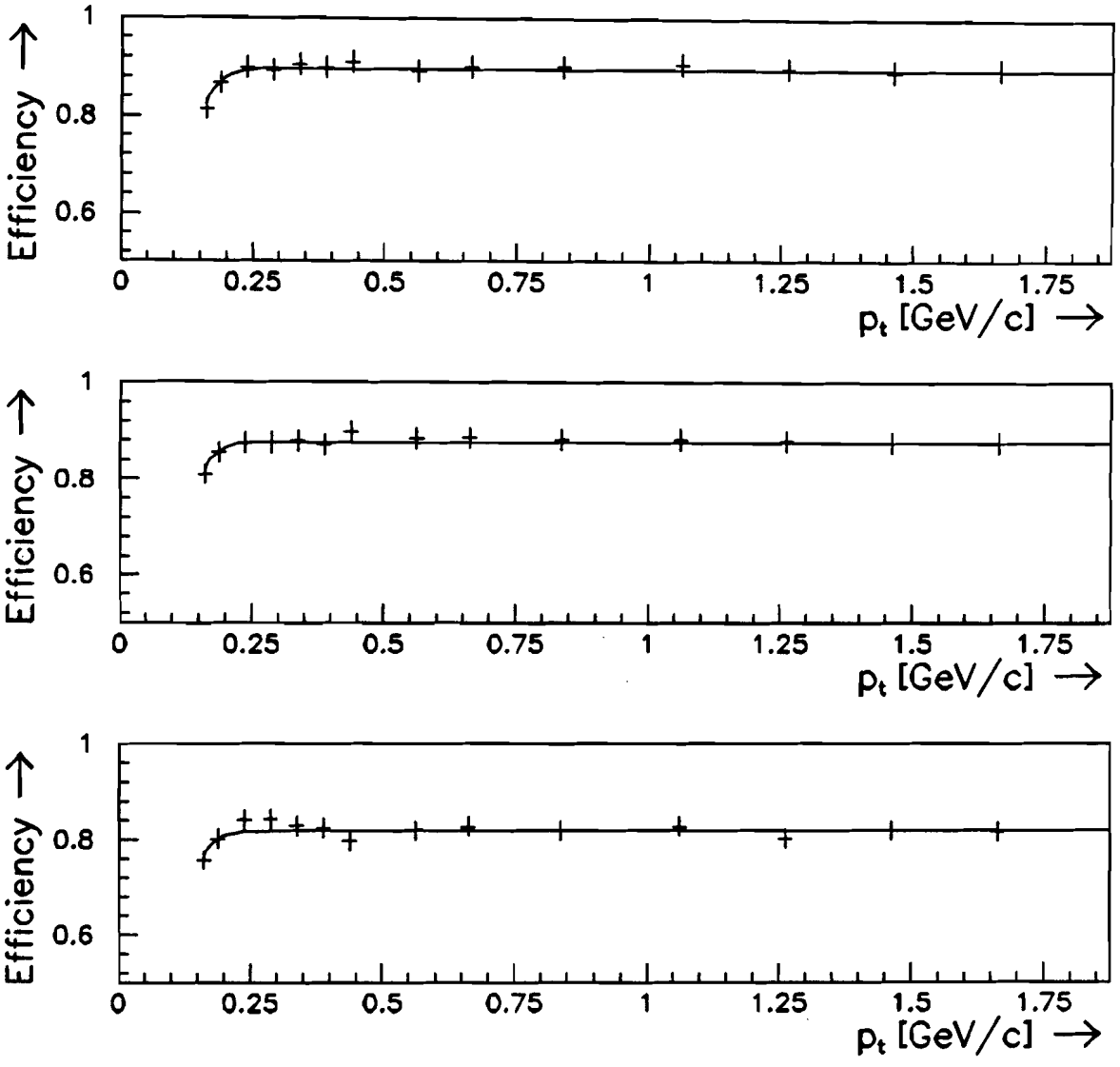

Figure 6.13 Track reconstruction efficiency for π^+ (a) $40 < N_c \leq 50$, (b) $90 < N_c \leq 100$ and (c) $190 < N_c \leq 200$.

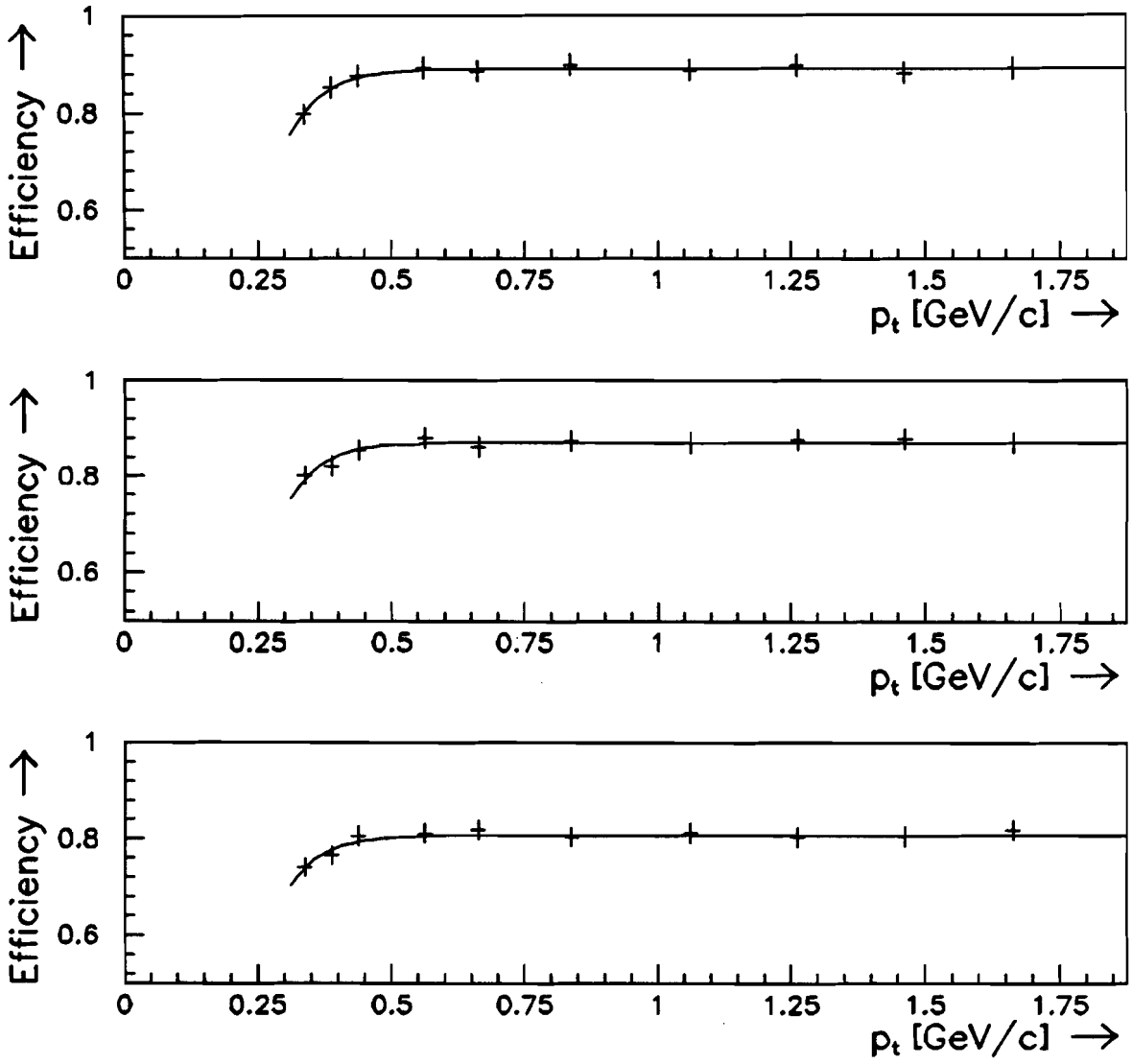

Figure 6.14 Track reconstruction efficiency for $\bar{p}$ (a) $40 < N_c \leq 50$, (b) $90 < N_c \leq 100$ and (c) $190 < N_c \leq 200$.

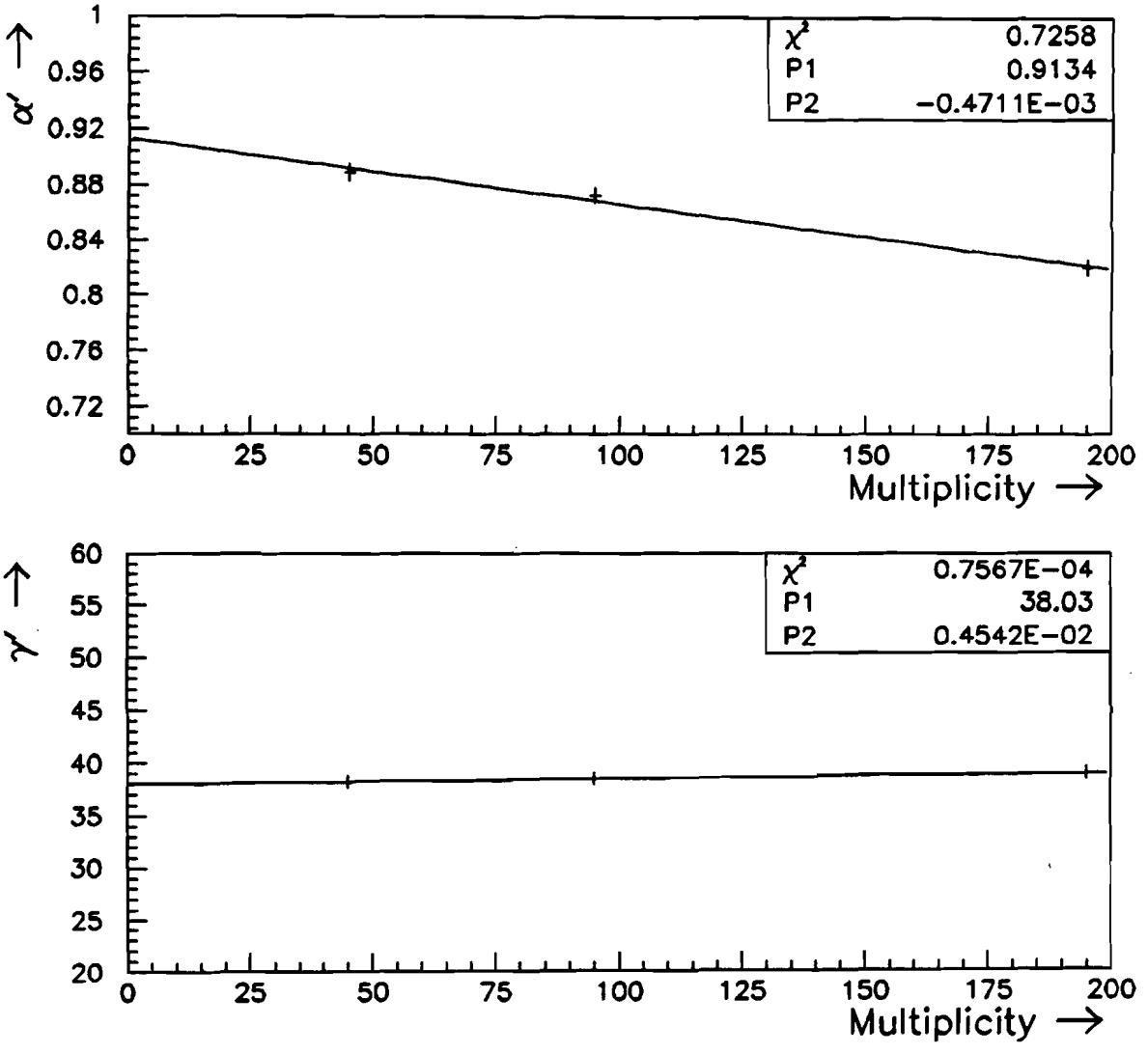

Figure 6.15 Linear decomposition of the α' and γ' fit parameters for the π^- track reconstrunction efficiency. Errors are from the MINUIT fit.

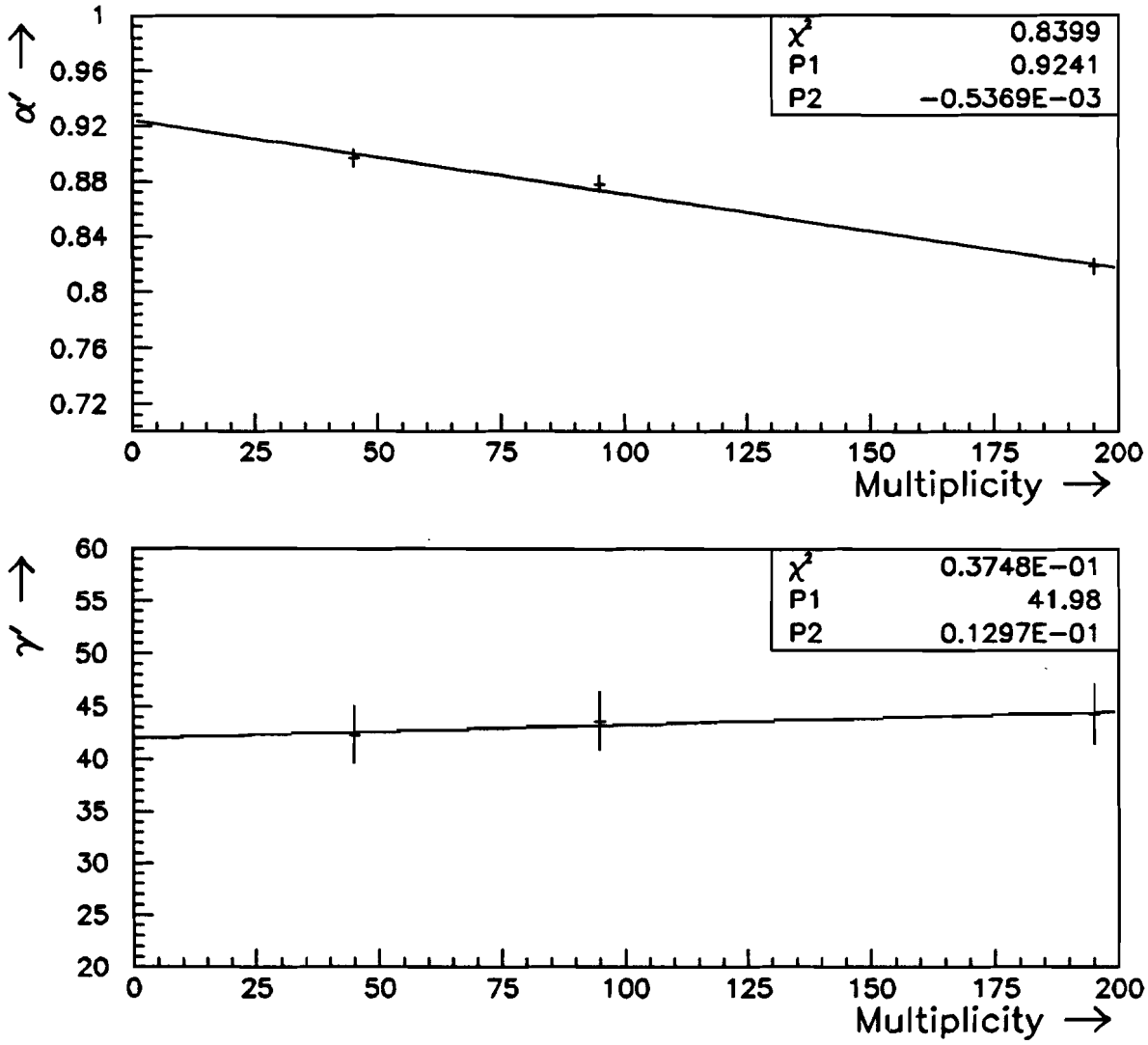

Figure 6.16 Linear decomposition of the α' and γ' fit parameters for the π^+ track reconstrunction efficiency. Errors are from the MINUIT fit.

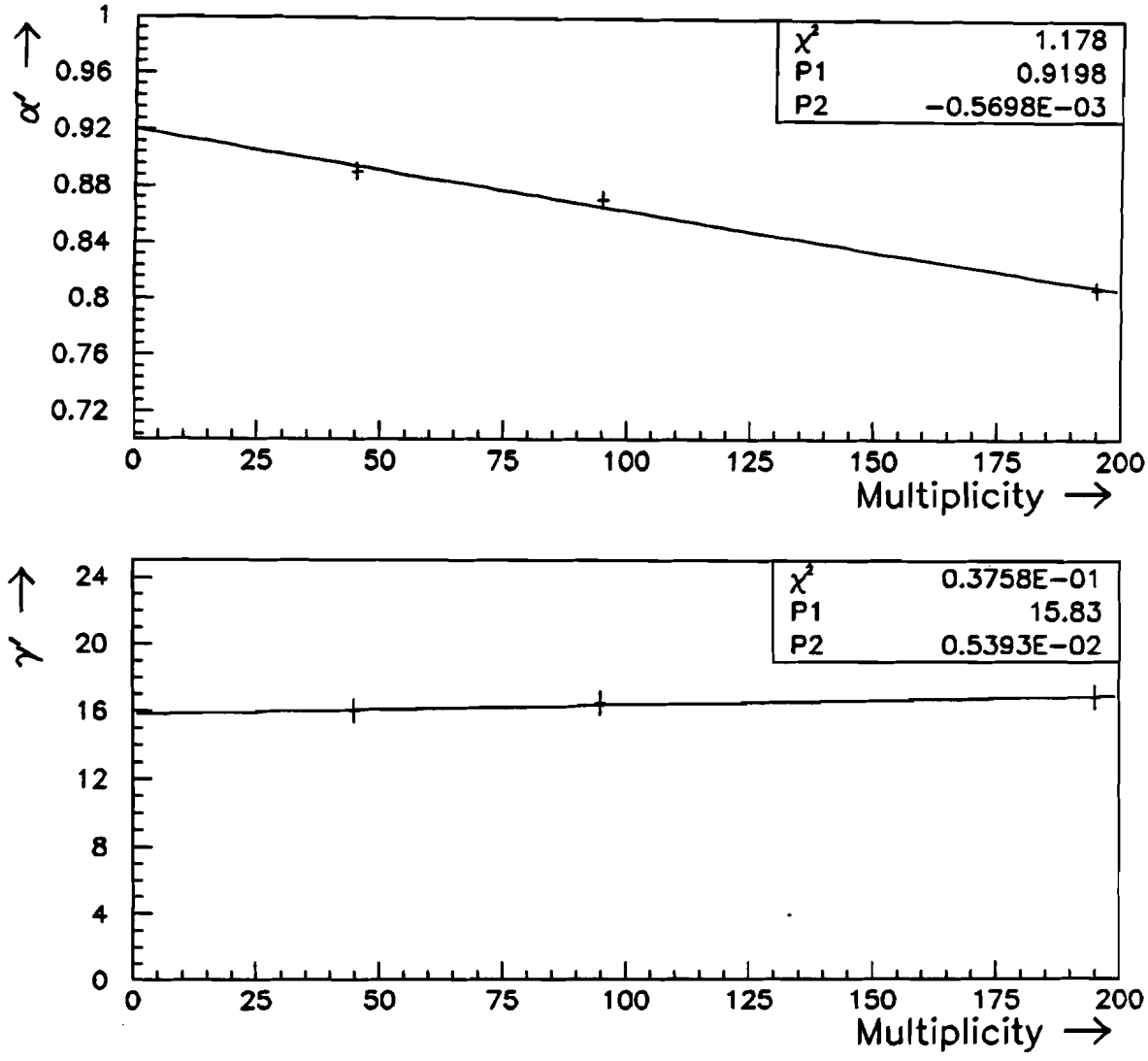

Figure 6.17 Linear decomposition of the α' and γ' fit parameters for the $\bar{p}$ track reconstrunction efficiency. Errors are from the MINUIT fit.

Table 6.15 Track reconstruction efficiency fit parameters.

π^-

Multiplicity	α'	β'	γ'	$\chi^2_{\rm dof}$
$40 < N_c \leq 50$	0.8893	105.0	38.24	0.35
$90 < N_c \leq 100$	0.8728	105.0	38.46	0.44
$190 < N_c \leq 200$	0.8203	105.0	38.92	1.11

π^+

Multiplicity	α'	β'	γ'	$\chi^2_{\rm dof}$
$40 < N_c \leq 50$	0.8968	81.00	42.29	0.35
$90 < N_c \leq 100$	0.8776	81.00	43.66	0.38
$190 < N_c \leq 200$	0.8181	81.00	44.36	0.73

$\bar{\rm p}$

Multiplicity	α'	β'	γ'	$\chi^2_{\rm dof}$
$40 < N_c \leq 50$	0.8905	20.05	16.00	0.07
$90 < N_c \leq 100$	0.8710	20.05	16.45	0.18
$190 < N_c \leq 200$	0.8072	20.05	16.84	0.36

Table 6.16 Track reconstruction efficiency fit parameters.

ID	$a_{\alpha'}$	$b_{\alpha'}$	$\chi^2_{\rm dof}$	$a_{\gamma'}$	$b_{\gamma'}$	$\chi^2_{\rm dof}$
π^-	0.9134	-4.711×10^{-4}	0.7258	38.03	4.542×10^{-3}	7.567×10^{-4}
π^+	0.9241	-5.369×10^{-4}	0.8399	41.98	1.297×10^{-2}	0.0375
$\bar{\rm p}$	0.9198	-5.698×10^{-4}	1.178	15.83	5.393×10^{-3}	.0376

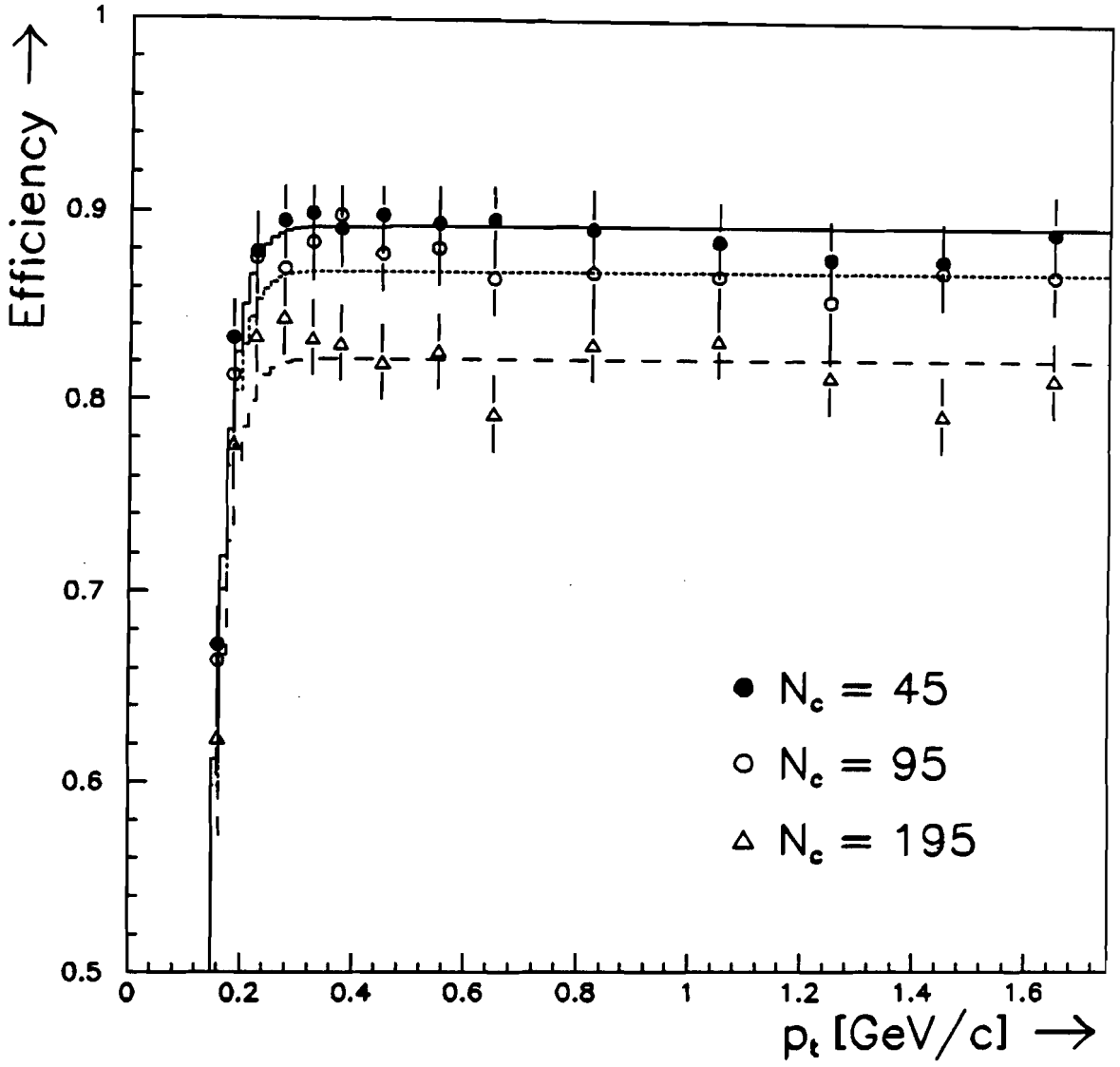

Figure 6.18 The π^- track reconstruction formula for the three different multiplicities superimposed on the Monte Carlo data points. (Solid line: $N_c = 45$, short dashed line: $N_c = 95$ and long dashed line: $N_c = 195$).

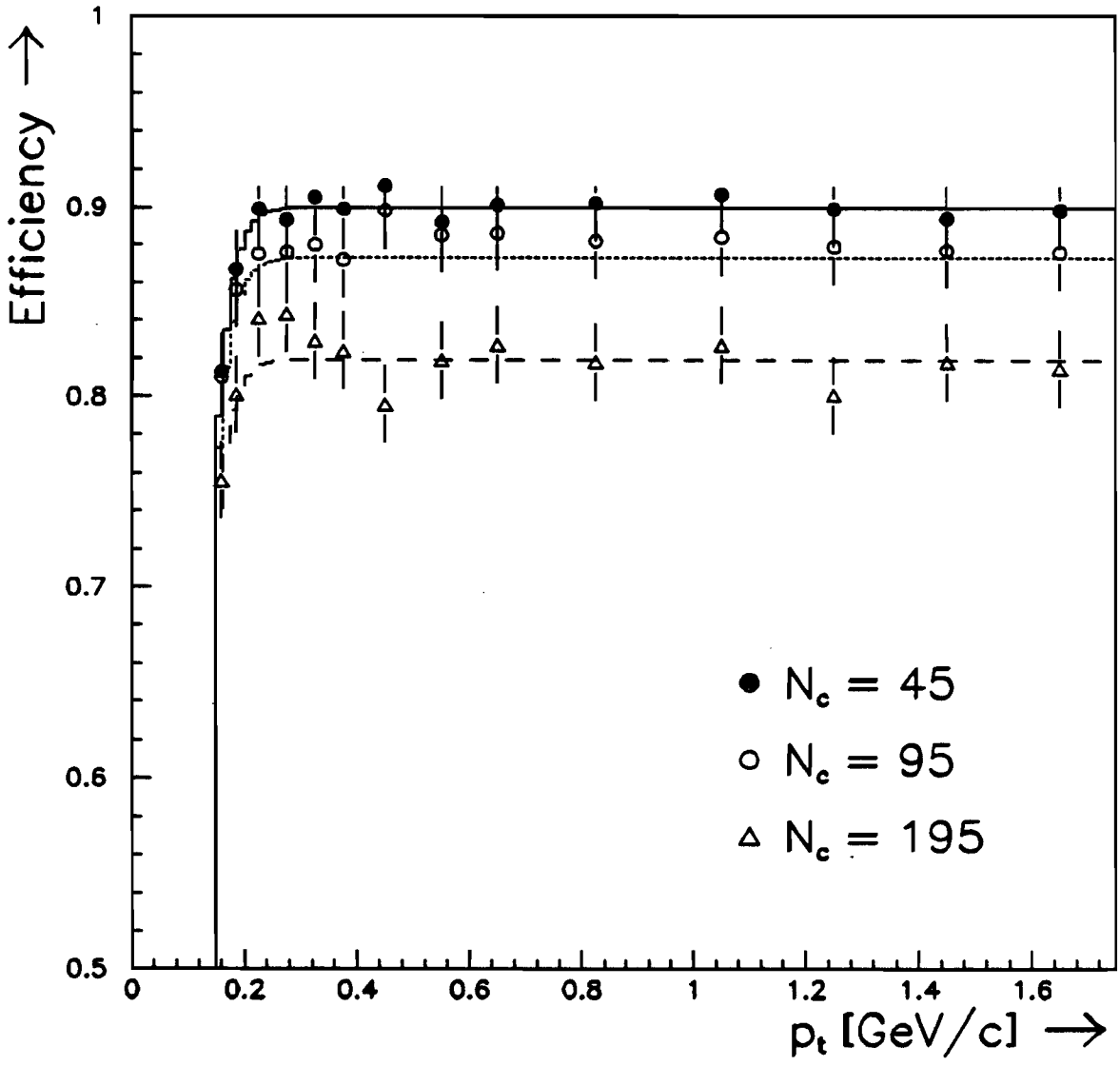

Figure 6.19 The π^+ track reconstruction formula for the three different multiplicities superimposed on the Monte Carlo data points. (Solid line: $N_c = 45$, short dashed line: $N_c = 95$ and long dashed line: $N_c = 195$).

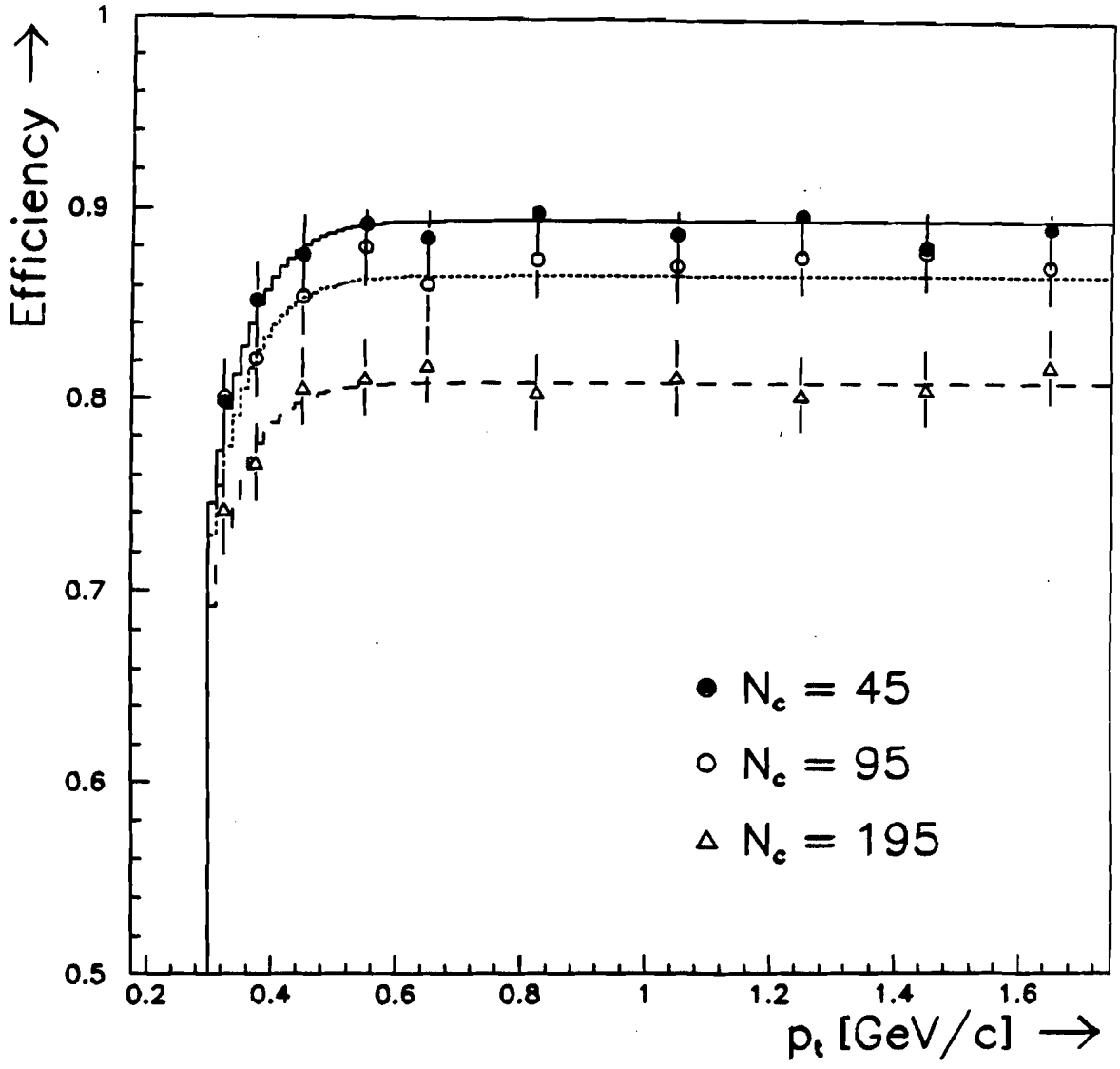

Figure 6.20 The $\bar{p}$ track reconstruction formula for the three different multiplicities superimposed on the Monte Carlo data points. (Solid line: $N_c = 45$, short dashed line: $N_c = 95$ and long dashed line: $N_c = 195$).

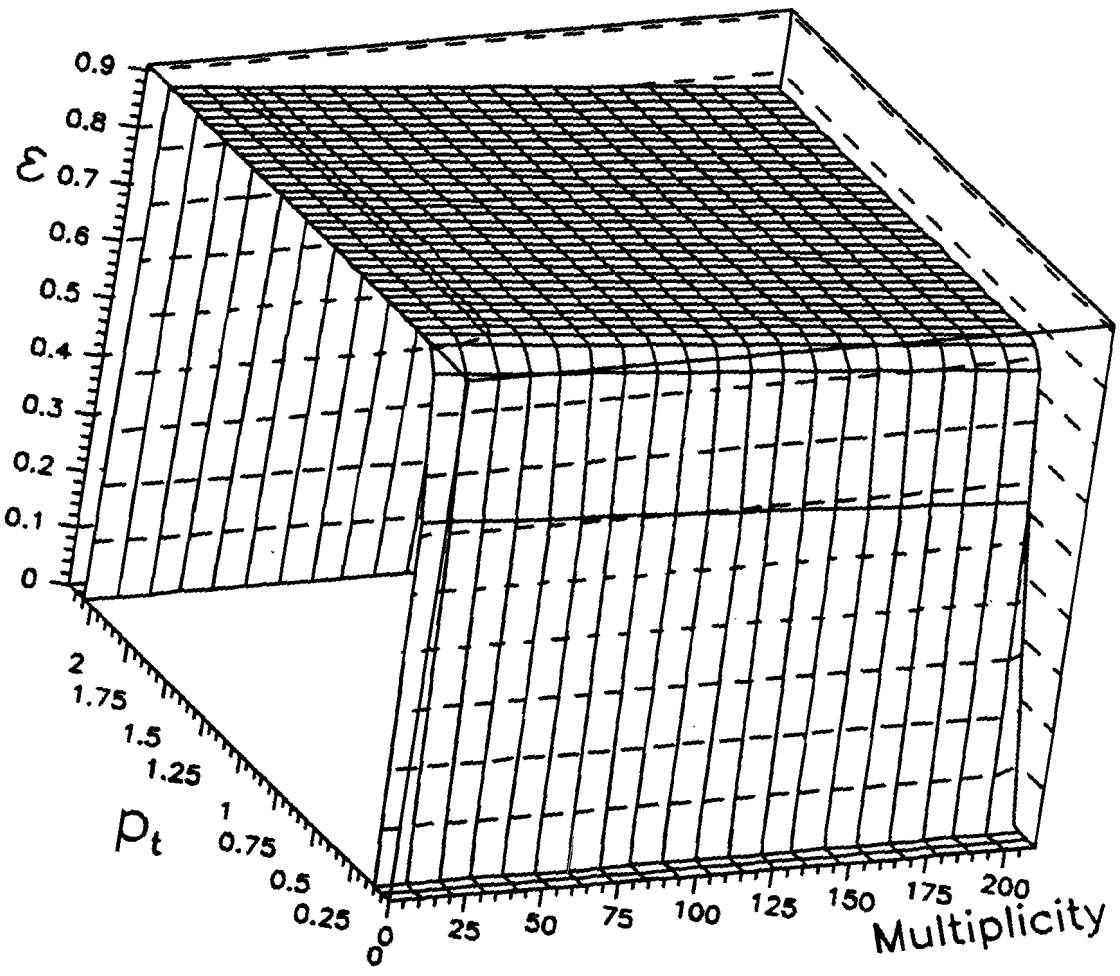

Figure 6.21 Three dimensional representation of the track reconstruction efficiency as a function of full phase space charged multiplicity and transverse momentum for π^-.

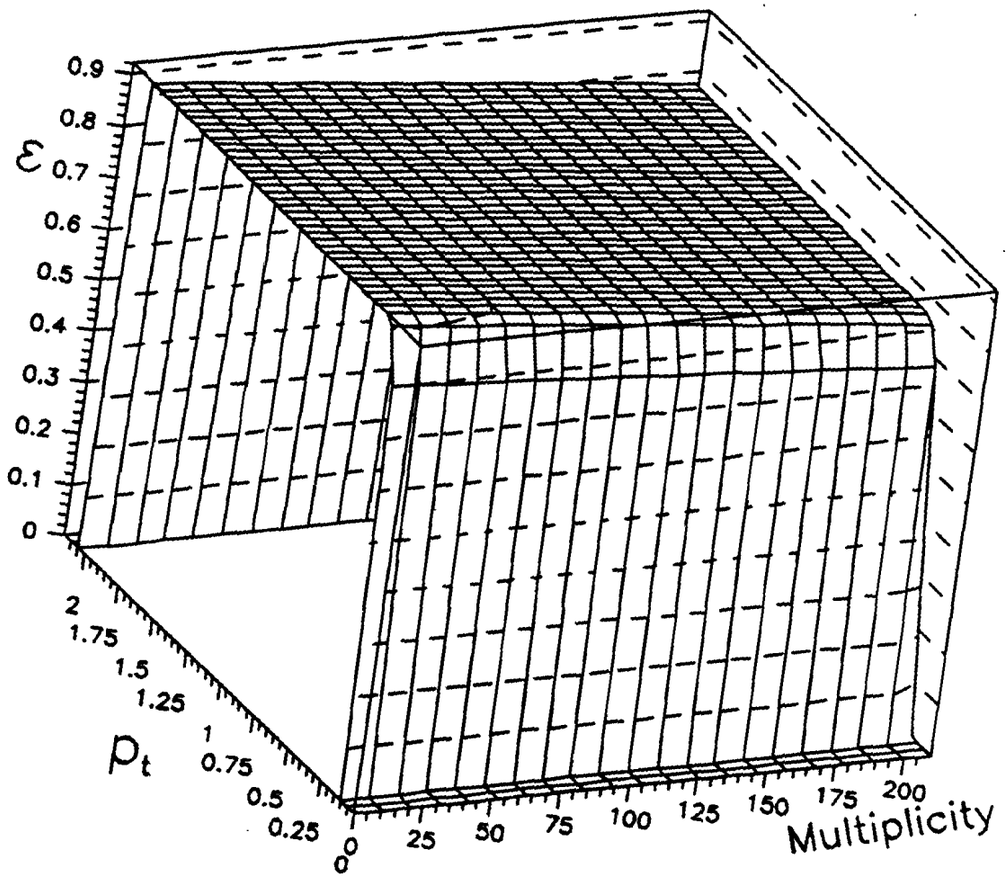

Figure 6.22 Three dimensional representation of the track reconstruction efficiency as a function of full phase space charged multiplicity and transverse momentum for π^+.

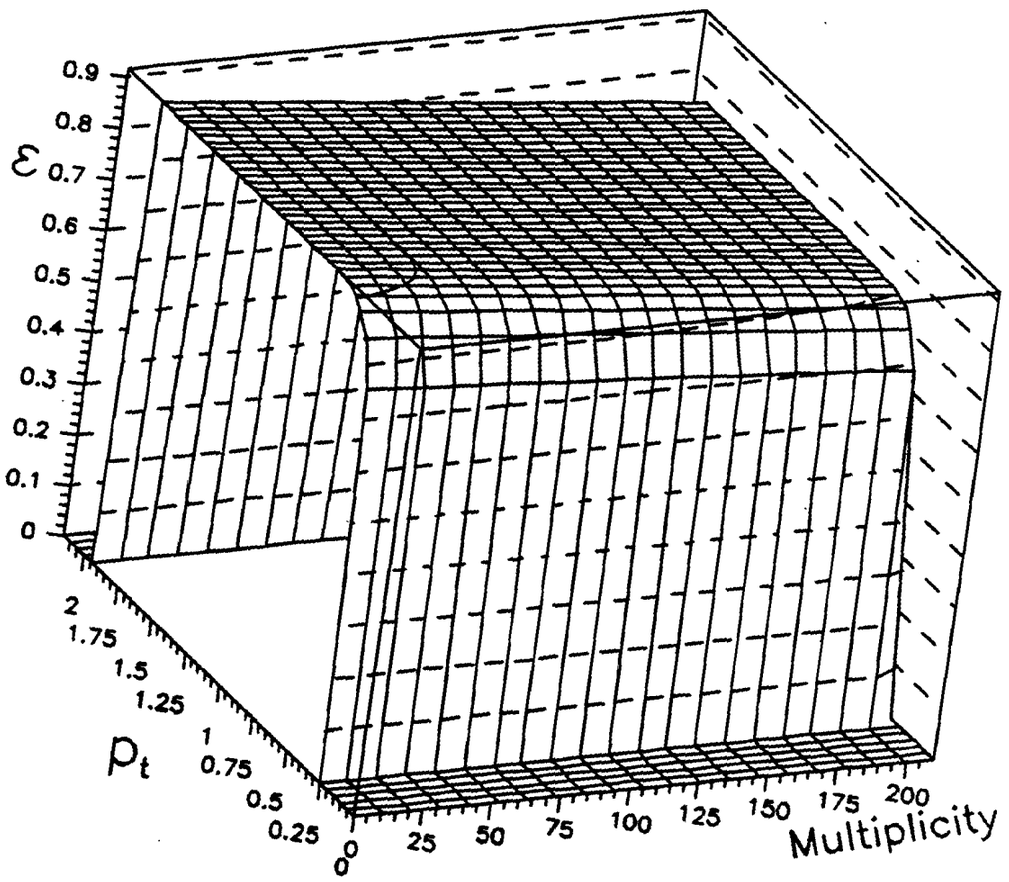

Figure 6.23 Three dimensional representation of the track reconstruction efficiency as a function of full phase space charged multiplicity and transverse momentum for $\bar{p}$.

6.3.7 Momentum Resolution

The momentum resolution of our tracking algorithms was modeled in our $[(N-1)+1]-(N-1)$ studies. As in the case of our investigations into the track reconstruction acceptance, we superimposed a ***known track*** upon the PYTHIA multiplicity background and studied the degradation of the signal as a function of the multiplicity and transverse momentum. The momentum resolution was determined by fitting a gaussian to the difference distribution of the reconstructed $p_\perp$ and the known transverse momentum given by the track parameters of the Monte Carlo. Almost all the reduced χ^2's (dof = 32) of the gaussian fit were well within 2. The results for the three particle types, i.e. $\pi^\pm$ and $\bar{\mathrm{p}}$ are plotted in Fig.'s 6.24, 6.25 and 6.26. The relationship between $\sigma_{p_\perp}$ and $p_\perp$ was best parameterized with the function of the form:

$$\sigma_{p_\perp}(p_\perp, N_c) = \frac{A}{p_\perp} + Bp_\perp + C$$

We find that the transverse momentum resolution is identical for both species of the charged pions and ranges from 2.5 to 5.0%. For the antiprotons, $\sigma_{p_\perp}$ varies between 4 and 8% depending on multiplicity and $p_\perp$.

Note that these results compare favorably with our published momentum formula of [7]

$$\Delta p/p = \sqrt{ap^2 + b\beta^{-2}}$$

where $a = b = .0016$.

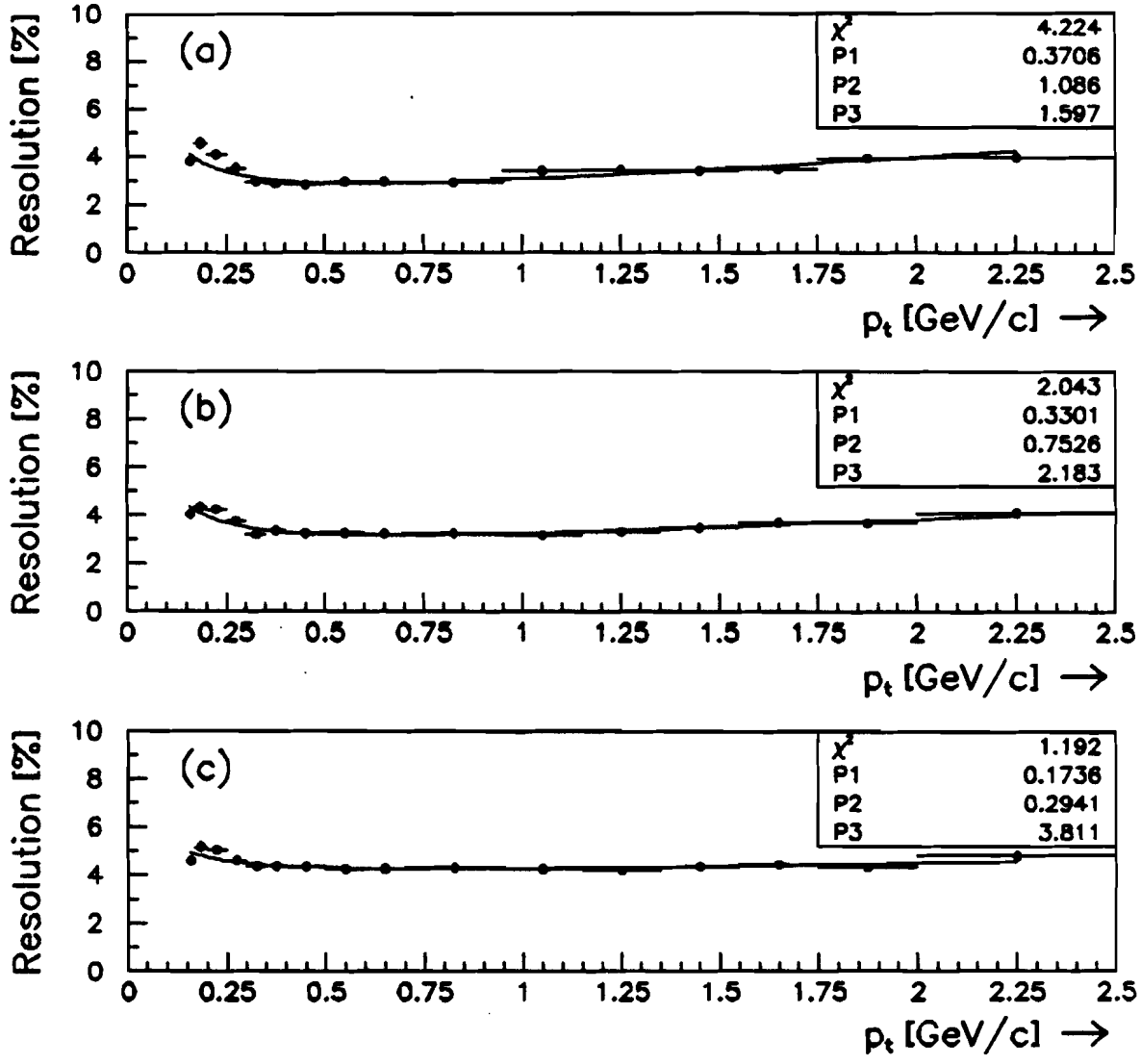

Figure 6.24 Transverse momentum resolution as a function of $p_\perp$ for the π^-'s. Data points are fit with the formula $\sigma_{p_\perp}(p_\perp, N_c) = P1\frac{1}{p_\perp} + P2 \cdot p_\perp + P3$. (a) $40 < N_c \leq 50$, (b) $90 < N_c \leq 100$ and (c) $190 < N_c \leq 200$.

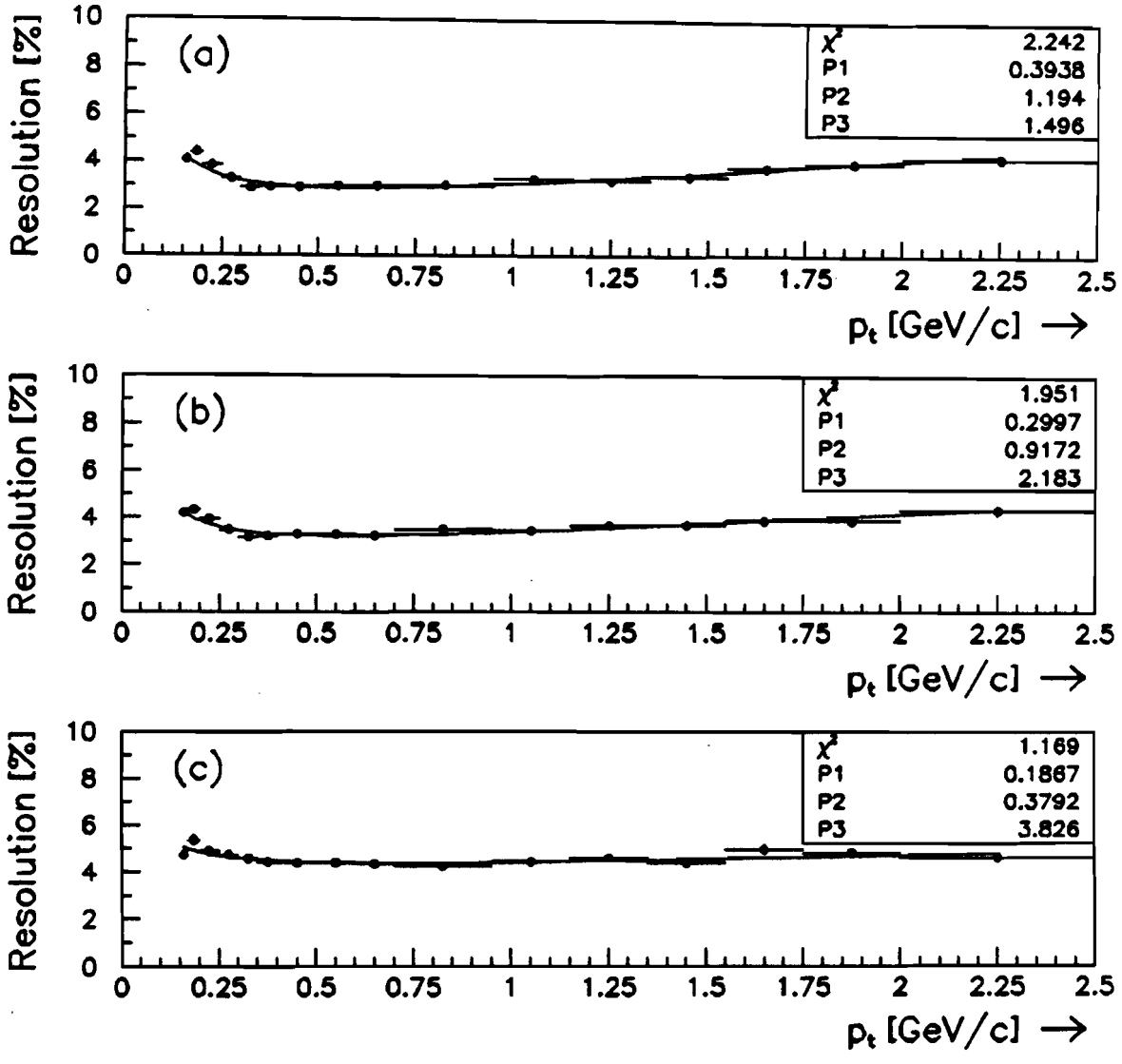

Figure 6.25 Transverse momentum resolution as a function of $p_\perp$ for the π^+'s. Data points are fit with the formula $\sigma_{p_\perp}(p_\perp, N_c) = P1\frac{1}{p_\perp} + P2 \cdot p_\perp + P3$. (a) $40 < N_c \leq 50$, (b) $90 < N_c \leq 100$ and (c) $190 < N_c \leq 200$.

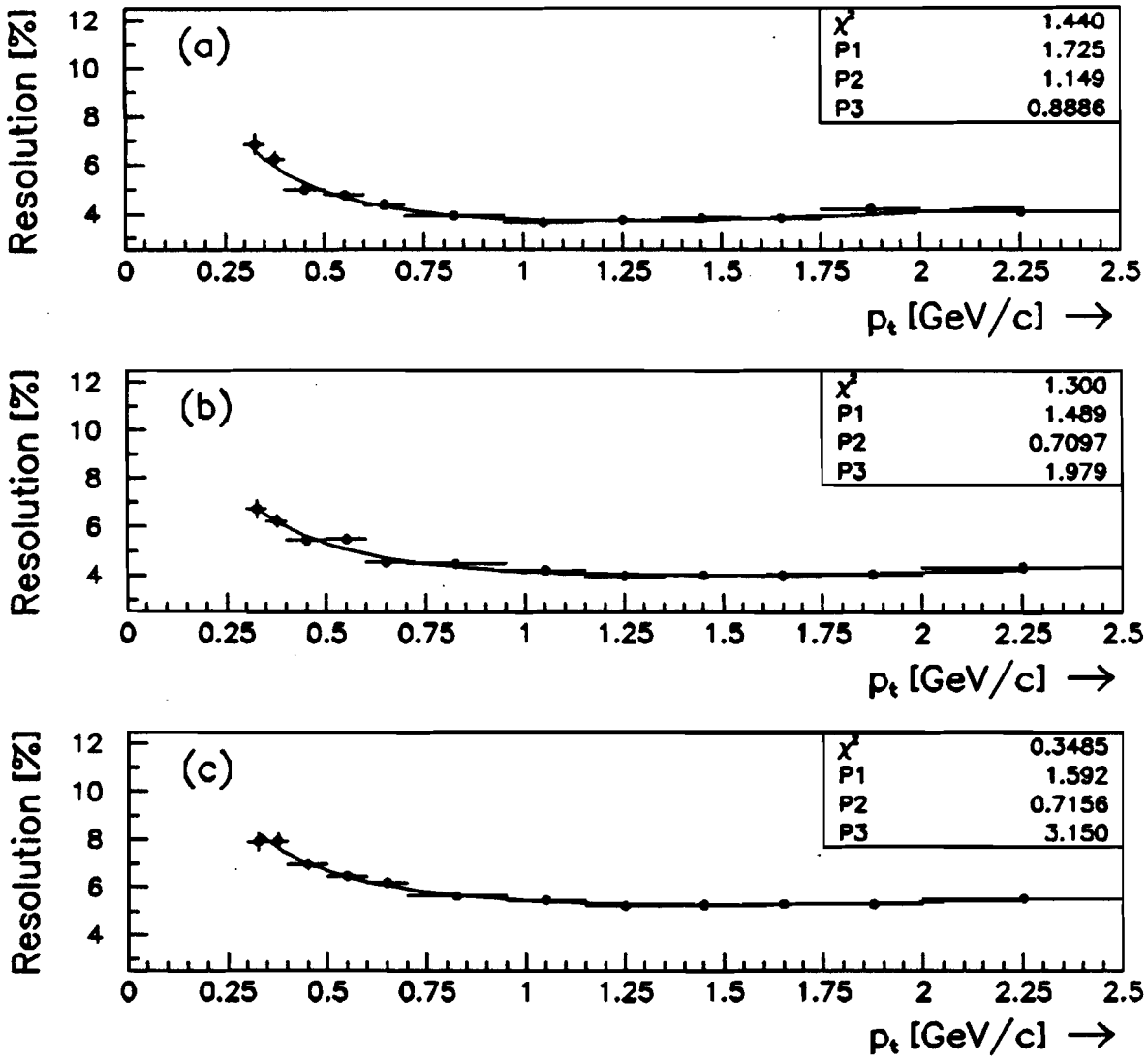

Figure 6.26 Transverse momentum resolution as a function of $p_\perp$ for the $\bar{p}$'s. Data points are fit with the formula $\sigma_{p_\perp}(p_\perp, N_c) = P1\frac{1}{p_\perp} + P2 \cdot p_\perp + P3$. (a) $40 < N_c \leq 50$, (b) $90 < N_c \leq 100$ and (c) $190 < N_c \leq 200$.

6.3.8 Pion Decay Effects

99.99 % of the time a pion will decay into a muon and a neutrino. Because the decay length ($c\tau \approx 7.8$ m) is not all that much longer than the distance between TOF1 and the beamline, a fair fraction of the pions could conceivably decay into muons before striking a TOF1 counter. Moreover, should the trajectory of the muon be colinear with the parent pion, our reconstruction algorithms will identify this particle as a pion. How many muons, then, mask as pions?

We divided the Monte Carlo *known track* data into two classes of events, which were:

1. π's that deposit energy in a TOF1 counter.

2. μ's that deposit energy in a TOF1 counter.

Next, we fed the hit information for the muon and pion events separately through our track reconstruction code. We then applied our canonical cuts on these events (see page 60). Those tracks passing the selection critera formed our data pool for the pion decay studies. In this study, we used only tracks with a $|z_o| \leq 2.5$ cm. The results are tabulated in Table 6.17. In Fig. 6.27, the ratio of the muons reconstructed as pions to the total number of pions accepted is plotted as a function of the transverse momentum. Here we averaged the contributions from μ^+/π^+ and μ^-/π^- to increase our statistics. The error is assumed to come chiefly from the muon number and is calculated in the standard way, i.e. $(N_{\mu^+} + N_{\mu^-})^{-\frac{1}{2}}$. We then fitted an exponential to the μ/π vs $p_\perp$ Monte Carlo data points and obtained a χ^2 of 1.6. Therefore, in order not to underestimate the number of pions due to misidentifying the decay muon as the pion, we need to include the normalization term:

$$\epsilon_{\text{decay}} = \frac{1}{1 - Ae^{-bp_\perp}}$$

where $A = 0.06$ and $b = 1.44$ (GeV/c)$^{-1}$. In the range $0.15 < p_\perp \leq 1.5$ GeV/c, ϵ_{decay} will vary from 1.05 to 1.01. This effect is on the order of our systematics, see page 153.

Table 6.17 $\pi \rightarrow \mu\nu$ Effects. $R_+ = \mu^+/\pi^+$, the ratio of μ^+'s from π^+ decay reconstructed as π^+'s to the number of π^+'s accepted. R_- is defined similarly.

$p_\perp$[Gev/c]	μ^-	π^-	R_- [%]	μ^+	π^+	R_+ [%]	$\frac{R_- + R_+}{2}$ [%]
0.15 – 0.17	32	673	4.76	62	1578	3.93	4.35 ± 0.45
0.17 – 0.20	32	1015	3.15	49	1035	4.73	3.94 ± 0.44
0.20 – 0.25	54	1308	4.13	56	1175	4.77	4.45 ± 0.42
0.25 – 0.30	69	1419	4.86	54	1322	4.08	4.47 ± 0.40
0.30 – 0.35	60	1590	3.77	68	1371	4.96	4.36 ± 0.38
0.35 – 0.40	46	1598	2.88	67	1466	4.57	3.73 ± 0.35
0.40 – 0.50	61	1666	3.66	42	1673	2.51	3.09 ± 0.30
0.50 – 0.60	46	1737	2.65	55	1754	3.14	2.90 ± 0.29
0.60 – 0.70	46	1743	2.64	40	1791	2.23	2.44 ± 0.26
0.70 – 0.95	29	1791	1.62	29	1769	1.64	1.63 ± 0.21
0.95 – 1.15	16	1752	0.91	17	1836	0.93	0.92 ± 0.16
1.15 – 1.35	19	1761	1.08	19	1803	1.05	1.07 ± 0.17
1.35 – 1.55	11	1777	0.62	18	1839	0.98	0.80 ± 0.15
1.55 – 1.75	17	1790	0.95	15	1865	0.80	0.88 ± 0.16

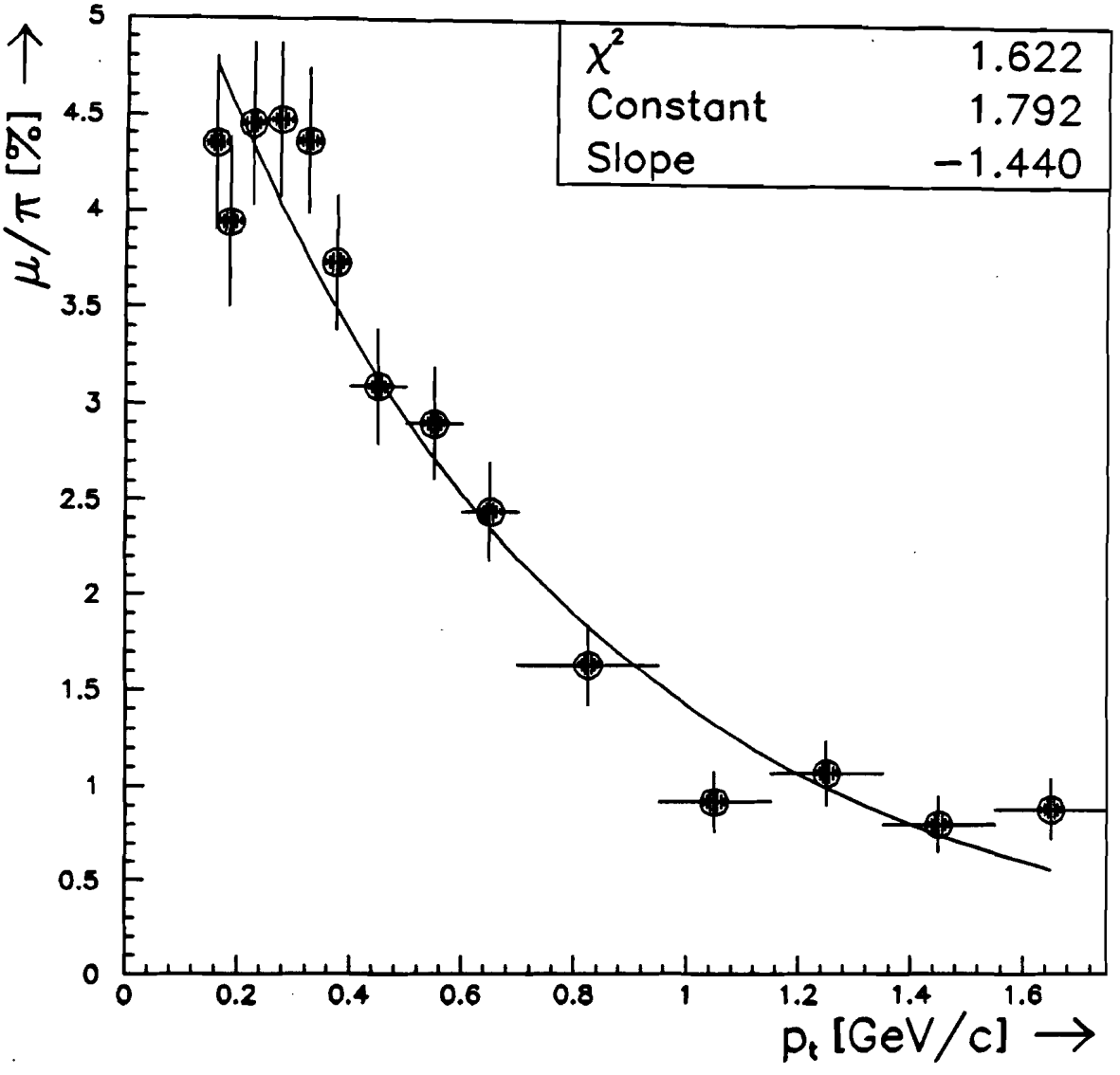

Figure 6.27 Ratio of μ's to π's plotted as a function of $p_\perp$ for μ's reconstructed as π's.

6.3.9 Mass Reconstruction Efficiency

The final step of our acceptance studies is to understand the mass reconstruction efficiency. A particle entering the spectrometer aperture experiences a 50 MeV/c transverse momentum kick from the field of the 3.8 kilogauss dipole magnet. Two sets of wire chambers, situated within the aperture of the magnet, and 14 layers of straw drift tubes, positioned behind the magnet, furnished the tracking information. Two banks of TOF counters, located at 2 and 4 meters from the beamline, provided the particle identification information. We can reconstruct the mass of the via the relationship.

$$m^2 = \frac{p^2}{\gamma^2\beta^2}$$

(See page 50)

Instead of simulating the mass reconstruction efficiency in Monte Carlo, we turned to the data to address the question of how well pions and antiprotons can be identified by TOF1. TOF2 information is not included in this study. The π^-, K^- and $\bar{p}$ mass squared peaks for four different momentum intervals are plotted in Figure 6.28. As the transverse momentum increases, we see that the kaon and pion masses meld into one another. Separating the K's from π's is currently under active Monte Carlo study and will be reported elsewhere [19].

Because we calculate the mass as a function of p and not $p_\perp$, the natural binning for the mass reconstruction efficiency, ϵ_{mre}, is in p (Fig. 6.28). That is to say, we correct for the geometrical, track reconstruction and decay acceptances in terms of $p_\perp$, but $\epsilon_{\text{mre}} = \epsilon_{\text{mre}}(p)$.

Any particle that falls within the mass squared range of $-0.07 < m^2 < .16$ $(\text{GeV/c}^2)^2$ is called a pion. These slices are shown as a function of momentum in Fig. 6.30. Note that for momenta exceeding 1.0 GeV/c, the kaon tail seeps into the mass range of the pions. In Fig. 6.29, a double gaussian is fit to the π^- and K^- mass peaks. I estimate the contribution of the kaon tail to be within 4% for $0.9 < p \leq 1.0$ GeV/c. In the final analysis, we wish to retrieve the momentum

distributions for identified particles as a function of pseudorapidity density. The kaon contamination will substantially alter the relationship between $p_\perp$ and $dN/dydp_\perp^2$. Without detailed Monte Carlo studies simulating the timing resolution of the TOF1 counters, π's cannot be unambiguously identified for momenta above 1.0 GeV/c and therefore sets the upper bound for what we call a pion.

We studied the antiproton mass reconstruction efficiency in detail. We employed two methods of fitting the kaon tail and the antiproton mass squared peak. We found a double gaussian fit and an exponential (for the K^- tail) + gaussian (for the $\bar{p}$ signal) gave reasonable χ^2's for 103 degrees of freedom. The centroid of the fitted gaussian to the $\bar{p}$ mass squared peak did not vary beyond 3% from the canonical $m^2_{\rm prot}$ value of .8804 GeV/c^2. Comparing the results of the two fits provided independent measures of the severity of the kaon pollution. First, a particle was declared an antiproton if it were negatively charged and its mass squared resided within the *antiproton zone* of $0.65 < m^2 \leq 1.4$ GeV/c^2. We next asked what the percentage of the antiprotons were excluded by this m^2 cut and how many kaons, overall, fell within the *antiproton zone*. These conditions suggest the following formula

$$\epsilon_{\rm mre} = \frac{N_{\bar{p}}^{\rm zone}}{N_{\bar{p}}^{\rm tot}}[1 - \frac{N_{K^-_{\rm tail}}}{N_{\bar{p}}^{\rm zone}}]$$

where $N_{\bar{p}}^{\rm zone}$ is the number of $\bar{p}$'s falling between the m^2 mass limits, $N_{\bar{p}}^{\rm tot}$ is the total number of enclosed by the fitted gaussian to the $\bar{p}$ signal and $N_{K^-_{\rm tail}}$ is the number of kaons that seep into the *antiproton zone*. The results are tabulated in Tables 6.19 and 6.20. In Fig. 6.31 the two fits to the kaon tail and antiproton signal for the momentum slice of $1.4 < p \leq 1.5$ GeV/c. The gaussian and exponential fits to the K^- tail are extrapolated to zero to give the reader a sense of the magnitude of the kaon contribution within the *antiproton zone*. Note the excellent agreement between the $\epsilon_{\rm mre}$'s for the double gaussian and exponential + gaussian fits. The average of these two $\epsilon_{\rm mre}$'s formed our mass reconstruction efficiency for antiprotons.

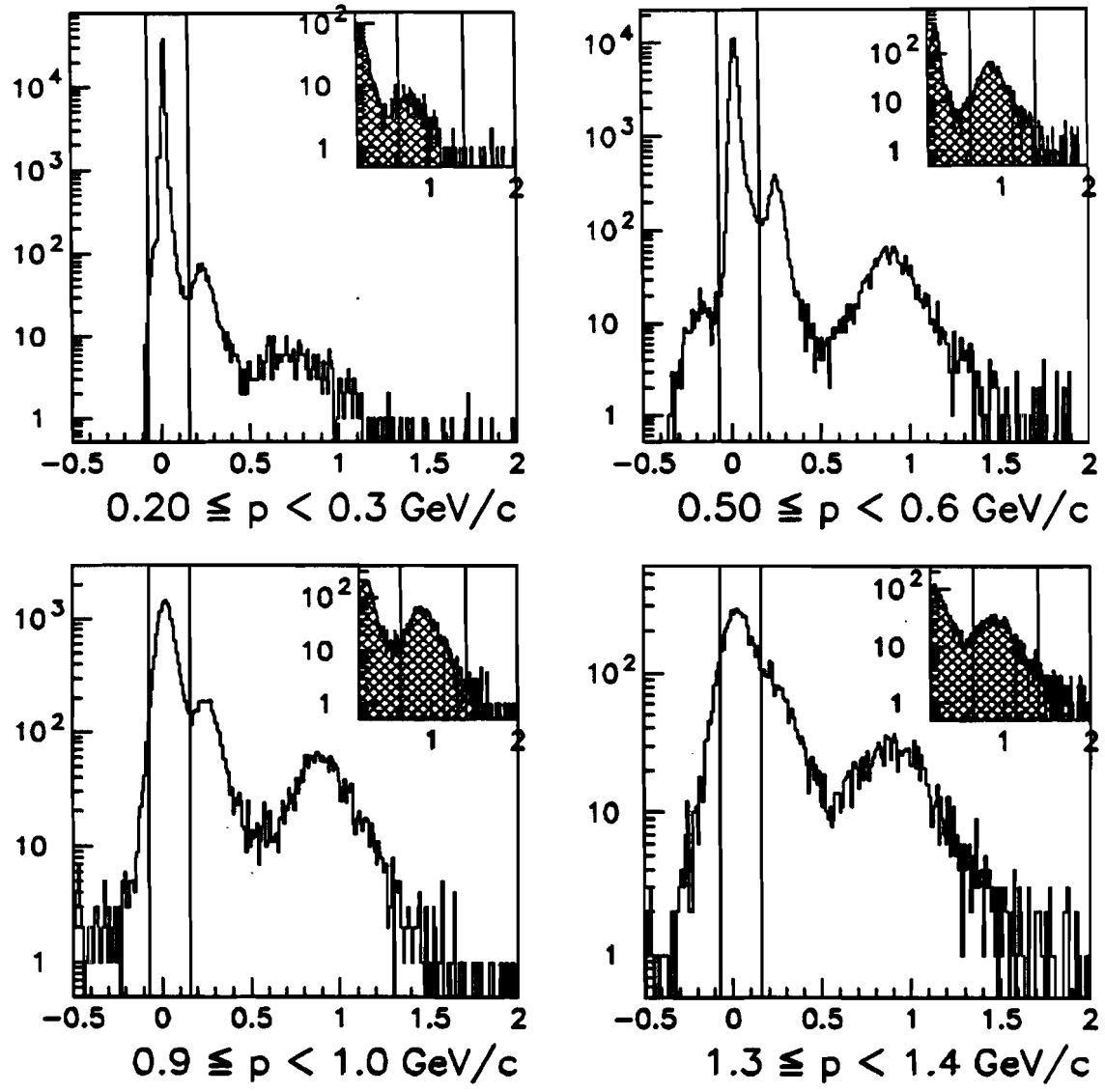

Figure 6.28 Mass squared distributions for four different momentum bins. m^2 is reckoned in units of $[(\mathrm{GeV/c^2})^2]$.

Table 6.18 Mass range for π and $\bar{p}$.

Particle Type	*Mass Range* [GeV/c^2]	*Momentum Range* [GeV/c]
$\pi^{\pm}$	$-0.265 < m < .400$	$0.15 < p_{\perp} \leq 1.0$
$\bar{p}$	$0.806 < m < 1.183$	$0.40 < p_{\perp} \leq 1.6$

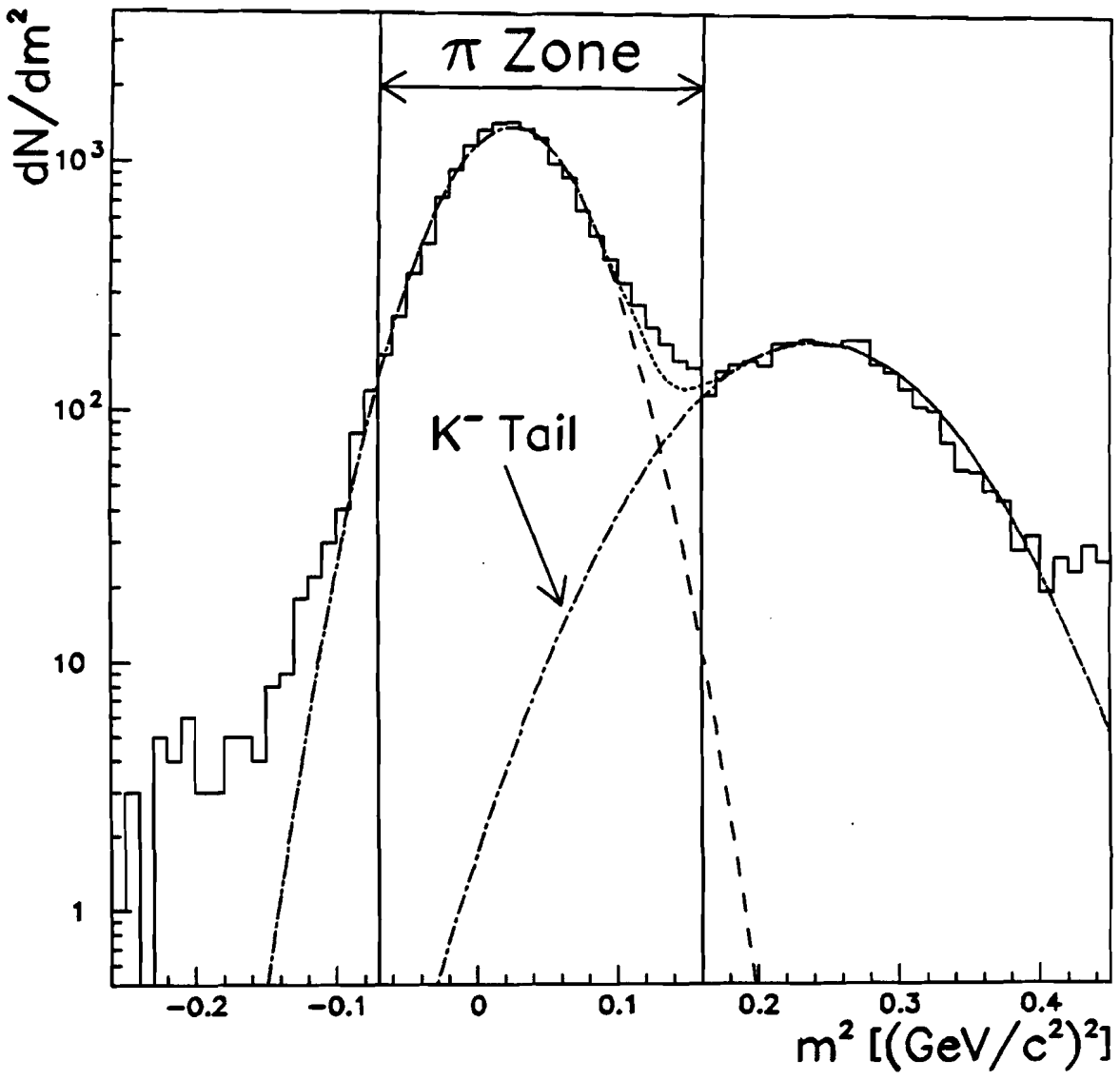

Figure 6.29 Double gaussian fit to π^- and K^- mass peaks for estimating the kaon tail contribution within the pion mass limits. ($0.9 < p \leq 1.0$ GeV/c).

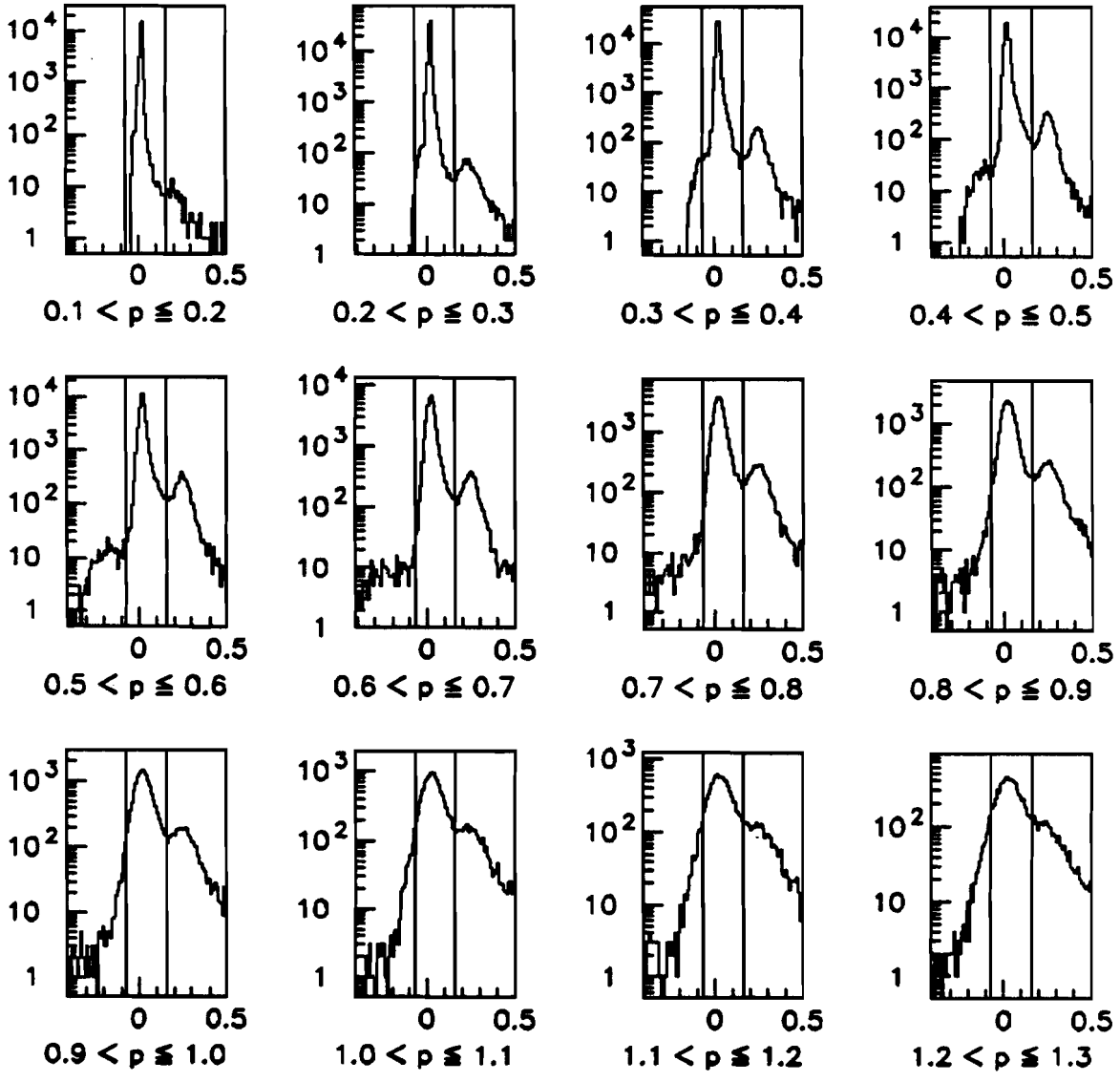

Figure 6.30 Slices of π as a function of momentum for $-0.07 < m^2 < .16$ $(\mathrm{GeV/c^2})^2$. Momentum is measured in units of GeV/c.

Table 6.19 Extracted parameters for the antiprotons using the methods of a double gaussian fit and an exponential + gaussian fit. The number of degrees of freedom, dof, is 103.

	Double Gaussian Fit			Exponential + Gaussian Fit		
Momentum [GeV/c]	$\langle\bar{p}\rangle$	σ	χ^2/dof	$\langle\bar{p}\rangle$	σ	χ^2/dof
$0.4 < p \leq 0.5$	.8775	.1587	1.803	.8778	.1577	1.704
$0.5 < p \leq 0.6$	.8846	.1456	1.904	.8850	.1446	1.779
$0.6 < p \leq 0.7$	.8964	.1418	2.303	.8967	.1411	2.125
$0.7 < p \leq 0.8$	.8962	.1392	2.088	.8967	.1379	1.883
$0.8 < p \leq 0.9$	.8988	.1490	1.635	.9003	.1468	1.506
$0.9 < p \leq 1.0$	.8914	.1528	1.675	.8930	.1507	1.585
$1.0 < p \leq 1.1$	.8842	.1555	1.538	.8866	.1530	1.478
$1.1 < p \leq 1.2$	.8883	.1628	1.347	.8912	.1603	1.326
$1.2 < p \leq 1.3$	.8832	.1761	0.883	.8871	.1730	0.871
$1.3 < p \leq 1.4$	.8878	.1833	0.903	.8928	.1799	0.904
$1.4 < p \leq 1.5$	.8947	.2105	0.949	.9013	.2059	0.941
$1.5 < p \leq 1.6$	.9020	.1979	0.871	.9078	.1940	0.867
$1.6 < p \leq 1.7$	.8721	.2306	1.149	.8819	.2253	1.142

Table 6.20 Mass reconstruction efficiency for antiprotons using the methods of a double gaussian fit and an exponential + gaussian fit.

Momentum [GeV/c]	$N_{\bar{p}}^{\text{some}}$	$N_{\bar{p}}^{\text{tot}}$	$N_{K^-_{\text{tail}}}$	ϵ_{g+g}	$N_{\bar{p}}^{\text{some}}$	$N_{\bar{p}}^{\text{tot}}$	$N_{K^-_{\text{tail}}}$	ϵ_{e+g}
$0.4 < p \leq 0.5$	1276	1382	–	0.92	1280	1382	–	0.93
$0.5 < p \leq 0.6$	1756	1857	–	0.95	1758	1854	–	0.95
$0.6 < p \leq 0.7$	2083	2172	–	0.96	2084	2171	–	0.96
$0.7 < p \leq 0.8$	2127	2214	–	0.96	2123	2206	1	0.96
$0.8 < p \leq 0.9$	2124	2232	2	0.95	2120	2217	6	0.95
$0.9 < p \leq 1.0$	2017	2140	4	0.94	2009	2124	8	0.94
$1.0 < p \leq 1.1$	1797	1925	13	0.93	1787	1903	20	0.93
$1.1 < p \leq 1.2$	1617	1744	11	0.92	1577	1691	21	0.92
$1.2 < p \leq 1.3$	1483	1638	21	0.89	1554	1667	46	0.90
$1.3 < p \leq 1.4$	1265	1405	19	0.89	1246	1369	37	0.88
$1.4 < p \leq 1.5$	1025	1180	19	0.88	1007	1143	37	0.85
$1.5 < p \leq 1.6$	889	997	29	0.86	865	959	51	0.87
$1.6 < p \leq 1.7$	708	860	20	0.80	685	818	40	0.79

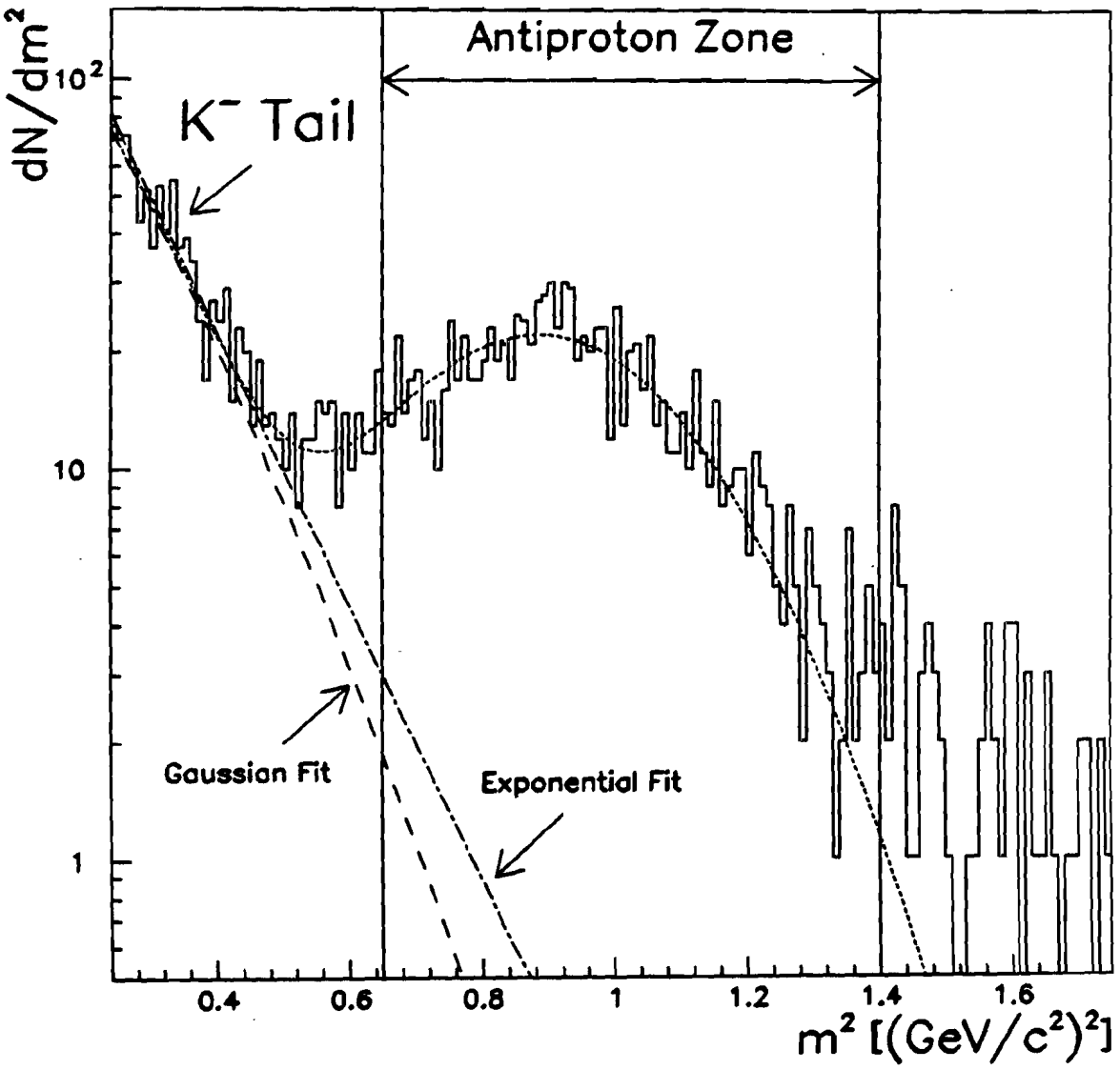

Figure 6.31 Double gaussian and exponential + gaussian fits to the $\bar{p}$ signal and the K^- signal. The *antiproton zone* resides within the range of $0.65 < m^2 < 1.4$ $(GeV/c^2)^2$.

6.3.10 Estimation of the Systematic Errors for the Magnetic Field

In this subsection, I address the issue of systematic errors. First, I explore whether an equal number of π^+'s and π^-'s enter the spectrometer [56]. We collected data from over 50 runs with the magnetic field reversed ($\simeq$ 4% of the nominal field data). Let the following quantities be defined as

$N_u^+ = \epsilon^+ N_{\pi+}$	Number of π^+ reconstructed with field up.
$N_u^- = \epsilon^- N_{\pi-}$	Number of π^- reconstructed with field up.
$N_d^+ = \epsilon^- N_{\pi-}$	Number of π^+ reconstructed with field down.
$N_d^- = \epsilon^+ N_{\pi+}$	Number of π^- reconstructed with field down.
$N_{\pi\pm}$	Number of $\pi^\pm$ which aim towards the spectrometer.

Where $\epsilon^\pm$ is the efficiency of reconstructing a π^+/π^- with the field up.

We find:

$$\frac{N_{\pi+}}{N_{\pi-}} = \sqrt{(\frac{N_u^+}{N_u^-})(\frac{N_d^+}{N_d^-})}$$

The above relationship is plotted in Fig 6.32 and we see that $N_{\pi+}/N_{\pi-}$ is consistent with unity for $p_\perp > 0.30$ GeV/c. In the range $0.15 < p_\perp < .30$ GeV/c, there appears to be a $\sim$ 2.5% excess of π^+'s. Because the Digital Volt Meter used in setting the current for the magnet was accurate to 0.5%, variations in current setting cannot explain this 2.5% excess. We systematically accept more lower transverse momentum positive pions.

6.3.11 Consistency Check of the Acceptance Corrections

The final step in the acceptance analysis is to check whether our corrections do indeed correctly correct. In the next chapter, we will show that the acceptance corrected $\frac{1}{N}\frac{d^2N}{dydp_\perp^2}$ versus $p_\perp$ distributions for both the π^-'s and π^+'s can be fit with a power law function of the form:

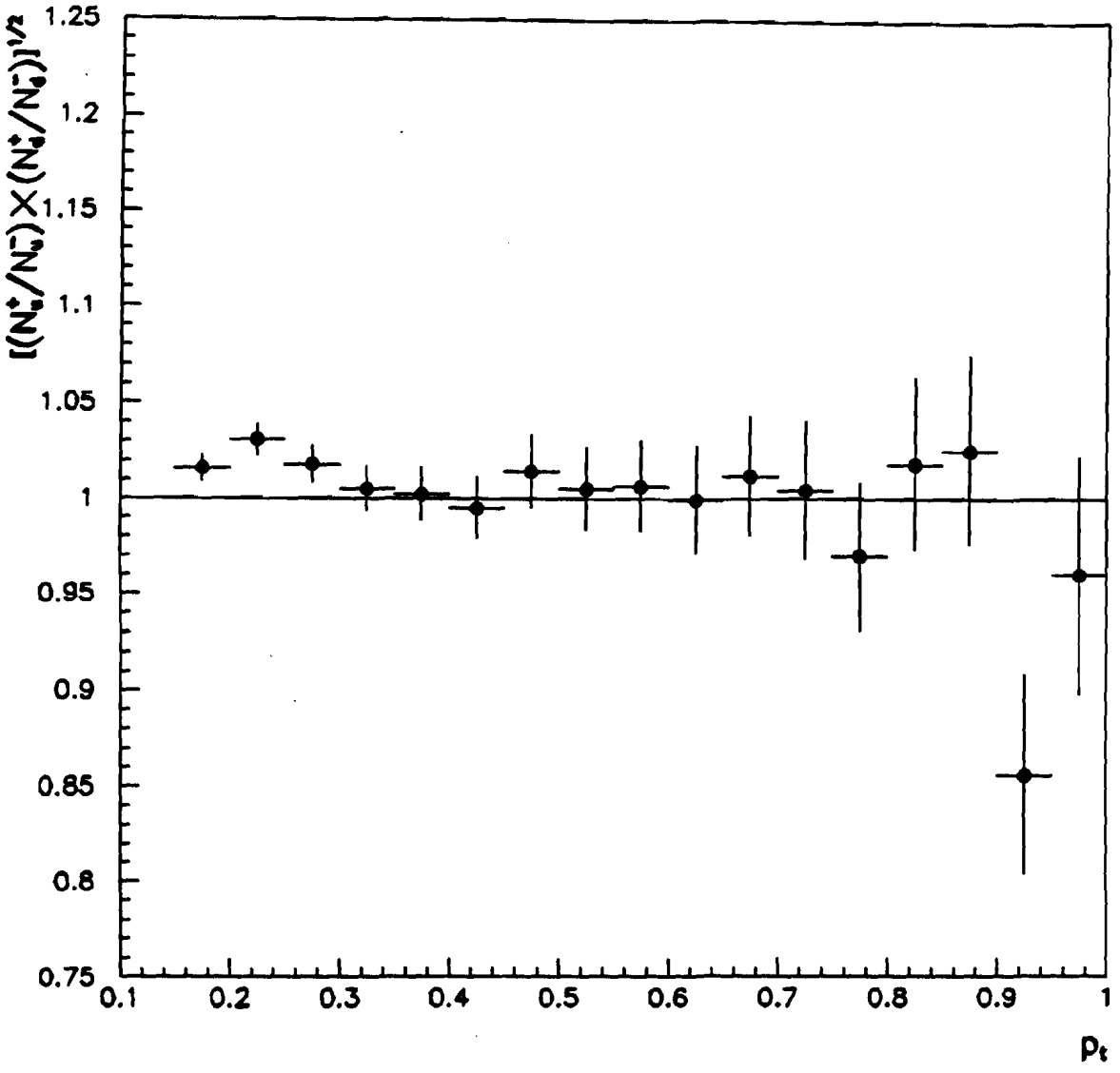

Figure 6.32 The square root of the product of the ratios of π^+ to π^+ for nominal and reversed magnet fields as a function of transverse momentum. The line drawn at constant abscissa = 1 is meant only to guide the eye.

$$\frac{1}{N}\frac{d^2N}{dydp_\perp^2} = A\frac{p_o^n}{(p_o + p_\perp)^n}$$

If we set $p_o = 1$ GeV/c, we find that for π^-'s, $n = 8.41 \pm 0.06$ and for the π^+'s, $n = 8.65 \pm 0.06$.

The tranverse momentum of the input $\pi^\pm$ were sampled from the above power law distibution, where we set $n = 8.5$. The generated particles were then distributed in accordance to:

- $|z_o| \leq -25$ cm, $\langle z_o \rangle = 0$ and $\sigma_{z_o} = 31$ cm.
- Uniform in rapidity in the interval: $-0.9 \leq y \leq 1.6$.
- Uniform in azimuth in the range: $+2° \leq \phi \leq +18°$.

These particles were next processed through our detector simulation package and the trajectories were reconstructed using the DST tracking code. The standard cuts were then applied to the reconstructed tracks. In Fig. 6.33, the superimposed uncorrected and corrected π^+ and π^- transverse momentum distributions are plotted. Each track was corrected via the product of the $\varepsilon_{\text{decay}}$, $\varepsilon_{\text{geom}}$ and ε_{tre} formulas. We see in Fig. 6.34 that the π^+ to π^- ratio is consistent with unity. The corrections perform as advertized!

6.3.12 Summary

Because the results are completely predicated on just how well we understand the acceptance of our asymmetric spectrometer, I chose to thoroughly document the technique of our corrections.

To recapitulate, the total acceptance is factored into four components:

- The geometrical efficiency, $\varepsilon_{\text{geom}}$.
- The track reconstruction efficiency, ε_{tre}.

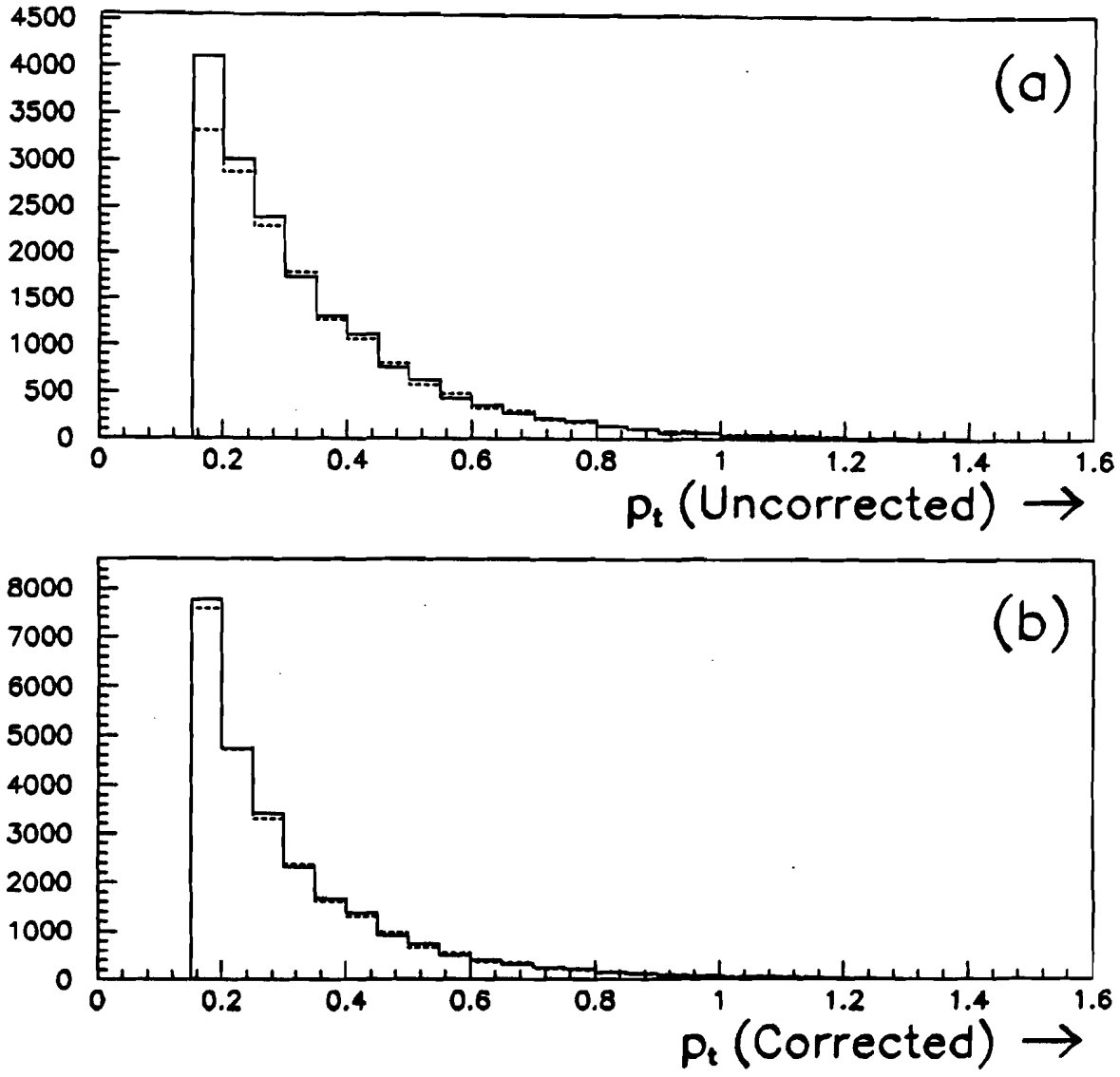

Figure 6.33 Consistency check of the acceptance corrections for the $\frac{dN}{dp_\perp^2}$ vs $p_\perp$ distributions for: (a) Reconstructed tracks after passing through the GEANT detector simulation package and (b) Acceptance corrected tracks. Solid line: π^+, Dashed line: π^-.

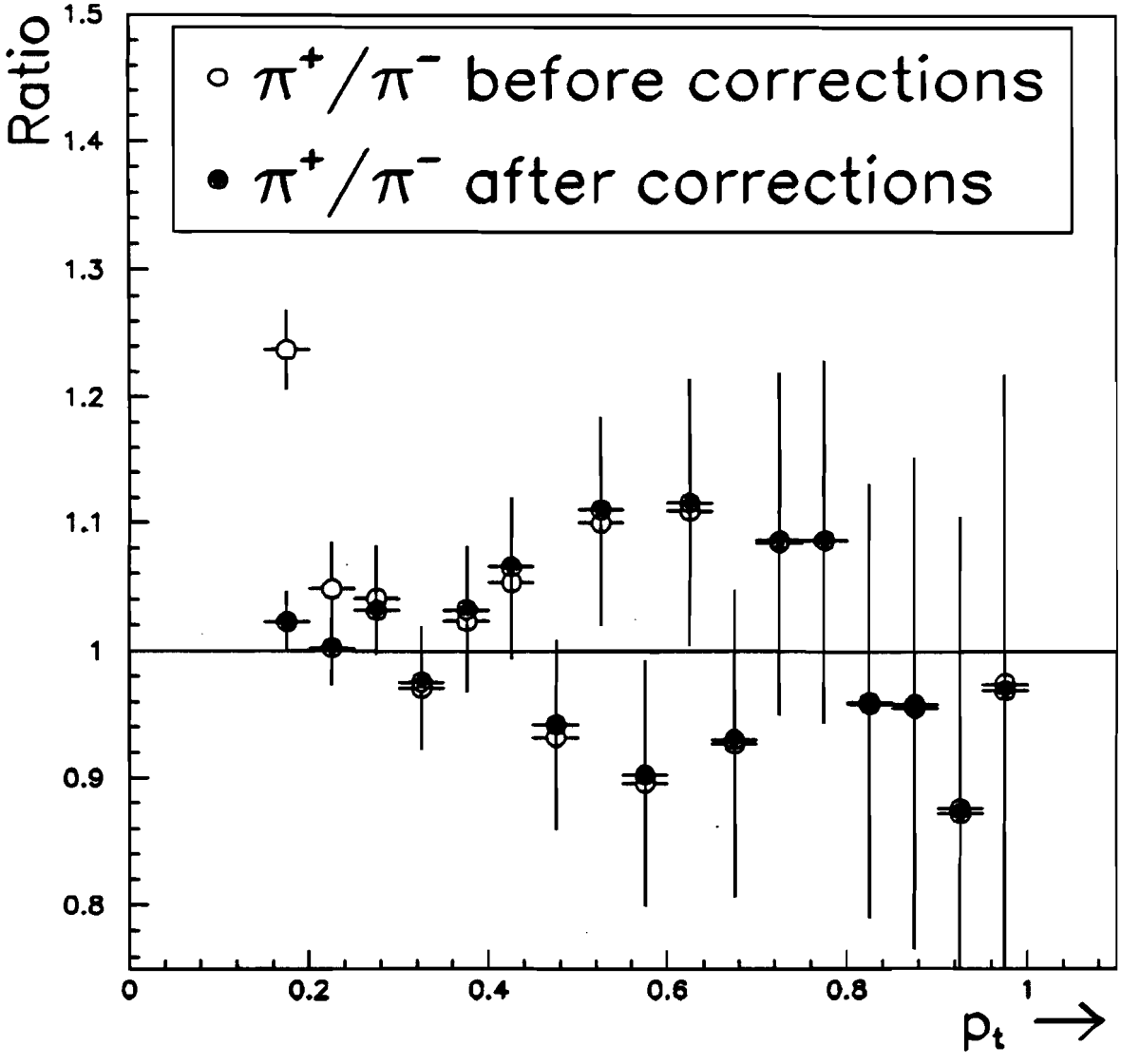

Figure 6.34 ***Unnormalized*** **Ratio of π^+ to π^- as a function of $p_\perp$ before and after acceptance corrections were applied to the Monte Carlo data.**

- The $\pi \rightarrow \mu$ efficiency, $\epsilon_{\mathrm{decay}}$.
- The mass reconstruction efficiency, ϵ_{mre}.

In applying ϵ_{tre} to the data sample, we must convert the event multiplicity to the full phase space multiplicity, $N_{\mathrm{c}}(4\pi)$. The conversion formula is [16]:

$$N_{\mathrm{c}}(4\pi) = a + bN_{\mathrm{h}} + cN_{\mathrm{h}}^2 + dN_{\mathrm{h}}^3$$

where N_{h} denotes the hodoscope multiplicity and the coefficients a, b, c and d are set to 7.8955, 0.998, $-4.679 \cdot 10^{-4}$ and $1.448 \cdot 10^{-5}$, respectively.

For lower transverse momentum particles, the acceptance corrections are on the order of 50%, but as $p_{\perp} \rightarrow \infty$, the corrections approach the asymptotic value of 20%.

7. RESULTS

We present the results of the inclusive transverse moment spectra for π^+, π^- and $\bar{p}$ and investigate the structure of the transverse momentum distributions as a function of CTC and hodoscope multiplicity for the pions and antiprotons at the center of mass energies of $\sqrt{s} = 546$, 1000 and 1800 GeV. The average transverse momentum, $\langle p_\perp \rangle$, for each of the multiplicity binned $p_\perp$ distributions is extracted from the fits:

- $p_o^n \cdot (p_o + p_\perp)^{-n}$ for the pions
- $e^{-\alpha p_\perp}$ for the antiprotons.

We also explore the relationship between $\sqrt{s}$ and $\langle p_\perp \rangle$ for pions and antiprotons at four different center of mass energies ($\sqrt{s} = 300$, 546, 1000 and 1800 GeV).

In this study, we could not distinguish pions resulting from resonance decay from those directly created in the $\bar{p}p$ collision. Likewise, we have not accounted for antiprotons arising from $\bar{\Lambda}_0$ decay.

As we shall later see, the $\langle p_\perp \rangle$ vs $dN/d\eta$ for π^+ and π^- agree to within 5%.

7.1 Corrections and Cuts

7.1.1 Effect of the Corrections on the $p_\perp$ Distributions

The corrections to the $p_\perp$ distributions are of the order of 60% (50%) in the lowest $p_\perp$ bins and approach the asymptotic value of 20% as $p_\perp$ exceeds 0.3 GeV/c for the π^- (π^+). In Fig's. 7.1a and 7.1b, the ratios of the uncorrected and corrected $dN/dp_\perp^2$ vs $p_\perp$ distributions are plotted for π^+ and π^-'s. Note the characteristic $\alpha - \beta e^{-\gamma p_\perp}$ behavior of these ratios. If we impose the *intersecting spectrometer track* cut, which

demands that there be at least two spectrometer tracks in the event and that the z intercepts of these tracks at $x = 0$ (beamline axis) be within 2 cm of one another and agree to within 10 cm of the weighted z event vertex, we find the same functional relationship in the ratio of the uncorrected to the corrected $p_\perp$ distributions (Fig. 7.2a and 7.2b).

7.1.2 The π^+ to π^- Ratio Problem

Because of the asymmetric nature of the one armed spectrometer, π^+'s were preferentially accepted over π^-'s. In the last chapter, we discussed at length the technique of our data corrections to account for the varying efficiencies in accepting pions and antiprotons. We found that the efficiencies for the different particle types were primarily a function of the transverse momentum and multiplicity. Moreover, the Monte Carlo was self-consistent (see section 6.3.11). An equal number of π^+'s and π^-'s were generated ($\sim$ 14000 events with one track per event) according to the distribution $\frac{p_0^n}{(p_0+p_\perp)^n}$, where we set $p_0 = 1$ GeV/c and $n = 8.5$. After sending the particles through our GEANT detector simulation package, reconstucting the trajectories and applying our standard cuts and acceptance corrections on a track by track basis, we found that the π^+ to π^- ratio to be unity.

When we turn to the data, however, the ratio between the π^+ and π^- is not as exact. First, if we relax the intersecting spectrometer track cut, we discover a surfeit of positive pions. In Fig. 7.3a we have superimposed the uncorrected $dN/dp_\perp^2$ vs $p_\perp$ distributions for the π^+ and π^-'s. We performed the same operation in Fig. 7.3b for the acceptance corrected distributions. We find after corrections that we still have a 20% excess of π^+'s in the range $0.15 \leq p_\perp < 0.20$ GeV/c.

However, if we impose the intersecting spectrometer track condition, we find the π^+ to π^- ratio to be within 10% (see Fig. 7.5) In Fig. 7.4 we plot the uncorrected and corrected ratios of π^+ to π^- for the all data sample and the sample after the intersecting spectrometer track condition has been imposed. In comparing the π^+ and π^- rapidity distributions for events not subject to the *intersecting spectrometer*

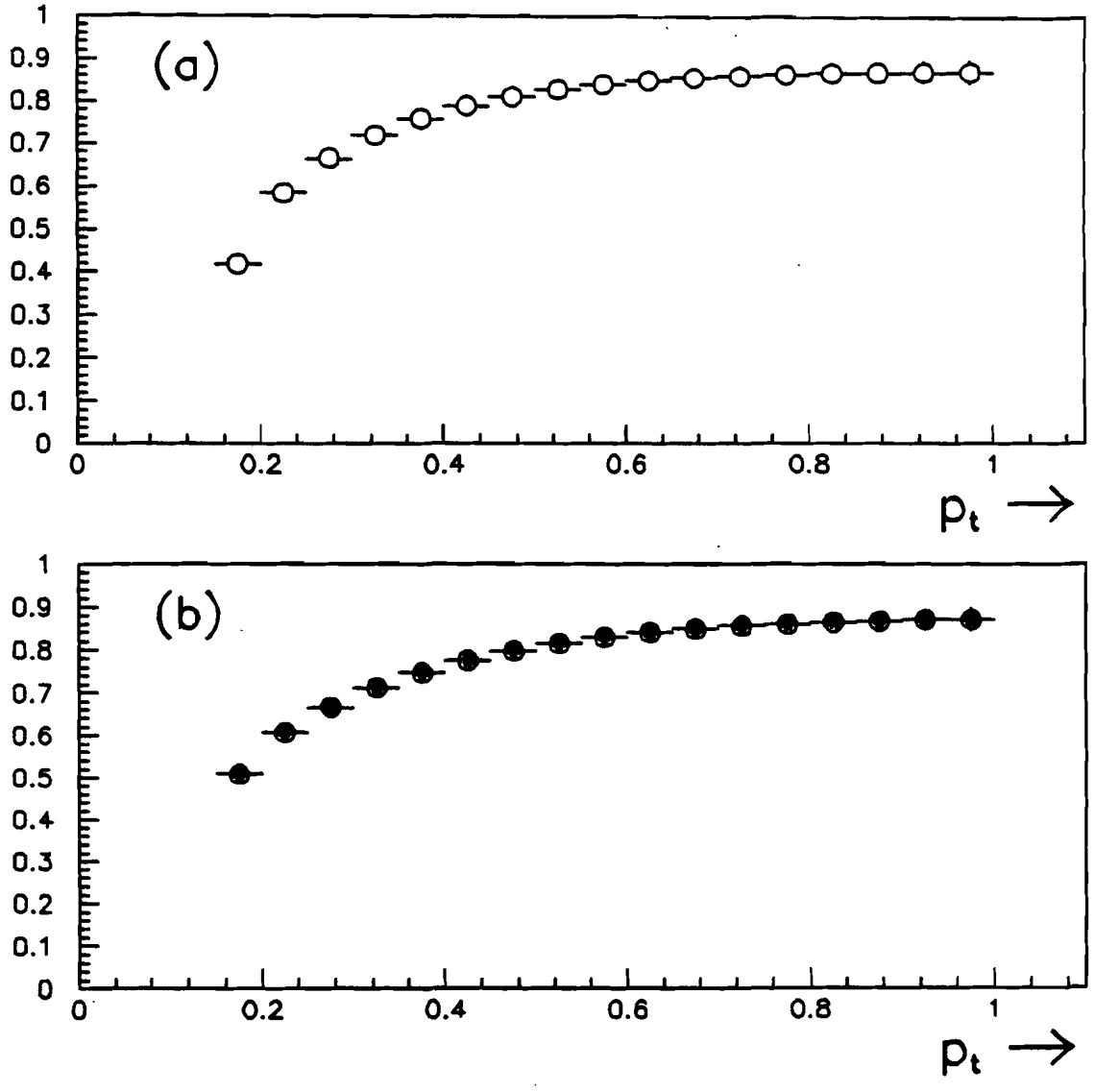

Figure 7.1 Ratio of uncorrected and corrected $dN/dp_\perp^2$ distributions as a function of $p_\perp$. Intersecting spectrometer track condition not imposed. (a) π^- and (b) π^+.

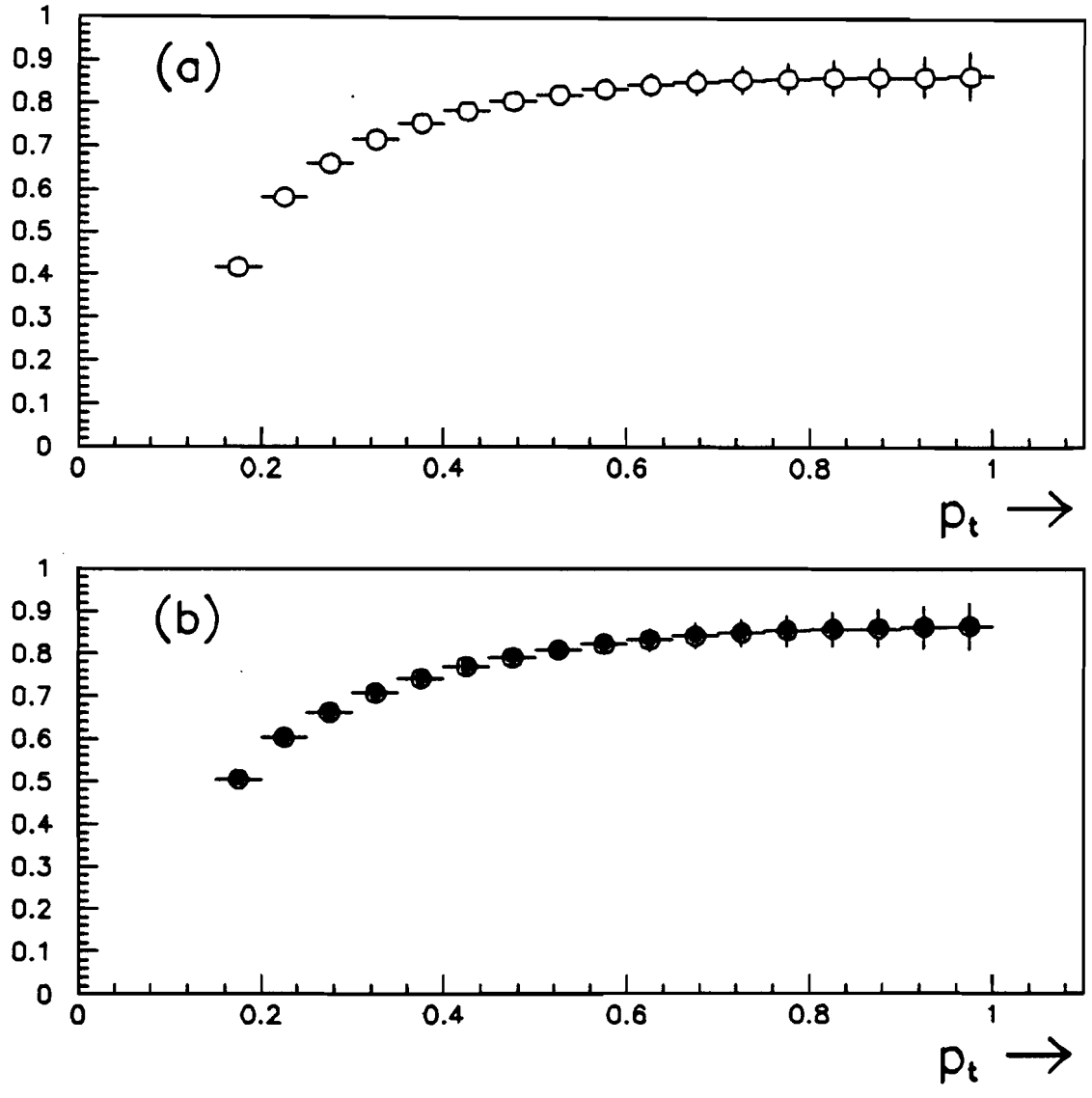

Figure 7.2 Ratio of uncorrected and corrected $dN/dp_\perp^2$ distributions as a function of $p_\perp$. Intersecting spectrometer track condition imposed. (a) π^- and (b) π^+.

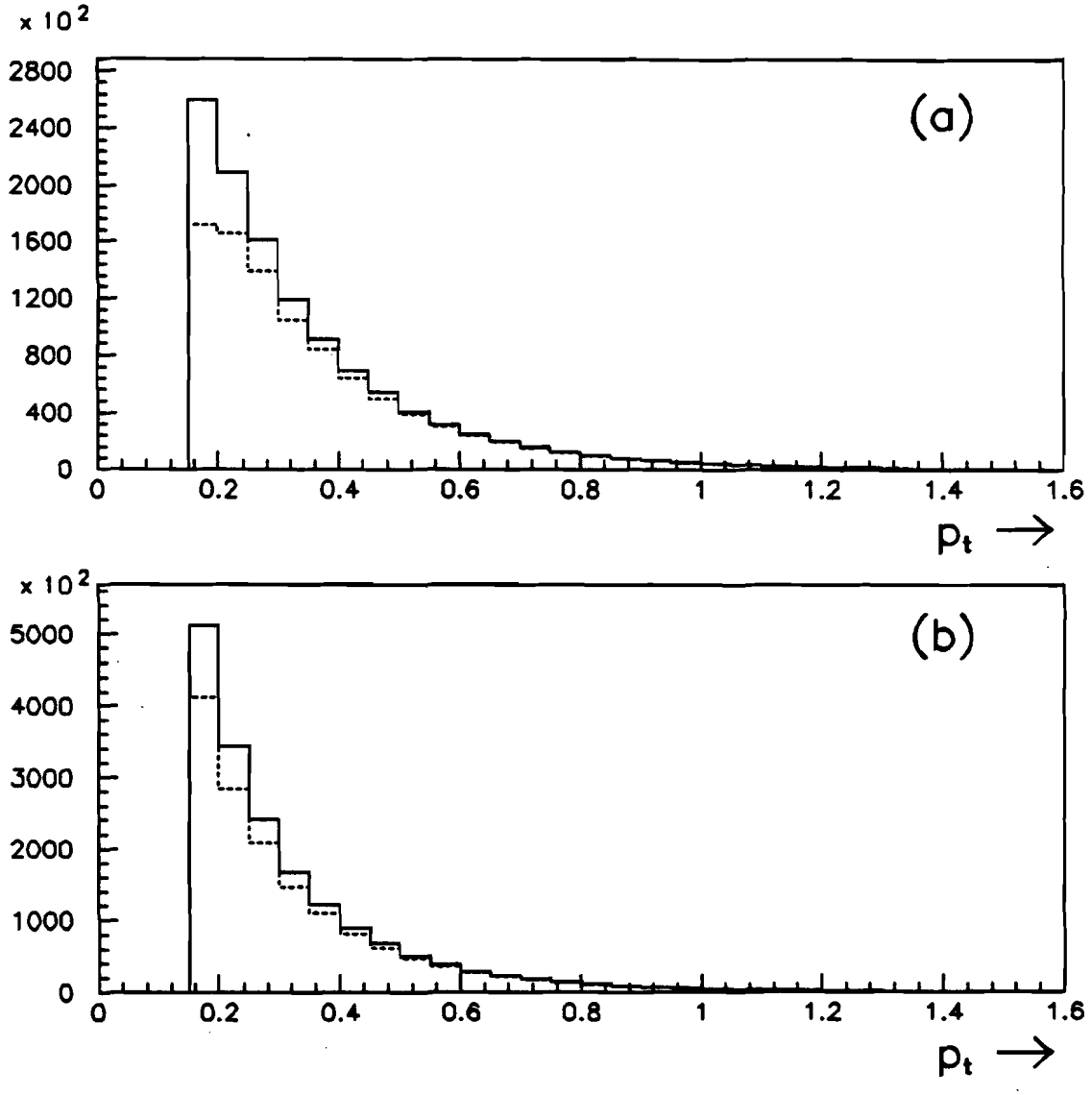

Figure 7.3 Superimposed π^- and π^+ $dN/dp_\perp^2$ vs $p_\perp$ distributions for (a) uncorrected for acceptance and (b) acceptance corrections applied. Intersecting spectrometer track not invoked.

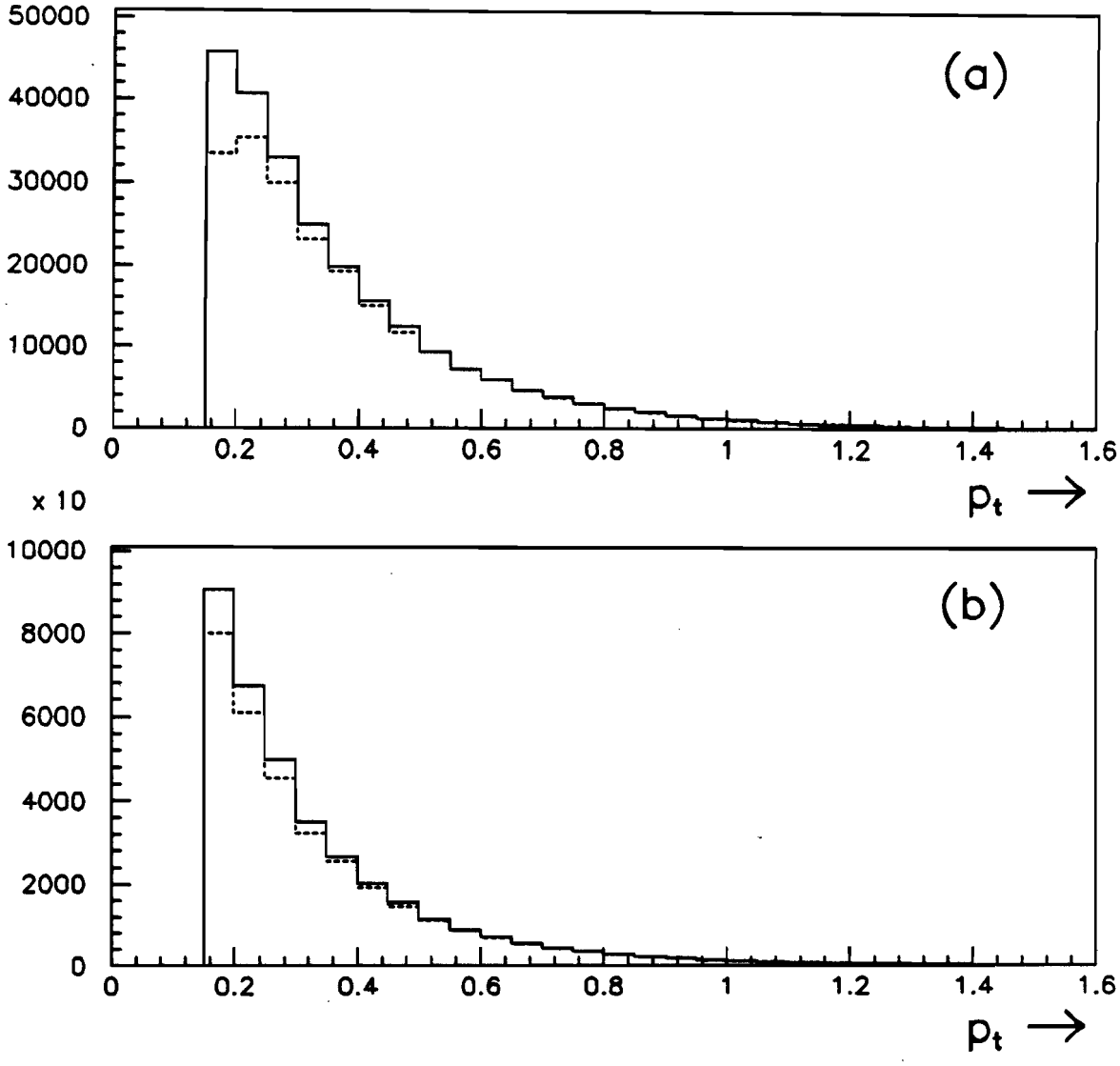

Figure 7.4 Superimposed π^- and π^+ $dN/dp_\perp^2$ vs $p_\perp$ distributions for (a) uncorrected for acceptance and (b) acceptance corrections applied. Two or more intersecting spectrometer tracks in the event.

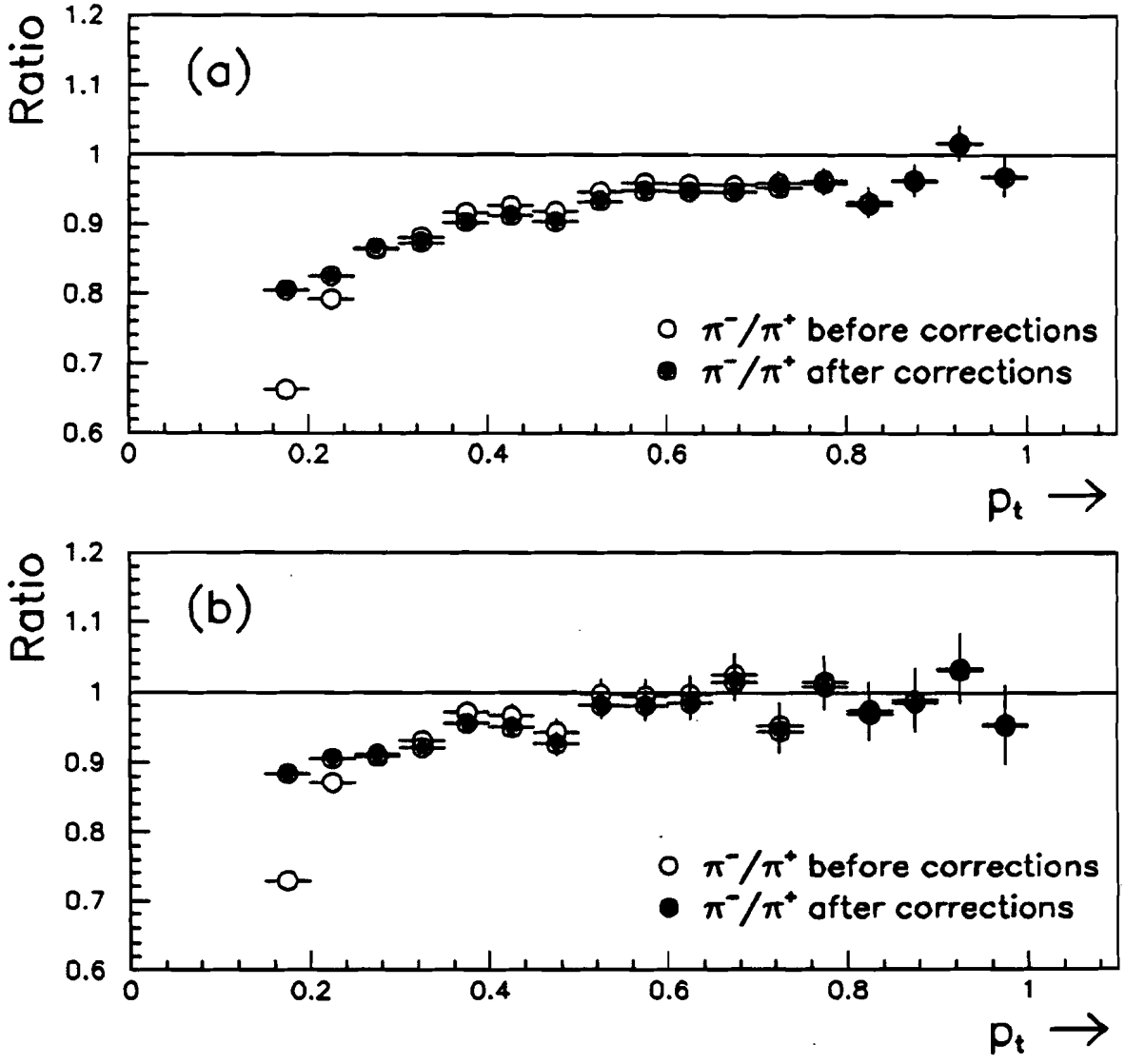

Figure 7.5 Superimposed ratios of π^- to π^+ for uncorrected and acceptance corrected data (a) All data and (b) Intersecting spectrometer track cut imposed.

track cut, one sees a marked increase of π^+'s in the positive regions of rapidity. This forward π^+ effect is most pronounced at high multiplicities. In Fig's. 7.6a and 7.6b, the rapidity distributions for the π^+ and π^- spectrometer tracks are plotted for low ($N_{\rm hodo} < 50$) and high multiplicity ($N_{\rm hodo} > 100$) events. Note that the structure of the rapidity distributions for π^- remain unchanged for increasing multiplicity. The π^+ and π^- rapidity distributions for $p_\perp \geq 0.5$ GeV/c are plotted in Fig. 7.6c. The superimposed $\pi^\pm$ rapidity distibutions for events collected with reversed magnetic field are shown in Fig.'s 7.7a through 7.7c. The situation is reversed; we now have an excess of low transverse momentum π^-'s in the forward rapidity regions for high multiplicity events. We can therefore conclude that the excess of low momentum π^+'s is dominated by the asymmetric acceptance of the spectrometer and not by a physical process which preferentially produces positive pions.

Demanding that an event contain intersecting spectrometer tracks, which originate from the same point along the collision axis, brings the π^+ to π^- ratio to within 10% for $0.15 \leq p_\perp \leq 0.35$ GeV/c and to within 5% for $0.35 \leq p_\perp \leq 0.55$ GeV/c. For $p_\perp > 0.55$ GeV/c, the π^+ to π^- ratio is consistent with unity. The acceptance correction operates on π^+'s and π^-'s differently and from subsection 6.3.11, the ratio of these two particle types are brought to unity. Apparently, the Monte Carlo is failing to completely model the excessive acceptance of low $p_\perp$ π^+'s for high multiplicity events in the forward rapidity intervals for the nominal magnetic field configuration. This uncertainty will be folded into an overall systematic error of 5%.

7.2 Transverse Momentum Spectra at 1.8 TeV

In this section, we present the inclusive transverse momentum spectra for the pions and antiprotons. We also will investigate the effects of the intersecting spectrometer track condition on the $p_\perp$ distributions. The average transverse momentum, $\langle p_\perp \rangle$, is extracted from the fits to the $p_\perp$ distributions. We conclude this section with the study of the relationship between $\langle p_\perp \rangle$ and $dN_c/d\eta$ for the pions and antiprotons.

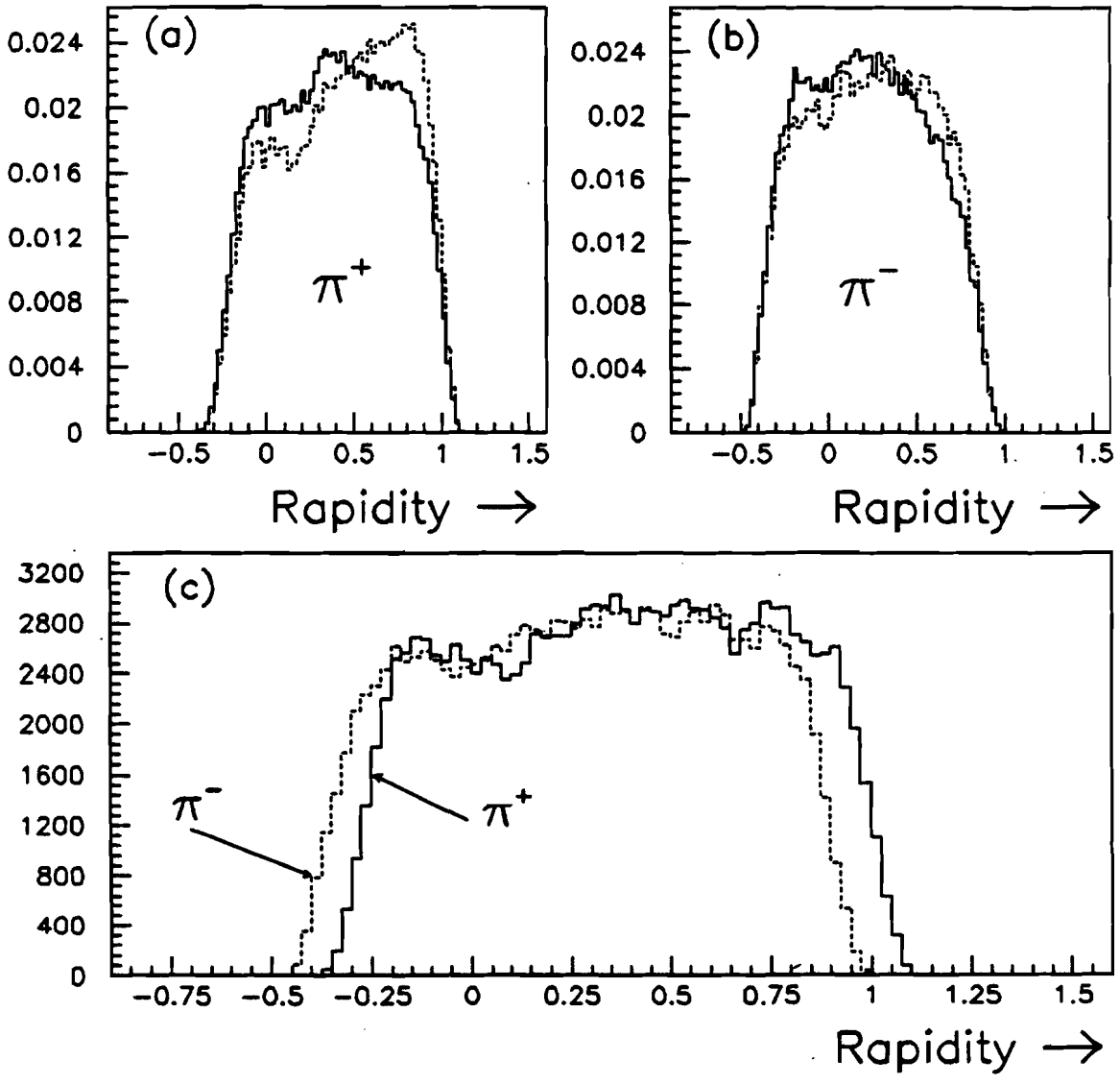

Figure 7.6 Rapidity distributions for nominal field. $N_{\text{hodo}} < 50$ (solid) overlayed upon $N_{\text{hodo}} > 100$ (dashed) for (a) π^+ and (b) π^-. For (c) $p_\perp \geq 0.5$ GeV/c.

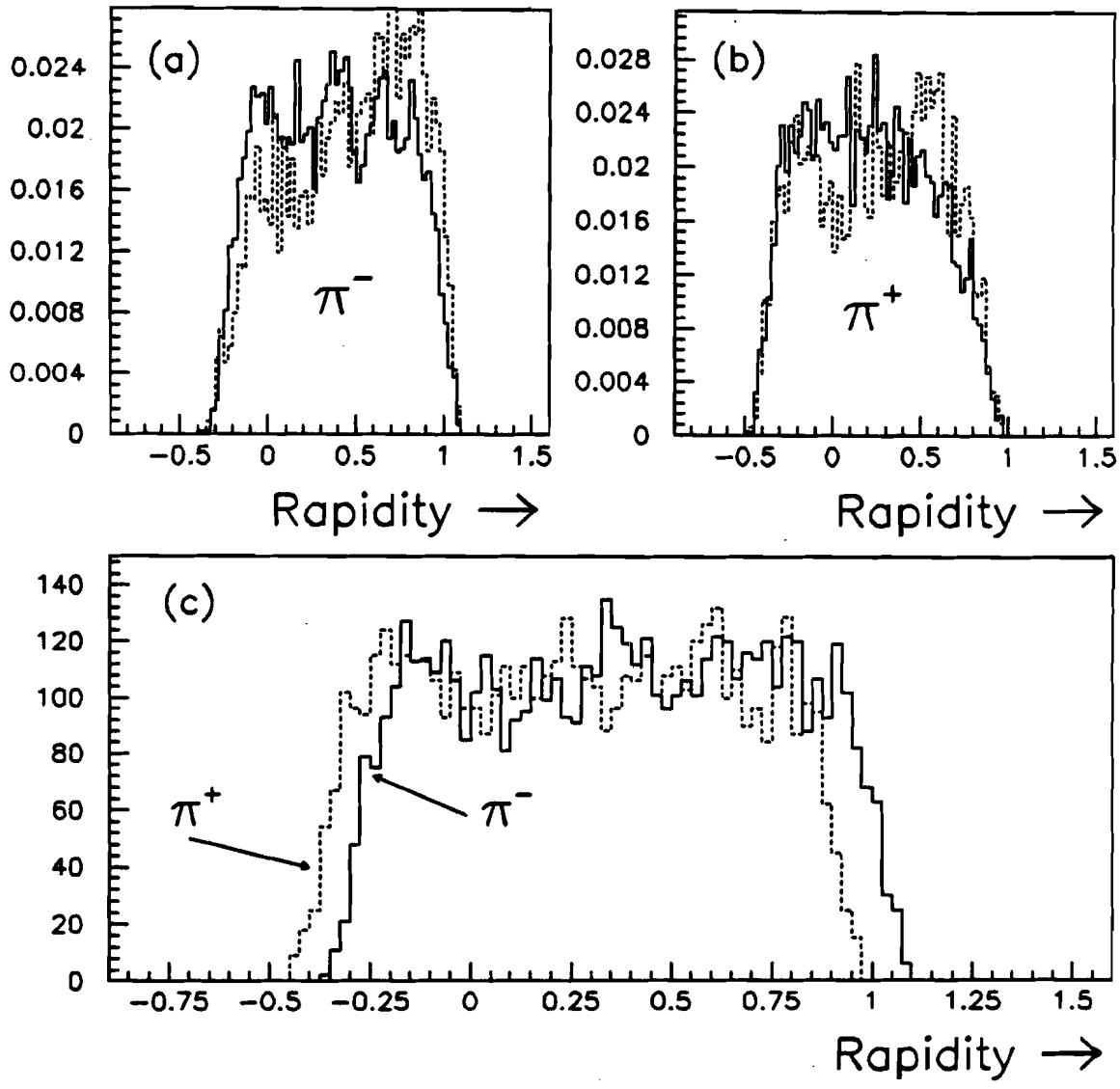

Figure 7.7 Rapidity distributions for reversed field. $N_{\text{hodo}} < 50$ (solid) overlayed upon $N_{\text{hodo}} > 100$ (dashed) for (a) π^- and (b) π^+. For (c) $p_\perp \geq 0.5$ GeV/c.

7.2.1 Multiplicity Binned $p_\perp$ Distributions

We investigate the inclusive transverse momentum spectra as a function of Central Tracking Chamber (CTC) primaries and hodoscope hits. We define a CTC primary as a track with an x-y impact parameter of less than 2 cm. That is to say, the perpendicular distance of the extrapolated CTC track must be within 2 cm at closest approach to the collision axis. A hodoscope hit must pass the standard amplitude and timing selection criterea [16]. In Fig.'s 7.8a and 7.8b, the normalized $d^2N/dydp_\perp^2$ vs $p_\perp$ distributions are plotted for two separate hodoscope multiplicities for π^+ and π^-. From these plots, it is evident that the transverse momentum spectrum flattens with increasing multiplicity in both the CTC and hodoscope. We now will explore the nature of this flattening.

7.2.2 Fits to the Inclusive $p_\perp$ Distributions

We are now in the position to extract the $\langle p_\perp \rangle$ for each of the multiplicity binned $d^2N/dydp_\perp^2$ vs $p_\perp$ distributions. For the π^+ and π^-'s, we fit a function of the form:

$$\frac{d^2N}{dydp_\perp^2} \propto \frac{p_o^n}{(p_o + p_\perp)^n} \tag{7.1}$$

In the range $0 < p_\perp < \infty$, the average transverse momentum reduces to:

$$\langle p_\perp \rangle = \frac{2p_o}{n-3} \tag{7.2}$$

We find that the antiproton inclusive transverse momentum spectra is well fit by an exponential function,

$$\frac{d^2N}{dydp_\perp^2} \propto e^{-\alpha p_\perp} \tag{7.3}$$

which gives for the interval (0,∞):

$$\langle p_\perp \rangle = \frac{2}{\alpha} \tag{7.4}$$

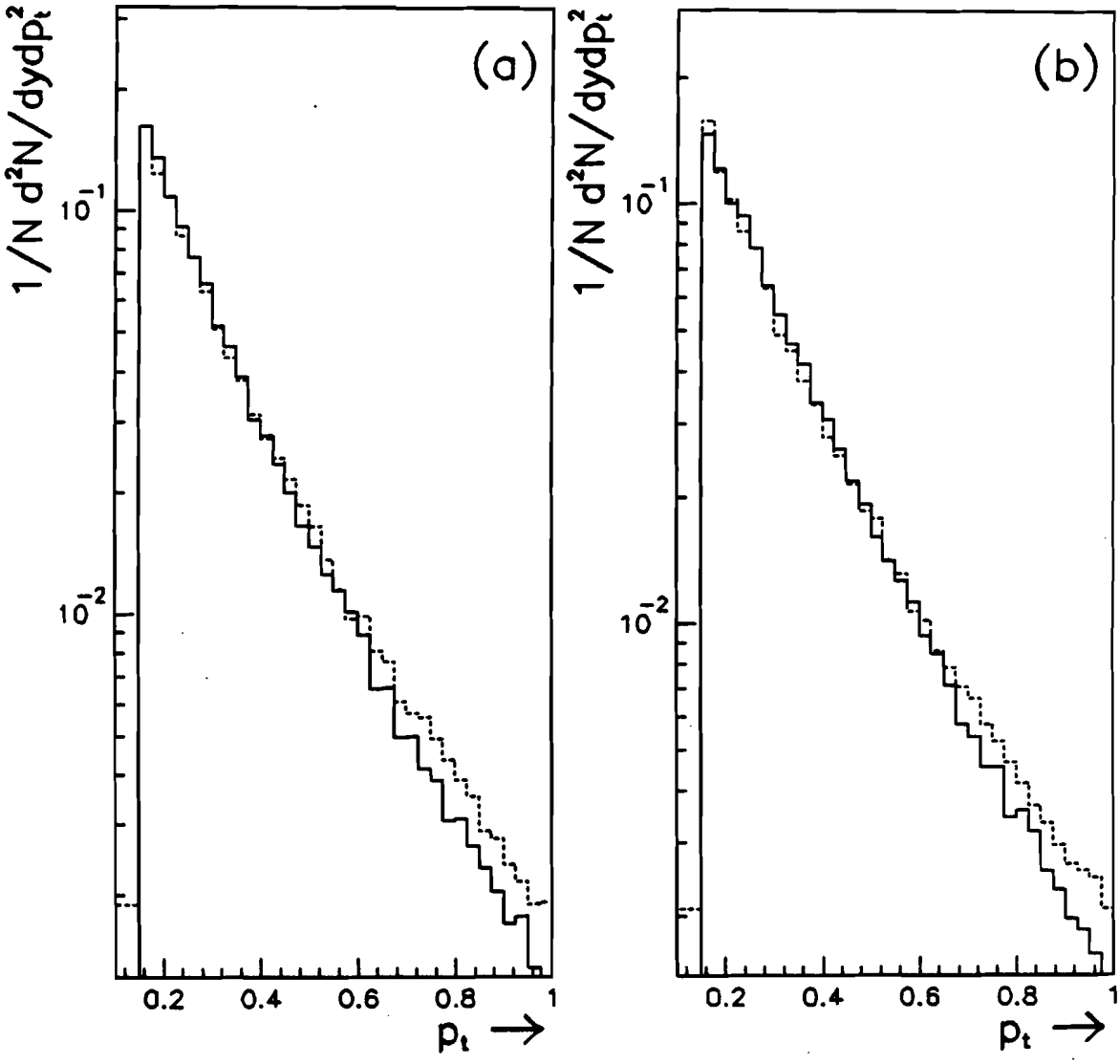

Figure 7.8 Superimposed $\frac{1}{N}\frac{d^2N}{dydp_\perp^2}$ vs $p_\perp$ distributions for $30 < N_{\text{hodo}} \leq 40$ (solid) and $110 < N_{\text{hodo}} \leq 120$ (dashed). (a) π^+ and (b) π^-.

Because of our high statistics, the errors are chiefly systematic. In fitting the data points, we will add a 5% systematic[1] error in quadrature to the minute statistical errors.

7.2.3 Power Law Fits to the π^+ and π^- $p_\perp$ Spectra

In this section, we discuss the power law fits to the multiplicity binned inclusive $p_\perp$ spectra for π^+ and π^- for CTC and hodoscope data. We found that the parameter p_o did not vary more than a few percent from unity when allowed to float in fitting the pion transverse momentum distributions. In their work of fitting the inclusive $p_\perp$ spectra, UA1 [6] set $p_o \equiv 1.0$ GeV/c (see eqn. 7.1). For the purposes of comparing our results to earlier works, we shall also set this parameter to unity [35], [36]. The reduced χ^2 for these fits are routinely around one, which implies that we are neither grossly overestimating nor underestimating the systematic errors. The fits span the interval of $0.15 \leq p_\perp \leq 1.0$ GeV/c. Beyond 1.0 GeV/c, we cannot unambiguously separate the pions from the kaons. The results of the fits to the hodoscope and CTC multiplicity binned $p_\perp$ distributions for the all data sample are entered in Tables 7.1 and 7.2, respectively. For the intersecting spectrometer track sample, the results are tabulated in Tables 7.3 and 7.4. In Fig's 7.9 through 7.12, the fits to the CTC and hodoscope multiplicity binned inclusive transverse momentum spectra for both π^+ and π^- data are plotted.

[1]We have observed that the ratio of π^+ to π^- can vary to as much as 20% as $p_\perp \to 0$ for the all spectrometer track sample (see Fig. 7.5a). The asymptotic value of the uncertainty in the ratio is 5%.

Table 7.1 Power law fits to the all spectrometer sample. Multiplicities measured by the hodoscope.

	π^-			π^+			
Multiplicity	n	χ^2	$\langle p_\perp \rangle$	n	χ^2	$\langle p_\perp \rangle$	$\langle p_\perp \rangle_{\pi^+} / \langle p_\perp \rangle_{\pi^-}$
$10 \leq N_h < 20$	8.829	2.8	0.343	9.401	1.4	0.313	0.91
$20 \leq N_h < 30$	8.808	1.5	0.344	9.170	0.8	0.324	0.94
$30 \leq N_h < 40$	8.619	0.6	0.356	9.047	0.6	0.331	0.93
$40 \leq N_h < 50$	8.438	0.4	0.368	8.834	0.6	0.343	0.93
$50 \leq N_h < 60$	8.301	0.5	0.377	8.740	0.6	0.348	0.92
$60 \leq N_h < 70$	8.200	0.6	0.385	8.531	0.6	0.362	0.94
$70 \leq N_h < 80$	8.071	0.7	0.394	8.441	0.7	0.368	0.93
$80 \leq N_h < 90$	8.024	0.9	0.398	8.315	1.0	0.376	0.95
$90 \leq N_h < 100$	8.022	0.5	0.398	8.341	0.9	0.375	0.94
$100 \leq N_h < 110$	7.960	0.7	0.403	8.278	0.9	0.379	0.94
$110 \leq N_h < 120$	7.958	0.8	0.403	8.278	0.9	0.379	0.94
$120 \leq N_h < 130$	7.874	1.2	0.410	8.292	1.2	0.378	0.92
$130 \leq N_h < 140$	7.909	1.2	0.407	8.116	1.5	0.391	0.96

Table 7.2 Power law fits to the all spectrometer sample. Multiplicities measured by the CTC.

	π^-			π^+			
Multiplicity	n	χ^2	$\langle p_\perp \rangle$	n	χ^2	$\langle p_\perp \rangle$	$\langle p_\perp \rangle_{\pi^+} / \langle p_\perp \rangle_{\pi^-}$
$0 \leq N_{\text{prim}} < 10$	8.982	2.9	0.334	8.878	2.5	0.340	1.02
$10 \leq N_{\text{prim}} < 20$	8.770	1.4	0.347	9.013	2.4	0.333	0.96
$20 \leq N_{\text{prim}} < 30$	8.393	1.3	0.371	8.919	0.9	0.338	0.91
$30 \leq N_{\text{prim}} < 40$	8.388	1.1	0.371	8.648	0.8	0.354	0.95
$40 \leq N_{\text{prim}} < 50$	8.137	1.9	0.389	8.470	1.4	0.366	0.94
$50 \leq N_{\text{prim}} < 60$	8.209	1.4	0.384	8.280	1.5	0.379	0.99
$60 \leq N_{\text{prim}} < 70$	8.283	2.3	0.379	8.319	1.8	0.376	0.99
$70 \leq N_{\text{prim}} < 80$	7.894	1.8	0.410	8.521	1.5	0.362	0.89
$80 \leq N_{\text{prim}} < 90$	7.839	2.7	0.413	8.560	2.1	0.360	0.87
$90 \leq N_{\text{prim}} < 100$	7.989	3.6	0.401	8.432	3.1	0.368	0.92

Table 7.3 Power law fits to the intersecting spectrometer track sample. Multiplicities measured by the hodoscope.

	π^-			π^+			
Multiplicity	n	χ^2	$\langle p_\perp \rangle$	n	χ^2	$\langle p_\perp \rangle$	$\langle p_\perp \rangle_{\pi^+} / \langle p_\perp \rangle_{\pi^-}$
$10 \leq N_h < 20$	8.759	5.2	0.347	8.841	3.0	0.342	0.99
$20 \leq N_h < 30$	8.287	2.0	0.378	8.302	2.8	0.377	0.99
$30 \leq N_h < 40$	7.918	2.3	0.407	8.442	2.4	0.367	0.90
$40 \leq N_h < 50$	7.886	2.0	0.409	8.296	1.0	0.378	0.92
$50 \leq N_h < 60$	7.818	1.0	0.415	8.302	1.2	0.377	0.91
$60 \leq N_h < 70$	7.696	1.1	0.426	7.967	1.1	0.403	0.95
$70 \leq N_h < 80$	7.683	1.0	0.427	7.960	0.7	0.403	0.94
$80 \leq N_h < 90$	7.774	1.1	0.419	7.923	1.2	0.406	0.97
$90 \leq N_h < 100$	7.633	1.0	0.432	7.791	1.3	0.417	0.97
$100 \leq N_h < 110$	7.668	0.8	0.428	7.768	0.8	0.420	0.98
$110 \leq N_h < 120$	7.582	0.8	0.437	7.786	0.8	0.418	0.96
$120 \leq N_h < 130$	7.407	1.1	0.454	7.970	1.2	0.402	0.89
$130 \leq N_h < 140$	7.500	1.4	0.444	7.739	1.8	0.422	0.95
$140 \leq N_h < 150$	7.480	2.6	0.446	7.374	1.7	0.457	1.02

Table 7.4 Power law fits to the intersecting spectrometer track sample. Multiplicities measured by the CTC.

	π^-			π^+			
Multiplicity	n	χ^2	$\langle p_\perp \rangle$	n	χ^2	$\langle p_\perp \rangle$	$\langle p_\perp \rangle_{\pi^+} / \langle p_\perp \rangle_{\pi^-}$
$0 \leq N_{\text{prim}} < 10$	–	–	–	–	–	–	–
$10 \leq N_{\text{prim}} < 20$	8.287	1.9	0.378	8.235	2.0	0.382	1.01
$20 \leq N_{\text{prim}} < 30$	8.023	2.7	0.398	8.555	2.9	0.360	0.90
$30 \leq N_{\text{prim}} < 40$	8.051	2.5	0.396	8.583	2.9	0.358	0.90
$40 \leq N_{\text{prim}} < 50$	7.657	3.9	0.429	7.980	2.5	0.402	0.94
$50 \leq N_{\text{prim}} < 60$	7.720	1.8	0.424	7.872	1.2	0.411	0.97
$60 \leq N_{\text{prim}} < 70$	7.567	2.7	0.438	7.902	1.3	0.408	0.93
$70 \leq N_{\text{prim}} < 80$	–	–	–	–	–	–	–
$80 \leq N_{\text{prim}} < 90$	–	–	–	–	–	–	–
$90 \leq N_{\text{prim}} < 100$	–	–	–	–	–	–	–

Table 7.5 Final average transverse momentum of pions. 1trk is the all track sample and 2trk denotes intersecting spectrometer track sample.

Hodoscope			CTC		
Multiplicity	$\langle p_\perp \rangle_{1trk}$	$\langle p_\perp \rangle_{2trk}$	Multiplicity	$\langle p_\perp \rangle_{1trk}$	$\langle p_\perp \rangle_{2trk}$
$10 \leq N_h < 20$	0.328	0.345	$0 \leq N_{prim} < 10$	0.337	–
$20 \leq N_h < 30$	0.334	0.378	$10 \leq N_{prim} < 20$	0.340	0.380
$30 \leq N_h < 40$	0.344	0.387	$20 \leq N_{prim} < 30$	0.355	0.379
$40 \leq N_h < 50$	0.356	0.394	$30 \leq N_{prim} < 40$	0.363	0.377
$50 \leq N_h < 60$	0.363	0.396	$40 \leq N_{prim} < 50$	0.378	0.416
$60 \leq N_h < 70$	0.374	0.415	$50 \leq N_{prim} < 60$	0.382	0.418
$70 \leq N_h < 80$	0.381	0.415	$60 \leq N_{prim} < 70$	0.378	0.423
$80 \leq N_h < 90$	0.387	0.413	$70 \leq N_{prim} < 80$	0.386	–
$90 \leq N_h < 100$	0.387	0.425	$80 \leq N_{prim} < 90$	0.387	–
$100 \leq N_h < 110$	0.391	0.424	$90 \leq N_{prim} < 100$	0.385	–
$110 \leq N_h < 120$	0.391	0.428			
$120 \leq N_h < 130$	0.394	0.428			
$130 \leq N_h < 140$	0.399	0.433			

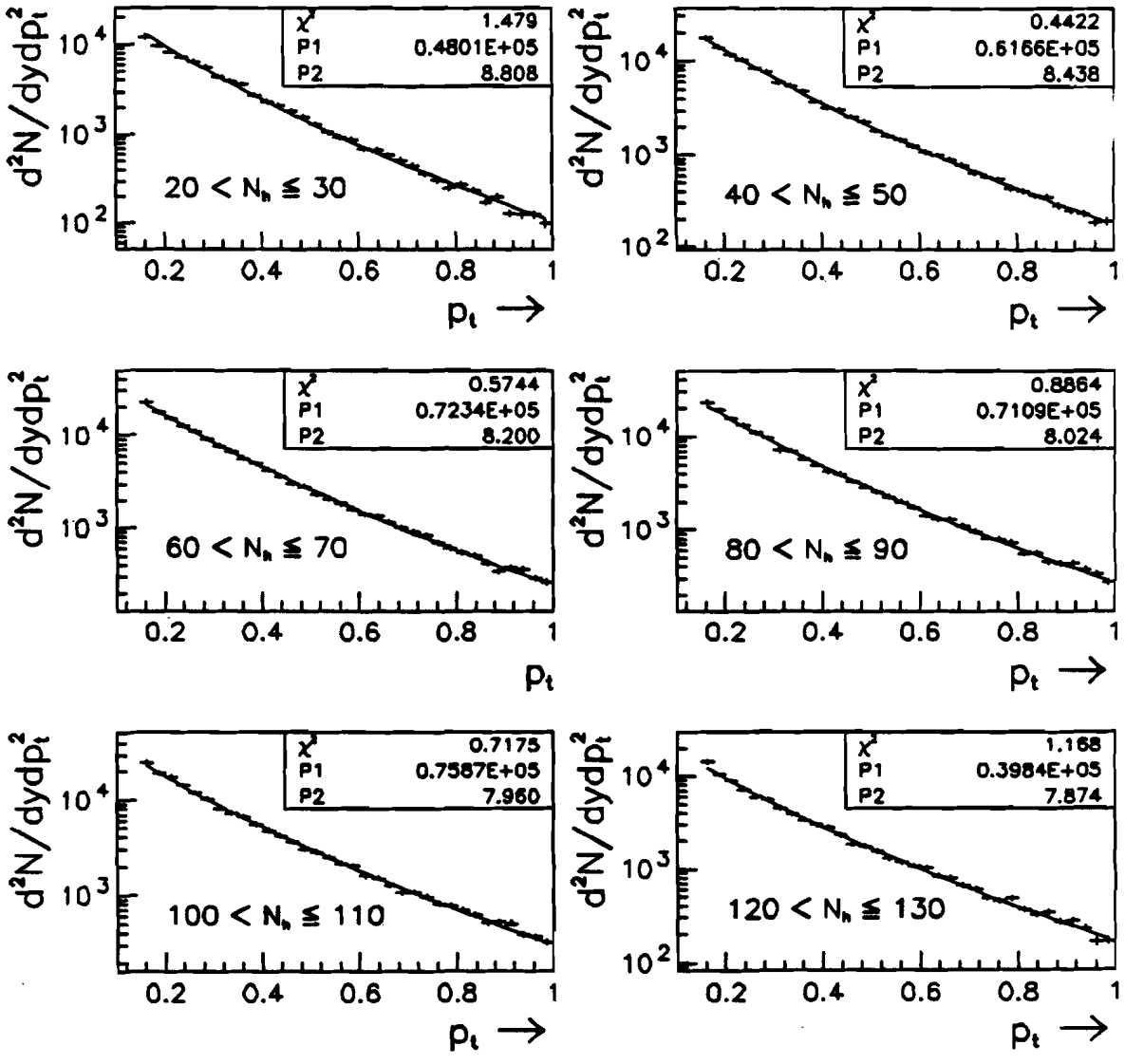

Figure 7.9 Inclusive π^- transverse momentum spectra binned by hodoscope multiplicity. P1 is the normalization and P2 is the power.

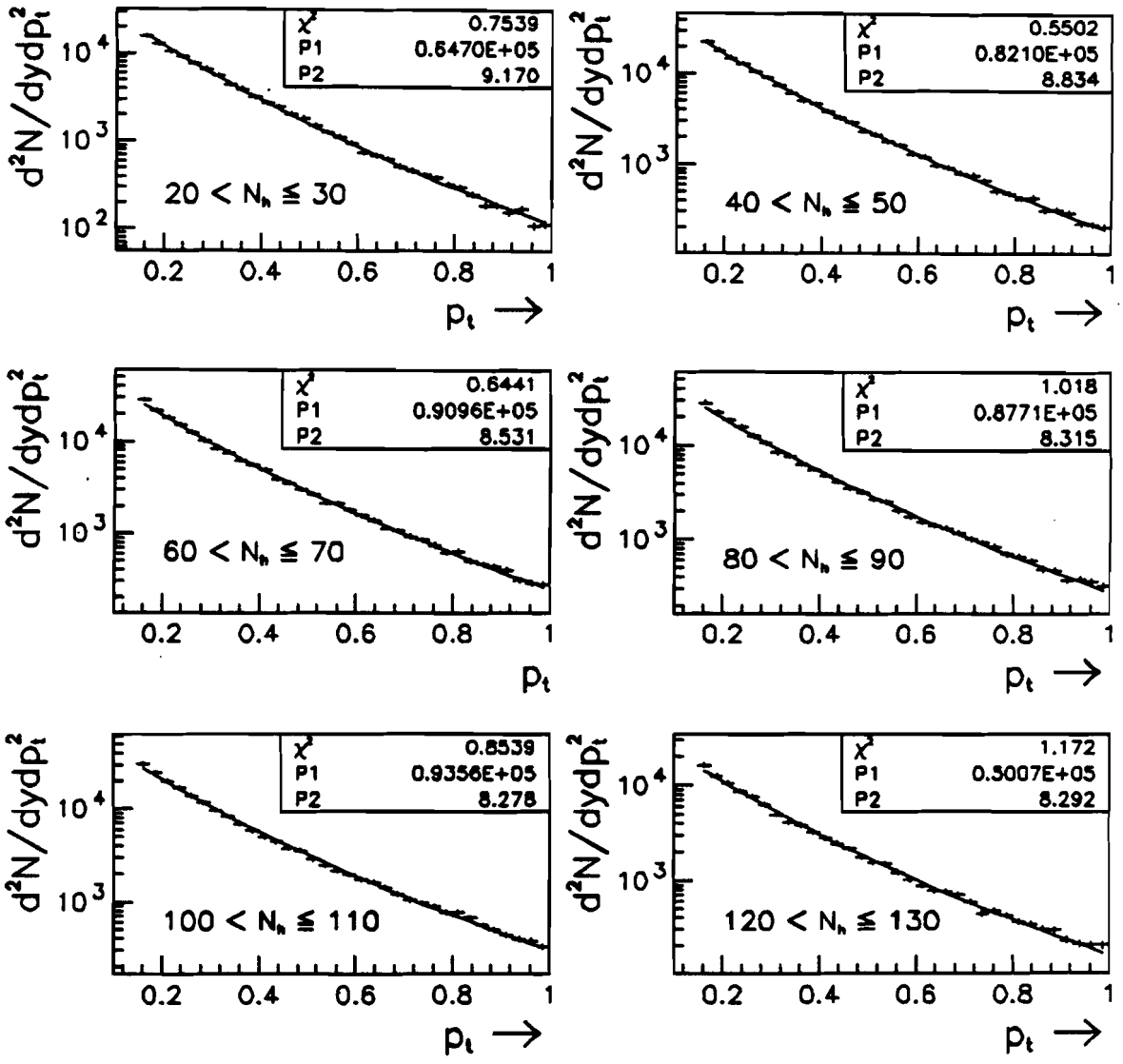

Figure 7.10 Inclusive π^+ transverse momentum spectra binned by hodoscope multiplicity. P1 is the normalization and P2 is the power.

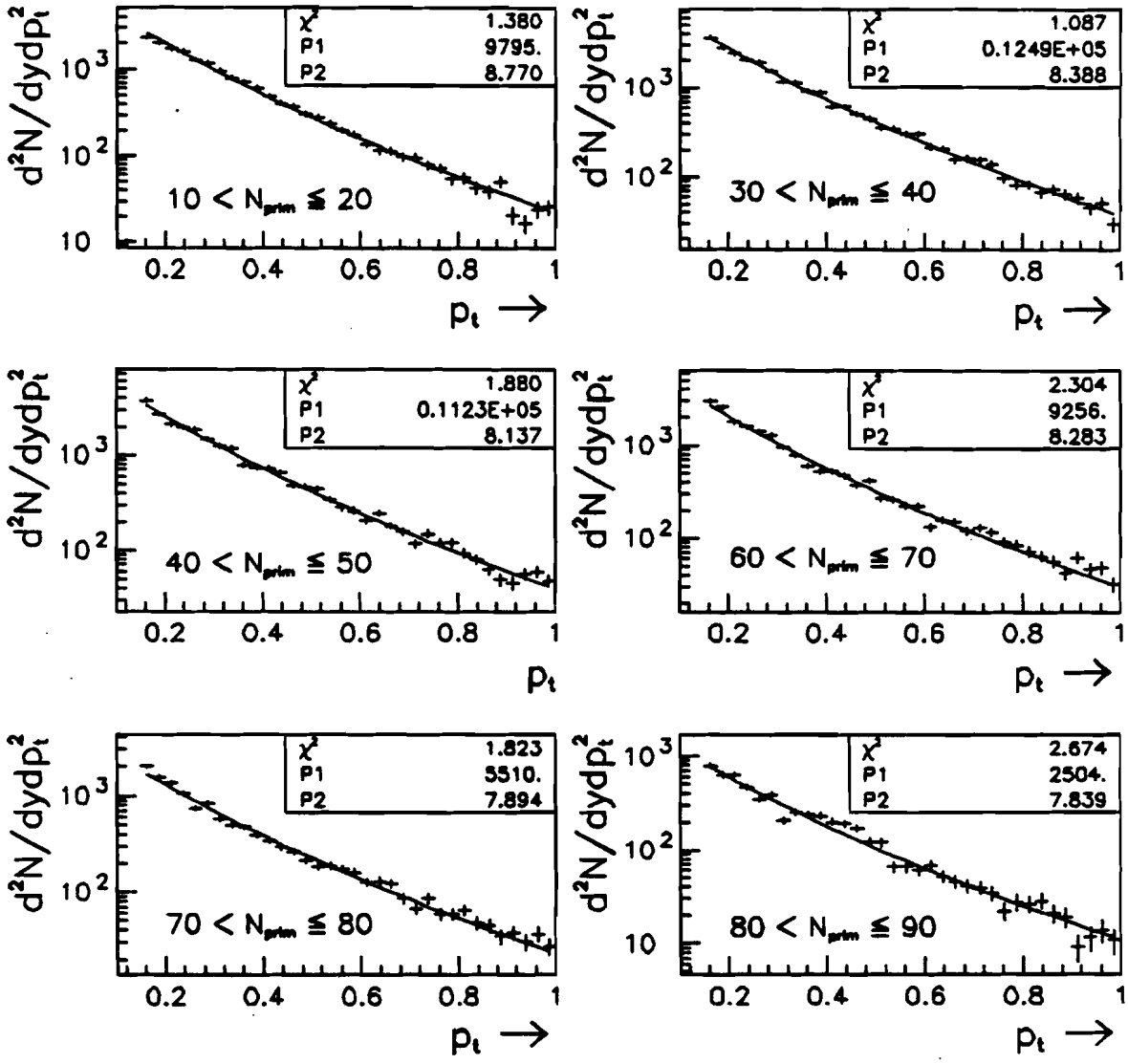

Figure 7.11 Inclusive π^- transverse momentum spectra binned by CTC primaries. P1 is the normalization and P2 is the power.

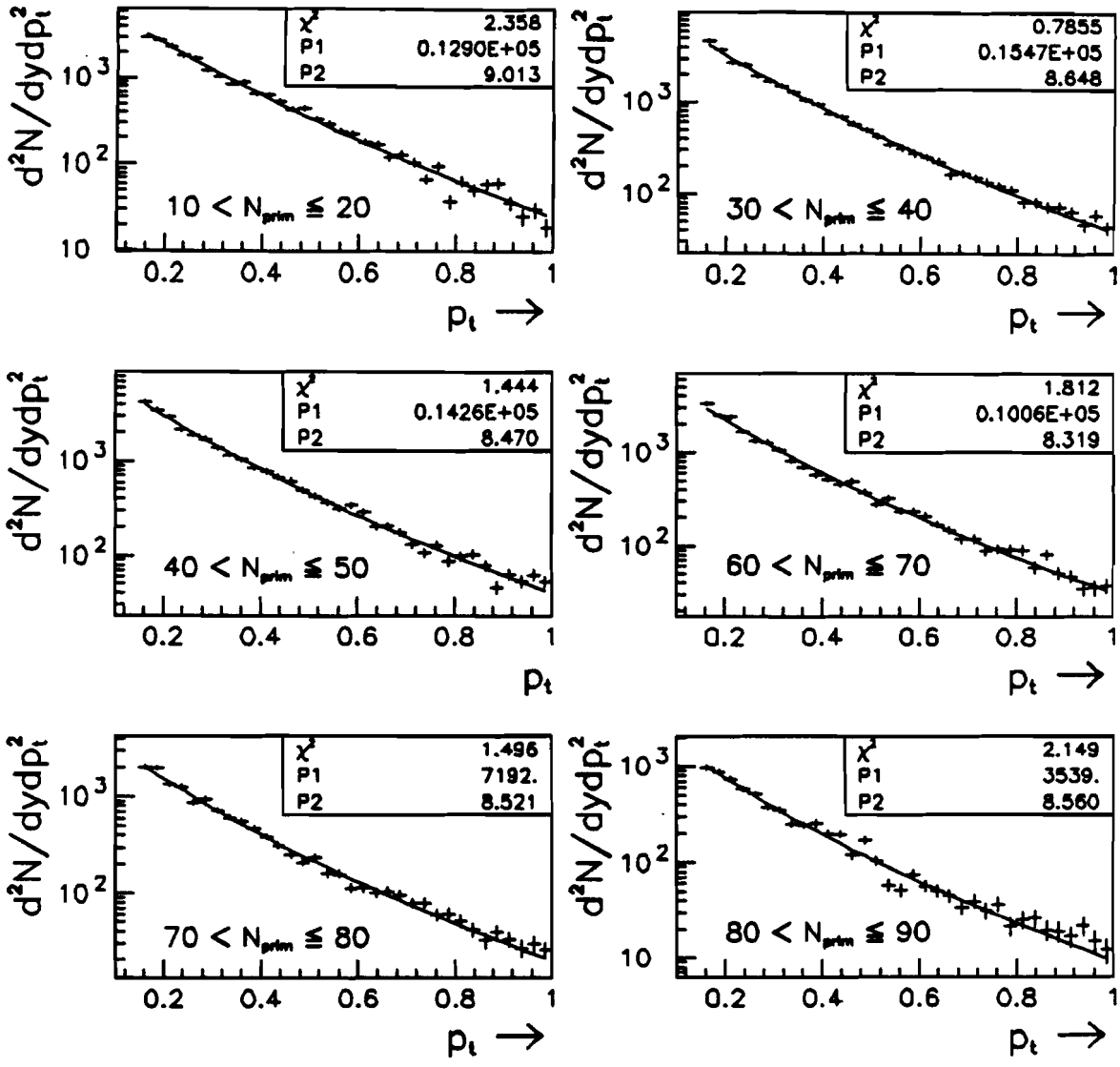

Figure 7.12 Inclusive π^+ transverse momentum spectra binned by CTC primaries. P1 is the normalization and P2 is the power.

7.2.4 Exponential Fits to Antiprotons

We found that the inclusive tranverse momentum spectra for the antiprotons binned in terms of CTC and hodoscope multiplicities could be well fit with an exponential function. The results of the fits are tabulated in Tables 7.6 and 7.7 for hodoscope and CTC multiplicities, respectively. Exponentials fit over the interval $0.4 \leq p_\perp \leq 1.5$ GeV/c for several hodoscope and CTC multiplicity binned $p_\perp$ distributions are plotted in Figures 7.13 and 7.14. Note that the entries for the slope, α, in Table 7.6 are not identical to the values listed in the inbedded upper boxes for the fits depicted in Fig. 7.13. This is a measure of the robustness of the fit. I 'randomly' varied the starting values of the normalization and the slope parameters of the exponential fit in the second case in order to check how sensitive the fit is to the initial conditions. As the reader can see, the slopes for the two cases agree to within 0.5%. We see that α decreases as N_c increases. This implies (see eqn. 7.4) that $\langle p_\perp \rangle$ increases with multiplicity. This is not an expected result.

Next, I calculated the average of the multiplicity binned $p_\perp$ spectra in the interval $0.4 \leq p_\perp \leq 1.5$ GeV/c *without* performing any exponential fitting. This provides an independent check of the relationship between $\langle p_\perp \rangle$ and N_c. The results are tabulated in Table 7.8. It is clear that $\langle p_\perp \rangle$ increases with N_c.

Table 7.6 Exponential fits to antiprotons. multiplicities measured by the hodoscope. Errors from MINUIT fit.

	Fit interval: $0.4 \leq p_\perp \leq 1.5$ GeV/c			Fit interval: $0.6 \leq p_\perp \leq 1.5$ GeV/c		
Multiplicity	α	$\langle p_\perp \rangle$	χ^2	α	$\langle p_\perp \rangle$	χ^2
$10 \leq N_h < 20$	−4.110	0.487 ± .073	2.6	–	–	–
$20 \leq N_h < 30$	−3.811	0.525 ± .033	1.8	−4.074	0.491 ± .083	1.3
$30 \leq N_h < 40$	−3.334	0.600 ± .026	1.9	−3.682	0.543 ± .081	1.1
$40 \leq N_h < 50$	−2.989	0.669 ± .030	1.9	−3.369	0.594 ± .015	1.2
$50 \leq N_h < 60$	−2.756	0.726 ± .030	1.2	−2.964	0.675 ± .100	0.9
$60 \leq N_h < 70$	−2.859	0.700 ± .027	1.6	−3.115	0.642 ± .010	1.3
$70 \leq N_h < 80$	−2.402	0.833 ± .038	2.8	−2.649	0.755 ± .023	1.3
$80 \leq N_h < 90$	−2.358	0.848 ± .037	1.9	−2.512	0.796 ± .022	1.4
$90 \leq N_h < 100$	−2.515	0.795 ± .031	1.8	−2.848	0.702 ± .019	1.0
$100 \leq N_h < 110$	−2.052	0.975 ± .045	1.9	−2.227	0.898 ± .154	1.5
$110 \leq N_h < 120$	−2.016	0.992 ± .054	1.7	−2.213	0.904 ± .178	1.0
$120 \leq N_h < 130$	−1.987	1.007 ± .056	3.0	−2.275	0.879 ± .195	2.2
$130 \leq N_h < 140$	−1.839	1.088 ± .119	1.8	−1.931	1.036 ± .405	1.4

Table 7.7 Exponential fits to antiprotons. Multiplicities measured by the CTC. Errors from MINUIT fit.

	Fit interval: $0.4 \leq p_\perp \leq 1.5$ GeV/c			Fit interval: $0.6 \leq p_\perp \leq 1.5$ GeV/c		
Multiplicity	α	$\langle p_\perp \rangle$	χ^2	α	$\langle p_\perp \rangle$	χ^2
$10 \leq N_{\text{prim}} < 20$	-3.135	$0.638 \pm .152$	2.2	-3.106	$0.644 \pm .296$	1.3
$20 \leq N_{\text{prim}} < 30$	-3.235	$0.618 \pm .080$	1.8	-3.352	$0.597 \pm .210$	1.4
$30 \leq N_{\text{prim}} < 40$	-2.616	$0.765 \pm .074$	2.8	-3.265	$0.613 \pm .208$	2.1
$40 \leq N_{\text{prim}} < 50$	-2.103	$0.951 \pm .083$	2.2	-2.900	$0.690 \pm .229$	1.3
$50 \leq N_{\text{prim}} < 60$	-2.688	$0.744 \pm .147$	1.8	-3.021	$0.662 \pm .266$	1.4
$60 \leq N_{\text{prim}} < 70$	-2.194	$0.914 \pm .191$	2.7	-2.472	$0.809 \pm .398$	2.0
$70 \leq N_{\text{prim}} < 80$	-2.095	$0.955 \pm .640$	2.2	-2.111	$0.947 \pm .676$	1.6

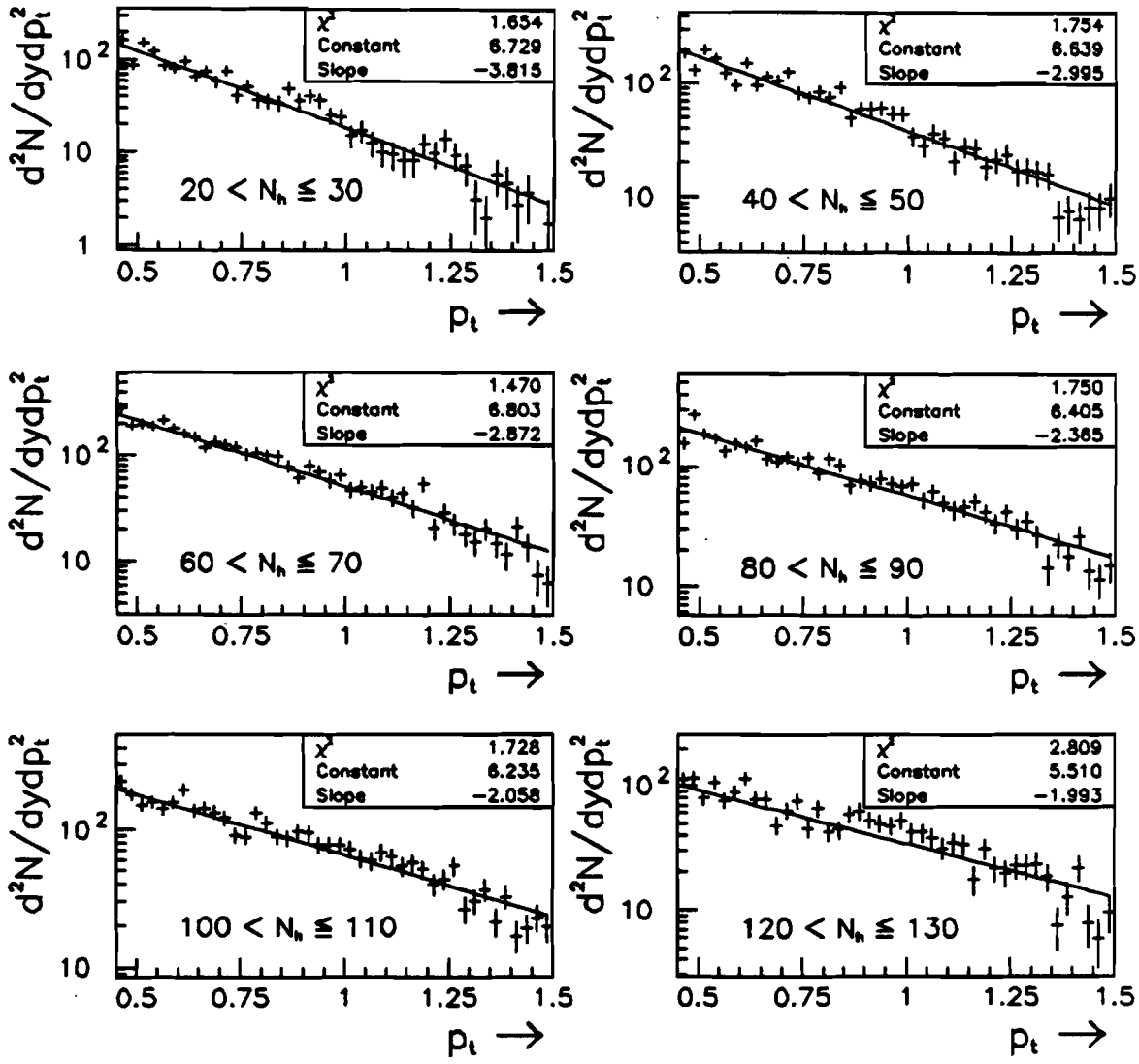

Figure 7.13 Inclusive $\bar{p}$ transverse momentum spectra binned by hodoscope hits.

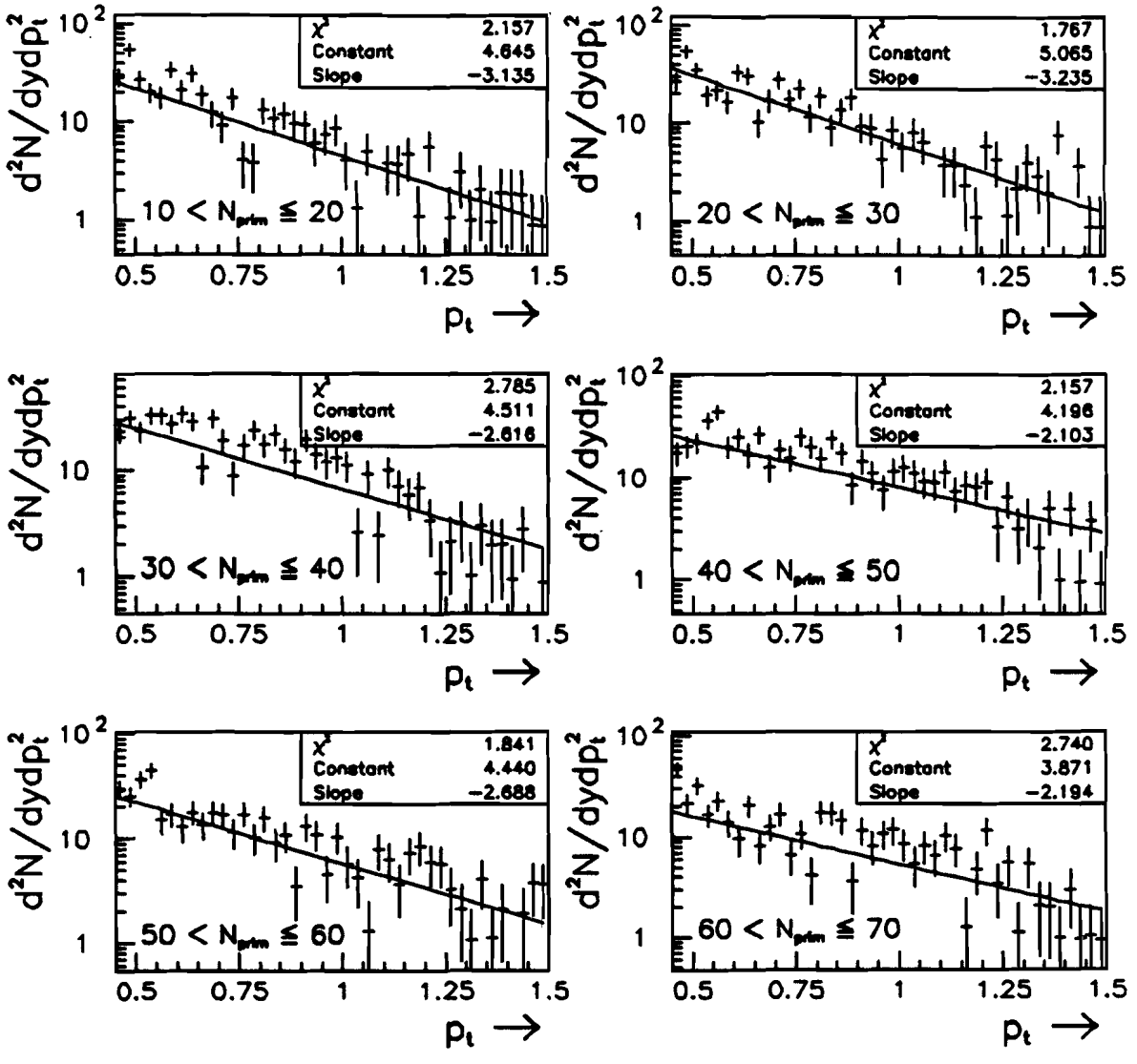

Figure 7.14 Inclusive $\bar{p}$ transverse momentum spectra binned by CTC primaries.

Table 7.8 Averages and rms errors for the multiplicity binned inclusive $p_\perp$ spectra for $\bar{p}$ ($0.4 \leq p_\perp \leq 1.5$ GeV/c). No fitting performed.

Hodoscope

Multiplicity	$\langle p_\perp \rangle$	rms
$20 \leq N_h < 30$	0.652	0.225
$30 \leq N_h < 40$	0.680	0.240
$40 \leq N_h < 50$	0.703	0.254
$50 \leq N_h < 60$	0.717	0.260
$60 \leq N_h < 70$	0.716	0.261
$70 \leq N_h < 80$	0.739	0.272
$80 \leq N_h < 90$	0.747	0.278
$90 \leq N_h < 100$	0.737	0.267
$100 \leq N_h < 110$	0.773	0.288
$110 \leq N_h < 120$	0.775	0.293
$120 \leq N_h < 130$	0.785	0.286
$130 \leq N_h < 140$	0.790	0.292

CTC

Multiplicity	$\langle p_\perp \rangle$	rms
$10 \leq N_{\text{prim}} < 20$	0.684	0.241
$20 \leq N_{\text{prim}} < 30$	0.689	0.249
$30 \leq N_{\text{prim}} < 40$	0.734	0.239
$40 \leq N_{\text{prim}} < 50$	0.781	0.269
$50 \leq N_{\text{prim}} < 60$	0.741	0.286
$60 \leq N_{\text{prim}} < 70$	0.762	0.278
$70 \leq N_{\text{prim}} < 80$	0.761	0.285
$80 \leq N_{\text{prim}} < 90$	0.789	0.302
$90 \leq N_{\text{prim}} < 100$	0.877	0.316

7.2.5 $\langle p_\perp \rangle$ vs $dN/d\eta$ for Pions and Antiprotons

We now tie in the chief components of our experiment—we correlate the sampled transverse momentum distribution to the centrally produced charged multiplicities. E-735 independently measures the charge multiplicity with the CTC and the 240 element hodoscope. The hodoscope spans 6.5 units in η and for the CTC, $\eta < 3.2$ units, where both detectors are centered at $\eta_o = 0$. The analysis for converting measured primaries and hodoscope hits to the true charged multiplicity within the fiducial η of the CTC and Hodoscope, respectively, is thoroughly documented in references [16] and [17]. The relationship between the measured multiplicity and the actual multiplicity are plotted Fig.'s 7.15 and 7.16. This conversion acts in opposite ways for these two detectors. The CTC tends to overestimate the primary charged multiplicity until saturation effects take over. It is difficult to separate secondaries originating from interactions in the beampipe from primaries created in the $\bar{p}p$ collision. As CTC multiplicities exceed 90 tracks, primaries cannot be readily distinguished from secondaries (see [17]). Because of the coarse granularity of the hodoscope counters, the multiplicities tend to be underestimated for $N_c > 70$. A counter cannot distinguish whether the hit was due to only one or several tracks.

To transform the raw multiplicities measured in either the hodoscope array or the CTC to the charged pseudorapidity density, we first convert the CTC primaries or hodoscope hits to N_c. Since the hodoscope array and the CTC span a $\Delta\eta$ of 6.5 and 3.2 units of pseudorapidity, respectively, we then divide this N_c by $\Delta\eta$ to obtain $dN_c/d\eta$.

The relationship between the acceptance corrected $\langle p_\perp \rangle$ (averaged between the limits 0 and ∞) and $dN_c/d\eta$ for pions and antiprotons are plotted in Fig.'s 7.17 and 7.18. The CTC and hodoscope events are completely independent.

In Tables 7.1 and 7.2, the ratio of the average transverse momentum of the π^+ and π^- for each of the CTC or hodoscope binned multiplicities may vary between 1 and 11% and does not appear to be related to increasing multiplicity. We see that

most of these ratios are within 6%. Since our statistical errors are negligible, I ascribe a systematic error of 3% to each data point in Fig. 7.17. We see that even with this small systematic error, the CTC and hodoscope data points agree remarkably well.

As for the antiprotons, I could not use its antiparticle for studying the systematics, since we cannot distinguish knockon protons from primordial protons in our spectrometer. In Tables 7.6 and 7.7, the results of exponential fits to two separate intervals is tabulated. The average transverse momentum for the two fits agree within errors. Since the MINUIT errors on the fit interval $0.4 \leq p_\perp \leq 1.5$ are smaller than for the interval $0.6 \leq p_\perp \leq 1.5$ and that we are including more data points in the former fit interval, I plot the extrapolated $\langle p_\perp \rangle$ obtained from this first fit as a function of $dN_c/d\eta$. The errors are from the MINUIT fit. Again the CTC and hodoscope data points agree within errors.

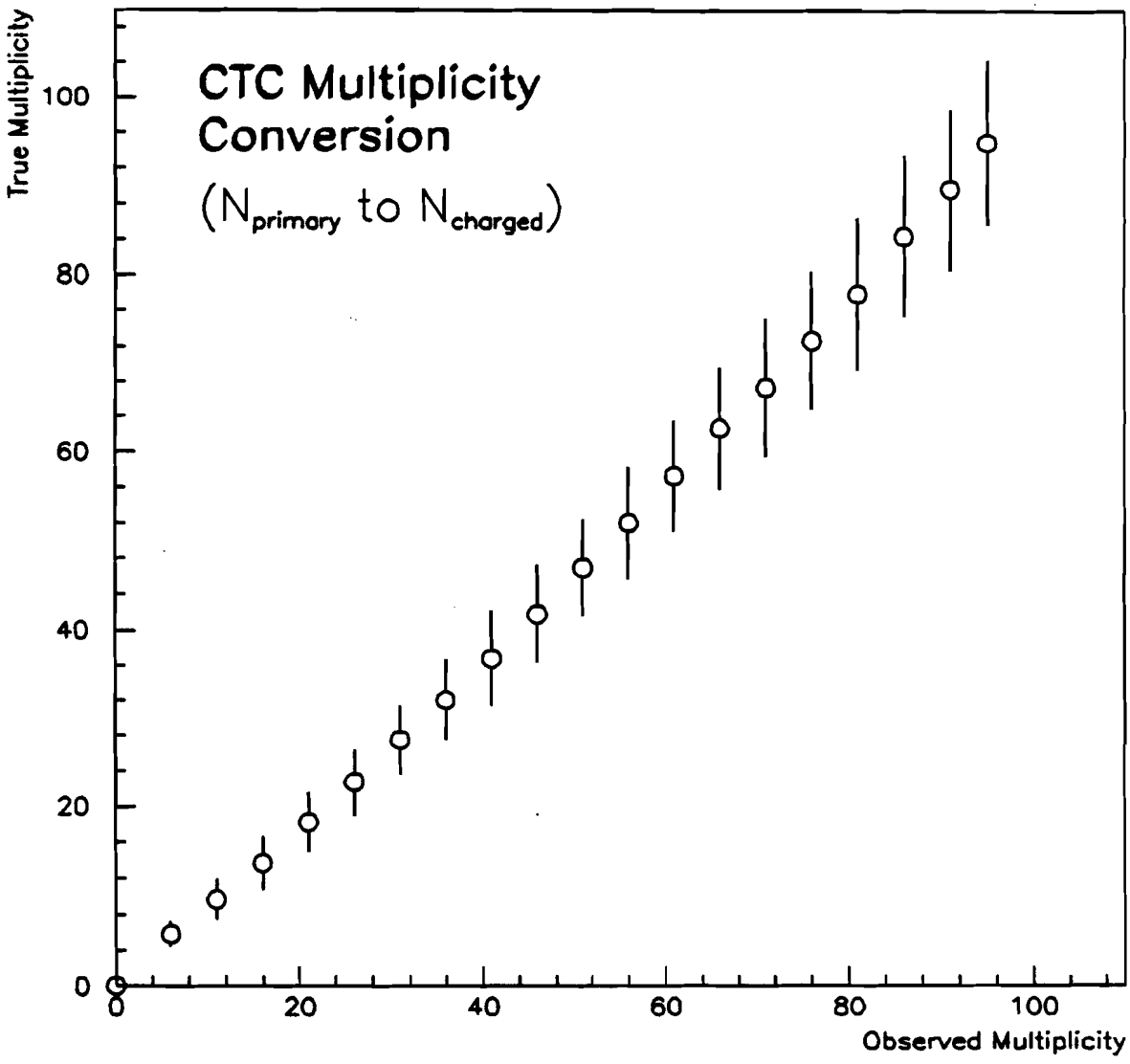

Figure 7.15 Relationship between CTC primaries and N_c for $-1.6 < \eta < +1.6$.

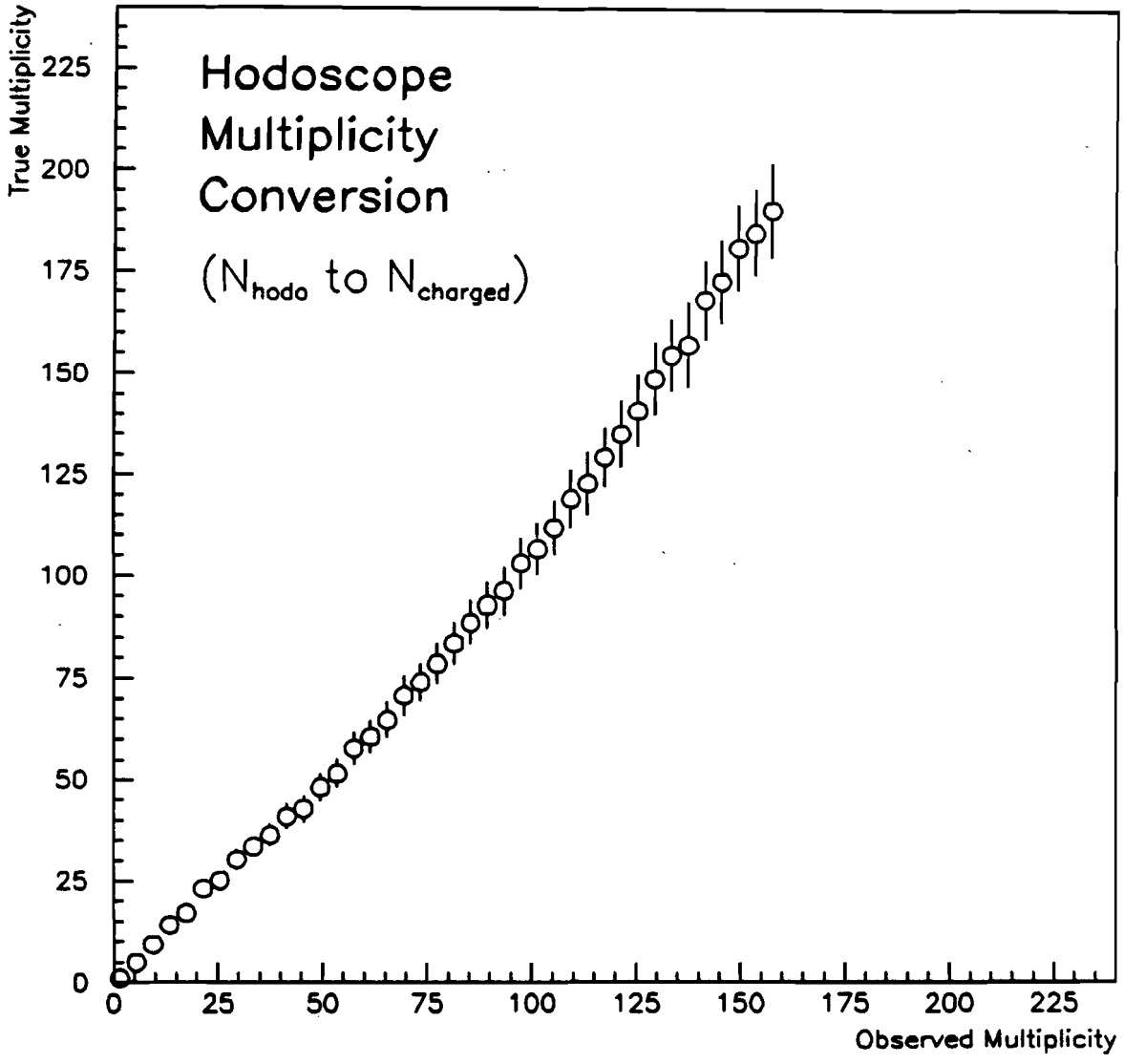

Figure 7.16 Relationship between hodoscope hits and N_c for $-3.2 < \eta < +3.2$.

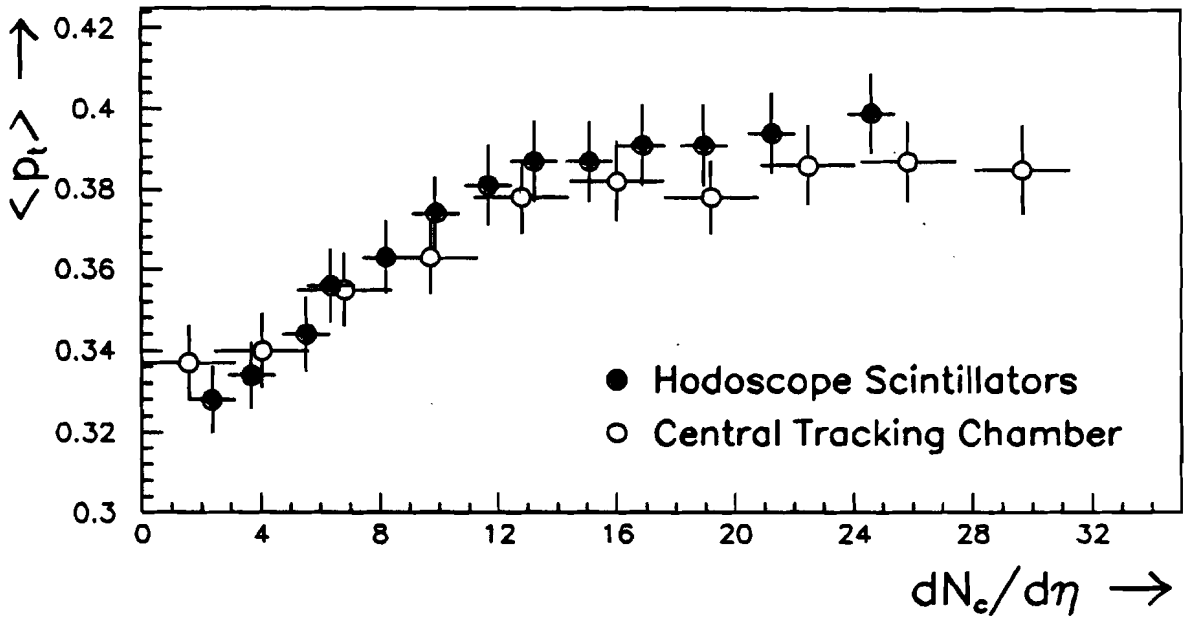

Figure 7.17 Relationship between $\langle p_\perp \rangle$ and $dN_c/d\eta$ for pions. The CTC and hodoscope data samples are independent. All errors are systematic.

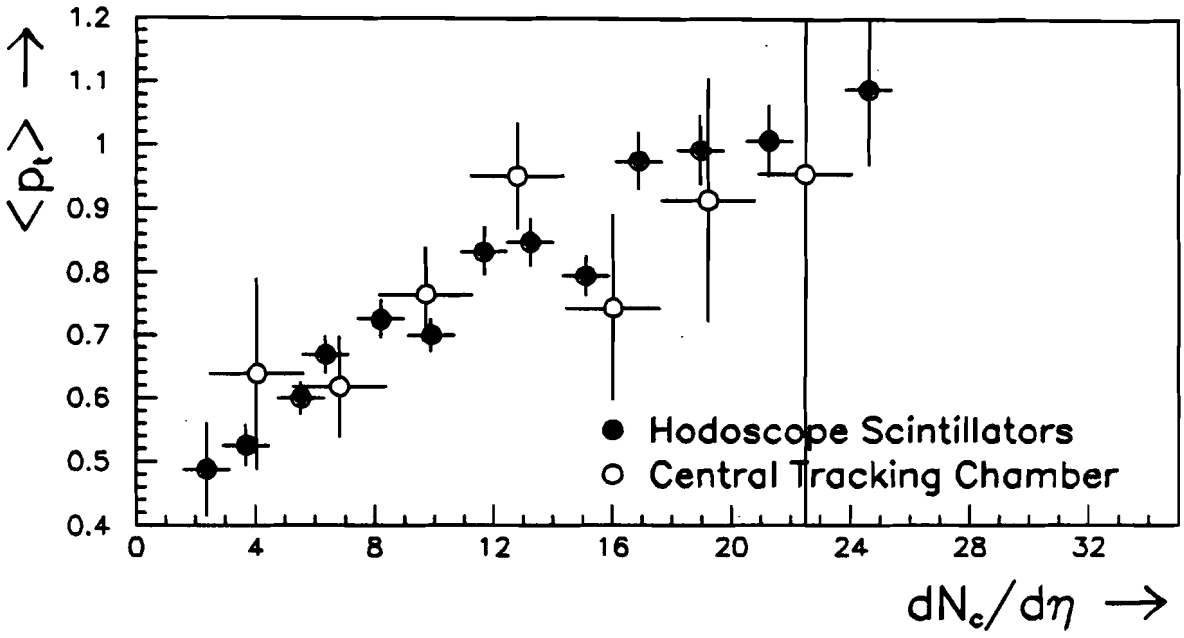

Figure 7.18 Relationship between $\langle p_\perp \rangle$ and $dN_c/d\eta$ for antiprotons. The CTC and hodoscope data samples are independent. Errors from MINUIT fit.

Table 7.9 Data sample broken down by energy. Each run represents roughly 10,000 events before cuts.

$\sqrt{s}$ [GeV]	Runs	[%]
1800	1550	92.76
1000	38	2.27
546	63	3.77
300	20	1.20

7.3 Average Transverse Momentum as a Function of Energy

In this section, we study the relationship between the average transverse momentum of pions emerging from $\bar{p}p$ collisions at four different center of mass energies. Although the bulk of our data was at 1800 GeV, we collected data at center of mass energies of 300, 546 and 1000 GeV. The percentage of data collected, broken down by $\sqrt{s}$, is listed in Table 7.9

We did not attempt to increase the statistics of the lower energy runs by relaxing event or track quality cuts — all cuts and acceptance corrections applied to the 1800 GeV data were applied to the spectrometer tracks from the lower energy runs. Moreover, this data has not been corrected to minimum bias — the trigger biases have not been scaled out.

Table 7.10 Average transverse momentum for π's integrated over all multiplicities at four different cms energies. 2trk denotes intersecting track condition. Errors are from MINUIT fit.

$\sqrt{s}$	$\langle p_\perp \rangle_{1trk}$	χ^2	$\langle p_\perp \rangle_{2trk}$	χ^2
300	0.350 ± 0.007	3.3	No Data	–
546	0.344 ± 0.003	1.0	0.358 ± 0.005	1.1
1000	0.353 ± 0.001	1.4	No Data	–
1800	0.375 ± 0.003	0.4	0.414 ± 0.003	0.2

Table 7.11 Average transverse momentum for $\bar{p}$'s for three different cms energies.

	Fit interval: $0.4 \leq p_\perp \leq 1.5$ GeV/c			Fit interval: $0.6 \leq p_\perp \leq 1.5$ GeV/c		
$\sqrt{s}$	α	$\langle p_\perp \rangle$	χ^2	α	$\langle p_\perp \rangle$	χ^2
546	-2.871	$.697 \pm .237$	3.2	-2.504	$.799 \pm .385$	1.8
1000	-3.026	$.661 \pm .046$	1.5	-3.266	$.612 \pm .158$	1.4
1800	-2.652	$.754 \pm .008$	2.6	-2.815	$.710 \pm .010$	2.0
$\overline{1800}$	-2.792	$.716 \pm .051$	1.4	-2.754	$.726 \pm .025$	1.3

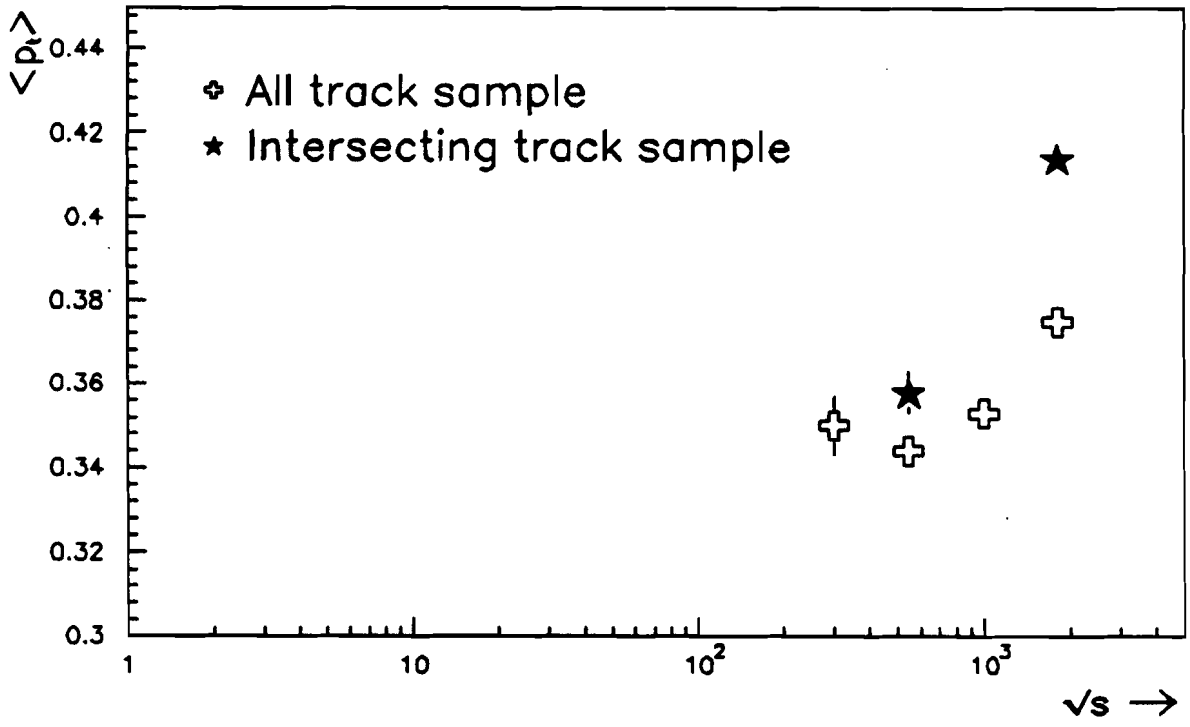

Figure 7.19 $\langle p_\perp \rangle$ [GeV/c] as a function of energy [GeV].

Table 7.12 $\langle p_\perp \rangle$ vs N_{hodo} for two energies. (dof = 34).

	$\sqrt{s} = 546$ GeV			$\sqrt{s} = 1000$ GeV		
Multiplicity	n	χ^2	$\langle p_\perp \rangle$	n	χ^2	$\langle p_\perp \rangle$
$10 \le N_h < 20$	8.626	4.1	$0.356 \pm .006$	9.549	3.3	$0.305 \pm .004$
$20 \le N_h < 30$	9.561	2.6	$0.305 \pm .008$	8.840	2.0	$0.343 \pm .008$
$30 \le N_h < 40$	8.808	1.3	$0.344 \pm .005$	8.808	1.5	$0.344 \pm .005$
$40 \le N_h < 50$	9.028	1.9	$0.332 \pm .004$	8.694	1.8	$0.351 \pm .003$
$50 \le N_h < 60$	8.803	2.0	$0.345 \pm .006$	8.568	1.1	$0.359 \pm .005$
$60 \le N_h < 70$	8.755	2.5	$0.348 \pm .006$	8.630	3.1	$0.355 \pm .005$
$70 \le N_h < 80$	8.733	3.6	$0.349 \pm .007$	8.666	3.1	$0.353 \pm .004$
$80 \le N_h < 90$	8.569	2.8	$0.359 \pm .010$	8.544	2.9	$0.361 \pm .007$

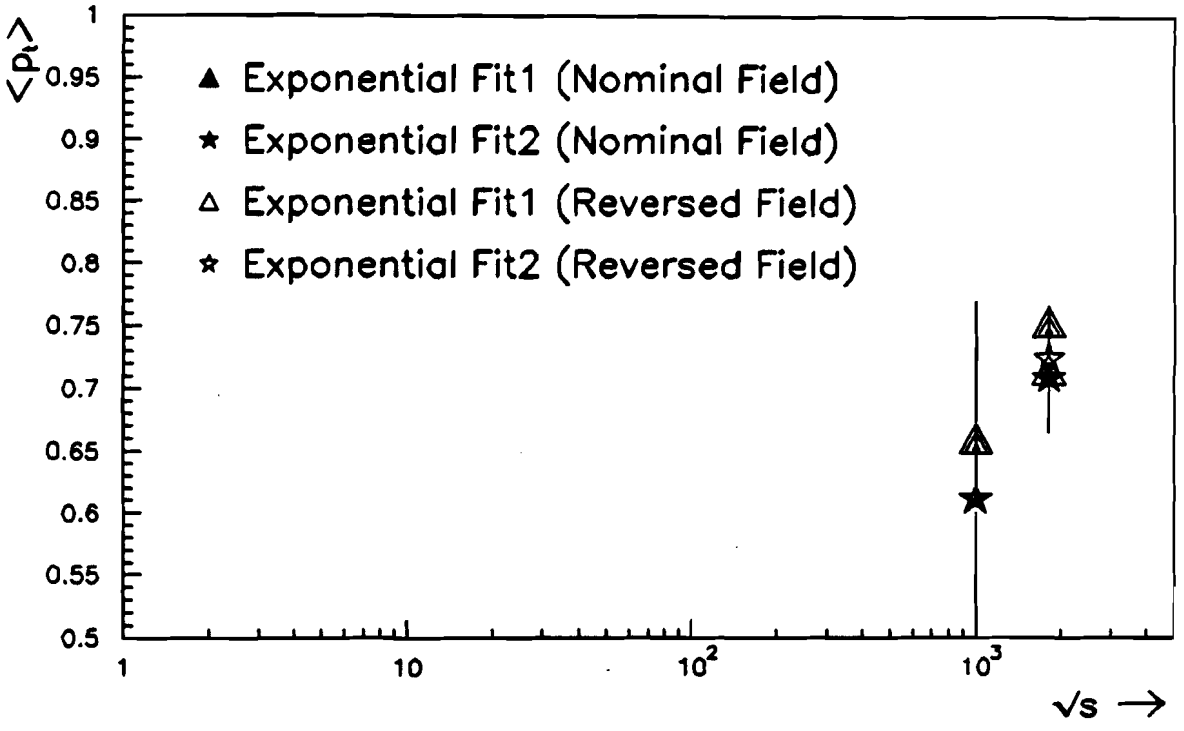

Figure 7.20 $\langle p_\perp \rangle$ [GeV/c] as a function of energy [GeV] for antiprotons.

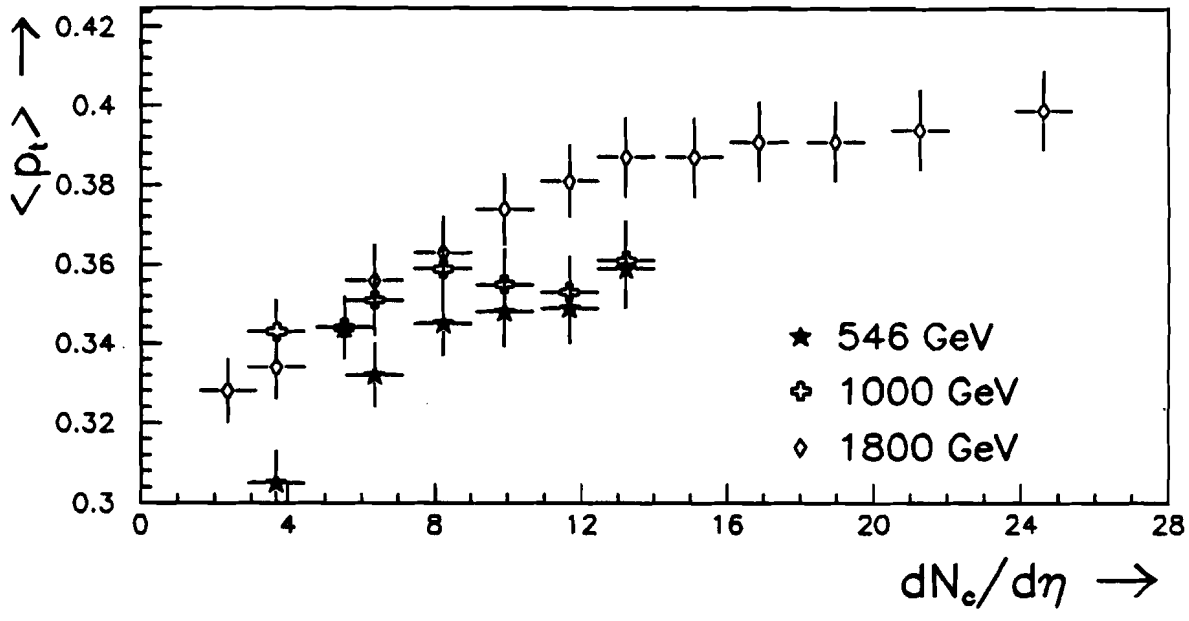

Figure 7.21 Relationship between the average transverse momentum and charged pseudorapidity density for three different energies. Errors are systematic. Hodoscope multiplicities only.

7.4 Comparison with 1987 Run

In this section, I compare my results of the $\langle p_\perp \rangle$ vs $dN/d\eta$ for pions and antiprotons (1988/89 run) with our published results from the 1987 run [8]. In the analysis of the 1987 data the $\langle p_\perp \rangle$ was calculated in the range $0 < p_\perp < 1.5$ GeV/c. In the above, all average transverse momenta were computed over the interval of 0 to ∞ (see eqn. 7.2 and eqn. 7.4). In order to compare the results of these analyses, $p_\perp$ must be averaged over the same interval.

For the antiprotons,

$$\frac{d^2N}{dydp_\perp^2} = A_o e^{-\alpha p_\perp} \tag{7.5}$$

which can be rewritten as

$$\frac{dN}{dy} = 2A_o e^{-\alpha p_\perp} p_\perp dp_\perp \tag{7.6}$$

Since particle production is constant in rapidity for the central region, we have:

$$N|_{p_\perp^i}^{p_\perp^f} = 2A_o' \int_{p_\perp^i}^{p_\perp^f} e^{-\alpha p_\perp} p_\perp dp_\perp \tag{7.7}$$

Setting $p_\perp^i$ to 0 gives (see also [35]):

$$N|_0^{p_\perp^f} = \frac{2A_o'}{\alpha^2}[1 - e^{-\alpha p_\perp^f}(1 + \alpha p_\perp^f)] \tag{7.8}$$

Applying the same logic, the total tranverse momentum integrated between the limits of $p_\perp = 0$ to $p_\perp = p_\perp^f$ becomes:

$$P_\perp|_0^{p_\perp^f} = \frac{4A_o'}{\alpha^3}[1 - e^{-\alpha p_\perp^f}(1 + \alpha p_\perp^f + \frac{(\alpha p_\perp^f)^2}{2})] \tag{7.9}$$

The average transverse momentum, then, for $0 < p_\perp < p_\perp^f$ reduces to:

$$\langle p_\perp \rangle|_0^{p_\perp^f} = \frac{P_\perp|_0^{p_\perp^f}}{N|_0^{p_\perp^f}} \tag{7.10}$$

In Table 7.13, the multiplicity binned $\langle p_\perp \rangle$ are tabulated for the 1987 and 1988/89 $\bar{p}$ data. The transverse momentum is averaged over the interval $0 < p_\perp < 1.5$ GeV/c. In Fig. 7.22, we plot the $\langle p_\perp \rangle$ versus $dN/d\eta$ for the 1987 and 1988/89 $\bar{p}$ data. The

α's used for the 1988/89 data are from the exponentials fitted over the range $0.4 \leq p_\perp \leq 1.5$ GeV/c. Note that there are no CTC data for the first run (see Tables 7.6 and 7.7). Moreover, all data sets are completely independent.

In the analysis of the 1987 pion data, a technique known as the 'counting method' was employed [35]. An exponential was fit in the limited interval of $0.15 \leq p_\perp < 0.4$ GeV/c. The extracted slope of the fit, α, was then used to determine the number of contents, $N|_0^{0.15}$, and the sum of the transverse momenta, $P_\perp|_0^{0.15}$, for $0 < p_\perp < 0.15$ GeV/c. These quantities were then incorporated into the definition for the average transverse momentum over the interval of $p_\perp = 0$ to $p_\perp = 1.5$, viz:

$$\langle p_\perp \rangle = \frac{P_\perp|_0^{0.15} + \sum_{p_\perp=0.15}^{p_\perp=1.50} \varepsilon(p_\perp) \cdot p_\perp}{N|_0^{0.15} + \sum_{p_\perp=0.15}^{p_\perp=1.50} \varepsilon(p_\perp)} \tag{7.11}$$

where $\varepsilon(p_\perp)$ is the acceptance efficiency.

In his thesis [35], Arthur McManus finds that calculating $\langle p_\perp \rangle$ for pions by means of the 'counting method' for $0 < p_\perp < 1.5$ gives nearly identical results to that of the average transverse momentum determined by the power law fit over the interval (0,∞) (see eqn. 7.2). In Fig. 7.23, the $\langle p_\perp \rangle$ versus $dN/d\eta$ for the 1987 and 1988/89 pion data are plotted. The average $p_\perp$ for 1987 data was determined by means of the 'counting method'. The 1988/89 $\langle p_\perp \rangle$, on the other hand, is averaged from 0 to ∞. The agreement for all three data sets, i.e. the CTC and hodoscope data from 1988/89 run and the 1987 hodoscope data, is within errors.

Table 7.13 Comparison of 1987 and 1988/89 data for the antiprotons. $p_\perp$ is averaged over the interval $0 < p_\perp < 1.5$ GeV/c.

Hodoscope			CTC	
Multiplicity	$\langle p_\perp \rangle_{87}$	$\langle p_\perp \rangle_{88/89}$	*Multiplicity*	$\langle p_\perp \rangle_{88/89}$
$10 \leq N_h < 10$	0.515 ± 0.030	0.467 ± 0.070	$0 \leq N_{\rm prim} < 10$	–
$20 \leq N_h < 30$	0.520 ± 0.030	0.496 ± 0.031	$10 \leq N_{\rm prim} < 20$	0.570 ± 0.136
$30 \leq N_h < 40$	0.560 ± 0.030	0.547 ± 0.024	$20 \leq N_{\rm prim} < 30$	0.559 ± 0.072
$40 \leq N_h < 50$	0.593 ± 0.033	0.588 ± 0.026	$30 \leq N_{\rm prim} < 40$	0.636 ± 0.062
$50 \leq N_h < 60$	0.623 ± 0.033	0.617 ± 0.026	$40 \leq N_{\rm prim} < 50$	0.706 ± 0.062
$60 \leq N_h < 70$	0.627 ± 0.033	0.604 ± 0.023	$50 \leq N_{\rm prim} < 60$	0.626 ± 0.124
$70 \leq N_h < 80$	0.628 ± 0.033	0.664 ± 0.030	$60 \leq N_{\rm prim} < 70$	0.693 ± 0.145
$80 \leq N_h < 90$	0.648 ± 0.040	0.670 ± 0.029	$70 \leq N_{\rm prim} < 80$	0.707 ± 0.474
$90 \leq N_h < 100$	0.724 ± 0.050	0.649 ± 0.025	$80 \leq N_{\rm prim} < 90$	–
$100 \leq N_h < 110$	0.744 ± 0.070	0.713 ± 0.033	$90 \leq N_{\rm prim} < 100$	–
$110 \leq N_h < 120$	0.791 ± 0.081	0.718 ± 0.039		
$120 \leq N_h < 130$	0.849 ± 0.110	0.722 ± 0.040		
$130 \leq N_h < 140$	–	0.743 ± 0.081		

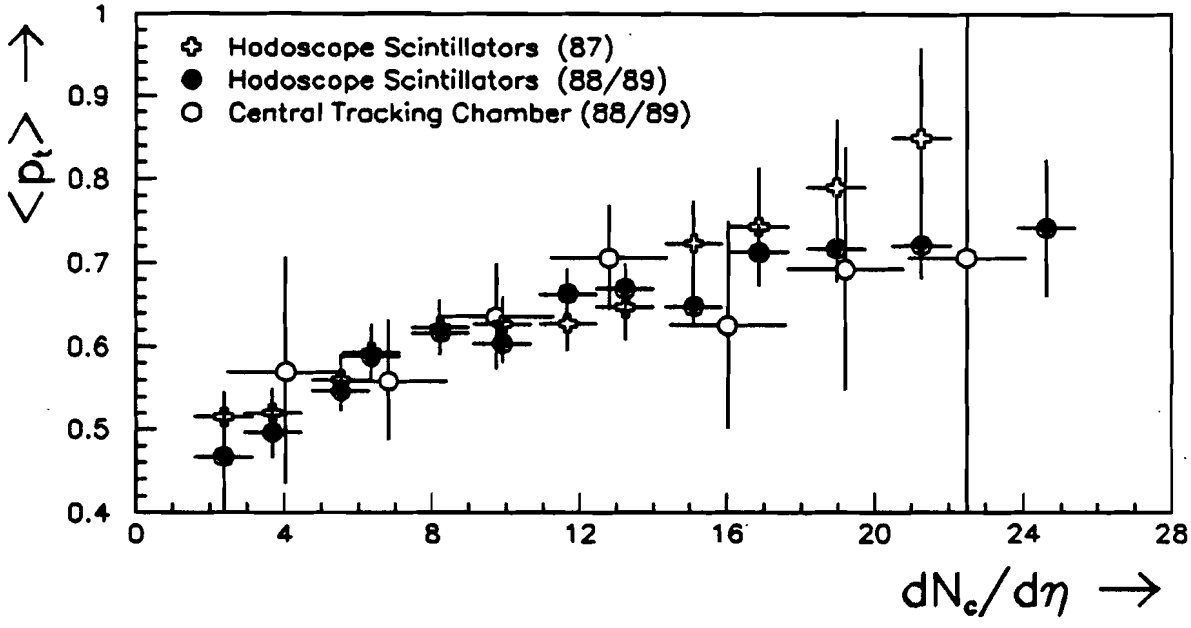

Figure 7.22 Relationship between the average transverse momentum and charged pseudorapidity density for three independent $\bar{p}$ data sets. $p_\perp$ is averaged between 0 and 1.5 GeV/c.

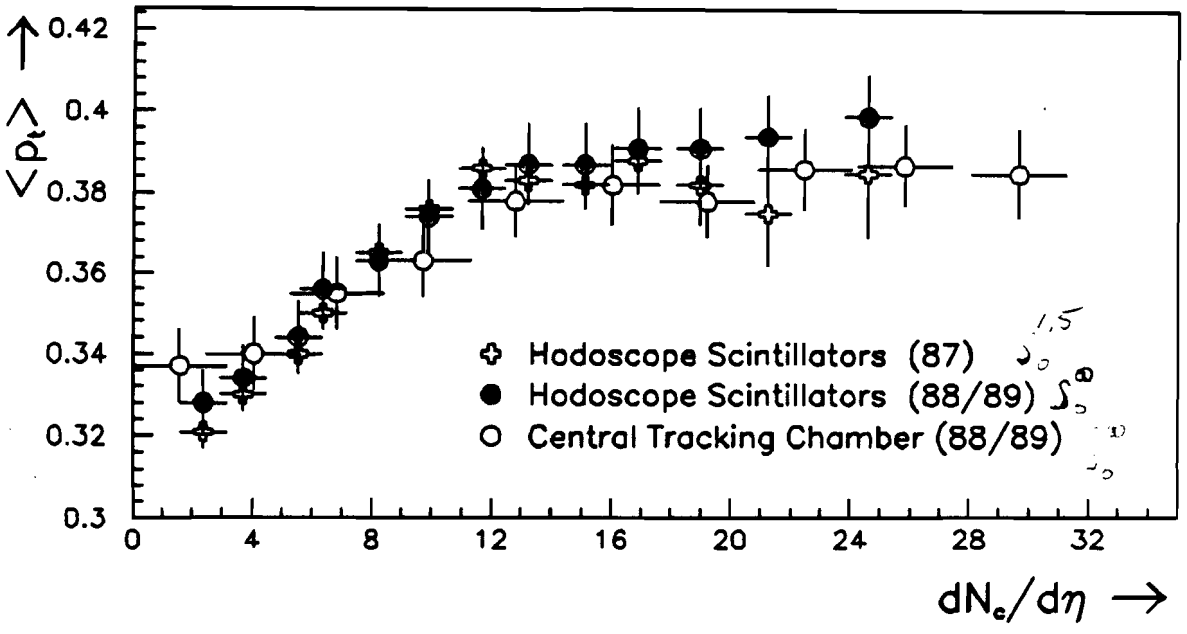

Figure 7.23 Relationship between the average transverse momentum and charged pseudorapidity density for three independent π data sets. $p_\perp$ is averaged between 0 and 1.5 GeV/c.

8. CONCLUSION

8.1 Summary of Results

In this thesis, we studied the relationship between the mean transverse momentum and the pseudorapidity density for π's and $\bar{p}$ at Tevatron energies.

We found:

- $\sqrt{s} = 1.8$ TeV
  - $\underline{\pi}$: The $\langle p_\perp \rangle$ rises with $dN/d\eta$ up to $dN/d\eta \simeq 12$. Thereafter $\langle p_\perp \rangle$ is fairly flat with $dN/d\eta$.
  - $\underline{\bar{p}}$: The $\langle p_\perp \rangle$ rises continuously with $dN/d\eta$; it does not turn over.
- $\sqrt{s} = 546$, 1000 and 1800 GeV for pions
  - The slope of the mean transverse momentum flattens at around a $dN/d\eta$ of around 8 charged particles per unit pseudorapidity for $\sqrt{s} = 546$ and 1000 GeV. The turn over for $\sqrt{s} = 1800$ GeV, however, appears at $dN/d\eta \simeq 12$. See Fig. 7.21.
- $\langle p_\perp \rangle$ as a function of $\sqrt{s}$ [1]
  - The average transverse momentum for both pions and antiprotons increases with center of mass energy. See Fig.'s 7.19 and 7.19

[1] I did not correct the events to correspond to minimum bias. This may alter the absolute value of $\langle p_\perp \rangle$ by a few percent.

8.2 Discussion

From the Bjorken formula (cf. eqn 1.1):

$$\epsilon = \frac{3}{2}\frac{dN_c}{d\eta}\frac{(\langle p_\perp \rangle^2 + m_\pi^2)^{1/2}}{\tau_o \pi r_o^2}$$

We have observed up to 30 particles per unit pseudorapidity. Assuming an interaction time and fireball radius of 1 fm and inserting $\langle p_\perp \rangle = 0.4$ GeV/c into the relationship above, we find the energy density, ϵ, to exceed 6 GeV/fm^3. This energy density is well into the range predicted by QCD studies for the onset of the plasma transition [13].

Other models have been proposed to explain a second rise. In particular, in the geometrical branching model for minijet production, R. C. Hwa and X. N. Wang argue that the second rise for the all charge spectra is governed by jet production and fragmentation [57], [58].

We see no evidence of a second rise in the relationship between the mean transverse momentum and the pseudorapidity density for neither the pions nor the antiprotons. We used the PYTHIA event generator to model the particle production. PYTHIA incorporates minijet phenomenology and predicts a flattening of the pions at a full phase space N_c of around 100 particles which corresponds to $dN/dy \simeq 10$ (see Fig. 6.3). Our data is in general agreement with this prediction (see Fig.'s 7.17 and 7.23). PYTHIA, however, anticipates a flattening for the antiproton spectrum as well (see Fig. 6.5). This prediction is not borne out by our results (see Fig.'s 7.18 and 7.22).

Resonance decays may drive the flattening of the pion $p_\perp$ spectra [59]. Since we cannot distinguish primordial pions from the decay pions from resonances, this interpretation may expain our results. Furthermore, PYTHIA predicts that 80% of the pions arise from resonance decays [60]. The continuous rise in the mean transverse momentum of the antiprotons for increasing pseudorapidity density cannot easily be explained by either the minijet or quark gluon plasma picture. Since jets fragment primarily into pions, the continuous rise in the antiproton average transverse momentum with multiplicity does not mesh with the minijet model.

Recent results from lattice gauge calculations [4] suggest that the deconfinement is of first order. If this is so, the second rise will therefore occur at energy densities exceeding 6 GeV/fm^3. It is not clear, however, how our results on the antiproton $p_\perp$ spectra fit within the quark gluon plasma model.

We await the arrival of the Relativistic Heavy Ion Collider to further probe hot hadronic matter and appeal to the high energy physics theory community to interpret these results.

BIBLIOGRAPHY

BIBLIOGRAPHY

[1] J. C. Collins and M. J. Perry, Phys. Rev. Lett. **34** (1975) 1353

[2] F. Turkot *et al.*, *7th Topical Workshop on Proton-Antiproton Collider Physics*, World Scientific, Ed. R. Raja, A. Tollestrup and J. Yoh, (1989) 157

[3] J. D. Bjorken, Phys. Rev. **D27** (1983) 138.

[4] F. Karsch, *Quark-Gluon Plasma*, World Scientific, Ed. R. C. Hwa (1990) 61

[5] L. McLerran, *Proc. of the* XXIII *Int'l Conf. on H.E.P.*, Vol. 1 (1986) 209 %

[6] G. Arnison *et al.* Phys. Lett. **118B** (1982) 167

[7] T. Alexopoulos *et al.*, Phys. Rev. Lett. **60** (1988) 1622

[8] T. Alexopoulos *et al.*, Phys. Rev. Lett. **64** (1990) 991

[9] A. V. Tollestrup, "Kinematical Relationship between dN/dy, $dN/d\eta$ and p_t Cut-off", CDF memo CDF/ANAL/MIN_BIAS/PUBLIC/584, October 1987

[10] L. van Hove, Phys. Lett. **118B**, (1982) 138;

[11] L. D. Landau Izk. Akad. Nauk SSSR **17** (1953) 51; *Collected Papers*, ed. D. Ter Haar (Pergamon, Oxford) 1965 (English translation)

[12] J.-P. Blaizot and J.-Y, Ollitrault, *Quark-Gluon Plasma*, World Scientific, Ed. R. C. Hwa (1990) 393

[13] L. D. McLerran and B. Svetitsky, Phys. Lett. **98B**, (1981) 195;
J. Kuti, J. Polonyi and K. Szlachanyi, Phys. Lett. **98B** (1981) 199;
J. Kogut *et al.*, Phys. Rev. Lett. **51** (1983) 869.

[14] P. Cole for the E–735 Collaboration. *Fourth Blois Elastic and Diffractive Scattering Conference*, to be published in Nucl. Phys. B (1992)

[15] T. Alexopoulos, *A Measurement of the Bose-Einstein Correlation for Two Pions in the Proton-Antiproton Collisions at the Center of Mass Energy 1.8 TeV*, University of Wisconsin-Madison, Ph.D. Dissertation, 1991

[16] C. H. Wang, *Multiplicity Distributions from $\bar{p}p$ Collisions at 1.8 TeV Center of Mass Energy*, Iowa State University, Ph.D. Dissertation, 1991.

[17] C. Allen, *Multiplicity and Pseudorapidity Distributions at $\sqrt{s} = 1.8$ TeV*, Purdue University, Ph.D. Dissertation, 1991.

[18] T. Alexopoulos, *et al.*, "Hyperon Production from Proton-Antiproton Collisions at $\sqrt{s} = 1.8$ TeV", (to be published)

[19] T. Alexopoulos, *et al.*, "Mass-Identified Particle Yields in Antiproton-Proton Collisions at $\sqrt{s} = 1.8$ TeV" (to be published)

[20] S. D. Holmes *A Practical Guide to Modern High Energy Particle Accelerators* Fermilab Publication Fermilab-Conf-87/160, October 1987.

[21] Design Report: Tevatron I Project. Fermi National Accelerator Laboratory. September 1984.

[22] C. Hojvat *et al.*, IEEE **NS26** (1979) 3149

[23] D. A. Edwards and M. J. Syphers, *An Introduction to the Physics of Particle Accelerators*, AIP Conference Proceedings **184** (1988) 2

[24] H. J. Moe and E. J. Vallario, "Operational Health Physics Training", DOE document ANL-88-26, September 1988

[25] P. Cole, *TLD's at the CØ Interaction Zone*, August 1989.

[26] I would like to acknowledge T. Carter's assistance in this project.

[27] B. Howell *et al.*, Nucl. Instr. and Meth. **A269** (1988) 121.

[28] F. Sauli *Principles of Operation of Multiwire Proportional and Drift Chambers* CERN Publication CERN 77-09, May 1977;
W. R. Leo, *Techniques for Nuclear and Particle Physics Experiments* Springer-Verlag 1987;
R. C. Fernow, *Introduction to Experimental Particle Physics*, Cambridge University Press (1986);
K. Kleinknecht *Detectors for Particle Radiation*, Cambridge University Press (1986)

[29] N. Morgan "Central Tracking Chamber Drift Velocity", E–735 memo, November 1988.

[30] T. Jensen and H. Kagan, private communications.

[31] G. Mildner, *Messungen an 100 MHz-Flash-Analog/ Digital-Konverter*, Ph.D. dissertation, Physikalisches Instut der Univerisät Heidelberg HD-PY, August 1986

[32] D. Schaile, O. Schaile and J. Schwartz, Nucl. Instr. and Meth. **A242** (1982) 247

[33] This FADC system is marketed in the USA by Lecroy.

[34] T. Alexopoulos, *et al.*,"A One Meter Long Low-mass Mini Drift Vertex Chamber Used at the Tevatron", to be published in Nucl. Instr. and Meth.

[35] A. McManus, *Inclusive Charged Particle Production in $p-\bar{p}$ Collisions at $\sqrt{s}$ = 1.8 TeV*, University of Notre Dame, Ph.D. Dissertation, 1989

[36] T. McMahon *Phase Transition, Thermodynamics and Transverse Momentum Spectra of Mass Identified Hadrons in 1.8 TeV Center of Mass Proton-Antiproton Collisions*, Purdue University, Ph.D. Dissertation, 1989

[37] ZIPTRACK Manual, A. Ito, *et al.*, (Fermilab) Fermilab-TM-1200, July 1983

[38] D. Wesson, Λ^0 *and* $\bar{\Lambda}^0$ *Production in $p\bar{p}$ Collisions at $\sqrt{s}$ = 1.8 TeV*, Duke University, Ph.D. Dissertation, 1990

[39] S. H. Oh *et al.*, Nucl. Instr. and Meth. **A303** (1991) 277

[40] E. W. Anderson, *et al.*, Nucl. Instr. and Meth., **A295** (1990) 86

[41] C. Allen *et al.*, Nucl. Instr. and Meth., **A294** (1990) 108

[42] S. Banerjee *et al.*, Nucl. Instr. and Meth., **A269** (1988) 121

[43] C. Hojvat *et al.*, "E–735 Trigger Processor" (to be published)

[44] Seog Oh, Electronic mail message to E–735 collaboration, January 1989

[45] "Runga-Kutta Tracking through a Magnetic Field using Nystroem Algorithm", National Bureau of Standards, Proc. 25.5.20

[46] Seog Oh developed the spectrometer tracking code used in this thesis.

[47] T. Carter, *Photon Production from $\bar{p}p$ Collisions at $\sqrt{s}$ = 1.8 TeV*, Duke University, Ph.D. Dissertation, 1990.

[48] Yu. A. Yatsunenko, Nucl. Instr. and Meth. **A287** (1990) 422

[49] R. Brun, O. Couet, C. Vandoni and P. Zanarini, PAW – *Physics Analysis Workstation*, CERN Program Library Entry Q121, Version 1.07 October 1989

[50] H-U. Bengtson and T. Sjöstrand, *A Manual to the Lund Monte Carlo for Hadronic Processes* PYTHIA *version 5.4*, July 1990, unpublished;
H-U. Bengtson and T. Sjöstrand, Comp. Phys. Comm. **46** (1987) 43;
T. Sjöstrand, Comp. Phys. Comm. **39** (1987) 347;
T. Sjöstrand and M. van Zijl, Phys. Rev **D36** (1987) 2017

[51] G. J. Alner *et al.*, Nuclear Physics **B291** (1987) 445

[52] R. Brun *et al.*, CERN Report DD/EE/84-1 "GEANT3 User's Guide", September 1987.

[53] Allen, Choi, Gilkes and Hirsch "A Study of the hit patterns in $p\bar{p}$ and endcap counters: data and MC comparison", E-735 Memo, November 1989

[54] Particle Properties Data Booklet, (1990) 149

[55] W. H. Press, B. P. Flannery, S. A. Teukolsky and W. T. Vetterling, Numerical Recipes — The Art of Scientific Computing, Cambridge University Press (1986)

[56] I am indebted to Silhacène Aïd for suggesting this tack.

[57] X. N. Wang and R. C. Hwa, Phys. Rev. D **39** (1989) 187

[58] R. C. Hwa and X. N. Wang, Phys Lett. **248B** (1990) 447

[59] J. Sollfrank, P. Koch and U. Heinz, Phys. Lett. **252B** (1990) 256

[60] John Jennings, private communication.

[61] N. A. Amos, *et al.*, Phys. Lett. **243B** (1990) 158

[62] L. Gutay, "A Data Rate Estimate of Charged Multiplicities for E–735" E–735 report (unpublished) 1985

[63] P. Cole, "Using the CTC for Determining the Pseudorapidity of a Charged Particle", E–735 memo (unpublished) January 1990

[64] N. Morgan, E–735 memo (unpublished) October 1989

[65] P. Bevington, *Data Reduction and Error Analysis for the Physical Sciences*, New York, McGraw-Hill (1969)

[66] R.-D. Heuer "Experience with the Jet Chamber of the JADE Experiment" (unpublished)

[67] A. Wagoner, "Operational Experience with the Jet Chamber of JADE ", talk given at FNAL, July 1983. (Copy of the transparencies were provided by Frank Turkot)

[68] N. Morgan, "CTC z correction", E–735 memo (unpublished) October 1989

[69] I wish to acknowledge Clark Lindsey for coming up with this idea.

APPENDICES

Appendix A Data Rate and Double Vertices

The Tevatron Collider accelerates six bunches of protons in one direction and an equal number of bunches of antiprotons in the opposite direction, at a center of mass energy of $\sqrt{s} = 1.8$ TeV. From the following expression we can estimate the expected luminosity per crossing, ℓ_0, at the CØ interaction region:

$$6f\ell_0 = \mathcal{L}\frac{\beta_0}{\beta} \tag{A.1}$$

where $\mathcal{L}$ = the luminosity at BØ and is measured in units of $[\mathrm{cm}^{-2}\cdot\mathrm{sec}^{-1}]$

β = beam β function at CØ, and is $\sim 100\beta_0$

f = 4.77×10^4 Hz, the frequency of bunch crossing at CØ

and the factor 6 takes the six bunches into account.

ℓ_0 can then be written as:

$$\ell_0 = \mathcal{L}\frac{1}{6f}\cdot\frac{1}{100} \tag{A.2}$$

A proton colliding into an antiproton will scatter elastically, inelastically or diffractively. In a diffractive event, either one of the nucleons or both will remain intact, i.e. will not give rise to a spray of particles. The former case is known as a single diffractive event and the latter is called a double diffractive event. The E-735 trigger cannot distinguish double diffractive events from inelastic $\bar{\mathrm{p}}\mathrm{p}$ collisions. The total cross-section, σ_t, is a measure of the overall probability of two particles interacting as they pass by one another and can be written as:

$$\sigma_t = \sigma_{\mathrm{nsd}} + \sigma_{\mathrm{sd}} \tag{A.3}$$

where σ_{nsd} and σ_{sd} are the non-single diffractive and single diffractive cross-sections, respectively. The total cross-section and total single diffractive cross-section were measured by the FNAL collider experiment E–710 [61]. They obtained the values of 11.7 ± 2.3 mb for σ_{sd} and 72.1 ± 3.3 for the total cross-section. Inserting these values

into the above equation, we find that the non-single diffractive cross-section is around 60 mb. The total number of non-single diffractive events per crossing is given by the relationship:

$$\mathrm{N}|_{\mathrm{nsd}} = \ell_0 \cdot \sigma_{\mathrm{nsd}} \tag{A.4}$$

At BØ luminosities of 10^{30} cm^{-2} s^{-1}, we find that a non-single diffractive interaction occurs once in every 500 crossings at CØ. With so many crossings per second and such a low chance of a proton colliding into an antiproton in a given crossing, suggests that we invoke the Poisson distribution to model the probability of $\bar{\mathrm{p}}\mathrm{p}$ interaction per crossing.

$$p_k = e^{-\alpha}\frac{\alpha^k}{k} \tag{A.5}$$

where $\alpha = \ell_0 \cdot \sigma_{\mathrm{nsd}}$

One can then show that even at the highest Tevatron luminosities, only one in every 6.5×10^7 crossings will result in an event formed of more than two $\bar{\mathrm{p}}\mathrm{p}$ collisions. We will therefore restrict our attention to bunch crossings that result in either one or two $\bar{\mathrm{p}}\mathrm{p}$ collisions.

The multiplicity probability distribution can be described by the negative binomial distribution:

$$P_n = \frac{\Gamma(n+k)}{\Gamma(n+1)\Gamma(k)} \cdot \frac{(\langle n\rangle/k)^n}{(1+\langle n\rangle/k)^{n+k}} \tag{A.6}$$

where n is the multiplicity in full phase space. The parameters k and $\langle n\rangle$ are found to be 0.335^{-1} and 42, respectively for $\sqrt{s} = 1.8$ TeV [51].

Particle production is therefore a product of two sources:

- The overall probability that a proton and an antiproton will interact in a given bunch crossing.
- The probability distribution of the number of yield products resulting from the $\bar{\mathrm{p}}\mathrm{p}$ collision.

We can now address the issue of what percentage of events are formed of two proton-antiproton interactions as a function of multiplicity. Consider first the case

of the single vertex and associate a cross-section, σ_n^c, with each charged particle multiplicity. The sum of these cross-sections will satisfy the following condition:

$$\sigma_{\rm nsd} = \sum_n P_n \sigma_n^c \tag{A.7}$$

where $n = 2, 4, \ldots, \infty$ (only even multiplicities due to charge conservation). Because the negative binomial is normalized and the contributions from the odd terms is equal to that of the even terms, we have:

$$\sum_n P_n(\text{even}) = \sum_n P_n(\text{odd}) = 1/2 \tag{A.8}$$

This implies:

$$\sigma_n^c = 2P_n \cdot \sigma_{\rm nsd} \tag{A.9}$$

The rate of particle production arising from one $\bar{\rm p}$p interaction is a product of two distributions:

$$R_n^1 = \frac{6\nu(\ell_0 \cdot \sigma_n^c)p_1}{1-p_0} = \frac{6\nu\ell_0(2P_n\sigma_{\rm nsd})p_1}{1-p_0} \tag{A.10}$$

where p_1 is the Poisson probability for one interaction

$1-p_0$	normalizes the rate
σ_n^c	is the 'multiplicity' cross-section
$\sigma_{\rm nsd}$	is the non-single diffractive cross-section
ℓ_0	is the luminosity per crossing
6ν	is the number of crossings per second for the six bunches

The derivation of the data rate for double vertex events is precisely the same as for the single vertex case with the exception that one has to consider two negative binomial distributions. With

$$\sigma_n^c = 2P_n' \cdot \sigma_{\rm nsd} \tag{A.11}$$

where

$$P_n' = \frac{1}{2}\sum_i P_i P_{n-i} \tag{A.12}$$

$i = 2, 4, \ldots, (n-2)$.

The data rate, then, for events possessing two vertices is:

$$R_n^2 = \frac{6\nu\ell_0(2P_n'\sigma_{\text{nsd}})p_2}{1-p_0} \tag{A.13}$$

This derivation is based upon [62].

Appendix B Crosstalk Compensation

In this appendix, I address the problem of the systematic variation of the measured longitudinal component, z_{meas}, of the CTC track and present the algorithms that we have developed which predicts the correct z from the measured z. Because of the relatively low resistance of the Gold-plated Tungsten-Rhenium sense wires (190 Ω/m), capacitive coupling between the wires degraded the charge division measurement, where the measured z is given by the relative ratio of the pulse amplitudes arriving at the ends of each sense wire that fired. I will also discuss the importance of constraining the refitted CTC track to the event vertex in order to attain a pseudorapidity resolution of 0.12 units [63].

Charge Division

Let the total charge of induced at point, p, on the sense wire by the slow moving ions be Q_{tot}. Because the wire is resistive and both ends are instrumented with preamplifiers, the charge Q_{tot} will divide into left and right portions in accordance with the principle of the voltage divider.

$$Q_R = Q_{tot} \cdot \frac{r_L}{r_{tot}} \tag{B.1}$$

$$Q_L = Q_{tot} \cdot \frac{r_R}{r_{tot}} \tag{B.2}$$

where $r_{tot} = r_R + r_L$. r_L is the combined resistance of the sense wire and the input impedance of the preamplifier to the left of point p. r_R is defined similarly. The coordinate of the hit along the sense wire (z coordinate) was found by invoking the formula:

$$z = z_0 + g\frac{\ell}{2}\frac{Q_R - Q_L}{Q_R + Q_L} \tag{B.3}$$

where z_0 is the offset due to differences in preamplifier input inpedances and makes $z = 0$ for p half way along the length of the sense wire [64]. The left and right charges,

Q_L and Q_R, are the time integrated linearized FADC[2] digitized pulses which, in principle, corresponds to solving $Q = \int i dt$. The length, ℓ, of the sense wire is 200 cm and the preamplifier input impedances and wire resistance are collapsed into the scale factor, g.

$$g = 1 + \frac{Z_L + Z_R}{r_{wire}} \tag{B.4}$$

where Z is the input impedance of the preamplifier. The test pulse distribution network was used to find g and z_0 for each of the 576 sense wires. The charge corresponding to the left or right pulse of a fired wire was found by integrating from 20 nsec before to 30 nsec after the FWHM (Full Width Half Maximum) of the signal. For overlapping hits or saturated FADC counts, we fit the signal to a reference pulse to extract the charge information and subtract out the pulse tail from subsequent hits.

Unfortunately, complications due to capacitive coupling between the wires and the reflections of the pulses induced on the gain wires at the end of the chamber adversely affected the quality of the charge division. Because the relative ratio of the time integrated value of the left or right pulses gives the z coordinate, anything distorting the pulse waveform will give faulty z information. These crosstalk pulses will either diminish or augment the original pulses

Prototype

In June of 1987 we ran calibration tests on the prototype CTC using hard cosmic rays. The prototype was a rectangular two meter long aluminum chamber with the same wedge shaped wire configuration as the CTC. It consisted of one complete *jet* cell with half cells on either side, mimicking the electrostatic conditions of the 2π symmetric CTC. The endplates of the prototype were made of a Carbon-Fiber-Epoxy shell wrapped around a rohacell core.

[2]We programmed a lookup table into the DL302 scanner module to convert the nonlinear counts to linear

A three way coincidence among scintillator paddles formed the cosmic ray trigger. The paddles, above and below the chamber, were centered about the sense wire plane of the central cell. To trigger only on the more energetic cosmic rays and eliminate measurement uncertainties of tracks most subject to multiple scattering effects, two inches of lead were placed between the cell and the bottom two scintillators. Incidentally, these paddles were formed of the same scintillating substance as the barrel hodoscope elements. The angular acceptance of the cosmic ray trigger was 18.5° in θ, the polar angle, and 26° in ϕ, the azimuthal angle. The were ten different calibration runs where the paddles were placed at separate locations spaced 20 cm apart along the length of the prototype chamber. Care was taken to randomize the calibration positions of the paddles, i.e. we incremented the paddle positions in random order along the length of the chamber. Each run sampled around 10,000 events. Comparing the average z component of the cosmic ray trajectories with the measured value of z_m, we found systematic variations of z_m as a function of:

- The angle of the particle's trajectory with respect to the sense wire plane.
- The position along the sense wire where the pulse was induced.

We observed the same shifting and skewing of the track in the prototype as reported by the JADE collaboration [66], [67]. In particular, we see a dramatic change in the difference between the true and the measured value of the polar angle of the track as the track becomes parallel to the sense wire plane, i.e. all the hits arriving at the same time. Figures B.1 and B.2 shows the effect of crosstalk.

To compensate for crosstalk effects, the CTC was instrumented with the identical resistor network as was used in the prototype, where the output of each preamplifier fed 7.8% of the signal pulse to the output lines of the neighboring preamplifiers and 3.5% to the next nearest neighbors.

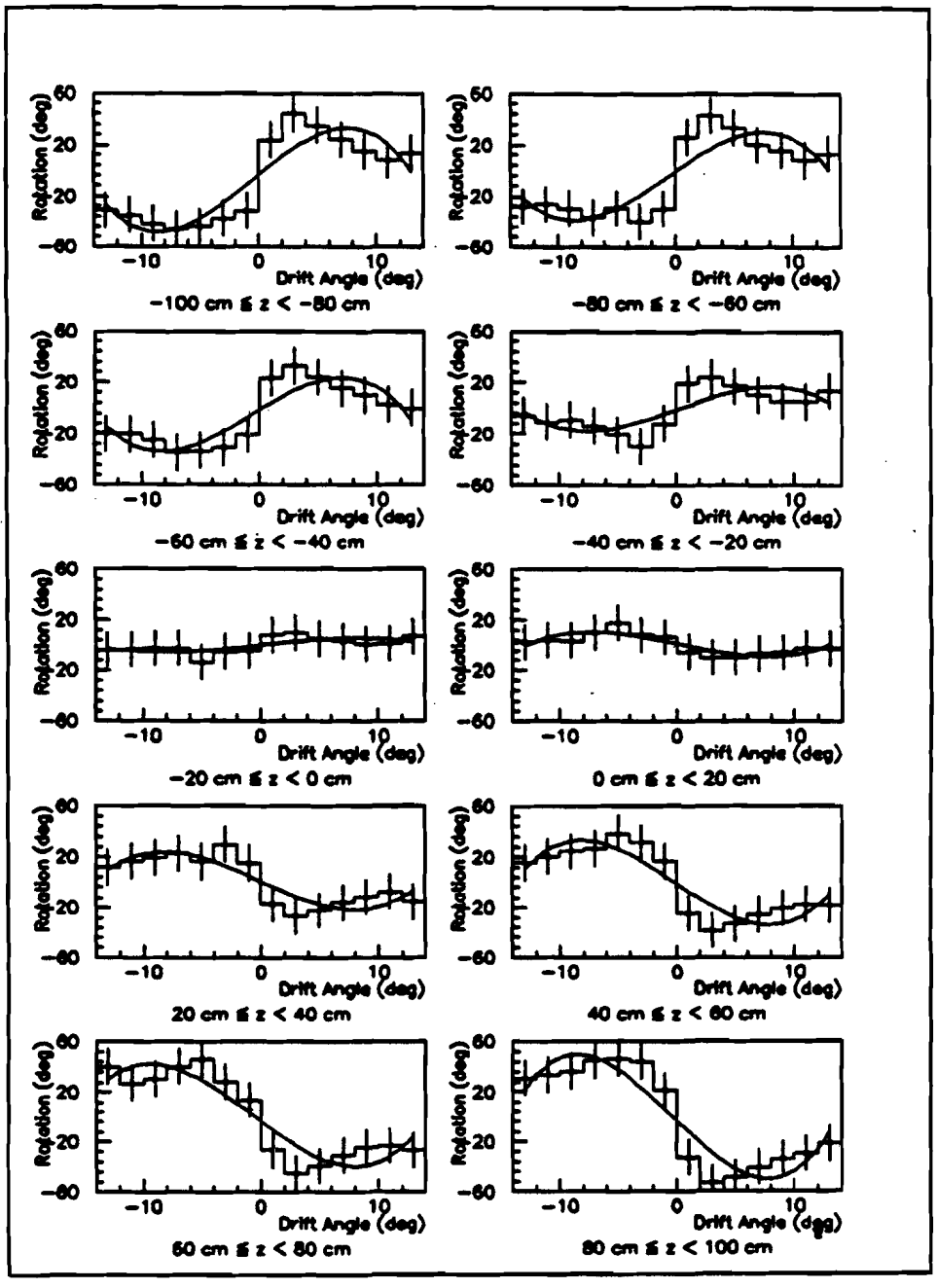

Figure B.1 Correlation between polar angle and drift angle.

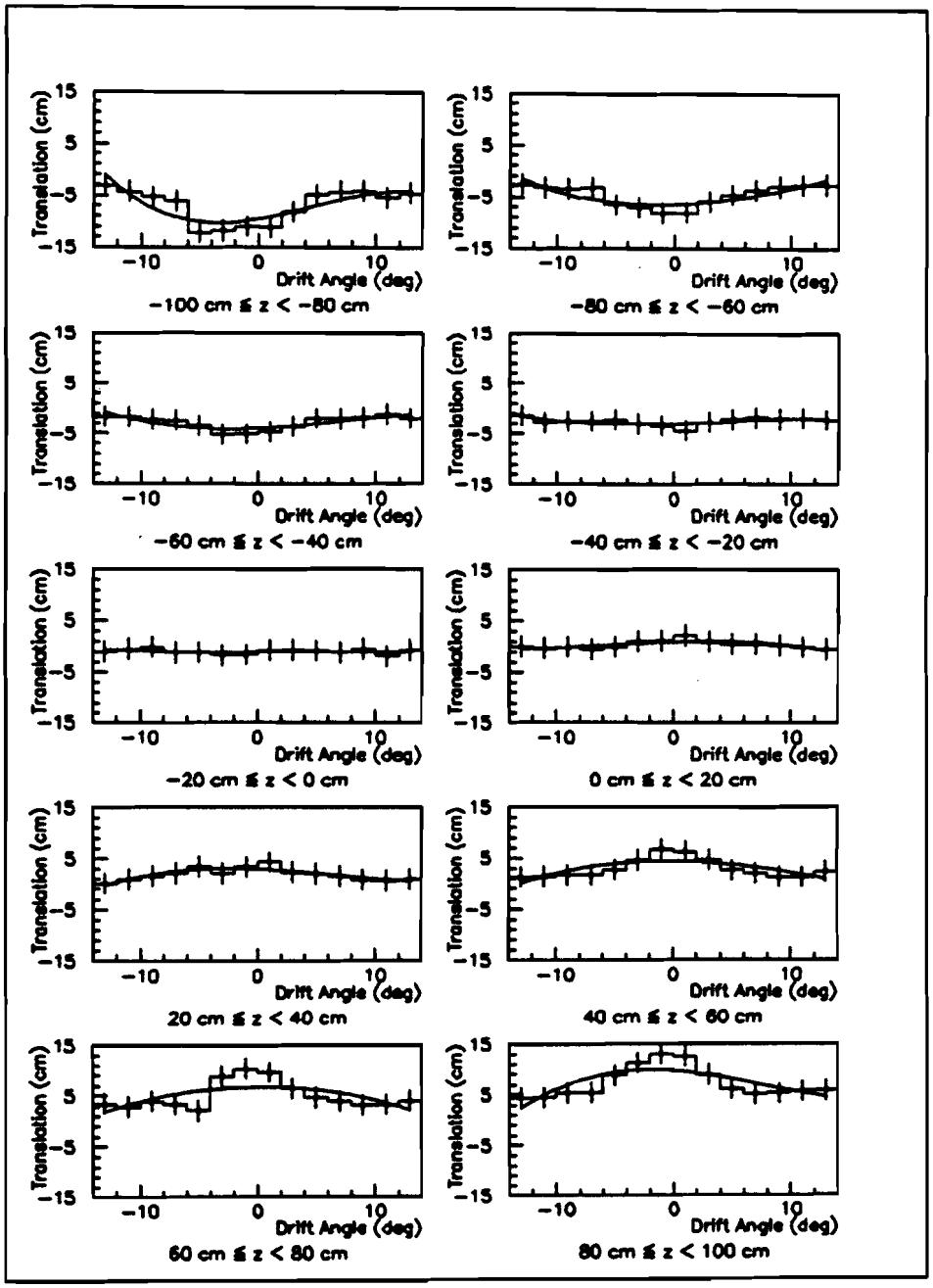

Figure B.2 Correlation between Δz and drift angle.

Matching CTC and Spectrometer Drift Chamber Tracks

We developed software that corrects for this shifting and skewing of the tracks and predicts the true z from the measured z, based upon matching those CTC tracks within the magnet aperture acceptance region (cell 6 of the CTC) with the reconstructed trajectories from the Straw Drift Chamber (SDC) hits. Matching the tracks was no simple task. For whereas the SDC measures well in x and z and poorly in y, the CTC resolves the x and y components accurately, but the z precision is severely compromised due to crosstalk.

Each straw tube has a resolution of 500 μm and a good track requires a minimum of 5 hits. Since the spacing of the tubes is on the order of 5 cm, the minimum lever arm is 5 $\times$ 5 cm = 25 cm. We can estimate the uncertainty of the slope from the following formula [65]:

$$\sigma_s = \frac{\sqrt{6}}{\Delta r\sqrt{N}}\sigma_z \tag{B.5}$$

Setting N to 5, Δr to 25 cm and σ_z to 0.05 cm, one obtains $\sigma_s = 0.0022$ radians. This means the uncertainty of z component for the SDC tracking at $x = 30$ cm is around 2 mm. We have estimated the z resolution of the CTC by fitting a least square line to the CTC hits in the ρ-z plane (see Fig. B.3) and histogramming the residuals. (The data in Fig. B.3 are subject to the cuts below). One sees that the rms error (σ_z) for the CTC tracking is 3.4 cm or 20 times worse than that of the SDC.

For this study we have used only the data from Magnet Off runs. Without a magnetic field deflecting the particle in the transverse (x-z) plane, one can use tracks with only SDC hits for calibrating the measured z of the CTC. (The premagnet chamber was inoperative for some of the Magnet Off runs so we chose to exclude the hits in the magnet chambers and exploit the long lever arm of the SDC for this study). Because the SDC tracks are absent of any systematic crosstalk effects, the z intercept of this track with the projection of the sense wires onto the ρ-z plane ought to be truly representative of the actual point where the avalanche electrons struck

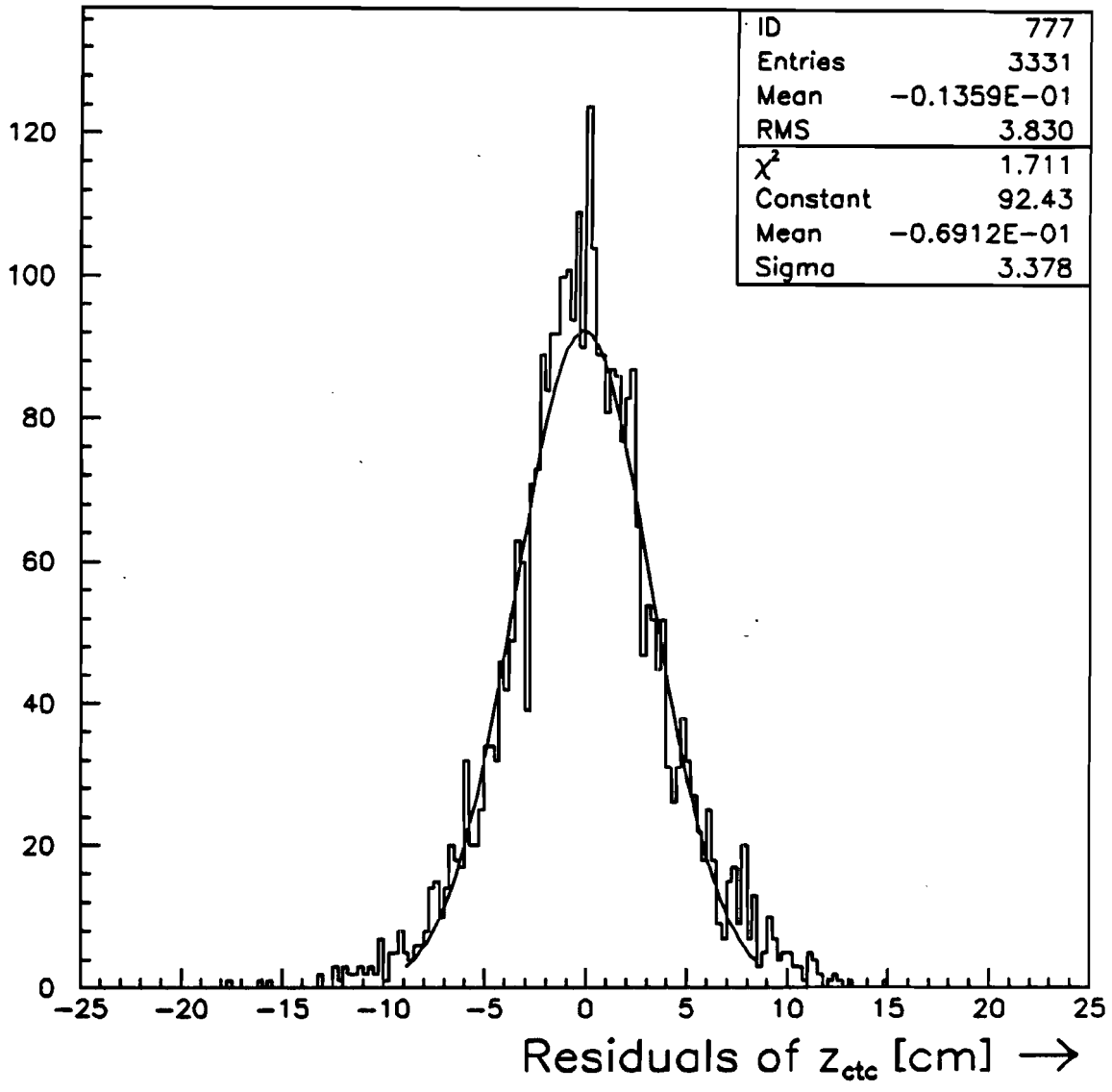

Figure B.3 Gaussian fit to the residual distribution of CTC track in ρ-z.

the sense wire. I will now discuss the means by which we used this $z_{\rm SDC}$ to calibrate the value of z as measured by the CTC.

First, the direction cosines of the spectrometer track were rotated and translated from the CØ frame to the CTC coordinate system by means of the Euler transformation matrix. Next, it was incumbent upon us to find a method which unambiguously identifies which CTC track belongs to which SDC track. There could be n CTC tracks in the cells subtended by the solid angle of the spectrometer acceptance aperture and m tracks in the spectrometer arm. We needed an unequivocal one-to-one correspondence, for mismatches would only destroy the integrity of the calibration. The cuts are listed in Table B.1

Condition (1) greatly reduces the likelihood of mismatching SDC and CTC tracks. Because of the poor SDC azimuthal resolution ($\sigma_{\phi}^{\rm SDC} \approx 3°$), for multiple tracks in the CTC and spectrometer arm, trying to unequivocally identify exactly which track in the CTC belongs to which SDC track quickly leads to combinatoric mayhem. We picked only pristine pairings. Although the full azimuthal spectrometer acceptance is 20°, condition (2) ranges over only 15°. One of the parameters contributing to crosstalk effects observed in the prototype was how close in time successive electron clusters arrived at the anode wires. Geometrically, this is related to the drift angle, ξ, the centrally produced charged particle makes with the sense wire plane (see Fig. B.4).

Because both cells 6 & 7 of the CTC reside within this azimuthal acceptance region, there are overlap problems. For instance, assuming the particles originate at $x = y = 0$ in the CTC frame, a $\phi = 19°$ gives a $\xi = 9.5°$ with respect to sense wire plane 6 and a $\phi = 4°$ gives the same drift angle with respect to sense wire plane 7. Both conditions (1) & (2) eliminate this ambiguity. Since the average number of hits per track is 16, condition (3) only cuts the most pathological cases.

Condition (4) is a cut on the mean absolute deviation. Instead of minimizing the χ^2, which assumes the the measurement error is gaussian distributed, we chose to fit the line by minimizing the absolute deviations, i.e. the merit function:

Table B.1 SDC and CTC track matching cuts.

1. Only one track in the spectrometer arm and only one track in cell 6 and no tracks in cell 7 of the CTC.
2. $5° \leq \phi_{\rm CTC} \leq 20°$.
3. There must be at least 10 hits to a CTC track.
4. $\langle|\text{residuals}|\rangle_x^{\rm CTC} \leq 10$ cm.
5. The slope error in the x-y plane of the fitted CTC track is less than or equal to twice the expected σ_s for 10 hits each with a drift resolution of 0.025 cm and $\sigma_\xi \leq 0.25°$.
6. That at least 50% of all hits in the CTC are associated with primaries.
7. That the SDC have y information, i.e. the tilted rows have registered hits.
8. $\phi \rightarrow \xi \rightarrow \phi$.
9. Tracks may neither cross the sense wire plane nor span sector boundaries.
10. $|\Delta y(x=0)|_{\rm SDC} \leq 10$ cm.
11. Only unsaturated and isolated CTC pulses accepted.
12. $|z_{\rm CTC}^{\rm iwire} - z_{\rm SDC}^{\rm iwire}| \leq 15$ cm.
13. $|\phi_{\rm CTC} - \phi_{\rm SDC}| \leq 3.6°$.

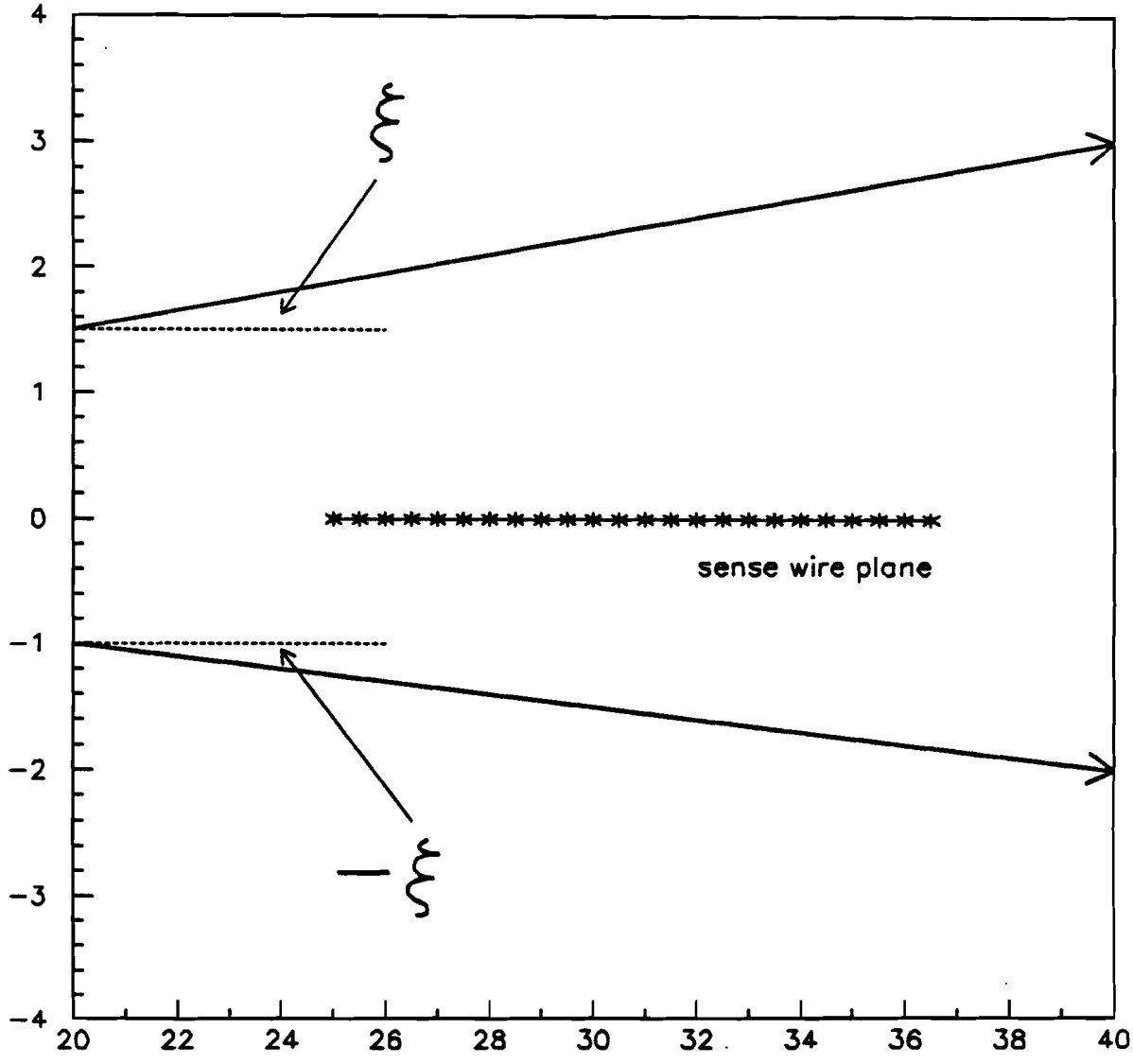

Figure B.4 Definition of the drift angle, ξ. Heavy arrow represents a track.

$\sum_{i=1}^{n} |z_i - (a + b\rho_i)|$ [55]. If the mean absolute deviation (the average residual) exceeds 10 cm in ρ-z, the distribution of the z_{CTC}'s is so scattered from any central value, the fitted track is rendered useless for calibration purposes.

Like condition (3), condition (5), is another loose cut. This cut is more than 3σ from the CTC ξ resolution. Condition (6) filters out events overwhelmed by secondaries. At least 50% of all the hits in the CTC have to be associated with primary tracks, i.e. a track originates from the beamline. We found that 4% of all spectrometer tracks that pass all the above cuts except for condition (7) lack y information from the tilted straw drift tubes.

Condition (8) is a consistency check. I used an earlier version of the CTC tracking algorithm[3] in my personal Magnet Off miniDST's and discovered that 0.2% of the hits were assigned unphysical ϕ's. In order to eliminate these hits from the z calibration, we first calculate the azimuthal angle, ϕ, this track makes with sense wire plane. We then transform this drift angle back to the azimuthal angle. If the initial and final ϕ disagree, the track is thrown out. See Table B.2 and Fig. B.5 for the relationship between ϕ and ξ.

The first part of condition (9) reflects the difficulty in ascertaining the correct time to spatial relationship for tracks that cross the sense wire plane, i.e. $\phi = 14°$. Secondly tracks that cross sector boundaries are not of interest, for they exhibit different crosstalk effects than for tracks confined to a single cell. This cut represents around 21% of all CTC tracks; 12% cross the sense wire plane and the remaining 11% span sector boundaries. Condition (10) requires that the reconstructed SDC tracks pass within 10 cm of the beamline. All CTC hits used in the calibration are isolated and well-formed (condition (11)), suffering neither from overlap nor FADC saturation problems.

[3]Unlike the line fit method [17], we first used a ϕ-filtering algorithm. Because the $\vec{B}$ field in the CTC is negligible, tracks will travel in straight line trajectories. Each hit will possess a unique ϕ and a cluster of hits possessing the same ϕ define a primary track, where the origin in x and y is at the beamline. The ϕ-filtering technique was discontinued because it cannot track secondaries.

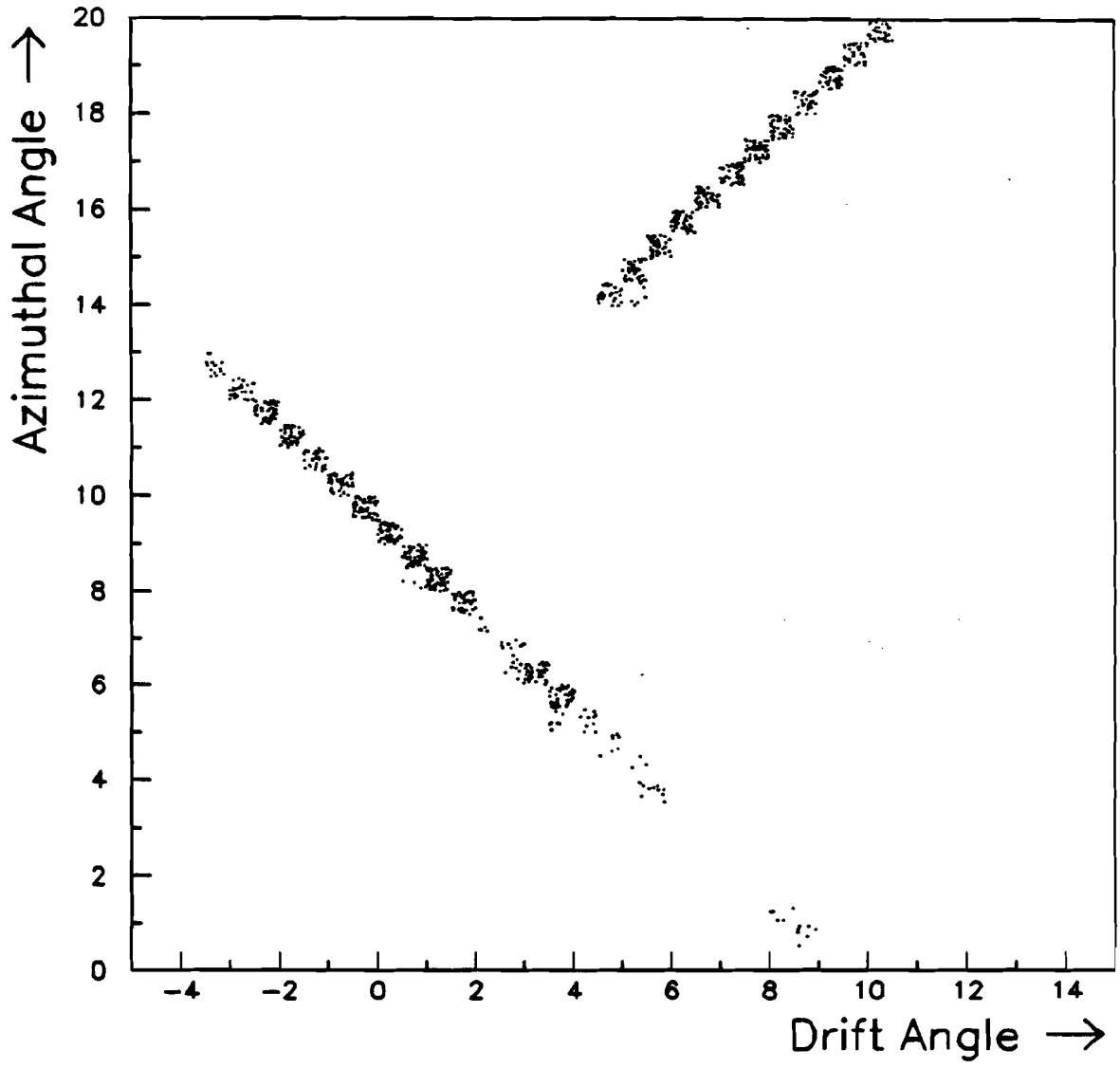

Figure B.5 Relationship between azimuth, ϕ, and drift angle, ξ. Angles measured in degrees.

Table B.2 Relationship between the azimuthal angle, ϕ, and the drift angle, ξ, for a particle produced at $x = y = 0$.

ϕ [*degrees*]	ξ_6 [*degrees*]	ξ_7 [*degrees*]
5	—	10.51
6	+3.49	11.51
7	+2.49	12.51
8	+1.49	—
9	+0.49	—
10	-0.51	—
11	-1.51	—
12	-2.51	—
13	-3.51	—
14	crosses sense plane	
15	+5.51	—
16	+6.51	—
17	+7.51	—
18	+8.51	—
19	+9.51	—
20	+10.51	—

Finally, we made cuts on $|\Delta\phi|$ and $|\Delta z|$. These two cuts combined filter out around 30% of the tracks (see Fig.'s B.6 & B.7). Because the spectrometer aperture acceptance ranges from $\eta = -0.36$ to $\eta = +1.0$, the positive rapidity tracks are preferentially sampled over their negative rapidity counterparts. This asymmetrical sampling is reflected in the negative shift of the mean in the gaussian fitted to the $z_{\rm CTC} - z_{\rm SDC}$ histogram in Fig. B.7

To estimate the effect of the above 13 cuts, I drew up a data sample of 28,520 merged CTC and spectrometer events. Applying the first 11 cuts reduced this data sample to 1496 events. Cuts 12 and 13 further decreased the sample to 1037 events. These 13 cuts *in toto* eliminated around 96.4% of the events.

Correcting the Measured Z

If both the SDC and CTC tracks pass the above 13 cuts we then have a match. We are now in the position to utilize the spectrometer track parameters to calibrate the z measurement of the CTC. First we calculate a Δz by subtracting the measured value of z, $z_{\rm CTC}$, from the "true" z, $z_{\rm SDC}$, for each hit of a matched pair. Δz is binned according to:

1. Which sense wire fired (outermost wires 1 & 24 neglected due to inefficiencies caused by fringe electrostatic fields).

2. Position along wire as measured by the CTC. (10 regions with a binwidth of 20 cm).

3. The angle that the CTC track makes with respect to the sense wire plane. (17 bins of 1° bin width, i.e. $-5° \leq \xi \leq +12°$).

And

$$\Delta z(\mathrm{iz}, \mathrm{j}\xi, \mathrm{kwire}) = z_{\rm SDC} - z_{\rm CTC}$$

There are then 3740 ($22 \times 10 \times 17$) elements to Δz. Parenthetically, the binning of the Δz's in terms of the innermost 22 sense wires is only for the sake of convenience

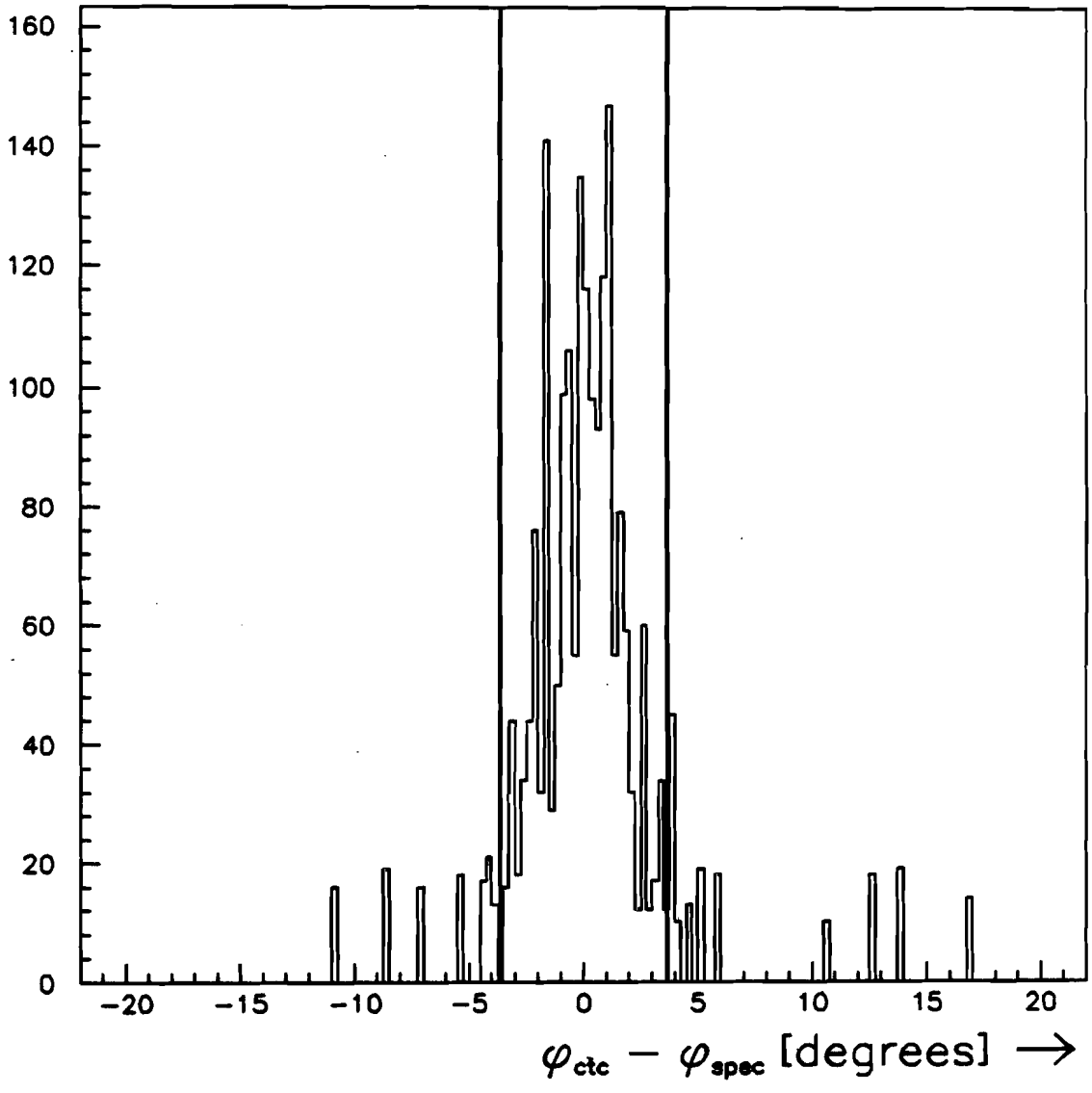

Figure B.6 $\phi_{CTC} - \phi_{SDC}$.

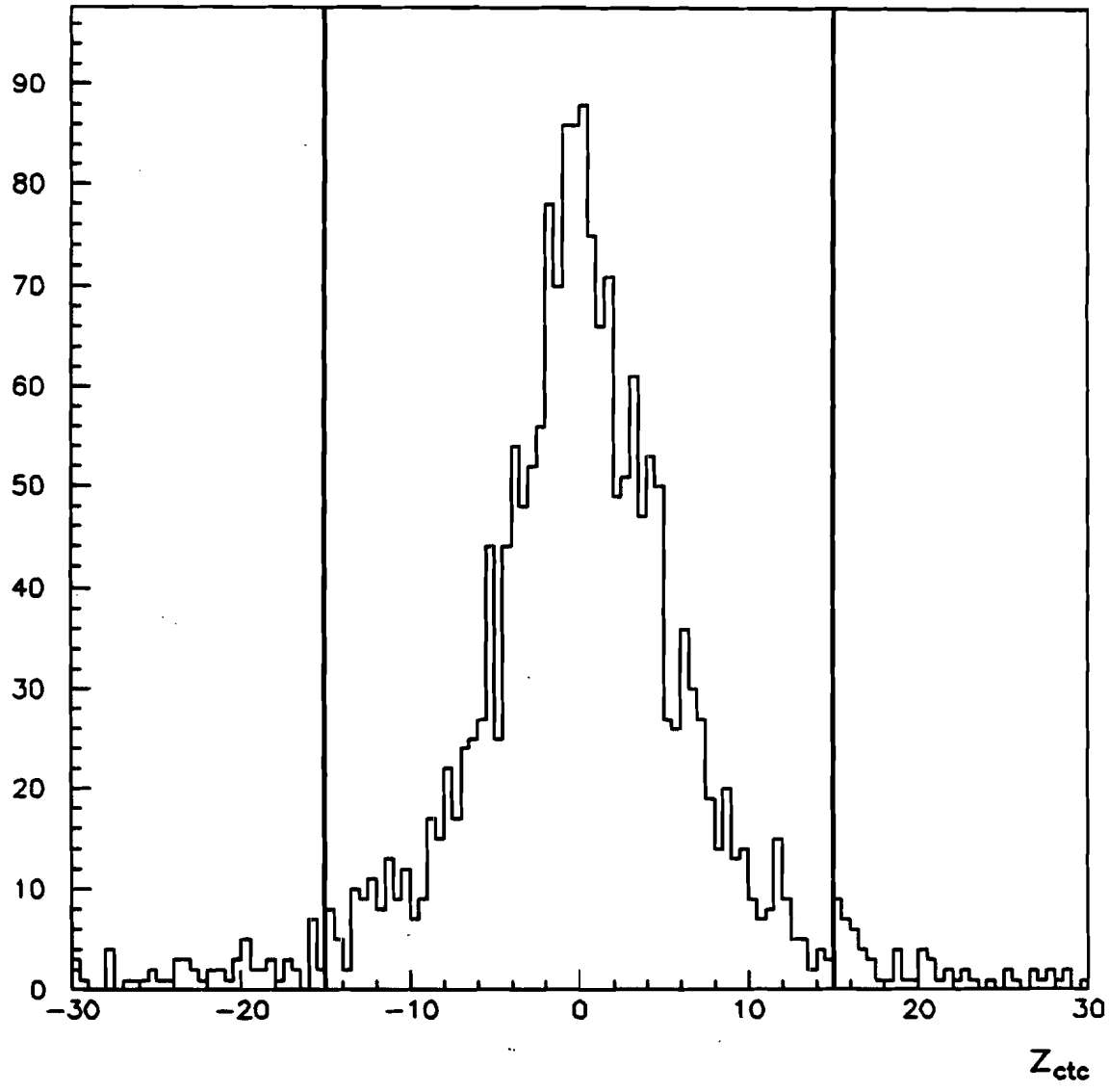

Figure B.7 $z_{CTC} - z_{SDC}$.

allowing the user to quickly form the corrected z, $z_{\rm cor}$, from a lookup table and physically has nothing to do with the effects of crosstalk. One can then form a corrected z from the measure $z_{\rm CTC}$ and the Δz.

$$z_{\rm cor} = z_{\rm SDC}({\rm iz, j}\xi, {\rm kwire}) + \langle \Delta z({\rm iz, j}\xi, {\rm kwire}) \rangle \tag{B.6}$$

Where for a given cell

$$\langle \Delta z \rangle = \frac{1}{N} \sum_{i=1}^{N} \Delta z_i \tag{B.7}$$

And N equals the total occupation population of the cell

Data Sample

Since there are 170 independent z correction cells ($3470 \div 22$) and because some of the cuts are restrictive, we needed a sizable data pool to obtain adaquate statistics for these studies. We used Magnet Off data primarily because we wished to avail ourselves of the long lever arm of the Straw Drift Chambers without the concern of reconstructing tracks through the magnetic field. The fitted SDC hits give precise slope and intercept information in the ρ-z plane. We merged the data[4] from 117 spectrometer and 117 CTC raw data tapes to make 71 Magnet Off merged tapes. On the Fermilab VAX cluster, we then made 65 compressed DST files. Each DST file took approximately 18 VAX 11/780 CPU hours to produce. The remaining 6 files were not used because these merged tapes were either minimum bias runs (few particles make it into the spectrometer arm) or proton only stores. A compressed DST file contains the SDC track parameters, e.g. direction cosines, the CTC hits in sectors 6 & 7 and sundry flags. I used a modified version of the SDC tracking program to handle magnet off data and an earlier version of the CTC tracking routines, which are sensitive only to primaries. I then applied the above 13 cuts on these compressed DST files to make two data samples; a dependent and an independent one. The latter sample is termed independent because it was not used in formulating the z correction lookup

[4]The CTC and spectrometer data were collected in dual independent streams.

table. From six compressed DST files, I extracted 864 events (13023 CTC hits) for the independent sample. The dependent sample contained 6096 events (95565 CTC hits).

Analysis

The z correction can reduce the error of the measured value of z to no better than $\sigma_z = 3.4$ cm, the intrinsic z resolution of the CTC (see Fig. B.3). The task, then, is to find a Δz to add to the measured z to form the corrected z for each and every bin.

The vertical axis is the difference between the true z and the corrected z. Since the distribution of the hits is vertically centered at $\Delta z = 0$ cm, the application of the correction introduces no untoward effects. In Fig. B.8 a gaussian is fitted to each of the superimposed difference histograms. The contents of these histograms are integrated over all bins.

The dashed line corresponds to $\Delta z = z_{\rm SDC} - z_{\rm CTC}$ and the solid line is for $\Delta z = z_{\rm SDC} - z_{\rm cor}$. The correction shifts the mean of the gaussian from $\Delta z = -1.1$ cm to $\Delta z = 0.1$ cm and compresses it from $\sigma = 5.3$ cm to $\sigma = 4.5$ cm. Table B.3 gives both the mean and the standard deviations of the fitted gaussians for each z bin.

Of more interest, perhaps, is how well the application of the z correction works on an independent sample. Like Fig. B.8, gaussians are fit to the uncorrected and corrected histograms in Fig. B.9. The correction shifts the mean positive from -2.5 cm to -1.0 cm and reduces the standard deviation from $\sigma = 5.8$ to $\sigma = 5.0$ cm. The fit parameters for Δz distributions, broken up by z bin, are found in Table B.4.

For both the independent and dependent sample the σ of the gaussian fit to the uncorrected Δz histograms exceeds $\sigma = 3.4$ cm, the σ of the gaussian fit to the residuals (see Fig. B.3). What accounts for this broadening? First, it could result from mismatching the CTC track with the spectrometer track. But with cut (1), this possibility is unlikely. Secondly, the z resolution of the SDC tracking could be significantly worse than 2 mm at $x = 30.0$ cm. but why then would the application of

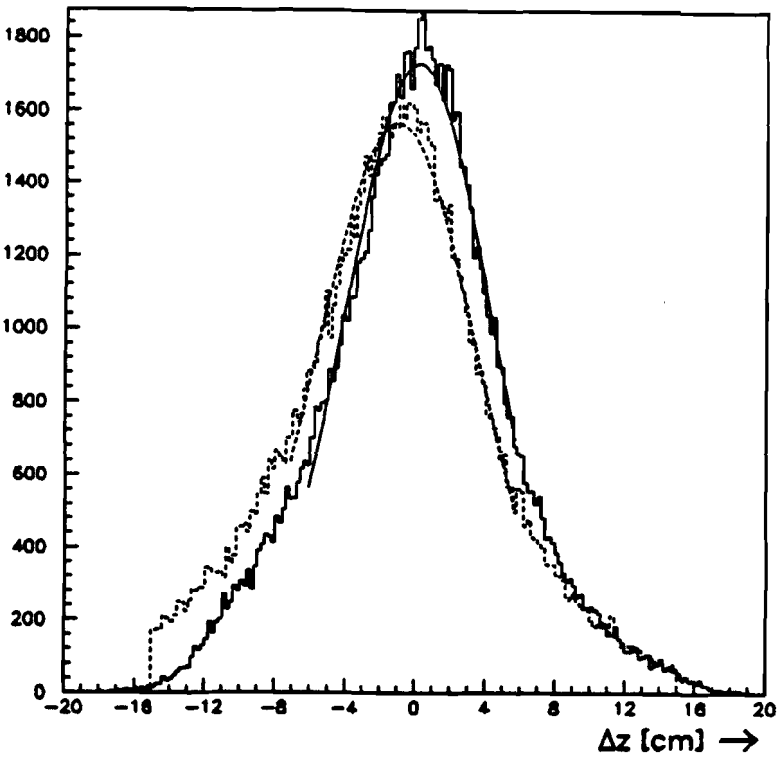

Figure B.8 Dependent sample. Overlayed Δz distributions.

Table B.3 Dependent sample (by z bin).

	Uncorrected		*Corrected*	
z bin [cm]	$\langle x \rangle$ [cm]	σ [cm]	$\langle x \rangle$ [cm]	σ [cm]
-60 to -40	-2.2	6.4	+0.2	5.0
-40 to -20	-1.5	5.8	+0.2	4.8
-20 to 000	-1.1	5.3	+0.2	4.7
000 to +20	-1.0	5.2	+0.1	4.7
+20 to +40	-1.3	5.0	+0.1	4.7
+40 to +60	-0.9	5.0	-0.3	4.5
+60 to +80	+1.2	6.3	-0.5	5.3

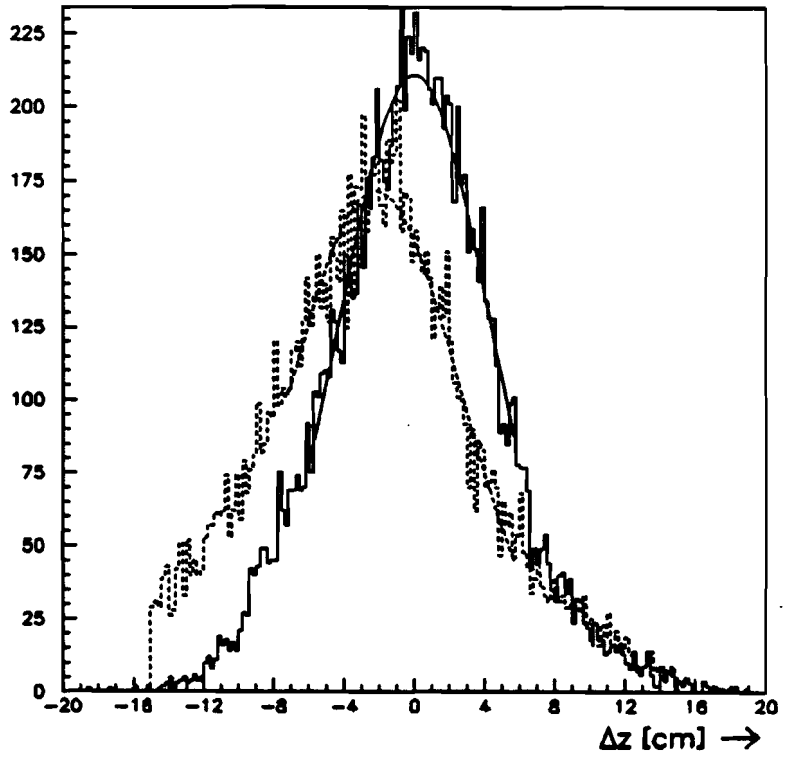

Figure B.9 Independent sample. Overlayed Δz distribution.

Table B.4 Independent sample (by z bin).

	Uncorrected		*Corrected*	
z bin [cm]	$\langle x \rangle$ [cm]	σ [cm]	$\langle x \rangle$ [cm]	σ [cm]
-60 to -40	-1.4	8.4	+0.6	7.6
-40 to -20	-3.2	6.4	-0.8	5.4
-20 to 000	-2.4	5.7	-0.9	4.9
000 to +20	-2.8	6.1	-1.3	5.2
+20 to +40	-2.9	5.5	-1.3	4.8
+40 to +60	-0.9	5.3	-0.6	4.4
+60 to +80	+4.6	10.4	+0.7	9.1

the z correction to the independent sample narrow and shift the gaussian? Or thirdly, are we seeing the effects of crosstalk? Imagine there are two colinear tracks; an SDC and a CTC track. Let the SDC remain fixed. Now shift and rotate the CTC track. Although the σ of the residual distribution for this new CTC track will not change, the separation distance between $z_{\rm SDC}$ and $z_{\rm CTC}$ for a fixed wire will tend to increase.

In an unpublished paper detailing the performance of the JADE central tracking chamber, R. Heuer reported that the JADE group had observed a systematic shifting and skewing of the measured track from the true track [66], [67]. We observed the same behavior in our prototype [68] (see Figures B.1 and B.2). In particular, the JADE group observed a drastic displacement in z for tracks parallel to the sense wire plane and a "Mark of Zorro" for $\Delta\theta = \Delta\theta(\xi)$. I cannot reproduce these results as witnessed by the JADE group and the CTC prototype.

So why are the results from the CTC so disparate from the JADE cylindrical drift chamber? I do not believe it is a matter of statistics, for the gross features would still be apparent. I think, rather, it has to do with the intrinsic z resolution. The prototype CTC had a z rms error of 2 cm as opposed to the CTC z resolution of around 4 cm. And the effects of crosstalk are blurred within the relatively large uncertainty in z. Moreover, the z resolution of the CTC is $\sim$ 2.5 times worse than that of the JADE CTC—this accuracy is comparable to the CTC prototype.

Let the intrinsic z resolution of the CTC be σ = 4 cm. The 24 sense wires are then packed within the radial dimensions of 3σ giving an interwire spacing of $\sim \sigma/10$. And since

$$\sigma_\theta = \sigma_z \cdot \cos^2(\langle\theta\rangle)$$

and assuming N = 10, $\langle\theta\rangle = 0°$, σ_z = 4 cm and Δr = 5 cm, then σ_θ can be no better than 36°. Because the radial distance from the beamline is

$$\frac{7.5\sigma}{\cos(\sigma_\theta)}$$

or 37 cm, referring to eq. B.5, we can estimate the error in slope in the ρ-z plane for both drift chambers. Assuming that N = 10 for both chambers and using their

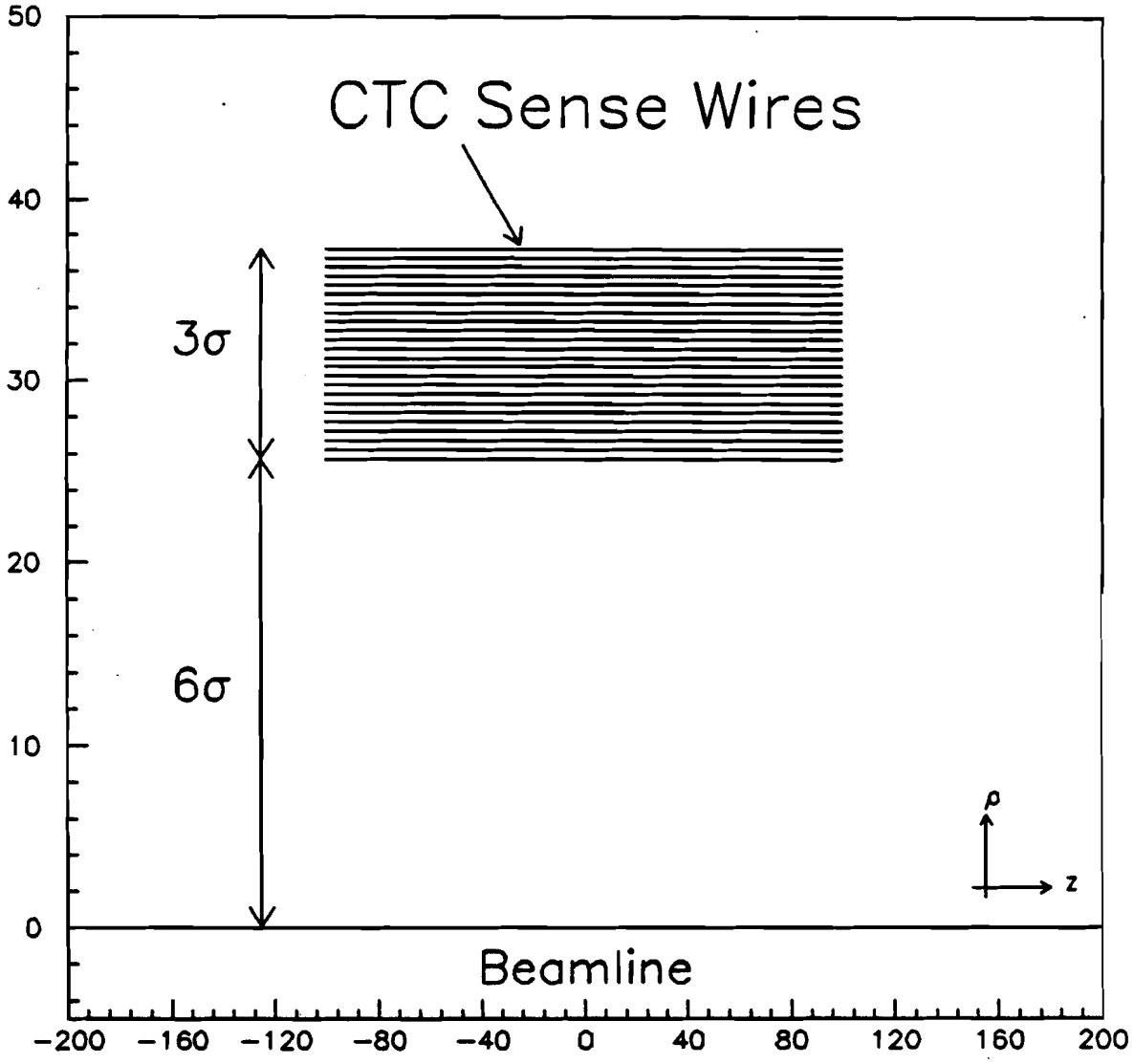

Figure B.10 Scale drawing of the sense wires of a CTC *jet* cell in relation to the beamline in the ρ-z plane. Dimensions are measured in terms of the intrinsic z resolution of the CTC. $\sigma = 4$ cm.

intrinsic z resolutions, one obtains for the JADE chamber a $\sigma_s = 7°$ compared to a σ_s of 36° for the E735 CTC. Because of the large σ_s for the CTC, the results of the CØ and JADE chambers neither affirm nor contradict one another.

Vertex Constraint

All is not lost. Although the error in the ρ-z slope smears out the systematic behavior of $\Delta\theta$ as a function of ξ, it does not imply that we cannot correct for crosstalk; we can constrain the refitted CTC track to pass through the event z vertex [69]. It turns out this contraint is the keystone for obtaining a reasonable pseudorapidity resolution. The event vertex provides a well defined pivot point ($\sigma_{\text{vert}} = 2$ cm) with a long moment arm (~30 cm).

Because we ultimately intended to apply this vertex correction to the CTC tracks contained on the DST,[5] I recalculated the CTC track parameters passed to my magnet off miniDST's to be of the identical form of those on the standard Amdahl DST's. On the Amdahl DST's, each CTC track has 6 spatial parameters, namely the initial (x_i, y_i, z_i) and the final space point (x_f, y_f, z_f) calculated from the raw t-z information [17]. In order to emulate these refined parameters, I first fit a least square line through the measured z's in the ρ-z plane. I then calculated the z_{fit} value for each sense wire that fired for the track, where

$$z_{\text{fit}}(\rho_{\text{wire}}) = \text{slope} \cdot \rho_{\text{wire}} + \text{z\_intercept} \tag{B.8}$$

This z_intercept is from the least square fit and not from the vertex. For each z_{fit}, I gave a resolution of $\sigma_z = 4.5$ cm, which is commensurate with the intrinsic z resolution of the CTC, as determined form the SDC and CTC track matching studies. Finally, I included the vertex in the refit of the track through the corrected z's, z_{cor}, where

$$z_{\text{cor}}(\rho_{\text{wire}}) = z_{\text{fit}}(\rho_{\text{wire}}) + \Delta z(z, \xi, \rho) \tag{B.9}$$

[5]At the time of this analysis the DST's were being produced on the Fermilab Amdahl 5890. The DST format, therefore, was fixed.

The weighted average of the z vertex found by the Z chamber and trigger time of flight detectors can resolve the vertex to within 2 cm. So even though the error in z at $\rho = 0$ for the spectrometer track is less than 0.5 cm for the magnet off runs, I weighted the vertex with a σ_z of 2 cm in order to simulate the data on the Amdahl DST's as closely as possible. I studied three cases of Δz. They are:

Case 1 $\Delta z = 0 \; \forall \; \rho$,$z$ and ξ

Case 2 $\Delta z = \langle \Delta z(z,\xi,\rho) \rangle_{cs}$. These calibration constants were determined by matching CTC and spectrometer tracks.

Case 3 $\Delta z = \langle \Delta z(z,\xi,\rho) \rangle_{p}$. These are the prototype calibration constants. Unlike the $\Delta z = \langle \Delta z(z,\xi,\rho) \rangle_{cs}$, the prototype calibration constants are not limited by the rapidity acceptance of the spectrometer and extend over the entire length of the chamber[6]. These constants exhibit systematic behavior as a function of z and ξ, as observed by both JADE and the Purdue subgroup of E735.

Table B.5 compares and contrasts the average and the standard deviation for the $\Delta\theta = \theta_{true} - \theta_{refit}$ and $\Delta\eta = \eta_{true} - \eta_{refit}$ distributions for the three cases above. The average and the standard deviation for the $\Delta\theta$ and $\Delta\eta$ distributions without the vertex constraint is listed in the last row.[7]

Although Case 2 shifts the average of both the $\langle \Delta\theta \rangle$ and $\langle \Delta\eta \rangle$ distributions closer to 0 than either Case 1 or Case 3, applying the CTC-Spec calibration constants to the CTC tracks on the Amdahl DST's is not useful. These calibration constants range over $-60 \leq z \leq +80$ cm. If the $\langle \Delta z(z,\xi,\rho) \rangle_{cs}$ demonstrated systematic behavior in z, one could analytically extend these constants as a function of z and ξ in order to cover the entire length of the CTC. But I have not observed any such systematic crosstalk effects. Besides, it is not surprising that Case 2 centers and narrows the

[6]The prototype calibration constants were formulated in the same manner as the CTC-Spec ones, except we used hard cosmic rays instead of tracks in the spectrometer as the reference.

[7]I have also fit a least square line through the crosstalk corrected raw hits in the ρ-z plane and found the improvement is only 1.8% better than Case 3.

Table B.5 Comparison of polar angle and pseudorapidity resolutions.

Case	$\langle\Delta\theta\rangle$ [*degrees*]	$\sigma_{\Delta\theta}$ [*degrees*]	$\langle\Delta\eta\rangle$	$\sigma_{\Delta\eta}$
1	-2.24	5.32	.043	.103
2	-0.25	5.06	.004	.098
3	-1.17	5.90	.020	.115
No Constraint l.s. fit - true	-10.41	27.14	.190	.546

$\Delta\theta$ and $\Delta\eta$ distributions better than Case 1 and 3, for these correction constants were applied on a dependent sample. Case 2 then reflects the best resolution that can be achieved. Although Case 1, improves the $\Delta\theta$ and $\Delta\eta$ by 10%, Case 3 centers $\langle\Delta\theta\rangle$ and $\langle\Delta\eta\rangle$ to zero by a factor of two better than Case 1. Because the centroids are shifted closer to zero with the application of the prototype calibration constants, Case 3, I believe, affords the best means for correcting the polar angle distribution.

Note that the application of the prototype calibration constants shifts the centroid towards zero and narrows the width of the distribution from 5.3 to 4.5 cm. Plotted in Figures B.12a and B.12b are the frequency distributions of the true (spectrometer) and the measured (CTC) polar angles, respectively.

The refitting of the CTC track maps Fig. B.12b to B.12c, which is, by eye, nearly identical to Fig. B.12a, i.e. the corrected values agree well with those of the spectrometer. To give scale to the success of the refit method, the difference histograms of $\Delta\theta = \theta_{\text{true}} - \theta_{\text{meas}}$ and $\Delta\theta = \theta_{\text{true}} - \theta_{\text{refit}}$ are overlayed in Fig. B.13 (see also Table B.5).

Figures B.14a through B.14c and Fig. B.15 are similarly defined for the pseudorapidity.

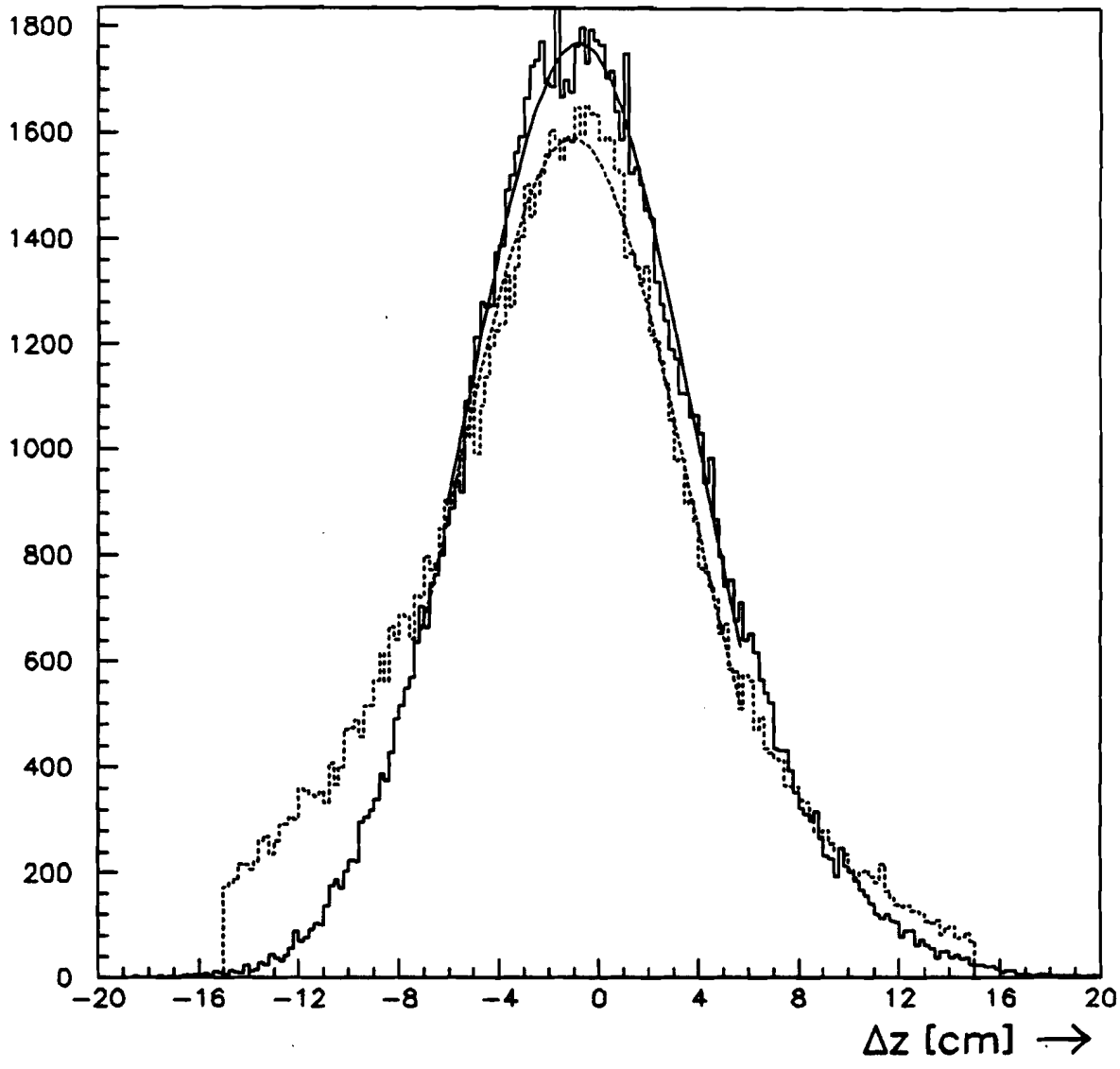

Figure B.11 $z_{\mathrm{SDC}} - z_{\mathrm{CTC}}$ (dashed) and $z_{\mathrm{SDC}} - z_{\mathrm{cor}}$ (solid).

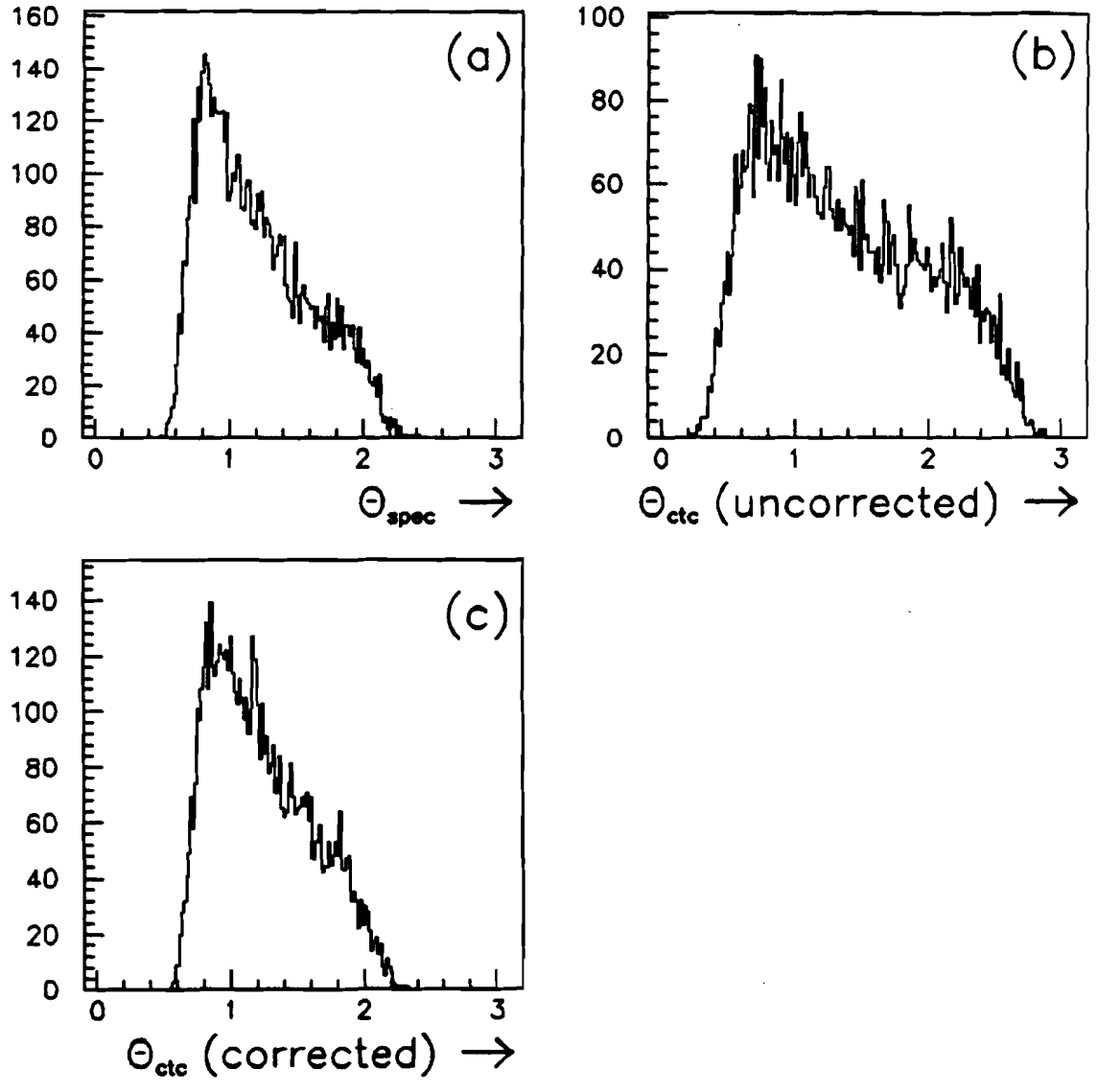

Figure B.12 Distributions for the spectrometer, CTC and corrected polar angles integrated over all tracks that passed the cuts.

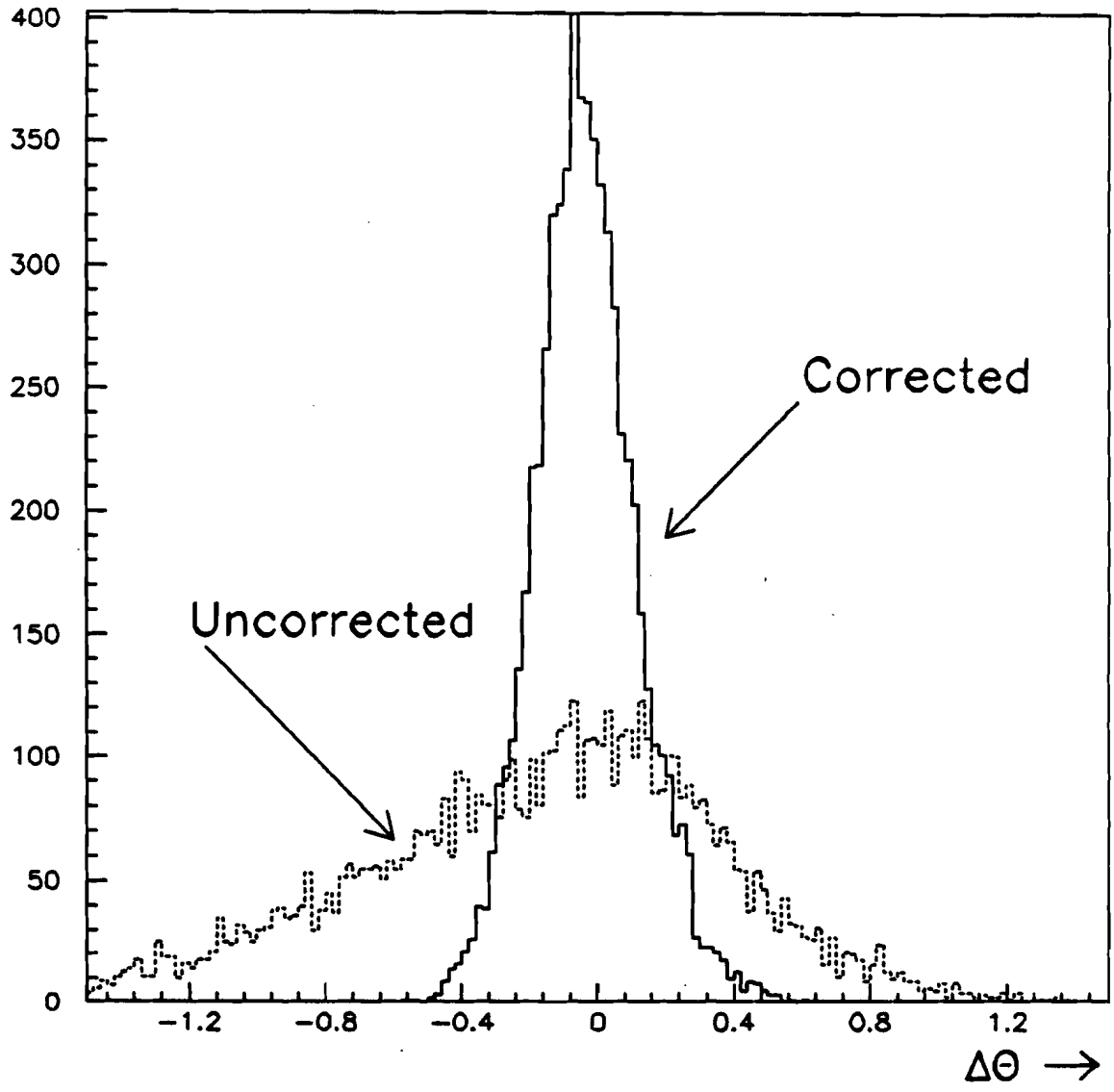

Figure B.13 Superimposed difference histograms of $\theta_{\mathrm{SDC}} - \theta_{\mathrm{CTC}}$ (dashed line) and $\theta_{\mathrm{SDC}} - \theta_{\mathrm{refit}}$ (solid line).

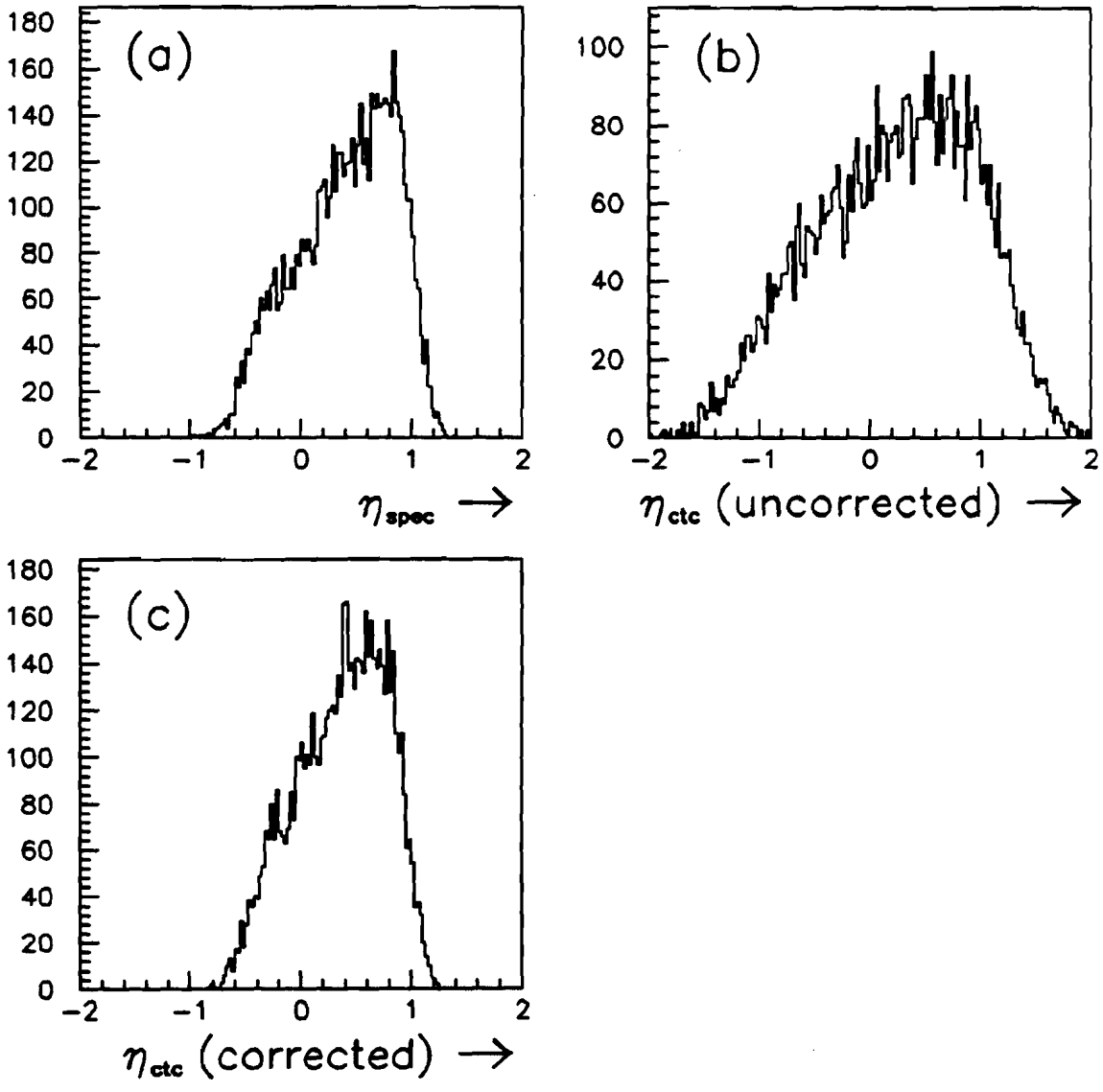

Figure B.14 Distributions for the spectrometer, CTC and corrected pseudorapidities integrated over all tracks that passed the cuts.

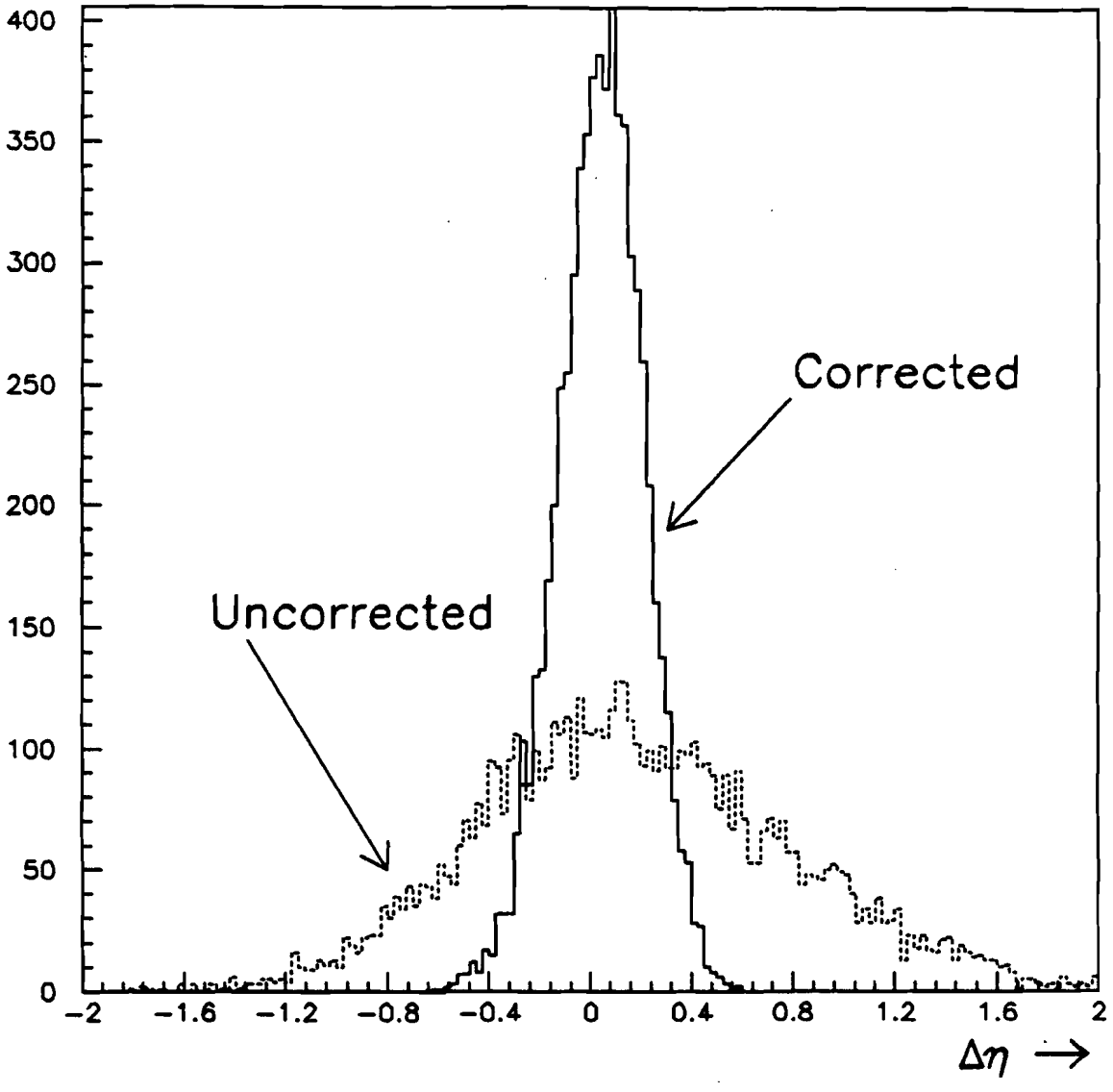

Figure B.15 Superimposed difference histograms of $\eta_{\mathrm{SDC}} - \eta_{\mathrm{CTC}}$ (dashed line) and $\eta_{\mathrm{SDC}} - \eta_{\mathrm{refit}}$ (solid line).

Conclusion

From Fig B.15 and Table B.5, we see the refitting of the CTC track with the event vertex constraint and correcting for crosstalk gives an η resolution of 0.12 units, or offering a five fold improvement in the rms error. The minimum bias pseudorapidity distributions using the CTC are discussed in [17].

Appendix C μDST Ntuple Definitions

```
*
*  Based upon C. Allen's work on the MiniDST format
*
 Integer       Evt_nt, CTCeta_nt, Window_nt, Strk_nt, TOF_nt

 Parameter    (Evt_nt     = 10)
 Parameter    (CTCeta_nt  = 11)
 Parameter    (Window_nt  = 12)
 Parameter    (Strk_nt    = 13)
 Parameter    (TOF_nt     = 14)


* Evt Ntuple

 Integer       Evttup_size
 Parameter    (Evttup_size = 31)

 Character*8   Evt_nt_tags(Evttup_size)
 Data          Evt_nt_tags /
:'SPCRUN  ', 'CTCRUN  ', 'ETCHIGH ', 'ETCLOW  ',
:'TOFD    ', 'TOFU    ', 'ECUA    ', 'ECUB    ',
:'ECUC    ', 'ECDA    ', 'ECDB    ', 'ECDC    ',
:'BARUA   ', 'BARUB   ', 'BARDA   ', 'BARDB   ',
:'XVERTEX ', 'YVERTEX ', 'ZVERTEX ',
:'CTCHITS ', 'CTCGHITS', 'CTCTRKS ',
:'CTCPRIME', 'ETACELLS',
:'ETAPTR  ', 'SPCTRKS ', 'SPCPTR  ', 'TOFCNTRS',
:'TOFPTR  ', 'WINTRKS ', 'WINPTR  ' /
```

```
 Integer    EVT_SPCRUN,   EVT_CTCRUN,    EVT_ETCHIGH,
:           EVT_ETCLOW,   EVT_TOFD,      EVT_TOFU,
:           EVT_ECUA,     EVT_ECUB,      EVT_ECUC,
:           EVT_ECDA,     EVT_ECDB,      EVT_ECDC,
:           EVT_BARUA,    EVT_BARUB,
:           EVT_BARDA,    EVT_BARDB,
:           EVT_XVERTEX,  EVT_YVERTEX,   EVT_ZVERTEX,
:           EVT_CTCHITS,  EVT_CTCTRKS,   EVT_CTCPRM,
:           EVT_CTCGHITS, EVT_ETACELLS,  EVT_ETAPTR,
:           EVT_SPCTRKS,  EVT_SPCPTR,    EVT_TOFCNTRS,
:           EVT_TOFPTR,   EVT_WINTRKS,   EVT_WINPTR

Parameter (EVT_SPCRUN    =  1) ! Spectrometer run number
Parameter (EVT_CTCRUN    =  2) ! CTC run number
Parameter (EVT_ETCHIGH   =  3) ! Upper 16 bits of the Evt Time Clock
Parameter (EVT_ETCLOW    =  4) ! Lower 16 bits of the Evt Time Clock
Parameter (EVT_TOFD      =  5) ! Bitmap for TOF Downstream       (0-14)
Parameter (EVT_TOFU      =  6) ! Bitmap for TOF Upstream         (0-14)
Parameter (EVT_ECUA      =  7) ! Bitmap for ups Endcap Hodo A    (0-23)
Parameter (EVT_ECUB      =  8) ! Bitmap for ups Endcap Hodo B    (0-23)
Parameter (EVT_ECUC      =  9) ! Bitmap for ups Endcap Hodo C    (0-23)
Parameter (EVT_ECDA      = 10) ! Bitmap for dns Endcap Hodo A    (0-23)
Parameter (EVT_ECDB      = 11) ! Bitmap for dns Endcap Hodo B    (0-23)
Parameter (EVT_ECDC      = 12) ! Bitmap for dns Endcap Hodo C    (0-23)
Parameter (EVT_BARUA     = 13) ! Bitmap for half ups Barrel Hodo (0-23)
Parameter (EVT_BARUB     = 14) ! Bitmap for half ups Barrel Hodo (0-23)
Parameter (EVT_BARDA     = 15) ! Bitmap for half dns Barrel Hodo (0-23)
Parameter (EVT_BARDB     = 16) ! Bitmap for half dns Barrel Hodo (0-23)
Parameter (EVT_XVERTEX   = 17) ! X Vertex.  {From CTC}   If no CTC info
```

```
Parameter (EVT_YVERTEX   = 18) ! Y Vertex.  {From CTC}   then unphysical
Parameter (EVT_ZVERTEX   = 19) ! Z Vertex - Weighted avg of TOF & Zchmbr
Parameter (EVT_CTCHITS   = 20) ! Total number of hits in the CTC
Parameter (EVT_CTCGHITS  = 21) ! Total number of good hits in the CTC
Parameter (EVT_CTCTRKS   = 22) ! Total number of tracks int the CTC
Parameter (EVT_CTCPRM    = 23) ! Total number of primaries in the CTC
Parameter (EVT_ETACELLS  = 24) ! Tot. # of occupied eta cells in CTC
Parameter (EVT_ETAPTR    = 25) ! Pointer to CTCeta_nt Ntuple
Parameter (EVT_SPCTRKS   = 26) ! Total number of Spectrometer tracks
Parameter (EVT_SPCPTR    = 27) ! Pointer to Strk_nt Ntuple
Parameter (EVT_TOFCNTRS  = 28) ! Total number of hit TOF counters
Parameter (EVT_TOFPTR    = 29) ! Pointer to TOF_nt Ntuple
Parameter (EVT_WINTRKS   = 30) ! Total # of CTC trks in sectors 6 & 7
Parameter (EVT_WINPTR    = 31) ! Pointer to Window_nt Ntuple



* CTC pseudorapidity Ntuple


 Integer      EtaCTCtup_size
 Parameter   (EtaCTCtup_size = 3)

 Character*8  EtaCTC_nt_tags(EtaCTCtup_size)
 Data         EtaCTC_nt_tags /
:      'CELL    ', 'TRKS    ', 'EVTPTR  ' /

 Integer    CTCETA_CELL, CTCETA_TRKS, CTCETA_EVTPTR

 Parameter (CTCETA_CELL   =  1) ! Which CTC Eta Cell the track occupies
```

```
      Parameter (CTCETA_TRKS    =  2) ! Number of tracks in that cell
      Parameter (CTCETA_EVTPTR  =  3) ! Pointer to the event Ntuple



*     CTC tracks in the solid angle of the Spectrometer Acceptance.
*     Sectors 6 and 7 reside within the Window.  Only z corrected
*     primaries included.

      Integer    Windowtup_size
      Parameter (Windowtup_size=10)

      Character*8 Window_nt_tags(Windowtup_size)
      Data        Window_nt_tags /
     :     'INNERX  ', 'INNERY  ', 'INNERZ ',
     :     'OUTERX  ', 'OUTERY  ', 'OUTERZ ',
     :     'HITMAP  ', 'DRIFTA  ', 'XYCHSQ ',
     :     'EVTPTR  ' /

      Integer    CTCWIN_INNERX, CTCWIN_INNERY, CTCWIN_INNERZ,
     :           CTCWIN_OUTERX, CTCWIN_OUTERY, CTCWIN_OUTERZ,
     :           CTCWIN_HITMAP, CTCWIN_DRIFTA, CTCWIN_XYCHSQ,
     :           CTCWIN_EVTPTR

      Parameter (CTCWIN_INNERX =  1) ! Innermost x
      Parameter (CTCWIN_INNERY =  2) ! Innermost y
      Parameter (CTCWIN_INNERZ =  3) ! Innermost z
      Parameter (CTCWIN_OUTERX =  4) ! Outermost x
      Parameter (CTCWIN_OUTERY =  5) ! Outermost y
      Parameter (CTCWIN_OUTERZ =  6) ! Outermost z
```

```
      Parameter (CTCWIN_HITMAP =  7) ! Bitmap of wires hit   (0-23)
      Parameter (CTCWIN_DRIFTA =  8) ! Drift Angle wrt to sense wire plane
      Parameter (CTCWIN_XYCHSQ =  9) ! Reduced Chi Square in x-y fit
      Parameter (CTCWIN_EVTPTR = 10) ! Pointer to the event Ntuple


*     Spectrometer Ntuple  (Identical to that of MiniDST)

      Integer    Strktup_size
      Parameter (Strktup_size = 20)

      Character*8 Strk_nt_tags(Strktup_size)
      Data        Strk_nt_tags /
     :       'FLG     ', 'P       ', 'PE      ', 'CHISQ   ',
     :       'HITMAP  ', 'YSX0    ', 'YIX0    ', 'ZSX0    ',
     :       'ZIX0    ', 'YSX0ESQ ', 'YIX0ESQ ', 'ZSX0ESQ ',
     :       'ZIX0ESQ ', 'YSX150  ', 'YIX150  ', 'ZSX150  ',
     :       'ZIX150  ', 'LNGTOF1 ', 'LNGTOF2 ', 'EVTPTR  ' /

      Integer    SSTRK_FLG,       SSTRK_P,         SSTRK_PE,
     :           SSTRK_CHISQ,     SSTRK_HITMAP,    SSTRK_YSX0,
     :           SSTRK_YIX0,      SSTRK_ZSX0,      SSTRK_ZIX0,
     :           SSTRK_YSX0ESQ,   SSTRK_YIX0ESQ,   SSTRK_ZSX0ESQ,
     :           SSTRK_ZIX0ESQ,   SSTRK_YSX150,    SSTRK_YIX150,
     :           SSTRK_ZSX150,    SSTRK_ZIX150,    SSTRK_LNGTOF1,
     :           SSTRK_LNGTOF2,   SSTRK_EVTPTR

      Parameter (SSTRK_FLG      =  1) ! Track Flag (1 = Y info)
      Parameter (SSTRK_P        =  2) ! Momentum
      Parameter (SSTRK_PE       =  3) ! Error in Momentum
```

```
      Parameter (SSTRK_CHISQ    =  4) ! Reduced Chi Square
      Parameter (SSTRK_HITMAP   =  5) ! Bit pattern of hit layers  (0-18)
      Parameter (SSTRK_YSX0     =  6) ! Y slope @ x=0        (Beamline)
      Parameter (SSTRK_YIX0     =  7) ! Y intercept @ x=0    (Beamline)
      Parameter (SSTRK_ZSX0     =  8) ! Z slope @ x=0        (Beamline)
      Parameter (SSTRK_ZIX0     =  9) ! Z intercept @ x=0    (Beamline)
      Parameter (SSTRK_YSX0ESQ  = 10) ! Error squared of Y slope @ x=0
      Parameter (SSTRK_YIX0ESQ  = 11) ! Error squared of Y intercept @ x=0
      Parameter (SSTRK_ZSX0ESQ  = 12) ! Error squared of Z slope @ x=0
      Parameter (SSTRK_ZIX0ESQ  = 13) ! Error squared of Z intercept @ x=0
      Parameter (SSTRK_YSX150   = 14) ! Y slope @ x=150cm     (Middle of SDC)
      Parameter (SSTRK_YIX150   = 15) ! Y intercept @ x=150cm (Middle of SDC)
      Parameter (SSTRK_ZSX150   = 16) ! Z slope @ x=150cm     (Middle of SDC)
      Parameter (SSTRK_ZIX150   = 17) ! Z intercept @ x=150cm (Middle of SDC)
      Parameter (SSTRK_LNGTOF1  = 18) ! Path length of track to TOF1
      Parameter (SSTRK_LNGTOF2  = 19) ! Path length of track to TOF2
      Parameter (SSTRK_EVTPTR   = 20) ! Pointer to Evt Ntuple


*  TOF ntuple (Identical to that of the MiniDST)

      Integer    TOFtup_size
      Parameter (TOFtup_size = 6)

      Character*8   TOF_nt_tags(TOFtup_size)
      Data          TOF_nt_tags  /
     :       'CNTRTOF ', 'TIMETOF ', 'XTOF    ',
     :       'YTOF    ', 'ZTOF    ', 'EVTPTR  ' /
```

```
      Integer    TTOF_COUNTER,    TTOF_TIME,     TTOF_X,
     :           TTOF_Y,          TTOF_Z,        TTOF_EVTPTR

      Parameter (TTOF_COUNTER   =  1) ! TOF element that registered hit
      Parameter (TTOF_TIME      =  2) ! Time of flight of hit
      Parameter (TTOF_X         =  3) ! x component of hit
      Parameter (TTOF_Y         =  4) ! y component of hit
      Parameter (TTOF_Z         =  5) ! z component of hit
      Parameter (TTOF_EVTPTR    =  6) ! Pointer to Evt Ntuple
```

VITA

VITA

Philip Lawrence Cole [redacted] In 1983 he graduated from Cornell University with a Bachelor of Arts degree. He majored in Physics. From 1983 to 1985 he was a Teaching Assistant at Purdue University and earned his Masters of Science degree in 1986. [redacted] In 1991, he finally completed his thesis and earned his doctorate degree in Physics. At the time of this writing, he is a postdoc at George Washington University in the field of experimental nuclear physics. And he and his wife lived happily ever after.